



HAL
open science

Synthesis, characterization and activity studies of bio-inspired metallic complexes with Metal-thiolate bond.

Nikita Hall

► **To cite this version:**

Nikita Hall. Synthesis, characterization and activity studies of bio-inspired metallic complexes with Metal-thiolate bond.. Inorganic chemistry. Université de Grenoble, 2013. English. NNT : 2013GRENV073 . tel-01552839

HAL Id: tel-01552839

<https://theses.hal.science/tel-01552839>

Submitted on 3 Jul 2017

HAL is a multi-disciplinary open access archive for the deposit and dissemination of scientific research documents, whether they are published or not. The documents may come from teaching and research institutions in France or abroad, or from public or private research centers.

L'archive ouverte pluridisciplinaire **HAL**, est destinée au dépôt et à la diffusion de documents scientifiques de niveau recherche, publiés ou non, émanant des établissements d'enseignement et de recherche français ou étrangers, des laboratoires publics ou privés.

THÈSE

Pour obtenir le grade de

DOCTEUR DE L'UNIVERSITÉ DE GRENOBLE

Spécialité : **Chimie inorganique et Bio inorganique**

Arrêté ministériel : 7 août 2006

Présentée par

Nikita HALL

Thèse dirigée par **Carole DUBOC**

préparée au sein du **Département de Chimie Moléculaire**
dans l'**École Doctorale Chimie et Sciences du Vivant**

Synthèse, caractérisation et étude de la réactivité de complexes métalliques bio-inspirés à liaison Métal-Thiol.

Thèse soutenue publiquement le **25 Septembre 2013**

devant le jury composé de :

Pr Jean-Pierre, MAHY

Professeur, Université d'Orsay

Rapporteur

Dr Jean-Marc, VINCENT

DR2, Institut des Sciences Moléculaires de Bordeaux

Rapporteur

Dr Jean-Marc, LATOUR

Ingénieur CEA, CEA Grenoble

Président

Dr Maylis, ORIO

CR2, Université de Lille1

Membre

Dr Marie-Noëlle, COLLOMB

DR2, Université Joseph Fourier

Membre

Dr Carole, DUBOC

DR2, Université Joseph Fourier

Membre



Table of Contents

Introduction	1
Résumé	2
Essential Elements for Life	3
Metal-Thiolate Bonds in Metalloproteins.....	3
Molecular Models of Metal-Thiolate Bonds in Metalloproteins	8
Plan of Thesis.....	10
Synthesis, Reactivity and Catalytic Abilities of Dioxo-Vanadium(V) and Oxo-Vanadium(IV) Thiolate Complexes	17
Résumé.....	18
Introduction.....	19
Results and Discussion	22
2.1 Ligand Synthesis.....	22
2.2 Synthesis and Characterisation of the $\text{Et}_3\text{NH}[\text{VO}_2\text{L}^{\text{NS}_2}]$ Complex	24
2.3 Characterisation of the $[\text{VOL}^{\text{N}_2\text{S}_2}]$ Complex	27
2.4 Catalytic Reactivity of $\text{HNet}_3[\text{VO}_2\text{L}^{\text{NS}_2}]$ and $[\text{VOL}^{\text{N}_2\text{S}_2}]$ toward Sulfoxidation	30
2.5 Mechanistic Investigations	35
2.6 Computational Investigation	37
Conclusion	39
Vanadium(III) Alkyl Thiolate Molecular Model in Relation to Vanadium Nitrogenase	43
Résumé.....	44
Introduction.....	45
Results and Discussion	49
3.1 Synthesis and Characterisation of the $[\text{VCl}_2\text{L}^{\text{NS}_2}]^-$ Complex.....	49
3.2 Reduction of $\text{K}[\text{VCl}_2\text{L}^{\text{NS}_2}]$	51
3.3 Reaction of V^{II} species with Hydrazine	53
Conclusion	54
Nickel Alkyl-Thiolate Molecular Models for Metalloenzymes CODH and NiSOD	57
Résumé.....	58
Introduction.....	59
Results and Discussion	63
4.1 Synthesis and Characterisation of the $[\text{Ni}_2(\text{L}^{\text{NS}_2})_2]$ Complex.....	63
4.2 Synthesis and Characterisation of the $[\text{NiL}^{\text{NS}_2}\text{dmpe}]$ Complex.....	65
4.3 Activation of Carbon Monoxide	67
4.4 Characterisation of the $[\text{NiL}^{\text{N}_2\text{S}_2}]$ Complex.....	68
4.5 Reactivity of the Intermediate Species toward Oxidation	72
Conclusion	73

Characterisation of the Electronic Structure of Cobalt (II) and (III) Thiolate Complexes and an Investigation of their Reactivity	77
Résumé	78
Introduction.....	79
Results and Discussion.....	82
5.1 Synthesis and Characterisation of the [CoL ^{N2S2}] Complex	82
5.2 Synthesis and Characterisation of the [Co ₂ (L ^{N2S2}) ₂](PF ₆) ₂ Complex.....	90
5.3 Synthesis and Characterisation of the [CoL ^{N2S2} Cl] Complex	92
5.4 Reactivity of [CoL ^{N2S2}] toward S-Alkylation	96
Conclusion.....	100
Jahn-Teller Effect in a Mononuclear Copper(II) Complex Containing a Hexadentate Ligand	105
Résumé	106
Introduction.....	107
Results and Discussion.....	109
6.1 Ligand Synthesis	109
6.2 X-Ray Structure Investigations	110
6.3 EPR Investigations	117
6.4 Comparison with Literature	123
Conclusion.....	126
Conclusion	129
Résumé	130
Conclusion.....	133
Experimental	137
General Methods.....	139
Ligand Preparation.....	141
Preparation of Complexes	145
Appendix	151
Abbreviations	159

CHAPTER I

Introduction

Résumé

Les ions de métaux de transition, présents dans environ 50% des protéines, sont impliqués dans un grand nombre de processus biologiques. Les sites actifs peuvent être décrits comme des complexes inorganiques sophistiqués et plus ou moins directement liés à la chaîne polypeptidique de la protéine. Les ligands les plus communément rencontrés sont de type azoté ou oxygéné. Il existe également toute une classe de clusters métalliques qui utilise des ligands soufrés : fonction thiol via la cystéine, fonction thioether via la méthionine, ou bien encore l'ion sulfure. La liaison métal-soufre confère à ces complexes des propriétés originales, tant au niveau de leur structure électronique, que de leurs propriétés redox ou de leur réactivité.

A travers des exemples variés de sites actifs de nombreuses métalloprotéines, les différents types de liaison métal-soufre et modes de coordination sont d'abord présentés dans ce mémoire. Ces protéines sont impliquées dans divers processus dont (i) les transferts d'électron(s), (ii) l'activation de petites molécules comme le dioxygène, l'hydrogène ou bien encore le diazote, (iii) les réactions d'oxydation via des transferts de groupes oxo et (iv) les réactions non redox comme les hydrolyses ou le transfert de groupement méthyle. Plus particulièrement, la liaison métal-thiol, de par son caractère covalent fort avec la plupart des ions de métaux de transition, est à l'origine de spectres d'absorption UV-visible particuliers avec des transitions intenses de faible énergie, ainsi que de propriétés RPE spécifiques. Les études reportées dans la littérature, pour trois séries de complexes synthétiques dans lesquels seule la nature du métal change, sont discutées pour illustrer la structure électronique particulière des complexes possédant une liaison métal-thiol.

Dans ce contexte, les différents projets développés au cours de cette thèse, qui concerne essentiellement l'étude des propriétés de complexes bioinspirés à liaison métal-thiol, sont présentés dans les quatre chapitres suivants. Deux types de ligands ont été utilisés : l'un tridentate L^{NS_2} , l'autre tétradentate, $L^{N_2S_2}$. Ces deux ligands possèdent deux fonctions thiolates aliphatiques encombrées et une ou deux fonctions azotées, issues respectivement d'une pyridine ou d'une bipyridine.

Enfin, le dernier chapitre concerne un travail initié au cours de mon Master. Il s'agit de l'étude d'un complexe mononucléaire de cuivre(II) contenant un ligand hexadentate de type N_6 , présentant une pseudo compression de type Jahn-Teller.

Essential Elements for Life

More than one third of the elements (excluding actinides and lanthanide elements), are essential for life (Scheme 1.1).¹ Of these, only eleven elements are found in all known organisms; hydrogen, carbon, nitrogen, oxygen, sodium, potassium, calcium, magnesium, potassium, sulfur and chlorine.² After discoveries in the 19th century demonstrating that plants and yeast depend on metals such as iron, manganese, copper, and zinc for growth, further studies were initiated on defining which other chemical elements are essential for life.³ Thus, after the eleven essential bulk elements, the remaining can be divided into two categories; (i) essential trace elements, including vanadium, chromium, manganese, iron, cobalt, nickel, copper, zinc, molybdenum, boron, silicon, selenium, fluorine and iodine, and (ii) possible essential trace elements for some species, including arsenic, bromine, strontium, cadmium, tin, barium and tungsten.

1 H 1.008 Hydrogen																	2 He 4.003 Helium
3 Li 6.941 Lithium	4 Be 9.012 Beryllium											5 B 10.81 Boron	6 C 12.01 Carbon	7 N 14.01 Nitrogen	8 O 16.00 Oxygen	9 F 18.99 Fluorine	10 Ne 20.18 Neon
11 Na 22.99 Sodium	12 Mg 24.31 Magnesium											13 Al 26.98 Aluminum	14 Si 28.09 Silicon	15 P 30.97 Phosphorus	16 S 32.06 Sulfur	17 Cl 35.45 Chlorine	18 Ar 39.95 Argon
19 K 39.10 Potassium	20 Ca 40.08 Calcium	21 Sc 44.96 Scandium	22 Ti 47.88 Titanium	23 V 50.94 Vanadium	24 Cr 52.00 Chromium	25 Mn 54.94 Manganese	26 Fe 55.85 Iron	27 Co 58.93 Cobalt	28 Ni 58.69 Nickel	29 Cu 63.55 Copper	30 Zn 65.38 Zinc	31 Ga 69.72 Gallium	32 Ge 72.64 Germanium	33 As 74.92 Arsenic	34 Se 78.96 Selenium	35 Br 79.90 Bromine	36 Kr 83.80 Krypton
37 Rb 85.47 Rubidium	38 Sr 87.62 Strontium	39 Y 88.91 Yttrium	40 Zr 91.22 Zirconium	41 Nb 92.91 Niobium	42 Mo 95.94 Molybdenum	43 Tc 98 Technetium	44 Ru 101.07 Ruthenium	45 Rh 102.91 Rhodium	46 Pd 106.42 Palladium	47 Ag 107.87 Silver	48 Cd 112.41 Cadmium	49 In 114.82 Indium	50 Sn 118.71 Tin	51 Sb 121.76 Antimony	52 Te 127.60 Tellurium	53 I 126.91 Iodine	54 Xe 131.29 Xenon
55 Cs 132.91 Cesium	56 Ba 137.33 Barium	57-71 La-Lu Lanthanum-Lutetium	72 Hf 178.49 Hafnium	73 Ta 180.95 Tantalum	74 W 183.84 Tungsten	75 Re 186.21 Rhenium	76 Os 190.23 Osmium	77 Ir 192.22 Iridium	78 Pt 195.08 Platinum	79 Au 196.97 Gold	80 Hg 200.59 Mercury	81 Tl 204.38 Thallium	82 Pb 207.2 Lead	83 Bi 208.98 Bismuth	84 Po 209 Polonium	85 At 210 Astatine	86 Rn 222 Radon
87 Fr 223 Francium	88 Ra 226 Radium	89 Ac Actinide	90 Th 232.04 Thorium	91 Pa 231.04 Protactinium	92 U 238.03 Uranium												

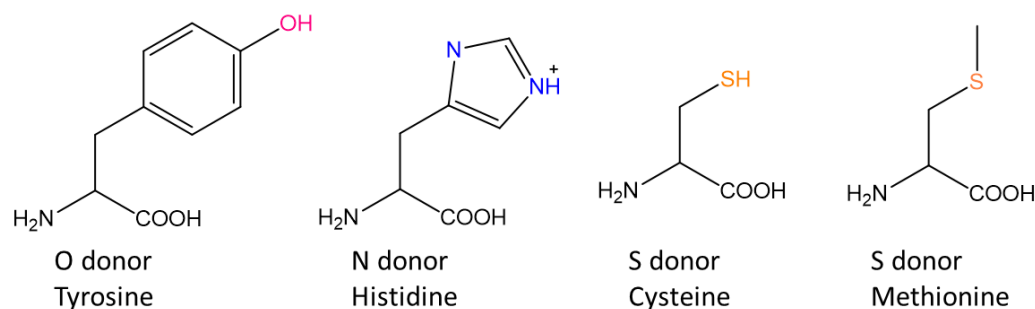
Bulk biological elements
 Trace elements believed to be essential for bacteria, plants or animals
 Possibly essential trace elements for some species

Scheme 1.1. Elements essential for life.³

Metal-Thiolate Bonds in Metalloproteins

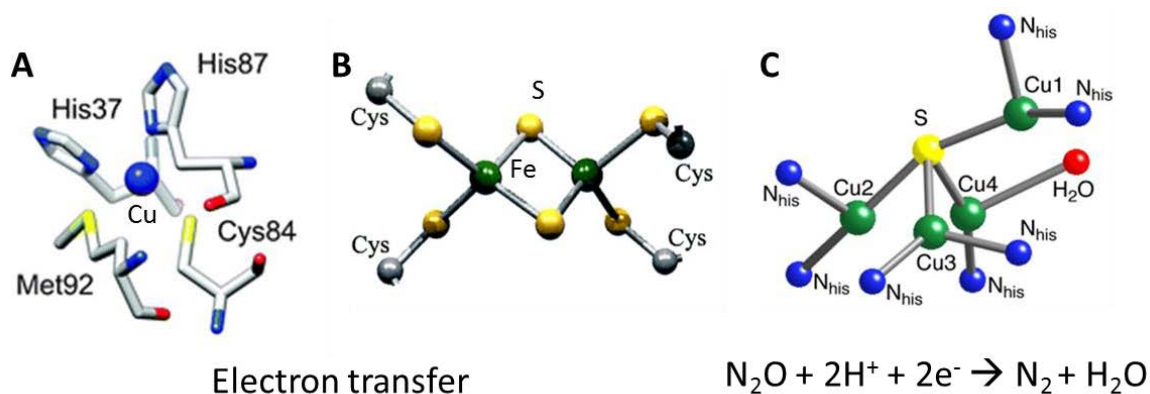
Metal cations are constituents of approximately 50 % of all proteins,⁴ and they are involved in a huge variety of different processes. These include important structural roles, electron transfer, activation of small molecules such as, molecular dioxygen, hydrogen and dinitrogen, oxo-transfer, and non-redox reactions. All of these processes take place at the active site of a metalloprotein, those that are involved in redox or chemical reactions are defined as metalloenzymes.^{1,5,6} Active sites can be regarded as elaborate inorganic complexes, where the metal ion is directly bound to the protein or

to enzyme-bound non-protein components mainly *via* nitrogen, oxygen, and sulfur donor atoms from amino acid residues. Some examples are shown in Scheme 1.2.



Scheme 1.2. Examples of N-, O-, and S- donor ligands from selected amino acids.

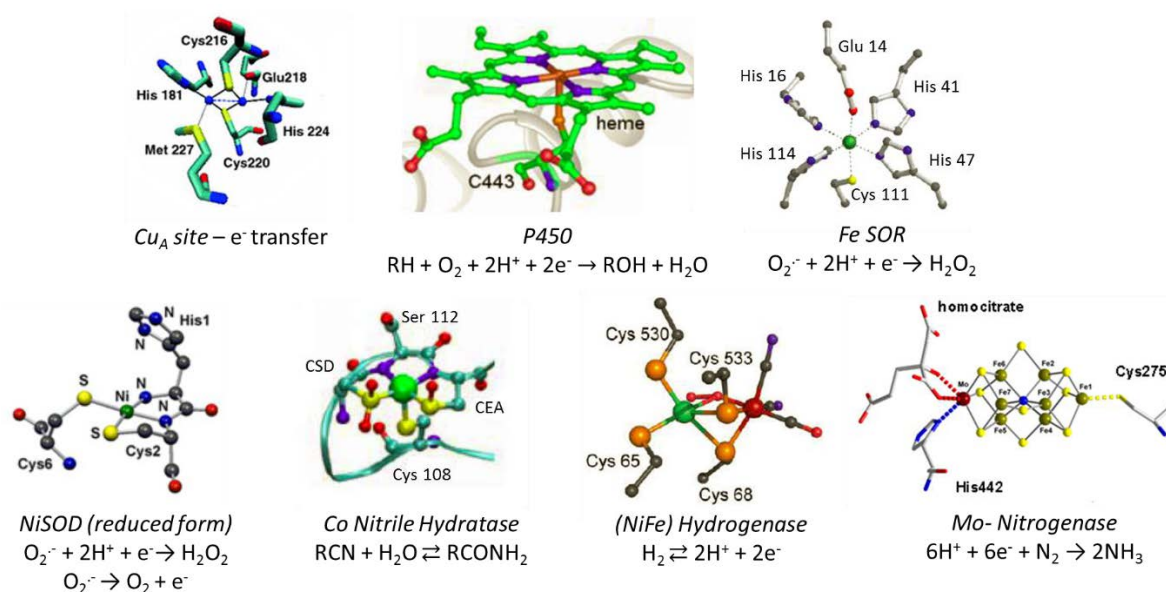
By far, the most studied active sites contain nitrogen and oxygen donor atoms. In fact, of the 21 amino acids, there are only two that contain sulfur donor atoms, cysteine and methionine (Scheme 1.2). In contrast to the 'more common nitrogen and oxygen 'hard' donor atoms, the sulfur atom is a 'soft' donor and thus in general, preferentially binds to soft cations. In turn, the utilisation of sulfur donor atoms in a coordination complex gives unique reactivity and electronic properties. One such example is that the sulfur atom confers a high redox potential to metal redox couples, due to the fact that low oxidation state metal ions are softer than their oxidised counterparts.



Scheme 1.3. Different sulfur coordination groups **A**) a mixed thioether, thiolate coordination in plastocyanin,⁷ **B**) Iron-thiolate in ferredoxin,⁸ and **C**) a tetranuclear copper-sulfur complex (Cu_z) in nitrous oxide reductase.

Sulfur atoms in the form of thiolates, thioethers or inorganic sulfide have been shown to act as donor ligands in a variety of metalloprotein active sites.⁹ Sulfur ligands can act either as a terminal or bridging ligand. Examples of various binding modes of the different sulfur ligand groups in active sites are shown in Scheme 1.3. The mononuclear copper centre of plastocyanin (Scheme 1.3A), which was the first characterised blue

copper protein, contains two bound histidines, one cysteine and one methionine residue, i.e. both a thiolate and a thioether ligand. Plastocyanin acts as an electron transfer agent between cytochrome *f* and cytochrome *b₆f* complex in photosystem II and P700+ from photosystem I.¹⁰⁻¹² The Fe₂S₂ ferredoxin (Scheme 1.3B) contains two sulfide bridges and also four bound cysteine residues. Along with other ferredoxin proteins, they are involved in electron transfer for a variety of metabolic reactions.¹³ Finally, the copper-sulfur cluster Cu_z (Scheme 1.3C), is the catalytic centre for nitrous oxide reductase, which reduces nitrous oxide into dinitrogen. The Cu_z centre is a unique μ₄-sulfur bridged tetracopper cluster complex in which the four copper ions are ligated by seven histidine, one oxygen (water or hydroxyl) and one sulfur (inorganic bridging sulfur) ligands.^{14,15} It has been shown from the investigation of these various centres that each different sulfur ligand group gives its own specific properties to the active site, i.e. the electronic, redox, and functional properties. We will focus specifically on the more common metal-thiolate bond, and the particular properties and reactivity associated with this bond.



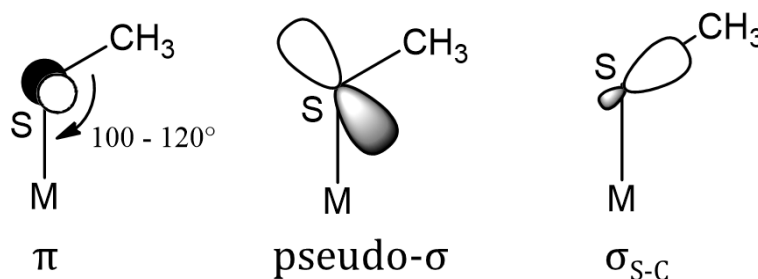
Scheme 1.4. Metal-thiolate-containing active sites.

Metal-thiolate bonds are present in many classes of metalloprotein active sites and make major contributions to function (see Scheme 1.4 for examples). As seen above in Scheme 1.3, the blue copper site, the iron-sulfur cluster sites, and also the mixed valence binuclear Cu_A site,^{9,16,17} are involved in the most efficient electron transfer reactions. The main heme enzyme involved in O₂ activation (P450), contains an axial Fe-thiolate bond.¹⁸ Also there are the enzymes involved in superoxide reactivity, including the

superoxide reductase (FeSOR), a non-heme Fe complex containing a cysteine residue,¹⁹ and the Ni superoxide dismutase (NiSOD) containing two Ni-thiolate bonds.²⁰ Metal-thiolate bonds are also found in enzymes involved in Lewis acid catalysis including nitrile hydratase (Fe^{III} and Co^{III})²¹⁻²³ and deformylase (Fe^{II}). Sulfur-rich Zn-containing metalloenzymes are found in the large domain of Zn-dependent hydrolases and S-alkylation enzymes.²⁴ Other metalloenzymes with bridging thiolate ligation include those which activate small molecules, such as hydrogenases, in which a binuclear cluster (Fe-Fe, or Ni-Fe) is involved in the reversible reduction of protons into dihydrogen,^{25,26} and also the Fe-, Mo- or V- nitrogenases, which exhibit an unprecedented heteronuclear sulfur-bridged complex.^{27,28}

Electronic Properties of the Metal –Thiolate Bond

The general feature of all these metalloproteins and enzymes is that they have unique spectral features; intense and low energy absorption bands together with unusual spin Hamiltonian parameters, reflecting highly covalent thiolate-metal bonding. This is due to the valence molecular orbitals of the sulfur atom (Scheme 1.5).



Scheme 1.5. Sulfur-based valence orbitals of a metal-methyl thiolate bond.⁵

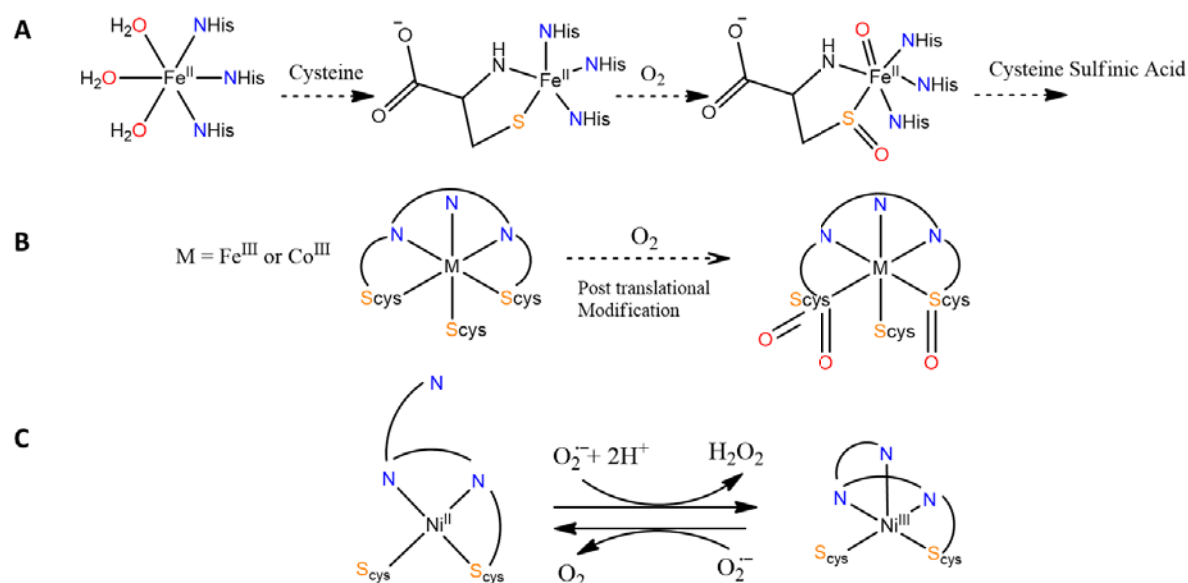
The thiolate ligand has three valence 3p orbitals, one of which is greatly stabilized in energy due to the carbon-sulfur σ bond, and thus does not significantly contribute to the thiolate sulfur-metal bond. The two remaining 3p orbitals perpendicular to the S-C bond dominate the thiolate interaction with the metal centre. The 3p orbital out of the C-S-M plane is involved in π bonding, while the in-plane 3p orbital pseudo σ bonds to the metal ion.⁵ It is pseudo σ as, when the C-S-M angle decreases below 90° , its electron density is shifted into the line of the metal–thiolate bond. Therefore the interaction of these two 3p orbitals depend on the C-S-M angle, normally between $100 - 120^\circ$. Evidently, the extent of covalency is also influenced by the electronic properties of the metal ion.

An example of this is seen clearly in the blue copper proteins, which are characterised by an intense $\text{Cys}^- \rightarrow \text{Cu}^{\text{II}}$ LMCT (ligand to metal charge transfer) transition near 600 nm

($\epsilon > 5000 \text{ M}^{-1}\text{cm}^{-1}$).⁹ The high covalent character of the Cu-thiolate bond is also evidenced by EPR spectroscopy. This high covalency reduces the parallel hyperfine coupling (A_{\parallel}), to less than half of the usual value observed in normal Cu^{II} complexes, and results in low g values.

Reactivity of the Metal-Thiolate Bond

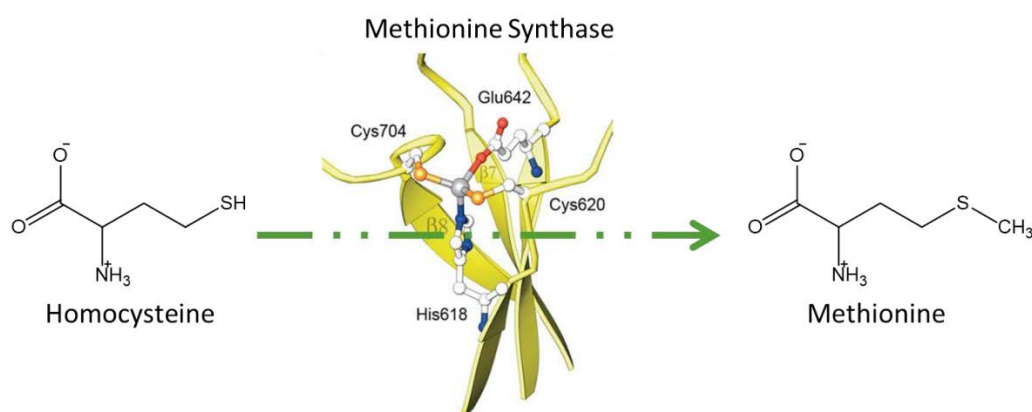
Another difference between S-thiolate donor atoms compared to N- and O- donor atoms is their reactivity. Bound thiolates exhibit two different reactivities; S-oxygenation and S-alkylation.



Scheme 1.6. Cysteine oxygenation in metalloenzymes **A)** cysteine dioxygenase and **B)** nitrile hydratase and **C)** the reactivity of the NiSOD.

S-oxygenation reactions play crucial biological roles. For example, cysteine dioxygenase and nitrile hydratase undergo cysteine S-oxygenation (Scheme 1.6 **A** and **B**). Cysteine dioxygenase, is a mammalian non-heme iron enzyme that catalyses the conversion of L-cysteine into cysteine sulfinic acid by molecular dioxygen.^{29,30} Nitrile hydratase is a mononuclear non-heme iron or non-corrinoid cobalt enzyme, which catalyses the reduction of diverse nitriles into their corresponding amines. An activation step is required, involving the oxygenation of two of the cysteines; one into cysteine sulfenate and the other into cysteine sulfinic acid.^{22,31,32} What causes this activation step is still unknown. What is particularly interesting is that, in contrast to the above examples, the two bound cysteines in the NiSOD active site do not undergo oxygenation in the presence of highly reactive oxidative species, i.e. the substrate (superoxide anion radical), and the products (dioxygen, and hydrogen peroxide) (Scheme 1.6C).^{33,34}

S-alkylation is also another important type of reactivity and is mediated by a number of zinc-containing enzymes. For example, the ADA protein, which participates in the repair of DNA, contains four bound cysteines in the zinc active site.³⁵⁻³⁷ Methionine synthases catalyse the formation of the amino acid methionine by methyl group transfer from either methyltetrahydrofolate (MetE) and/or methylcobalamin (MethH) to a zinc bound homocysteinate ligand (Scheme 1.7).³⁸



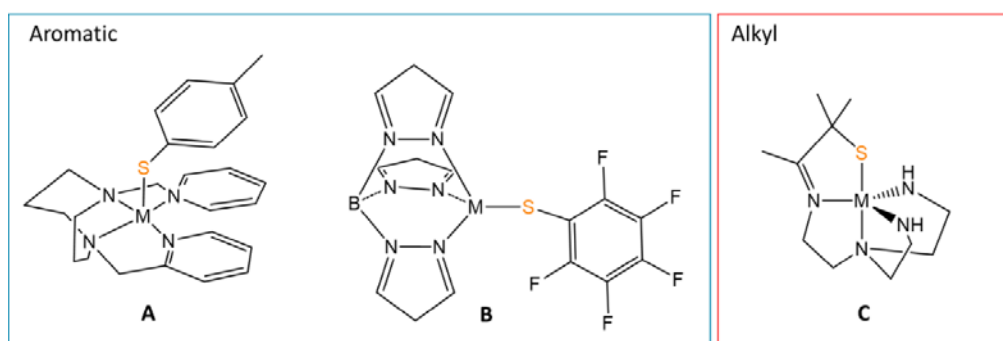
Scheme 1.7. S-alkylation reaction in methionine synthase. The X-ray structure shows the resting state of the Zn active site.

From the above examples, it can be seen that although the ligated thiolate groups give specific properties, the chosen metal ion, unsurprisingly, also plays a major role in the function of the metalloprotein. For example, active sites which carry out oxo transfer *via* S-oxygenation, are usually centred at an iron metal ion, whereas alkyl transfer *via* S-alkylation takes place in zinc-containing active sites. To fully understand why nature uses cysteinate residues to promote specific biological functions, a comprehensive understanding of the influence of thiolate ligands on the electronic, magnetic, and functional properties of first-row transition metal ions is required.³⁹ A correlation between structure, key properties, and function can be found by building small molecular analogues of these sites, termed molecular models.

Molecular Models of Metal-Thiolate Metalloproteins

In general, the use of molecular models is not only interesting for a further understanding of the mechanisms and the fundamentals of metalloproteins, but also because of the prospect of cheap, energy efficient catalysts for extremely important reactions. Such examples are the reduction of CO₂ and the production of H₂ as sources of energy, and many other reactions, which nature can carry out, efficiently and selectively. Therefore, over the second half of the 20th century, when X-ray structures of

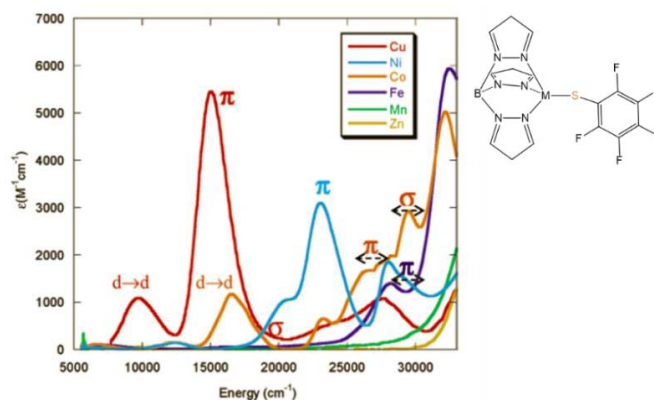
metalloproteins became routinely available, the area of bioinorganic chemistry exploded and is still now a fast moving field that is equally rich in substance and promise. In this section, I will focus on three molecular models, the reactivities and structures of which have been studied as a function of the first-row transition metals (Scheme 1.8). Molecular models related to metalloproteins of interest in this thesis will be presented in the corresponding later chapters.



Scheme 1.8. Molecular models for metal-thiolate metalloenzymes. **A)** $[M^{II}L(SPhMe)]$,⁴⁰ **B)** $[ML(SC_6F_5)]$,^{41,42} and **C)** $[M(S^{Me_2}N_4(tren))]^+$.³⁹

Two of the molecular models, **A** and **B**, contain monodentate aromatic thiolates, while the other (**C**) contains a pentadentate ligand with one alkyl thiolate. As stated above, one similarity between all metal-thiolate-containing active sites is their intense, low energy charge transfer transitions (except for d^{10} Zn^{II} and high spin d^5 Mn^{II} complexes). This is also a common factor in molecular models. The effect of the metal-thiolate electronic properties is clearly shown in **A** where the weak visible absorption features of both the cobalt(II) and nickel(II) precursors (Co^{II} (λ , nm(ϵ , $M^{-1} cm^{-1}$)); 319(2100), 491(140). Ni^{II} (λ , nm(ϵ , $M^{-1} cm^{-1}$)); 357(80), 502(120)), are replaced by intense absorptions (Co^{II} (λ , nm(ϵ , $M^{-1} cm^{-1}$)); 344 (3300), 378(2800), 430(1300), 560(1300), 560(200). Ni^{II} (λ , nm(ϵ , $M^{-1} cm^{-1}$)); 361(2100), 444(2500), 474(2600)) upon thiolate ligation.

Scheme 1.9 shows the electronic absorption spectra of the **B** series, including Mn^{II} , Fe^{II} , Co^{II} , Ni^{II} , Cu^{II} and Zn^{II} . It can be seen that each complex (with the exception of Mn^{II} and Zn^{II}) displays LMCT transitions attributed to the S-thiolate to metal transitions in the visible region. From series **A** and **B** the same trend is observed; the LMCT shifts to higher energy and decreases in intensity going from Cu^{II} to Co^{II} . For the alkyl thiolate series **C**, the LMCT features are in general at higher energy and exhibit lower intensity, consistent with higher covalency of the M-thiolate bond.³⁹



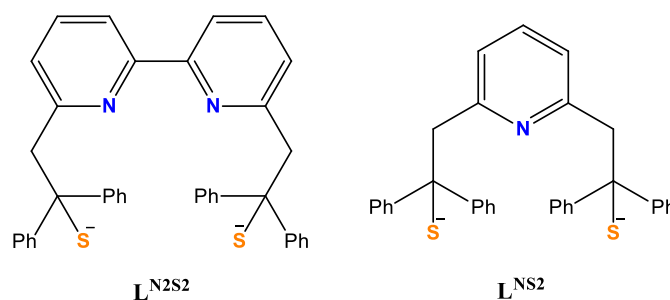
Scheme 1.9. Electronic absorption spectra of $[ML(SC_6F_5)](B)$.⁴²

Along with physical properties, molecular models can also be used to test specific reactions. The metal series of **A** (Fe^{II} , Co^{II} , Ni^{II} and Zn^{II}) has been investigated toward S-alkylation, using benzyl bromide as the alkylating agent. Fox *et. al.* found that the reaction kinetics for S-alkylation for both Fe^{II} and Co^{II} complexes are approximately one order of magnitude slower than that for the Ni^{II} and Zn^{II} derivatives. Furthermore, upon S-alkylation, decoordination of the thioether product is observed. In order to further study the properties of the metal thioether bond, DFT calculations were carried out. They have demonstrated that this bond is stronger in the Ni^{II} complex than in both the Zn^{II} and Co^{II} derivatives. This can perhaps partly explain why Zn^{II} is found in the active sites of metalloenzymes involved in S-alkylation reactions.⁴⁰

Plan of Thesis

The aim of the work described in this thesis is the synthesis and characterisation of bio-inspired molecular complexes containing metal alkyl thiolate bonds with the goal of modelling the associated metalloprotein. The synthesis of model complexes with alkyl thiolate ligands is far from trivial and remains a real challenge.⁴³ A major synthetic problem is that such metal–thiolate complexes are generally prone to metal-reduction processes with the concomitant formation of disulfides or, in the presence of dioxygen, S-oxygenation.⁴⁴ Also, thiolate groups are known to coordinate in a bridging mode generating polynuclear complexes. Steric bulk is usually required to avoid these undesirable reaction pathways.⁴⁵

For this purpose, two ligands, tetradentate $L^{N_2S_2}$ and tridentate L^{NS_2} , have been used (Scheme 1.10). Both ligands consist of aromatic nitrogen (bipyridine or pyridine) donor atoms and also bulky S-thiolate donor atoms.



Scheme 1.10. A schematic diagram of the ligands used in this thesis L^{N2S2} and L^{NS2} .

Both L^{N2S2} and L^{NS2} have been previously described.^{46–48} Before my arrival, a substantial amount of research had been carried out using L^{N2S2} in our group, with Cu^{II} ,^{43,49} Ni^{II} ,^{47,50} and Zn^{II} derivatives.⁵¹ From these investigations, the corresponding complexes have proven to be effective structural mimics for thiolate-containing metalloproteins, and more importantly have shown an ability to mimic specific functions, such as electronic properties, and thiolate reactivity. The L^{N2S2} ligand was used to isolate and characterise the first dicopper system with a $[Cu_2S_2]$ core, rendering an accurate structural and functional model for the biological Cu_A site.⁴³ The NiL^{N2S2} system was also shown to mimic the structural changes observed during the NiSOD catalytic cycle by the reversible apical binding of an imidazole upon oxidation (Scheme 1.6C).⁴⁷ This Ni^{II} complex has also been investigated toward S-alkylation in comparison with the Zn^{II} derivative.⁵¹ A significant difference was found in the electronic properties of the corresponding M-thioether bond. Upon S-methylation, the resulting thioether unit decoordinates from the Zn^{II} derivate, while in the Ni^{II} derivate, it remains bound, in agreement with the previous work of Fox *et. al.* with an aryl thiolate ligand.⁴⁰

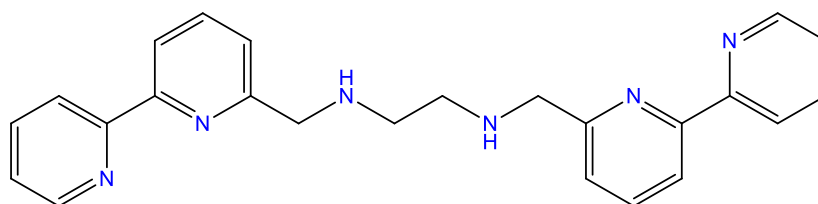
This thesis details the continuation and extension of this work to both the synthesis of a new tridentate ligand, and the study of new complexes as biologically relevant molecular models. The manuscript is divided into five chapters. The second reports the synthesis and characterisation of a dioxo V^V complex $[VO_2L^{NS2}](Et_3NH)$ and an oxo V^{IV} complex $[VOL^{N2S2}]$ along with their catalytic activity toward sulfoxidation. An in-depth mechanistic investigation, using EPR, ^{51}V NMR spectroscopy, and computational calculations has also been carried out on the active intermediate species involved during catalysis.

Chapter three presents a summary of work carried out on the synthesis and characterisation of a molecular model for vanadium dependent nitrogenases. For this purpose a V^{III} complex $[(VCl_2L^{NS2})K]$ has been synthesised and characterised by X-ray

crystallography. Due to the high instability of this complex only preliminary results for reduction of this V^{III} complex to a V^{II} species and its associated reactivity toward hydrazine is presented and discussed.

Chapter four concentrates on nickel-thiolate-containing metalloproteins, including CODH (carbon monoxide dehydrogenase) involved in CO activation, and NiSOD (Nickel superoxide dismutase), which disproportionates the superoxide radical anion into hydrogen peroxide and molecular dioxygen. In this chapter, two novel Ni^{II} complexes, $[(NiL^{NS2})_2]$, $[NiL^{NS2}dmpe]$, have been synthesised and characterised. Both have been tested toward the activation of CO. In the second part of this chapter, the reactivity of the previously described $[NiL^{N2S2}]$ in the presence of TBHP (*tert*-butyl hydroperoxide) has been investigated with the aim of isolating new peroxo intermediate species.

Chapter five reports the synthesis and characterisation of three Co-thiolate complexes. A mononuclear $[CoL^{N2S2}]$ has been studied as a spectroscopic probe for zinc-containing metalloproteins, involved in S-alkylation. In this context, we have tested the reactivity of $[CoL^{N2S2}]$ toward S-alkylation and have compared its reactivity with that of the previously described $[ZnL^{N2S2}]$ and $[NiL^{N2S2}]$ complexes.⁵¹ In order to model CoNHase, we have attempted to synthesise a mononuclear Co^{III} complex. However, in the absence of a strong donor ligand such as a chloride anion, the Co^{II} dimer $[Co_2(L^{N2S2})_2]$ was obtained. This dimer has subsequently been investigated and characterised. The Co^{III} complex $[CoL^{N2S2}Cl]$ has been obtained by the incorporation of a chloride anion in the Co^{III} coordination sphere. This complex has been fully characterised and its reactivity in the presence of hydrogen peroxide tested.



Scheme 1.11. Schematic diagram of the bmet ligand presented in chapter six.

Chapter six presents work continued from my MSc research performed at the University of Otago, under the supervision of Assoc. Prof. Allan Blackman. This work focuses primarily on the Jahn-Teller effect in Cu^{II} octahedral complexes. The ligand used for this work (Scheme 1.11), has been previously incorporated in various metal complexes including those containing Co^{III} ,⁵² Mn^{II} and Ni^{II} .⁵³ Therefore, in chapter six, we report the

synthesis and characterisation of two copper complexes, $[\text{Cu}(\text{bmet})](\text{Br})_2$ and $[\text{Cu}(\text{bmet})](\text{ClO}_4)_2$, differing only in their counter anion. An isostructural zinc complex $[\text{Zn}(\text{bmet})](\text{ClO}_4)_2$ is also reported here and has been used as a diamagnetic host lattice. An in depth investigation, using X-ray crystallography, EPR spectroscopy and theoretical calculations has been carried out to further understand the Jahn-Teller effect in these copper complexes.

In chapter II, IV, V and VI, we present DFT calculations along with experimental results. All theoretical calculations have been carried out in collaboration with Maylis Orio at the Université des Science et Technologies de Lille, LASIR.

References

- (1) Thomson, A. J.; Gray, H. B. *Curr. Opin. Chem. Biol.* **1998**, *2*, 155–158.
- (2) Silva, J. J. R. F. da; Williams, R. J. P. *The Biological Chemistry of the Elements: The Inorganic Chemistry of Life*; Oxford University Press, 2001.
- (3) *Metallomics* **2012**, *4*, 1017–1019.
- (4) Tus, A.; Rakipovic, A.; Peretin, G.; Tomic, S.; Sikic, M. *Nucleic Acids Res.* **2012**, *40*, W352–W357.
- (5) Solomon, E. I.; Gorelsky, S. I.; Dey, A. J. *Comput. Chem.* **2006**, *27*, 1415–1428.
- (6) Garner, C. D. *J. Chem. Soc. Dalton Trans.* **1997**, 3903–3908.
- (7) Nagasawa, Y.; Fujita, K.; Katayama, T.; Ishibashi, Y.; Miyasaka, H.; Takabe, T.; Nagao, S.; Hirota, S. *Phys. Chem. Chem. Phys.* **2010**, *12*, 6067–6075.
- (8) Frazzon, J.; Dean, D. R. *Proc. Natl. Acad. Sci.* **2001**, *98*, 14751–14753.
- (9) Belle, C.; Rammal, W.; Pierre, J.-L. *J. Inorg. Biochem.* **2005**, *99*, 1929–1936.
- (10) Díaz-Quintana, A.; Navarro, J. A.; Hervás, M.; Molina-Heredia, F. P.; Cerda, B. D. la; Rosa, M. A. D. la *Photosynth. Res.* **2003**, *75*, 97–110.
- (11) Redinbo, M. R.; Yeates, T. O.; Merchant, S. J. *Bioenerg. Biomembr.* **1994**, *26*, 49–66.
- (12) Bernroitner, M.; Zamocky, M.; Pailer, M.; Furtmüller, P. G.; Peschek, G. A.; Obinger, C. *Chem. Biodivers.* **2008**, *5*, 1927–1961.
- (13) Beinert, H.; Holm, R. H.; Münck, E. *Science* **1997**, *277*, 653–659.
- (14) Dell'Acqua, S.; Pauleta, S. R.; Moura, I.; Moura, J. J. G. *JBIC J. Biol. Inorg. Chem.* **2011**, *16*, 183–194.
- (15) Chen, P.; Gorelsky, S. I.; Ghosh, S.; Solomon, E. I. *Angew. Chem. Int. Ed.* **2004**, *43*, 4132–4140.
- (16) Gray, H. B.; Malmström, B. G.; Williams, R. J. P. *JBIC J. Biol. Inorg. Chem.* **2000**, *5*, 551–559.
- (17) Savelieff, M. G.; Lu, Y. *JBIC J. Biol. Inorg. Chem.* **2010**, *15*, 461–483.
- (18) Seward, H. E.; Roujeinikova, A.; McLean, K. J.; Munro, A. W.; Leys, D. J. *Biol. Chem.* **2006**, *281*, 39437–39443.
- (19) Yeh, A. P.; Hu, Y.; Jenney, Adams, M. W. W.; Rees, D. C. *Biochemistry (Mosc.)* **2000**, *39*, 2499–2508.
- (20) Fiedler, A. T.; Bryngelson, P. A.; Maroney, M. J.; Brunold, T. C. *J. Am. Chem. Soc.* **2005**, *127*, 5449–5462.
- (21) Huang, W.; Jia, J.; Cummings, J.; Nelson, M.; Schneider, G.; Lindqvist, Y. *Structure* **1997**, *5*, 691–699.
- (22) Kobayashi, M.; Shimizu, S. *Nat. Biotechnol.* **1998**, *16*, 733–736.
- (23) Peplowski, L.; Kubiak, K.; Nowak, W. J. *Mol. Model.* **2007**, *13*, 725–730.
- (24) McCall, K. A.; Huang, C.; Fierke, C. A. *J. Nutr.* **2000**, *130*, 1437S–1446S.
- (25) Allakhverdiev, S. I.; Thavasi, V.; Kreslavski, V. D.; Zharmukhamedov, S. K.; Klimov, V. V.; Ramakrishna, S.; Los, D. A.; Mimuro, M.; Nishihara, H.; Carpentier, R. *J. Photochem. Photobiol. C Photochem. Rev.* **2010**, *11*, 101–113.
- (26) McGlynn, S. E.; Mulder, D. W.; Shepard, E. M.; Broderick, J. B.; Peters, J. W. *Dalton Trans.* **2009**, 4274–4285.
- (27) Dance, I. *Dalton Trans.* **2010**, *39*, 2972.
- (28) Ramaswamy, S. *Science* **2011**, *334*, 914–915.
- (29) Joseph, C. A.; Maroney, M. J. *Chem. Commun.* **2007**, 3338–3349.
- (30) Aluri, S.; de Visser, S. P. *J. Am. Chem. Soc.* **2007**, *129*, 14846–14847.
- (31) Nagashima, S.; Nakasako, M.; Dohmae, N.; Tsujimura, M.; Takio, K.; Odaka, M.; Yohda, M.; Kamiya, N.; Endo, I. *Nat. Struct. Mol. Biol.* **1998**, *5*, 347–351.
- (32) Hopmann, K. H.; Guo, J.-D.; Himo, F. *Inorg. Chem.* **2007**, *46*, 4850–4856.
- (33) Barondeau, D. P.; Kassmann, C. J.; Bruns, C. K.; Tainer, J. A.; Getzoff, E. D. *Biochemistry (Mosc.)* **2004**, *43*, 8038–8047.
- (34) Bryngelson, P. A.; Maroney, M. J. In *Nickel and Its Surprising Impact in Nature*; Sigel, A.; Sigel, H.; Sigel, R. K. O., Eds.; John Wiley & Sons, Ltd, 2007; pp. 417–443.
- (35) Myers, L. C.; Terranova, M. P.; Ferentz, A. E.; Wagner, G.; Verdine, G. L. *Science* **1993**, *261*, 1164–1167.
- (36) Myers, L. C.; Cushing, T. D.; Wagner, G.; Verdine, G. L. *Chem. Biol.* **1994**, *1*, 91–97.
- (37) Ohkubo, T.; Sakashita, H.; Sakuma, T.; Kainosho, M.; Sekiguchi, M.; Morikawa, K. *J. Am. Chem. Soc.* **1994**, *116*, 6035–6036.
- (38) Drennan, C. L.; Huang, S.; Drummond, J. T.; Matthews, R. G.; Lidwig, M. L. *Science* **1994**, *266*, 1669–1674.
- (39) Brines, L. M.; Shearer, J.; Fender, J. K.; Schweitzer, D.; Shoner, S. C.; Barnhart, D.; Kaminsky, W.; Lovell, S.; Kovacs, J. A. *Inorg. Chem.* **2007**, *46*, 9267–9277.
- (40) Fox, D. C.; Fiedler, A. T.; Halfen, H. L.; Brunold, T. C.; Halfen, J. A. *J. Am. Chem. Soc.* **2004**, *126*, 7627–7638.
- (41) Matsunaga, Y.; Fujisawa, K.; Ibi, N.; Miyashita, Y.; Okamoto, K. *Inorg. Chem.* **2005**, *44*, 325–335.

- (42) Gorelsky, S. I.; Basumallick, L.; Vura-Weis, J.; Sarangi, R.; Hodgson, K. O.; Hedman, B.; Fujisawa, K.; Solomon, E. I. *Inorg. Chem.* **2005**, *44*, 4947–4960.
- (43) Gennari, M.; Pécaut, J.; DeBeer, S.; Neese, F.; Collomb, M.-N.; Duboc, C. *Angew. Chem. Int. Ed.* **2011**, *50*, 5662–5666.
- (44) Krishnamurthy, D.; Sarjeant, A. N.; Goldberg, D. P.; Caneschi, A.; Totti, F.; Zakharov, L. N.; Rheingold, A. L. *Chem. – Eur. J.* **2005**, *11*, 7328–7341.
- (45) Kovacs, J. A. *Chem. Rev.* **2004**, *104*, 825–848.
- (46) Artaud, I.; Chatel, S.; Chauvin, A. S.; Bonnet, D.; Kopf, M. A.; Leduc, P. *Coord. Chem. Rev.* **1999**, *190–192*, 577–586.
- (47) Gennari, M.; Orio, M.; Pécaut, J.; Neese, F.; Collomb, M.-N.; Duboc, C. *Inorg. Chem.* **2010**, *49*, 6399–6401.
- (48) Berg, J. M.; Holm, R. H. *J. Am. Chem. Soc.* **1985**, *107*, 925–932.
- (49) Gennari, M.; Pécaut, J.; Collomb, M.-N.; Duboc, C. *Dalton Trans.* **2012**.
- (50) Gennari, M.; Orio, M.; Pécaut, J.; Bothe, E.; Neese, F.; Collomb, M.-N.; Duboc, C. *Inorg. Chem.* **2011**, *50*, 3707–3716.
- (51) Gennari, M.; Retegan, M.; DeBeer, S.; Pécaut, J.; Neese, F.; Collomb, M.-N.; Duboc, C. *Inorg. Chem.* **2011**, *50*, 10047–10055.
- (52) Baird, L. J.; Black, C. A.; Blackman, A. G. *Polyhedron* **2007**, *26*, 378–384.
- (53) Hall, N. A.; Duboc, C.; Collomb, M.-N.; Deronzier, A.; Blackman, A. G. *Dalton Trans.* **2011**, *40*, 12075.

**Synthesis, Reactivity and Catalytic Abilities of
Dioxo-Vanadium(V) and Oxo-Vanadium(IV)
Thiolate Complexes.**

Hall, N. A., Orio, M., Jorge-Robin, A., Gennaro, B., Marchi-Delapierre, C., Duboc, C. *Inorg. Chem.*
Accepted November 2013.

Résumé

Le vanadium est un métal abondant dans la nature, où il est présent dans différents états d'oxydation de +II à +V. Dans les systèmes biologiques, on le trouve surtout dans deux types d'enzymes, les haloperoxydases à vanadium (VHPOs) qui catalysent l'halogénéation de substrats organiques, ainsi que la nitrogénase à vanadium capable de réduire le diazote en ammoniac. Au cours de cette thèse, nous avons synthétisé et étudié des complexes du vanadium relatifs à ces deux enzymes. Ces études sont présentées dans ce chapitre et dans le suivant.

Les VHPOs sont des enzymes dont le site actif est constitué d'un complexe mononucléaire de vanadium à ligands azotés et oxygénés, capable d'oxyder divers types de substrats. Il a été montré dans la littérature que les complexes oxo du vanadium(IV) et du vanadium(V) représentent une classe de catalyseurs actifs pour l'oxydation de nombreux substrats, dont les sulfures. Notre objectif étant de comprendre les facteurs influençant la réactivité des fonctions thiols aliphatiques coordonnées à un métal, il nous paraissait intéressant de tester la réactivité de complexes oxo du vanadium en utilisant les ligands $L^{N_2S_2}$ et L^{NS_2} avec un sulfure comme substrat externe, l'objectif étant de déterminer qui du ligand ou du substrat est oxydé. Dans ce contexte, nous avons synthétisé et caractérisé un complexe dioxo du vanadium(V) ($[V(O)_2L^{NS_2}]$) et un complexe oxo de vanadium(IV) ($[V(O)L^{N_2S_2}]$). Ainsi, nous avons pu obtenir la première structure cristallographique d'un complexe dioxo de vanadium(V) à ligands thiols. En effet, il est difficile de stabiliser de tels complexes à haut degré d'oxydation à cause de leur capacité à oxyder les ligands thiols pour former des ponts disulfures, de manière intra- ou inter-moléculaire, avec réduction concomitante du métal.

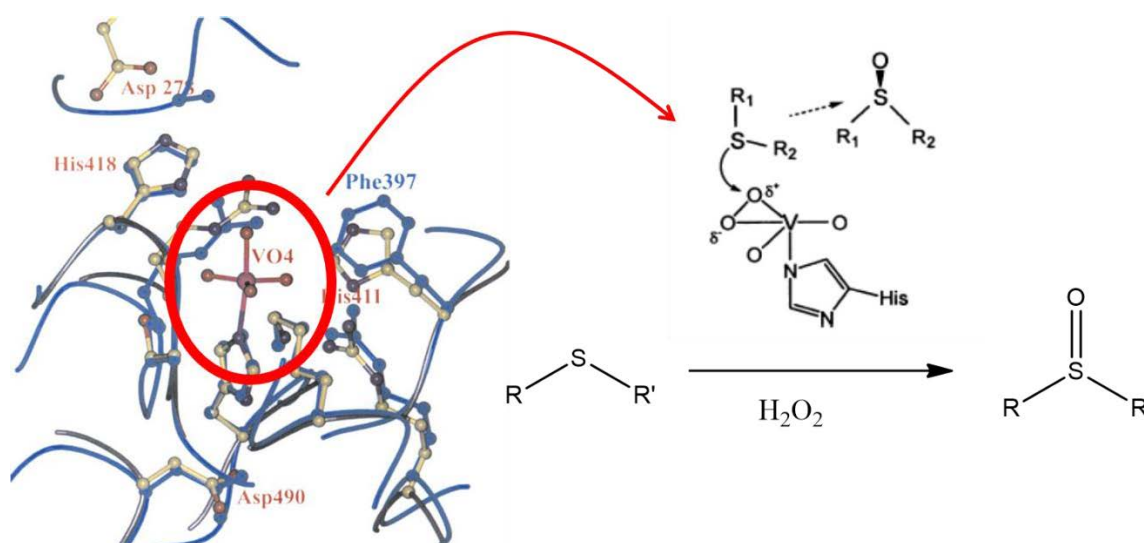
Les deux complexes se sont révélés être des catalyseurs efficaces et sélectifs de sulfoxydation, utilisant H_2O_2 comme oxydant et produisant exclusivement le méthylphénylsulfoxyde à partir du thioanisole. Plus intéressant encore, $[V(O)L^{N_2S_2}]$ a montré une stabilité remarquable, aucune perte de réactivité n'étant observée après cinq essais de catalyse. Une importante différence de réactivité a été observée entre les deux complexes : tandis que le catalyseur de vanadium(V) est plus efficace, donnant les meilleurs rendements et des réactions plus rapides, le complexe de vanadium(IV) est beaucoup plus stable.

Grâce à des études de RPE et de RMN du ^{51}V , combinée à des calculs théoriques, il a été possible de proposer que la différence de réactivité observée entre les deux complexes est en partie liée à une différence de stabilité des intermédiaires clés, à savoir des complexes cis-oxo peroxy de vanadium(V). Plus la symétrie de l'unité peroxy est basse, plus le catalyseur est réactif, mais moins il est stable.

On peut donc conclure de cette étude que les complexes du vanadium à ligands thiols aliphatiques s'avèrent être des catalyseurs de sulfoxydation efficaces et stables.

Introduction

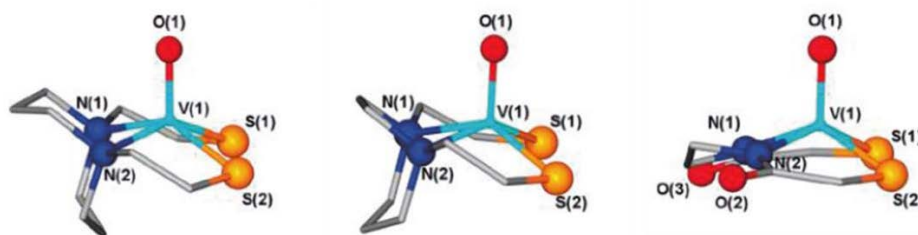
Vanadium is a trace element that is widely distributed in nature. After molybdenum, vanadium is the second most abundant transition metal in the ocean, it is also found in fresh water and the earth's crust. Vanadium exists in many oxidation states from +II to +V. However, to date only the V^{III} , V^{IV} and V^V oxidation states have been found to be involved in biological systems.¹ A considerable amount of attention has been paid to vanadium coordination chemistry since the 1980s, when its presence in biological systems, its ability to catalyse oxidations and oxo transfer reactions, and also its prospective therapeutic applications were first demonstrated.²⁻⁶ Vanadium is found in two classes of metalloenzymes, the V-dependent haloperoxidases (VHPOs) that catalyse the halogenation of organic substrates and the oxidation of sulfides,⁷ and in the V-containing nitrogenase that catalyses the concomitant reduction of N_2 and H^+ into NH_3 and H_2 .⁸ This chapter will focus on VHPOs, and in particular their ability to catalyse sulfoxidation (Scheme 2.1), while chapter III will focus on modelling the V-nitrogenase.



Scheme 2.1. Crystal structure of VHPOs (V-dependant chloroperoxidase and V-dependant bromoperoxidase superimposed), and the sulfoxidation reaction showing a schematic diagram of the mechanism of V-dependant bromoperoxidase.⁹

VHPOs can catalytically oxidise sulfides, with both complete selectivity towards sulfoxide and also high enantioselectivity. Nevertheless, this reaction is very slow, with a maximum yield of 40 % after 2 h at 25 °C, and only after 16 h do they approach 100 % yield.¹⁰ Oxo vanadium(IV) and *cis*-dioxo vanadium(V) complexes with N- and O- donor chelating ligands have been extensively studied as molecular models of the haloperoxidase enzymes.^{2,5,6} From these studies V^{IV} and V^V complexes have shown a considerable ability to catalytically oxidise various organic substrates, such as alkenes,

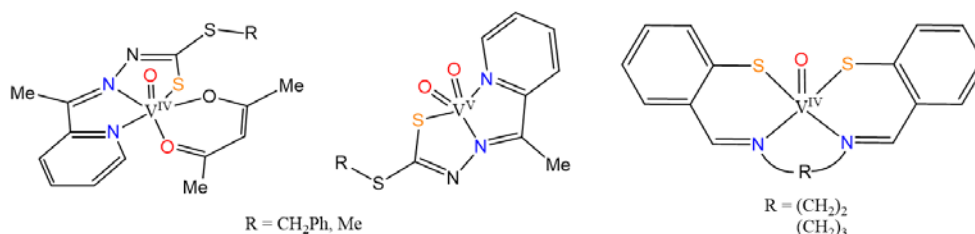
aromatics, sulfides and even alkanes in the presence of hydrogen peroxide (H_2O_2) or alkylhydroperoxides.^{7,11}



Alkyl thiolate V^{IV} complexes

Scheme 2.2. Previously reported alkyl thiolate vanadyl complexes.¹²

Thus far, the most successful oxo or dioxo-vanadium catalysts contain nitrogen- or oxygen- donor ligands, with very few catalysts containing thiolate ligands. In fact, there are only three oxo V^{IV} compounds with alkyl thiolate(s) ligands that have been characterized by X-ray diffraction (Scheme 2.2).^{12,13} Among them none have been tested as oxidation catalysts, only their capability to perform S-alkylation reactions has been investigated.¹² Furthermore, to the best of our knowledge, no structure has been reported so far for alkyl thiolate-containing dioxo V^{V} complexes, and only two for mono-oxo thiolate V^{V} compounds have been described.^{14,15} Yet, during the metabolism of the vanadium compounds, the metal could bind different types of biomolecules including cysteine or glutathione, which are alkyl thiolate S-based ligands. Recently, the controversial question of whether such thiolate derivatives will or will not reduce high oxidation states of V has been clarified. A study has demonstrated that in physiological conditions, high stability of V^{IV} and even V^{V} complexes with thiolate ligands can be afforded, depending on their redox potentials.¹⁶



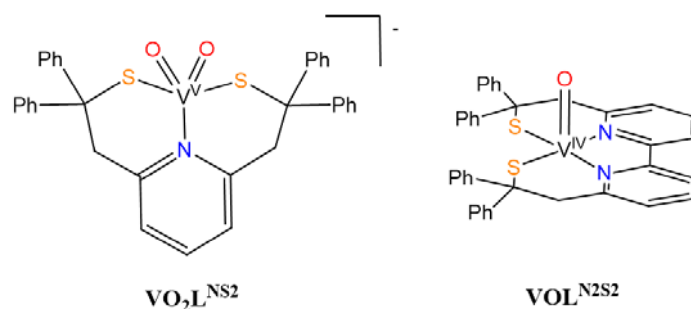
Aryl thiolate V^{IV} & V^{V} complexes

Scheme 2.3. Previously reported dioxo V^{V} and mono-oxo V^{IV} aryl thiolate complexes that have been tested toward sulfoxidation and epoxidation.

The reactivity of oxo V^{IV} and V^{V} complexes with S-based ligands has been tested for different types of oxidation, especially sulfoxidation and epoxidation. It is important to

note that all of the S-based vanadium catalysts have been synthesized with aromatic thiolate ligands (methyldithiocarbazate, dithiocarbonylhydrazone, thiosemicarbazone) shown in Scheme 2.3.^{17,18} These compounds present an activity comparable to that observed for O- and/or N- based ligands.

As we are interested in alkyl thiolate metal complexes, the work that we report in this chapter is focused on potential applications of alkyl thiolate vanadium compounds for catalytic sulfoxidation using the oxidant hydrogen peroxide. There is an obvious reason why such studies are rare and that is due to the susceptibility of an alkyl thiolate, which is bound to a metal ion, to generate sulfenic or sulfinic ligands in the presence of reactive oxygen species. An example, in nature, is seen in the active site of the nitrile hydratase enzymes. The cysteine residues bound to the metal (either a Co^{III} or an Fe^{III} ion) are oxidized.¹⁹ In contrast is the Ni-superoxide dismutase enzyme, where the cysteine residues bound to the Ni ion are stable in the presence of highly oxidising species, *i.e.* the superoxide radical anion substrate, and also the hydrogen peroxide product.²⁰ Therefore, with it in mind that, oxo vanadium complexes have proven to be efficient catalysts towards sulfoxidation, we will investigate an oxo V^{IV} complex and a dioxo V^{V} complex with coordinated alkyl thiolate sulfur atoms. Our objectives are to further investigate the influence of metal bound sulfur on the catalytic ability of the resulting complexes and the stability of the thiolate groups under these oxidative conditions.



Scheme 2.4. Schematic drawing of $\text{VO}_2\text{L}^{\text{NS}_2}$ and $\text{VOL}^{\text{N}_2\text{S}_2}$.

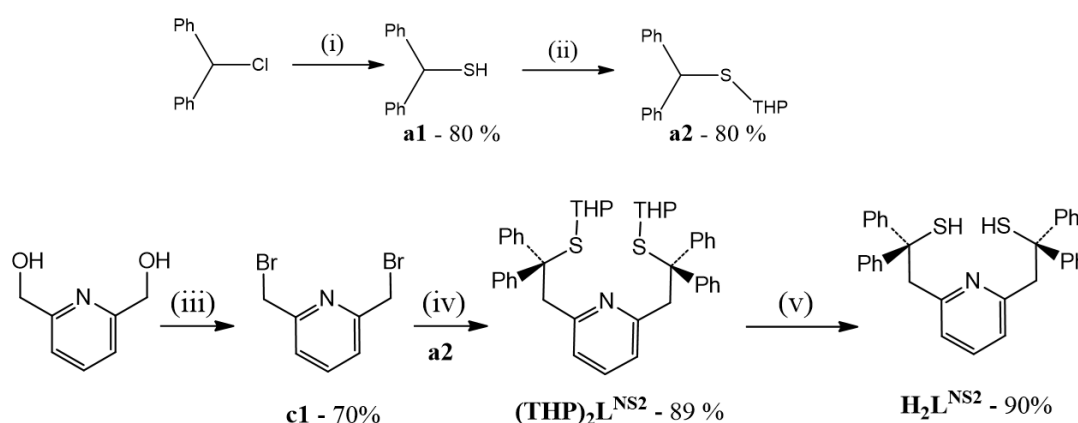
Two types of V compounds have been targeted, *i.e.* a very challenging dioxo V^{V} complex ($\text{VO}_2\text{L}^{\text{NS}_2}$) and an oxo V^{IV} complex ($\text{VOL}^{\text{N}_2\text{S}_2}$) (Scheme 2.4). In the present study, we report the synthesis and characterization of complexes $\text{VO}_2\text{L}^{\text{NS}_2}$ and $\text{VOL}^{\text{N}_2\text{S}_2}$ as well as their reactivity toward sulfoxidation. Furthermore, the electronic structure of both compounds has been explored by DFT calculations to investigate the effect of the thiolate, especially on the nature of the V-S bond. Indeed, it has been shown that

depending on the nature of the metal ion, high covalency of the M-S bond can be found, especially in the case of the Ni^{II} and Cu^{II} ions.²⁷ Curiously, as far as V^{IV} and V^V are concerned, such investigations have never been reported. Finally, we have explored the sulfoxidation mechanism with the help of experimental investigation and theoretical calculations, with a special focus on the identification of intermediates in order to rationalize the difference in reactivity and stability observed between VO₂L^{NS2} and VOL^{N2S2}.

Results and Discussion

2.1 Ligand Synthesis

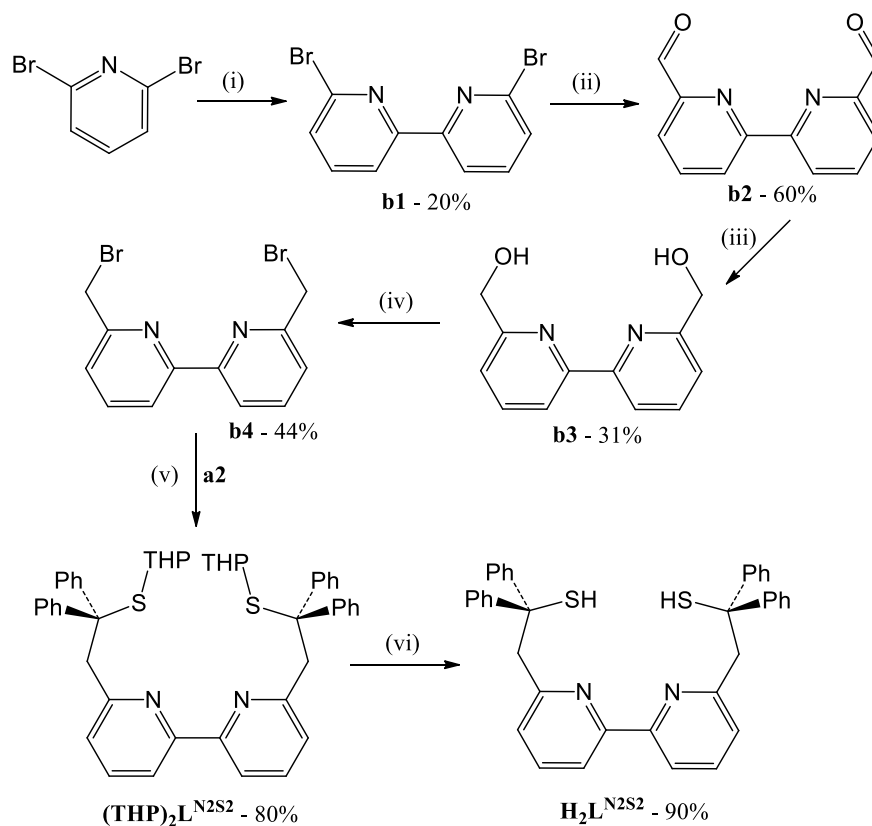
Two ligands have been synthesised, one tridentate and the other tetradentate (Scheme 2.5 and Scheme 2.6). As we are interested particularly in complexes, which contain at least one metal thiolate bond, both ligands contain terminal alkyl thiolate groups protected by two bulky phenyl groups on the C_α to reduce dimerization and/or to hinder the formation of disulfide bonds. The only difference between the two ligands is the linking unit; *i.e.* bipyridine or pyridine. They were chosen as they are well known as good coordinating ligands. A pyridine is therefore the linker between the two alkyl thiolates in the tridentate ligand (**H₂L^{NS2}** Scheme 2.4), and a bipyridine in the tetradentate one (**H₂L^{N2S2}** Scheme 2.5).



Scheme 2.5. Synthesis of **H₂L^{NS2}**. (i) thiourea EtOH reflux, NaOH (aq); (ii) 2,3-dihydropyran, HCl 37%; (iii) PBr₃ CHCl₃ reflux; (iv) **a2**/*n*-BuLi 2.5 M at -78 °C in Et₂O, **c1** THF; (v) AgNO₃/pyridine in MeOH/AcOEt, H₂S.

Both the **H₂L^{NS2}** and the **H₂L^{N2S2}** ligands have been previously described. The ligand **H₂L^{NS2}** was first reported by Berg and Holm²¹ from a lithiation coupling reaction between 2,6-bis(bromomethyl)-pyridine (**c1**) and 2-[(diphenylmethyl)thio]tetrahydro-2H-pyran (**a2**). **c1** was prepared by the bromination of 2,6-bis(methanol)-pyridine,

using tribromophosphine as a brominating agent. **a2** was prepared *via* a two-step reaction; diphenylmethyl chloride was reacted with thiourea, and the product was then protected with tetrahydropyran. **(THP)₂L^{N2S2}** was deprotected in a two-step procedure using silver nitrate and pyridine followed by bubbling hydrogen sulfide through the mixture, giving **H₂L^{N2S2}** with an overall yield of 80%.



Scheme 2.6. Synthesis of **H₂L^{N2S2}**. (i) *n*-BuLi 2.5 M at -78 °C in Et₂O, SOCl₂; (ii) *n*-BuLi 2.5 M at -78 °C in THF, DMF; (iii) NaBH₄ in MeOH; (iv) PBr₃ CHCl₃ reflux; (v) **a2**/*n*-BuLi 2.5 M at -78 °C in Et₂O, **b4** THF; (vi) AgNO₃/pyridine in MeOH/AcOEt, H₂S.

The **H₂L^{N2S2}** ligand was prepared by the method of Gennari and co-workers²² which was adapted from the Berg and Holm procedure previously stated.²¹ Note that this ligand has also been described by Artaud *et. al.*; while their procedure is shorter, the coupling reaction is not reproducible as **b4** cannot be obtained pure.²³ 6,6'-bis(bromomethyl)-2,2'-bipyridine (**b4**) was prepared *via* a four-step process. The first step consists of a lithiation coupling reaction with 2,6-dibromopyridine to give the 6,6'-bis-bromo-2,2'-bipyridine, followed by a further lithiation reaction to obtain the 6,6'-bis(methanoyl)-2,2'-bipyridine. This was then reduced with NaBH₄ to yield 6,6'-bis(methanol)-2,2'-bipyridine. The final step was the bromination of the alcohol using tribromophosphine as the brominating agent. The overall yield for this multi-step reaction is extremely low

(2-5 %). **b4** was then coupled *via* a lithiation reaction with **a2**. In addition to n-BuLi, hexamethylphosphoramide is needed to initiate the reaction.

2.2 Synthesis and Characterisation of the $\text{Et}_3\text{NH}[\text{VO}_2\text{L}^{\text{NS}_2}] \cdot \text{MeOH}$ Complex

The V^{V} complex was synthesised *via* the reaction of the $\text{H}_2\text{L}^{\text{NS}_2}$ ligand in THF with ammonium metavanadate and triethylamine in a 1:1:1 mole ratio leading to a yellow solution. After 12 h, a yellow precipitate corresponding to $\text{Et}_3\text{NH}[\text{VO}_2\text{L}^{\text{NS}_2}] \cdot \text{MeOH}$ ($\text{VO}_2\text{L}^{\text{NS}_2}$) was obtained. This complex was synthesised under an argon atmosphere due to the instability of the deprotected ligand to air. However, once obtained, the complex is stable in air.

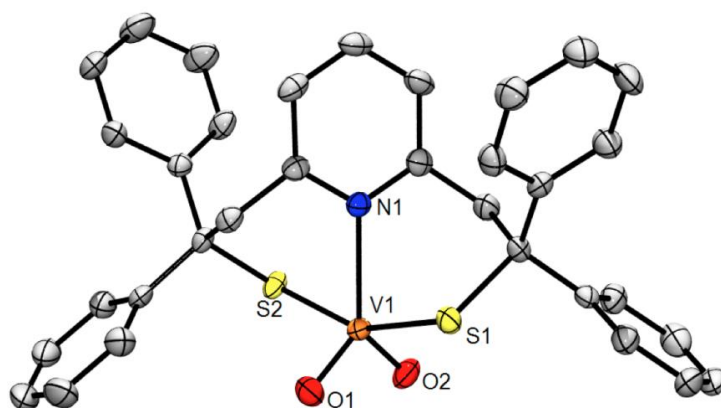
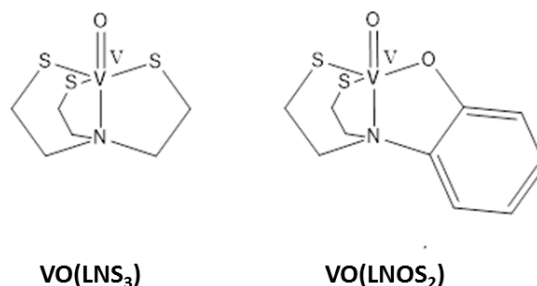


Figure 2.1. ORTEP diagram of the $[\text{VOL}^{\text{NS}_2}]^-$ anion. Thermal ellipsoids are drawn at the 50% probability level. Methanol solvent molecule and hydrogen atoms have been omitted for clarity.

Complex $\text{VO}_2\text{L}^{\text{NS}_2}$ was characterized by X-ray diffraction using a single yellow crystal obtained from a solution of the reaction mixture on standing. X-ray collection and refinement data are given in the Appendix. Its molecular structure is presented in Figure 2.1, while selected bond distances and angles are listed in Table 2.1.



Scheme 2.7. The two crystallographically characterised mono-oxo thiolate V^{V} compounds.

The structure reveals the first example of a dioxo V^V complex with two coordinated alkyl thiolate ligands. To the best of our knowledge, V^V thiolate complexes are rare and only two crystallographically characterized mono-oxo V^V complexes containing aliphatic thiolate ligands (Scheme 2.7) have been reported to date,^{14,15} while there are a few examples of dioxo and oxo V^V compounds with aromatic thiohydrazone,²⁴ or thiocarbamate²⁵ thiolate ligands.

The structure of VO_2L^{NS2} consists of a $[VO_2(L^{NS2})]^-$ anion, one $HNEt_3^+$ cation and one methanol solvent molecule. The V^V centre is bound to the two sulfur atoms of the aliphatic thiolates and to the nitrogen atom of the pyridine unit of the L^{NS2} ligand. In addition, two terminal oxo atoms are also bound in the *cis*- configuration, resulting in a distorted trigonal bipyramidal geometry about the V^V ion ($\tau = 0.78$).^{3,4}

Table 2.1. Selected bond lengths (Å) and angles (°) for the X-ray structure of VO_2L^{NS2} as well as for the DFT-optimized structure VO_2L^{NS2*} .

	VO_2L^{NS2} Exp.	VO_2L^{NS2*} Calc.
Bond Lengths (Å)		
V-O1	1.633(2)	1.636
V-O2	1.648(2)	1.654
V-S1	2.4103(10)	2.455
V-S2	2.4057(11)	2.433
V-N1	2.197(2)	2.231
O2-H1	1.983	1.719
Bond Angles (°)		
O1-V-O2	110.00(11)	112.7
O1-V-S1	91.67(8)	91.0
O1-V-S2	100.74(8)	102.2
O1-V-N1	122.76(10)	124.2
O2-V-S1	100.08(8)	100.3
O2-V-S2	93.72(8)	92.0
O2-V-N1	127.22(10)	123.0
S1-V-S2	157.09(3)	157.0
S1-V-N1	78.44(7)	78.7

The trigonal plane includes the two *cis*-oxo oxygen atoms and the nitrogen atom of the L^{NS2} ligand. The trigonal plane is notably distorted as the bond distances of the terminal oxo ligands are significantly shorter ($V-O2 = 1.634$ and $V-O1 = 1.649$ Å) than the V-N bond (2.197 Å). The sulfur atoms occupy the axial positions in a distorted fashion with a S1-V1-S2 angle of 157.08°. The V-S bond distances (2.406 and 2.410 Å) are notably longer than in the other oxo or dioxo V^V complexes (range 2.23-2.39 Å),^{14,15,24,26,27} while the V=O oxo and V-N lengths are in the usual range.

As can be seen in Figure 2.2 the main intermolecular interactions consist of two strong hydrogen bonds. One hydrogen bond is observed between O1 and the hydrogen coordinated to O3 of the methanol molecule (2.105 Å). The other significant hydrogen bond is found between O2 and the hydrogen atom of $^+\text{HNEt}_3$ (1.975 Å).

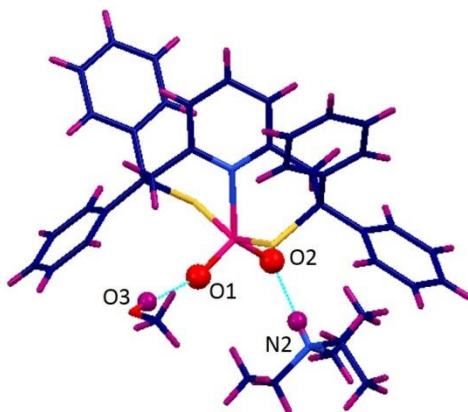


Figure 2.2. H-bonds between V-Oxo and solvent molecule and counter cation HNEt_3 .

An optimized geometry of $\text{VO}_2\text{L}^{\text{NS}2}$ has been calculated by DFT (denoted $\text{VO}_2\text{L}^{\text{NS}2*}$). To obtain better agreement between both experimental and optimized structures, a methanol molecule has been included to account for the interaction with one oxo ligand *via* hydrogen bonding, as seen in the X-ray structure of $\text{VO}_2\text{L}^{\text{NS}2}$. The principal structural parameters of $\text{VO}_2\text{L}^{\text{NS}2*}\cdot\text{MeOH}$ (Table 2.1) reproduce well those of $\text{VO}_2\text{L}^{\text{NS}2}$, especially the V=O oxo bond lengths. The calculated V-S/N distances are slightly longer (by 4 pm) than the experimental ones (Table 2.1), which is typical for such optimization procedures based on DFT methods.^{28,29}

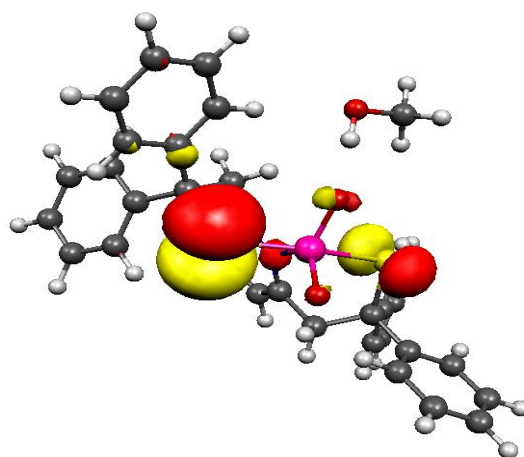


Figure 2.3. HOMO orbital of complex $\text{VO}_2\text{L}^{\text{NS}2}$.

To investigate the electronic structure of this complex, DFT calculations have been performed on the optimised structure $\text{VO}_2\text{L}^{\text{NS}2*}$. The highest occupied molecular orbital

(HOMO) presented in Figure 2.3 is almost exclusively localized on the two thiolate sulfur atoms (56 and 22%, respectively), in accordance with the expected strong ionic character of the V^V-S bond. Similar results have been found with alkyl thiolate Zn complexes (a *d*¹⁰ ion) by Darensbourg *et al.*³⁰ and our group.³¹

The electronic absorption spectrum of the yellow **VO₂L^{NS2}** complex in acetonitrile shows a single transition at 388 nm ($\epsilon = 2190 \text{ M}^{-1}\cdot\text{cm}^{-1}$) in the visible region, as shown in Figure 2.4. This transition can be assigned as an LMCT, from the sulfur to the vanadium. This has been seen previously in the case of **VONS₃** (Scheme 2.6),¹⁴ which displays intense transitions in the visible region (500 nm – 300 nm).

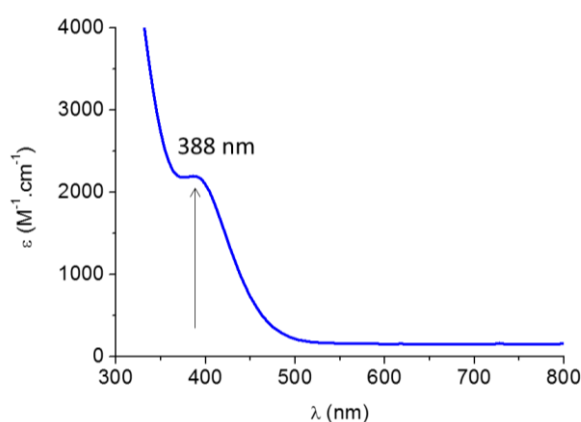


Figure 2.4. Electronic absorption spectrum of **VO₂L^{NS2}**.

VO₂L^{NS2} is a diamagnetic complex, V^V being a *d*⁰ ion. The ⁵¹V NMR spectrum recorded in CD₃CN shows a single peak at -389 ppm. In the literature, there is a wide range of ⁵¹V NMR chemical shifts (+600 ppm to -600 ppm).³² The only other V^V dithiolate complex (**VO(NOS₂)**, Scheme 2.7) that has been characterised by ⁵¹V NMR has a chemical shift of +338 ppm.¹⁵ Our data are consistent with the presence of two oxo donor ligands within the coordination sphere of the V^V ion in **VO₂L^{NS2}**. In fact, ⁵¹V NMR shifts are highly influenced by the coordination sphere of the vanadium centre and the sum of the electronegativity of the ligands; the greater the total electronegativity of the ligands, the more negative the ⁵¹V NMR shift observed.³² In addition, DFT calculations have been carried out on **VO₂L^{NS2}*** to predict its ⁵¹V NMR shift. A value of -390 ppm has been calculated, in perfect agreement with the experimental data.

2.3 Characterisation of the [VOL^{N2S2}] Complex

To obtain the V(IV) complex (**VOL^{N2S2}**), the **L^{N2S2}** ligand was first deprotonated by potassium hydride. The resulting K₂L^{N2S2} salt reacts with VOSO₄ in a 1:1 mole ratio

leading to a light green precipitate corresponding to $\text{VOL}^{\text{N}_2\text{S}_2}$. Like $\text{VO}_2\text{L}^{\text{NS}_2}$, $\text{VOL}^{\text{N}_2\text{S}_2}$ was also synthesised under an argon atmosphere, and after complexation $\text{VOL}^{\text{N}_2\text{S}_2}$ is stable in air. We have been unable to obtain crystals suitable to characterise $\text{VOL}^{\text{N}_2\text{S}_2}$ by X-ray crystallography. However, it has been characterised by mass spectrometry, elemental analysis, EPR spectroscopy and DFT calculations (Figure 2.5).

As we found that our DFT-based geometry optimization procedure was reliable the $\text{VO}_2\text{L}^{\text{NS}_2}$ complex, the optimized structure of $\text{VOL}^{\text{N}_2\text{S}_2}$ has been calculated ($\text{VOL}^{\text{N}_2\text{S}_2*}$) (Figure 2.5). The resulting structure displays the expected square-pyramidal coordination geometry with the N_2S_2 donor set arranged around the basal plane and the vanadyl oxygen atom at the apex. The vanadium is displaced from the basal plane toward the apical oxygen atom by 0.28 Å. The V=O oxo (1.592 Å) and V-S (2.340 and 2.343 Å) distances are within the ranges reported for N_2S_2 oxo vanadium(IV) complexes (1.58-1.63 and 2.34-2.37 Å, respectively).^{12,33} Consequently, the calculated optimized structure $\text{VOL}^{\text{N}_2\text{S}_2*}$ is consistent with the structural data obtained on previously reported X-ray structures of dithiolate vanadyl complexes.

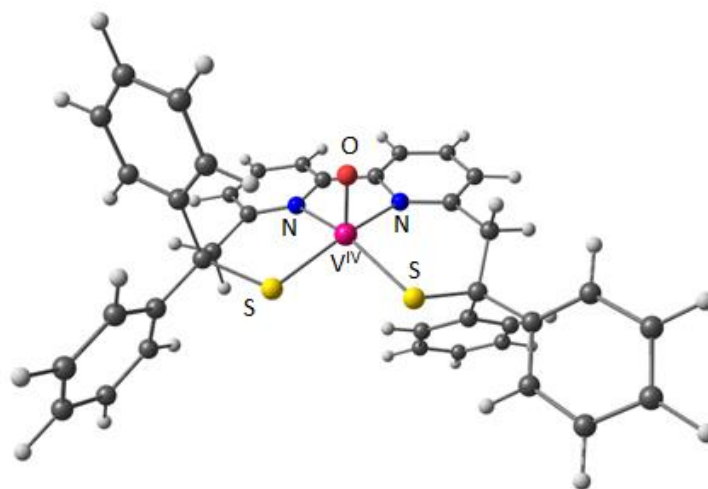


Figure 2.5. DFT-optimised structure of $\text{VOL}^{\text{N}_2\text{S}_2*}$. Selected bond lengths (Å); V-O1, 1.592; V-N1, 2.340; V-N2, 2.343; V-S1, 2.193; V-S2, 2.192.

EPR spectra of oxo V^{IV} complexes display near identical signatures. They generally display an axial $S = \frac{1}{2}$ signal consistent with a V^{IV} ion (d^1). Both transitions are split into eight lines due to the interaction between the unpaired electron and the ^{51}V (>99%) nuclear spin ($I = 7/2$).^{34,35} The EPR spectrum of $\text{VOL}^{\text{N}_2\text{S}_2}$ recorded in a frozen CH_2Cl_2 solution at 100 K is shown in Figure 2.6. The spin Hamiltonian parameters used for the simulation given in Table 2.2 are typical of square pyramidal oxo V^{IV} complexes under comparable sulfur-containing donor environments with notable small A values ($A_z = 100$

– 150 MHz).^{12,27,36,37} The DFT calculated EPR parameters obtained from the optimized **VOL^{N2S2}*** structure (Table 2.2) are consistent with the experimental data, demonstrating that the geometry of **VOL^{N2S2}** is retained in solution.

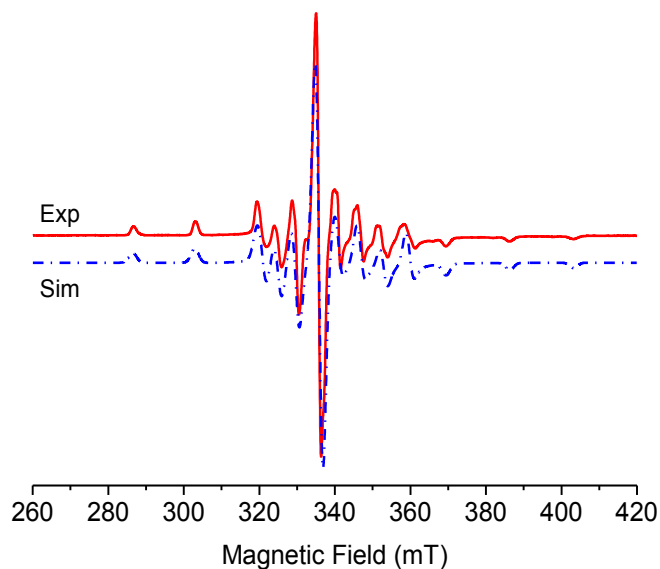


Figure 2.6. Experimental (red and solid line) and simulated (blue and dashed line) X-band EPR spectra of a frozen solution of **VOL^{N2S2}*** in CH_2Cl_2 (100 K). The parameters used for the simulation are given in Table 2.2.

Table 2.2. Experimental and calculated EPR parameters of **VOL^{N2S2}***.

	g_x	g_y	g_z	A_x (MHz)	A_y (MHz)	A_z (MHz)
Exp.	1.988	1.988	1.966	135	126	406
Calc.	1.991	1.985	1.969	102	109	405

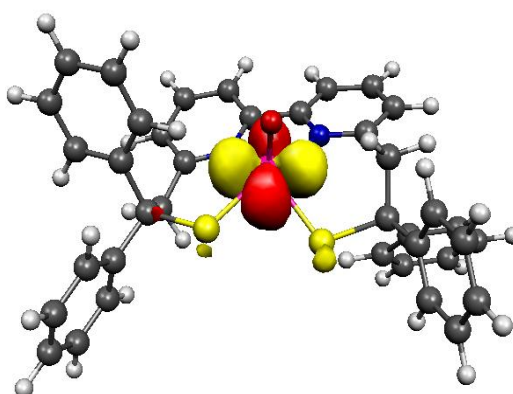


Figure 2.7. SOMO orbital of complex **VOL^{N2S2}***.

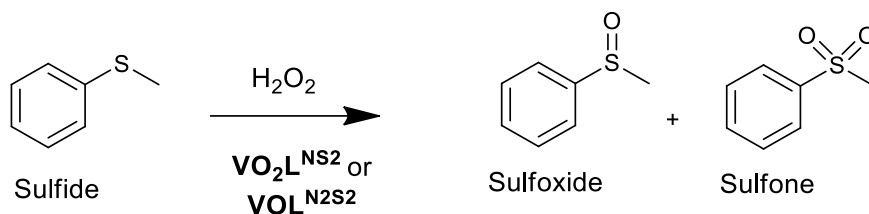
DFT calculations have also been performed on **VOL^{N2S2*}** to characterise its electronic structure. The singly occupied molecular orbital (SOMO) is exclusively localized on the V^{IV} ion (92%), the contribution of the sulfur atoms representing only 4% of the SOMO (Figure 2.7).

Generally, the SOMO of vanadyl complexes is mostly d_{xy} in character, as in **VOL^{N2S2*}**, where the x- and y- axes lie approximately along the sigma bonds of the equatorial ligands.³⁸ This orbital is largely nonbonding or participates in in-plane bonding with ligand orbitals of correct symmetry. In the present case, the sulfur or nitrogen atoms do not contribute to the SOMO, explaining the quasi-pure metal-based character of the SOMO in **VOL^{N2S2*}**. This is confirmed by the Mulliken population analysis showing that the metal bears all of the spin density with a positive spin populations of 1.19. The absence of thiolate contribution to the SOMO is in accordance with the low S-alkylation reactivity of a previously described vanadyl complex with a mixed amine/thiolate ligand.¹²

2.4 Catalytic Reactivity of $Et_3NH[VO_2L^{NS_2}]$ and $[VOL^{N_2S_2}]$ toward Sulfoxidation

As previously mentioned we are interested in the reactivity of bound thiolates. As we have seen, in biology, they react in a variety of different ways, *i.e.* S-methylation and/or S-oxygenation, depending on their surroundings. Of particular importance to our group is to determine the factors that influence the reactivity of bound thiolates. It has been shown that oxo V^V and V^{IV} complexes are good catalysts for various oxidations processes such as sulfoxidation. Therefore, it is of interest to study sulfoxidation reactions in the presence of an external substrate with complexes containing bound alkyl thiolates to see whether it is the bound thiolate which is oxidised, or the substrate. Currently only V^{IV} and V^V catalysts containing aromatic thiolates have been described, and none with aliphatic thiolates. Therefore, we present herein the first catalytic sulfoxidation study using the alkyl thiolate compounds **VO₂L^{NS₂}** and **VOL^{N₂S₂}**.

The oxidation reactions have been carried out with methylphenylsulfide (thioanisole) used as the model substrate, and hydrogen peroxide (H₂O₂) as oxidant. Scheme 2.8 represents the formation of the two potential oxidation products, phenylmethyl sulfoxide and phenylmethyl sulfone. Under all experimental conditions that we have used, we observed no production of sulfone, with both catalysts being completely selective towards formation of sulfoxide as shown below.



Scheme 2.8. Sulfoxidation reaction of thioanisole as substrate to give phenylmethyl sulfoxide and phenylmethyl sulfone as products.

Both catalysts were tested under two different conditions. In both cases, the concentration of catalyst and thioanisole was kept at 1 mM and 100 mM, respectively, while the catalyst:H₂O₂ ratio varied between 1:20 (standard conditions) and 1:100 (quantitative conditions). Under the standard conditions, an excess of substrate has been used in order to preserve the catalyst from degrading oxidation reactions, while the quantitative condition is used to determine the conversion of the reaction with both catalysts. The blanks (without catalyst) under both conditions show negligible production of sulfoxide or sulfone (< 1.5 %). We quantified the amount of product(s) formed by gas chromatography (GC).

The Reaction Time for Sulfoxide Formation

The reaction time for sulfoxide formation has been measured under the standard conditions (1:100:20, catalyst:thioanisole:H₂O₂). The solvent used was different for the two complexes due to their solubility; MeCN for **VO₂L^{NS₂}** and CH₂Cl₂ for **VOL^{N₂S₂}**. GC runs were recorded every five minutes until the reaction was completed.

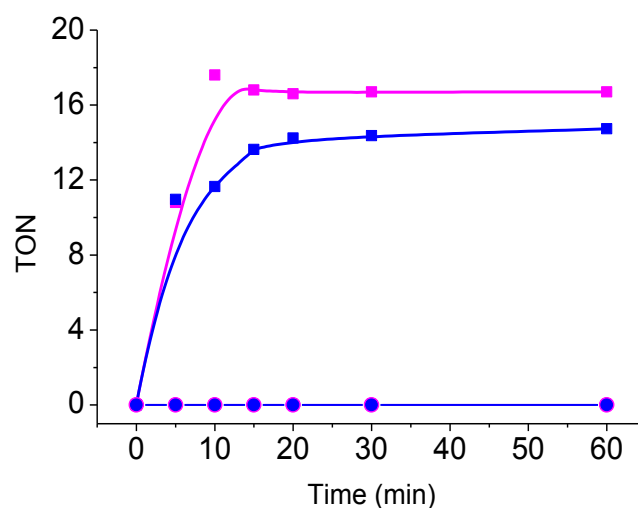


Figure 2.8. Turnover number (TON) of sulfoxide (square) and sulfone (circle) produced from thioanisole (100 mM) with **VOL^{NS₂}** (1 mM) (pink) or **VOL^{N₂S₂}** (1 mM) (blue) after the addition of H₂O₂ (20 mM) in the function of time.

The reaction data obtained for both catalysts $\text{VO}_2\text{L}^{\text{NS}_2}$ and $\text{VOL}^{\text{N}_2\text{S}_2}$ show that the reaction is complete after 10 and 15 minutes, respectively (Figure 2.8). Catalyst $\text{VO}_2\text{L}^{\text{NS}_2}$ shows a slightly higher turn-over number (TON = 17) than $\text{VOL}^{\text{N}_2\text{S}_2}$ (TON = 15), leading to a yield of 85 and 75 %, respectively for $\text{VO}_2\text{L}^{\text{NS}_2}$ and $\text{VOL}^{\text{N}_2\text{S}_2}$.

Efficiency of the Catalysts

For the quantitative catalytic studies the ratio 1:100:100 (catalyst:thioanisole: H_2O_2) has been used. Only two time points at 30 minutes and one hour were taken for these experiments. The results show a significant difference between the efficiency of the two catalysts (Figure 2.9).

$\text{VO}_2\text{L}^{\text{NS}_2}$ shows similar results to those obtained when using standard conditions, with a yield of 81 %. In contrast, $\text{VOL}^{\text{N}_2\text{S}_2}$ shows a notable decrease in efficiency with only 45 TON, corresponding to a yield of 45 %. This evidences that the efficiency of this complex is sensitive to the reaction conditions, as a 75 % yield was observed under the standard conditions.

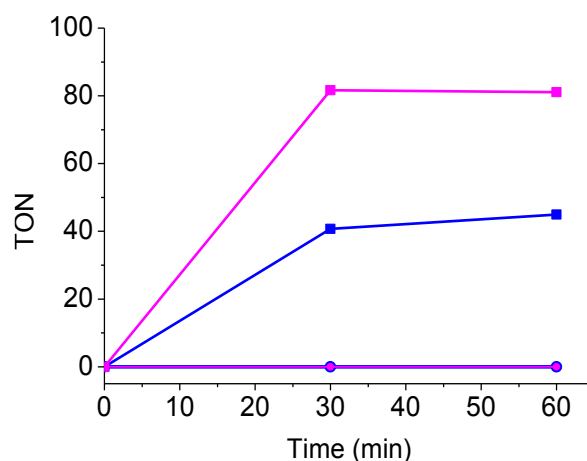


Figure 2.9. TON of sulfoxide (square) and sulfone (circle) produced from thioanisole (100 mM) with $\text{VO}_2\text{L}^{\text{NS}_2}$ (1 mM) (pink) or $\text{VOL}^{\text{N}_2\text{S}_2}$ (1 mM) (blue) after the addition of H_2O_2 (100 mM) in the function of time.

Stability of the Catalysts

The stability of both catalysts has also been investigated. We have carried out stability experiments using the standard conditions (1:100:20). Test A corresponds to the successive additions of H_2O_2 (20 mM) every 30 minutes. In the case of $\text{VO}_2\text{L}^{\text{NS}_2}$, after the second addition of H_2O_2 , no further production of either sulfoxide or sulfone has been observed, suggesting that $\text{VO}_2\text{L}^{\text{NS}_2}$ is completely degraded after one run.

Test A carried out with **VOL^{N2S2}** showed a 10 % decrease in activity after the second addition to a 50 % decrease in activity after the fourth addition (Figure 2.10). However, since we have observed that the efficiency of this catalyst depends on the thioanisole:H₂O₂ ratio, another test (Test B) has been carried out. To keep an excess of thioanisole, Test B corresponds to the successive additions of H₂O₂ (20 mM) and thioanisole (100 mM) every 30 minutes. As can be seen from Figure 2.10, after four additions of thioanisole and H₂O₂ the efficiency is similar, demonstrating a remarkable stability of the **VOL^{N2S2}** catalyst. Table 2.4 summarizes the principal results obtained from both catalysts.

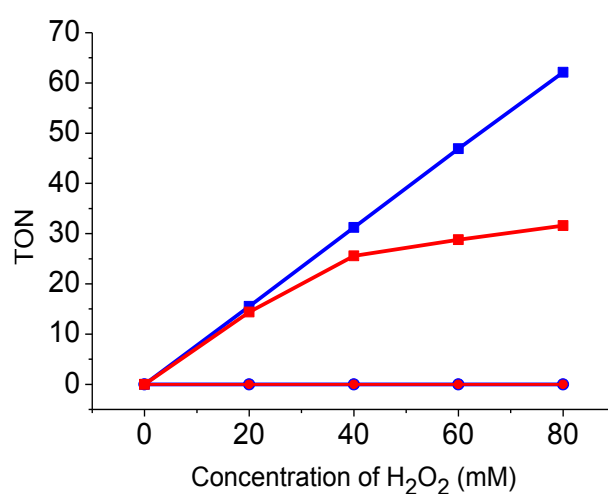
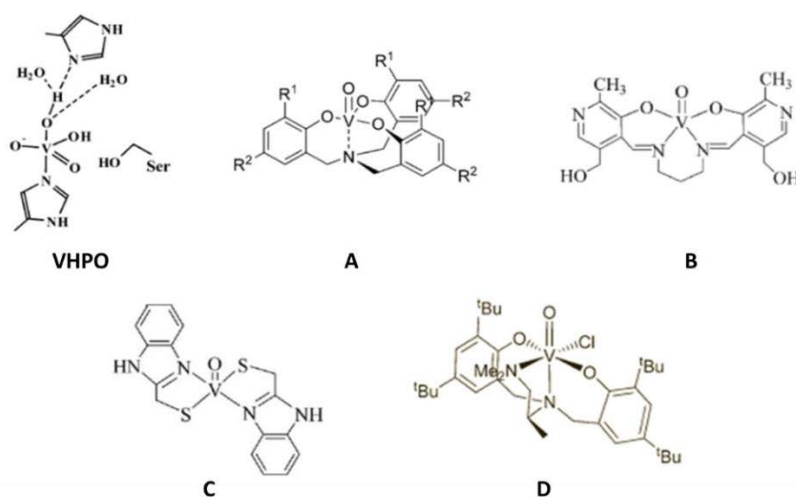


Figure 2.10. Turnover number (TON) of sulfoxide (square) and sulfone (circle) produced from test A (red) or test B (blue) with **VOL^{N2S2}**.

Comparison with Literature

The system reported here is the first catalytic study using vanadium complexes which contain alkyl thiolate ligands. To the best of our knowledge, the only vanadium-sulfur complex that has been previously studied for sulfoxidation contains aromatic thiolate ligands (Scheme 2.8C).³⁹ Using 0.1 mol % of catalyst with a thioanisole:H₂O₂ ratio of 1:1 Maurya *et. al.* achieved 82 % conversion with 10 % sulfone production in three hours (Table 2.4). The results obtained with catalyst **C** are comparable to those found for the more common vanadium-based catalysts which contain oxygen and nitrogen ligands. Three examples of this type are shown in Scheme 2.9 (**A**, **B** & **D**) along with the active site of vanadium dependent haloperoxidases (**VPO**).



Scheme 2.9. Relevant vanadium sulfoxidation catalysts.

Table 2.4. Sulfoxidation of thioanisole with $\text{VO}_2\text{L}^{\text{NS}_2}$ and $\text{VOL}^{\text{N}_2\text{S}_2}$ using the oxidising agent H_2O_2 , together with relevant vanadium sulfoxidation catalysts.

Catalysts	Ratio ^a	Yield (%) ^b	Time (min)	TON ^c	SO/SO ₂ ^d	Ref
$\text{VO}_2\text{L}^{\text{NS}_2}$	1:100:20	85	10	17	100/0	
$\text{VOL}^{\text{N}_2\text{S}_2}$	1:100:20	75	15	15	100/0	
$\text{VO}_2\text{L}^{\text{NS}_2}$	1:100:100	81	≤ 30	81	100/0	
$\text{VOL}^{\text{N}_2\text{S}_2}$	1:100:100	45	≤ 30	45	100/0	
VPO			1200	450-520		9
A	1:100:100	97	25	97	96/4	39
A	0.1:100:100	98	80	980	98/2	39
A	0.01:100:100	97	850	9700	97/3	39
B	0.02:100:100	79	150	2290	81/19	40
C	0.1:100:100	82	180	738	90/10	38
D	1:100:100	78	240	78	97/3	41

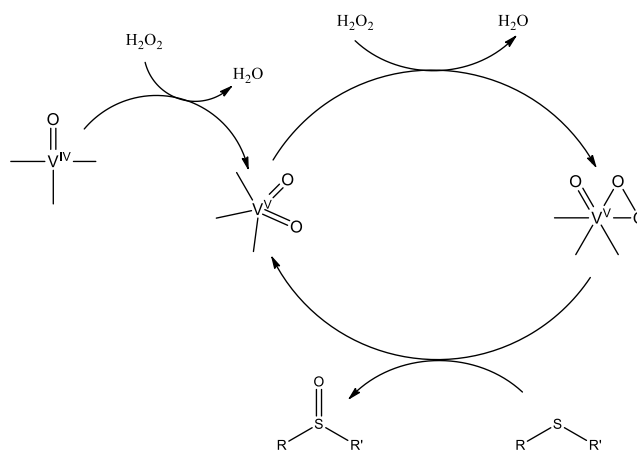
^a Ratio (catalyst:substrate:oxidant); ^b percentage yield based on the oxidant; ^c TON: number of mole of product formed per mole of V catalyst; ^d The ratio sulfoxide:sulfone

Important results are presented in Table 2.4. By far the most efficient catalyst is **A**,⁴⁰ which presents a TON up to 9700 with only 3% production of sulfone in 14 hours. However, to obtain such a large TON low catalyst loadings are needed (≤ 0.1 %), with a 1:1 ratio between thioanisole and H_2O_2 . The only potential problem with these conditions is a decrease in the selectivity of the reaction. As an example, with catalyst **B** a high production of sulfone (19 %) is observed with a very low (0.1 %) catalyst loading.⁴¹ Furthermore, the use of such a high excess of H_2O_2 is not possible in our catalysts, due to the reactivity of the alkyl thiolates. As was already observed in $\text{VOL}^{\text{N}_2\text{S}_2}$, increasing the amount of H_2O_2 compared to the thioanisole leads to a decrease in

efficiency. However, as shown in the stability study, higher TONs are able to be achieved by successive additions of H_2O_2 and thioanisole. Both catalysts **A** and **D**⁴² have been run under similar conditions to our studies (1:100:100) and show comparable results to what has been obtained with $\text{VO}_2\text{L}^{\text{NS}2}$ & $\text{VOL}^{\text{N}2\text{S}2}$ (Table 2.4). Consequently, it can be concluded that our results represent some of the fastest kinetics for sulfoxidation using vanadium-based catalysts. In addition, the main advantage of our catalysts is their complete selectivity towards the production of sulfoxide.

2.5 Mechanistic Investigations

From the above study concerning the reactivity of both complexes $\text{VO}_2\text{L}^{\text{NS}2}$ and $\text{VOL}^{\text{N}2\text{S}2}$, we can conclude that, although $\text{VOL}^{\text{N}2\text{S}2}$ has a lower efficiency with respect to $\text{VO}_2\text{L}^{\text{NS}2}$, $\text{VOL}^{\text{N}2\text{S}2}$ displays a remarkably higher stability. To investigate these differences we have carried out experiments in order to further investigate the mechanism.



Scheme 2.10. Adapted from the generally accepted mechanism for the oxidation of sulfide (or sulfoxide) *via* a vanadium peroxo-intermediate.^{41,43}

Scheme 2.10 is adapted from the generally accepted catalytic cycle for sulfoxidation by vanadium(IV) or (V) complexes.^{41,43} The commonly proposed active species is a *cis*-oxo peroxo V^{V} intermediate. Consequently, when considering V^{IV} complexes, the activating step corresponds to their oxidation into V^{V} species, which will correspond to the “real” catalysts.

Looking first at catalyst $\text{VOL}^{\text{N}2\text{S}2}$, the reaction has been followed by EPR spectroscopy. Firstly no change in the EPR spectrum has been observed when thioanisole (100 equivalents vs $\text{VOL}^{\text{N}2\text{S}2}$) is added, in agreement with the fact that the reaction does not involve the coordination of the substrate on the vanadium centre. Secondly, after the addition of H_2O_2 (20 equivalents), the EPR spectrum became silent, consistent with the oxidation of $\text{VOL}^{\text{N}2\text{S}2}$ into a diamagnetic V^{V} species. We also used ^{51}V NMR to investigate

the catalytic cycle. While no peak is observed with the initial solutions, as soon as the oxidant is added, a peak appears at -707 ppm (Figure 2.11B). After one hour, a decrease of this peak and concomitant formation of a new peak at -555 ppm is observed. Based on the mechanism shown in Scheme 2.9, the -707 ppm peak can be attributed to a peroxo V^V intermediate, while that at -555 ppm to the active catalyst related to VOL^{N2S2} , which corresponds to a V^V species.

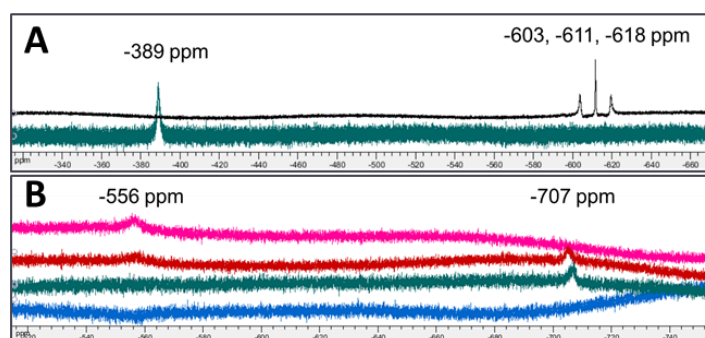


Figure 2.11. ^{51}V NMR spectra recorded during thioanisole sulfoxidation catalysed by (A) VO_2L^{NS2} (5.0 mM in CD_3CN) and (B) VOL^{N2S2} (5.0 mM in $CDCl_3$). Conditions (catalyst:thioanisole: H_2O_2 , 1:100:20).

For catalyst VO_2L^{NS2} , the reaction has been followed by ^{51}V NMR only (Figure 2.11A). The initial spectrum displays a signal at -389 ppm, which is insensitive to the addition of thioanisole. After the addition of H_2O_2 , this peak instantaneously disappears with the concomitant appearance of three peaks at -603, -611 and -618 ppm (relative intensity: 1/2/1). Their intensity remains the same for the next 12 hours. Based on the fact that catalyst VO_2L^{NS2} is completely inactive after one run, we attribute these peaks to degraded form(s) of VO_2L^{NS2} . Mass spectral analysis of this solution has been performed and the spectrum displays several peaks, some of which can be attributed to S-oxygenated forms of VO_2L^{NS2} with the addition of 1 to 2 oxygen atoms. This has also been observed with both VO_2L^{NS2} and VOL^{N2S2} catalysts; if the experiments are carried out in the absence of thioanisole the oxygenation of one or both thiolate(s) is observed on the L^{NS2} or L^{N2S2} ligands. These oxygenation reactions are not selective and lead to a mixture of products, precluding their characterisation. This is consistent with what has been previously found in the case of $VO(NOS_2)$ (shown previously in Scheme 2.6) a V^V dithiolate complex, in which the bound-thiolates can be oxidised either into monosulfenate or disulfenate with H_2O_2 .¹⁵

2.6 Computational Investigation

Based on these data, a computational investigation has been carried out in order to better describe the active species of catalysts $\text{VO}_2\text{L}^{\text{NS}_2}$ and $\text{VOL}^{\text{N}_2\text{S}_2}$, and also with the aim of providing information to rationalize their differences in reactivity and stability.

Three different structures displayed in Figure 2.12, have been optimized: (i) the catalytically active form of $\text{VOL}^{\text{N}_2\text{S}_2}$, $[\text{V}(\text{O})_2\text{L}^{\text{N}_2\text{S}_2}]^-$ (ii) the oxo peroxy vanadium(V) complex derived from $\text{VOL}^{\text{N}_2\text{S}_2}$, $[\text{VO}(\text{O}_2)\text{L}^{\text{N}_2\text{S}_2}]^-$, and (iii) the oxo peroxy vanadium(V) complex derived from $\text{VO}_2\text{L}^{\text{NS}_2}$, $[\text{VO}(\text{O}_2)\text{L}^{\text{NS}_2}]^-$. Selected bond distances are reported in Table 2.5.

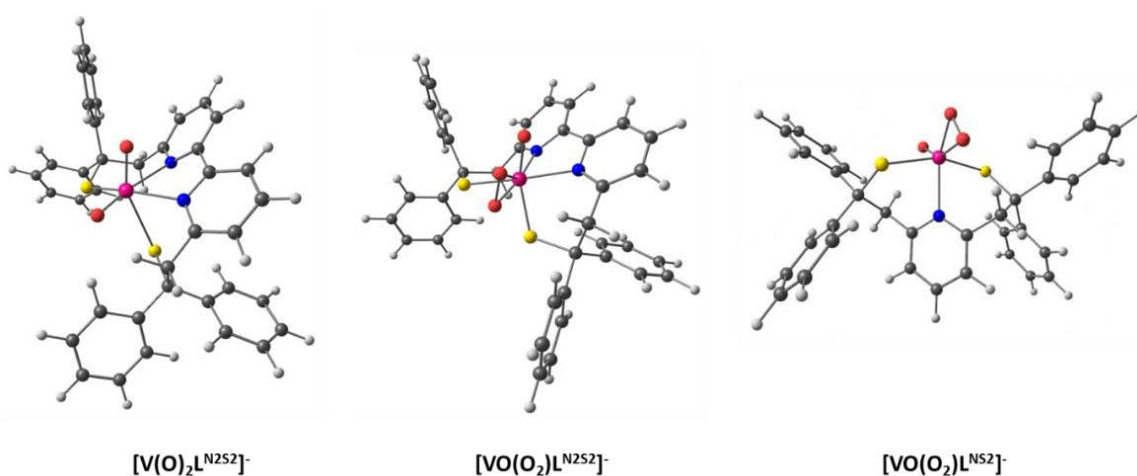


Figure 2.12. DFT optimised structures of $[\text{V}(\text{O})_2\text{L}^{\text{N}_2\text{S}_2}]^-$, $[\text{VO}(\text{O}_2)\text{L}^{\text{N}_2\text{S}_2}]^-$, and $[\text{VO}(\text{O}_2)\text{L}^{\text{NS}_2}]^-$.

Table 2.5. Important bond distances of optimised structures, $[\text{V}(\text{O})_2\text{L}^{\text{N}_2\text{S}_2}]^-$, $[\text{VO}(\text{O}_2)\text{L}^{\text{N}_2\text{S}_2}]^-$, and $[\text{VO}(\text{O}_2)\text{L}^{\text{NS}_2}]^-$.

	$[\text{V}(\text{O})_2\text{L}^{\text{N}_2\text{S}_2}]^-$		$[\text{VO}(\text{O}_2)\text{L}^{\text{N}_2\text{S}_2}]^-$		$[\text{VO}(\text{O}_2)\text{L}^{\text{NS}_2}]^-$
V-O1*	1.617	V-O1*	1.651	V-O1*	1.600
V-O2*	1.600	V-O2*	2.003	V-O2*	2.036
V-S1	2.394	V-O3*	1.800	V-O3*	1.758
V-S2	2.743	V-S1	2.212	V-S1	2.394
V-N1	2.192	V-S2	2.285	V-S2	2.443
V-N2	2.462	V-N1	2.190	V-N1	2.241
		V-N2	2.134		

*O1 and O2, O3 stand for oxygen atom from oxo and peroxy function, respectively.

The DFT-calculated ^{51}V NMR shifts have been predicted for these models and the values are reported in Table 2.6. They are all in the expected range for such complexes. In fact, as previously mentioned the $\delta(^{51}\text{V})$ range for complexes with only O-, N- or/and S-based ligands is extremely broad, between +600 to -600 ppm. In addition, the $\delta(^{51}\text{V})$ is mainly

affected by ligands with large electronegativity values such as oxo ligands, while variations of the coordination number between 4 and 6 do not influence shielding significantly.³² Consequently, the exchange of an oxo ligand for a peroxy one should lead to a more negative $\delta(^{51}\text{V})$, as has been previously observed in several cases. Even though the experimental $\delta(^{51}\text{V})$ observed for $[\text{V}(\text{O})_2\text{L}^{\text{N2S2}}]^-$ and $[\text{VO}(\text{O}_2)\text{L}^{\text{N2S2}}]^-$ are not perfectly reproduced, the substantial shielding seen when going from the dioxo- V^{V} species to the oxo peroxy one is well predicted by the computations. Thus, all these data confirm the experimental ^{51}V NMR analysis presented above and also validate the optimized structure of the computational models.

Table 2.6. NMR parameters for $\text{VO}_2\text{L}^{\text{NS2}}$, $[\text{V}(\text{O})_2\text{L}^{\text{N2S2}}]^-$, $[\text{VO}(\text{O}_2)\text{L}^{\text{N2S2}}]^-$, and $[\text{VO}(\text{O}_2)\text{L}^{\text{NS2}}]^-$.

System	Calc. δ (ppm)	Expt. δ (ppm)
VOL^{NS2}	-390	-389
$[\text{V}(\text{O})_2\text{L}^{\text{N2S2}}]^-$	-477	-550
$[\text{VO}(\text{O}_2)\text{L}^{\text{N2S2}}]^-$	-652	-707

To rationalize the difference in stability and efficiency during the sulfoxidation catalysis between $\text{VO}_2\text{L}^{\text{NS2}}$ and VOL^{N2S2} , we focus on the structure of the active species, *i.e.* the *cis*-oxo peroxy V^{V} complexes. In the reported structures of *cis*-oxo peroxy vanadium(V) complexes, the two $\text{V}-\text{O}_{\text{peroxy}}$ bond lengths are very similar ($\Delta_d < 10$ pm, with Δ_d being the difference between the two $\text{V}-\text{O}_{\text{peroxy}}$ bond distances). Conversely, in the case of both peroxy models presented here, the $\text{V}-\text{O}_{\text{peroxy}}$ distances are notably different, *i.e.* $\Delta_{\text{distance}} = 28$ pm and 20 pm in $[\text{VO}(\text{O}_2)\text{L}^{\text{NS2}}]^-$ and $[\text{VO}(\text{O}_2)\text{L}^{\text{N2S2}}]^-$, respectively. This could be related to their reactivity. Indeed, those that have been characterized by X-ray crystallography must be very stable species, whereas, on the other hand, the $[\text{VO}(\text{O}_2)\text{L}^{\text{NS2}}]^-$ and $[\text{VO}(\text{O}_2)\text{L}^{\text{N2S2}}]^-$ peroxy complexes are both very reactive, the kinetics of the reactions with $\text{VO}_2\text{L}^{\text{NS2}}$ and VOL^{N2S2} being especially fast when compared to the majority of the vanadium catalysts. We therefore propose that the larger the dissymmetry observed in the peroxy complexes, the more reactive they are, consistent with the fact that the sulfoxidation kinetics for $\text{VO}_2\text{L}^{\text{NS2}}$ are faster than with VOL^{N2S2} and that $\text{VO}_2\text{L}^{\text{NS2}}$ is less stable than VOL^{N2S2} during the catalysis.⁴⁴ To the best of our knowledge we did not find any computational studies related to the stability and/or structure of very reactive peroxy V^{V} complexes, and therefore our proposition is only based on the present results. However, we are aware that other structural factors can

also contribute to the reactivity of these peroxo complexes, for example the distance between the peroxo ligand and the vanadium-bound sulfur atoms.

Conclusion

It was widely proposed that high oxidation states of alkyl thiolate vanadium complexes should be difficult to stabilize due to their propensity to oxidize the thiolate ligands into intra- or intermolecular S-S units with the concomitant reduction of the metal ion. However, the alkyl dithiolate V^{IV} and even V^V complexes investigated here, exhibit a great stability in solution in aerobic conditions.

The tridentate L^{NS2} ligand allows the isolation of the first dioxovanadium(V) thiolate complex which has been resolved by X-ray crystallography. It has also proven to be an efficient and selective catalyst for sulfoxidation. It can produce phenylmethylsulfoxide from thioanisole quasi quantitatively using H_2O_2 as oxidant in less than a 10 minutes. This catalytic species is, however, not stable; after one single run we observe degradation into S-oxidised species. We have carried out DFT calculations to further investigate the *cis*-oxo peroxo active species. From this study we have observed low symmetry of the V-peroxo unit, consistent with high reactivity and high efficiency, thereby providing an explanation for the low stability of VO_2L^{NS2} . The reactivity of the VO_2L^{NS2} complex has been compared with a vanadyl compound synthesized with the tetradentate L^{N2S2} ligand. We have found significant differences between the two catalysts; the activity (yield), and stability of both systems are different. With respect to the difference in activity, this depends on the conditions of the reaction, especially the quantity of H_2O_2 , with VO_2L^{NS2} , displaying similar efficiency between the standard conditions (1:100:20) and quantitative conditions (1:100:100). However, in the case of catalyst VOL^{N2S2} a 30 % decrease in activity is observed under the quantitative conditions. We have also seen a substantial difference between the stability of the two catalysts. Where VO_2L^{NS2} is not stable at all, we see an outstanding stability from catalyst VOL^{N2S2} . Remarkably, both catalysts show 100 % selectivity towards the sulfoxide with no sulfone detected at all.

In regards to the discrepancy observed in reactivity between the two catalysts, combined experimental and computational investigations have been carried out. The results have allowed us to propose that this is in part related to a difference in the symmetry observed in the peroxo unit of the two complexes; the peroxo unit in

$[\text{VO}(\text{O}_2)\text{L}^{\text{NS}_2}]^-$ is less symmetric than that in the $[\text{VO}(\text{O}_2)\text{L}^{\text{N}_2\text{S}_2}]^-$ complex. Therefore the $[\text{VO}(\text{O}_2)\text{L}^{\text{NS}_2}]^-$ complex should be more reactive but less stable, consistent with the experimental findings.

This work opens an entire field for the synthesis of new vanadium catalysts based on alkyl thiolate ligands for oxidation reactions, in view of their efficiency and selectivity.

References

- (1) Winter, J. M.; Moore, B. S. *J. Biol. Chem.* **2009**, *284*, 18577–18581.
- (2) Ligtenbarg, A. G. ; Hage, R.; Feringa, B. L. *Coord. Chem. Rev.* **2003**, *237*, 89–101.
- (3) Rehder, D. *Inorg. Chem. Commun.* **2003**, *6*, 604–617.
- (4) Crans, D. C.; Smee, J. J.; Gaidamauskas, E.; Yang, L. *Chem. Rev.* **2004**, *104*, 849–902.
- (5) Da Silva, J. A. L.; da Silva, J. J. R. F.; Pombeiro, A. J. L. *Coord. Chem. Rev.* **2011**, *255*, 2232–2248.
- (6) Conte, V.; Coletti, A.; Floris, B.; Licini, G.; Zonta, C. *Coord. Chem. Rev.* **2011**, *255*, 2165–2177.
- (7) Rehder, D. *Angew. Chem. Int. Ed. Engl.* **1991**, *30*, 148–167.
- (8) Eady, R. R. *Coord. Chem. Rev.* **2003**, *237*, 23–30.
- (9) Ten Brink, H. B.; Schoemaker, H. E.; Wever, R. *Eur. J. Biochem.* **2001**, *268*, 132–138.
- (10) Andersson, M.; Willetts, A.; Allenmark, S. *J. Org. Chem.* **1997**, *62*, 8455–8458.
- (11) Bertini, I.; Sigel, A. *Handbook on Metalloproteins*; CRC Press, 2001.
- (12) Jenkins, R. M.; Pinder, T. A.; Hatley, M. L.; Reibenspies, J. H.; Darensbourg, M. Y. *Inorg. Chem.* **2011**, *50*, 1849–1855.
- (13) Farchione, D.; Wedd, A. G.; Tiekink, E. R. T. *Acta Crystallogr. C* **1991**, *47*, 650–651.
- (14) Nanda, K. K.; Sinn, E.; Addison, A. W. *Inorg. Chem.* **1996**, *35*, 1–2.
- (15) Cornman, C. R.; Stauffer, T. C.; Boyle, P. D. *J. Am. Chem. Soc.* **1997**, *119*, 5986–5987.
- (16) Crans, D. C.; Zhang, B.; Gaidamauskas, E.; Keramidias, A. D.; Willsky, G. R.; Roberts, C. R. *Inorg. Chem.* **2010**, *49*, 4245–4256.
- (17) Maurya, M. R.; Khurana, S.; Zhang, W.; Rehder, D. *Eur. J. Inorg. Chem.* **2002**, *2002*, 1749–1760.
- (18) Wang, D.; Ebel, M.; Schulzke, C.; Grüning, C.; Hazari, S. K. S.; Rehder, D. *Eur. J. Inorg. Chem.* **2001**, *2001*, 935–942.
- (19) Kovacs, J. A. *Chem. Rev.* **2004**, *104*, 825–848.
- (20) Bryngelson, P. A.; Maroney, M. J. In *Nickel and Its Surprising Impact in Nature*; Sigel, A.; Sigel, H.; Sigel, R. K. O., Eds.; John Wiley & Sons, Ltd, 2007; pp. 417–443.
- (21) Berg, J. M.; Holm, R. H. *J. Am. Chem. Soc.* **1985**, *107*, 925–932.
- (22) Gennari, M.; Orio, M.; Pécaut, J.; Neese, F.; Collomb, M.-N.; Duboc, C. *Inorg. Chem.* **2010**, *49*, 6399–6401.
- (23) Artaud, I.; Chatel, S.; Chauvin, A. S.; Bonnet, D.; Kopf, M. A.; Leduc, P. *Coord. Chem. Rev.* **1999**, *190–192*, 577–586.
- (24) Maurya, M. R.; Kumar, A.; Bhat, A. R.; Azam, A.; Bader, C.; Rehder, D. *Inorg. Chem.* **2006**, *45*, 1260–1269.
- (25) Wheeler, D. E.; Wu, J.-F.; Maatta, E. A. *Polyhedron* **1998**, *17*, 969–976.
- (26) Maurya, M. R.; Khurana, S.; Shailendra; Azam, A.; Zhang, W.; Rehder, D. *Eur. J. Inorg. Chem.* **2003**, *2003*, 1966–1973.
- (27) Samanta, S.; Ghosh, D.; Mukhopadhyay, S.; Endo, A.; Weakley, T. J. R.; Chaudhury, M. *Inorg. Chem.* **2003**, *42*, 1508–1517.
- (28) Neese, F. *Coord. Chem. Rev.* **2009**, *253*, 526–563.
- (29) Orio, M.; Pantazis, D. A.; Neese, F. *Photosynth. Res.* **2009**, *102*, 443–453.
- (30) Almaraz, E.; Foley, W. S.; Denny, J. A.; Reibenspies, J. H.; Golden, M. L.; Darensbourg, M. Y. *Inorg. Chem.* **2009**, *48*, 5288–5295.
- (31) Gennari, M.; Retegan, M.; DeBeer, S.; Pécaut, J.; Neese, F.; Collomb, M.-N.; Duboc, C. *Inorg. Chem.* **2011**, *50*, 10047–10055.
- (32) Rehder, D.; Weidemann, C.; Duch, A.; Priebisch, W. *Inorg. Chem.* **1988**, *27*, 584–587.
- (33) Dutton, J. C.; Fallon, G. D.; Murray, K. S. *Inorg. Chem.* **1988**, *27*, 34–38.
- (34) Solomon, E. I.; Gorelsky, S. I.; Dey, A. *J. Comput. Chem.* **2006**, *27*, 1415–1428.
- (35) Hanson, G. R.; Berliner, L. J. *Metals in Biology: Applications of High-Resolution EPR to Metalloenzymes*; Springer, 2010.
- (36) Klich, P. R.; Daniher, A. T.; Challen, P. R.; McConville, D. B.; Youngs, W. J. *Inorg. Chem.* **1996**, *35*, 347–356.
- (37) Triantafillou, G. D.; Tolis, E. I.; Terzis, A.; Deligiannakis, Y.; Raptopoulou, C. P.; Sigalas, M. P.; Kabanos, T. A. *Inorg. Chem.* **2004**, *43*, 79–91.
- (38) Munzarová, M. L.; Kaupp, M. *J. Phys. Chem. B* **2001**, *105*, 12644–12652.
- (39) Maurya, M. R.; Chandrakar, A. K.; Chand, S. *J. Mol. Catal. Chem.* **2007**, *278*, 12–21.
- (40) Mba, M.; Pontini, M.; Lovat, S.; Zonta, C.; Bernardinelli, G.; Kündig, P. E.; Licini, G. *Inorg. Chem.* **2008**, *47*, 8616–8618.
- (41) Maurya, M. R.; Saini, P.; Kumar, A.; Costa Pessoa, J. *Eur. J. Inorg. Chem.* **2011**, *2011*, 4846–4861.
- (42) Barroso, S.; Adão, P.; Madeira, F.; Duarte, M. T.; Pessoa, J. C.; Martins, A. M. *Inorg. Chem.* **2010**, *49*, 7452–7463.

- (43) Rehder, D.; Ebel, M.; Wikete, C.; Santoni, G.; Gätjens, J. *Pure Appl. Chem.* **2005**, *77*, 1607–1616.
- (44) Du, G.; Espenson, J. H. *Inorg. Chem.* **2005**, *44*, 2465–2471.

**Vanadium(III) Alkyl Thiolate Molecular Model in
Relation to Vanadium Nitrogenase**

Résumé

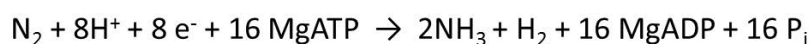
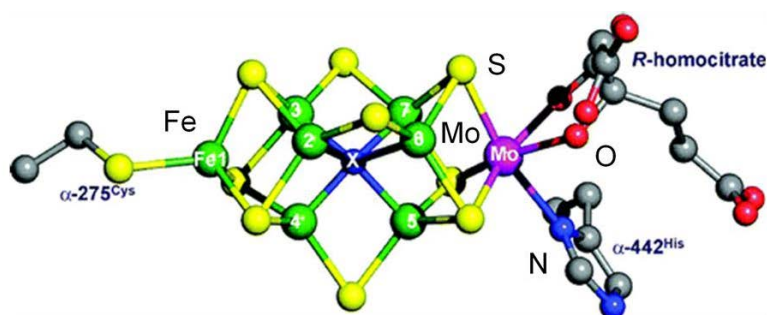
La nitrogénase à vanadium est une enzyme capable de réduire le diazote en ammoniac grâce à un processus faisant intervenir 6 électrons et 6 protons. Son site actif contient un cluster original constitué de 7 atomes de fer et d'un atome de vanadium dans un environnement riche en soufre. Actuellement, seuls deux systèmes moléculaires synthétiques sont capables de mimer l'activité catalytique de cette enzyme. Ces catalyseurs sont peu efficaces, le meilleur effectuant moins de 12 cycles catalytiques. Dans ce chapitre, nous présentons la synthèse et la caractérisation d'un complexe du vanadium(III) avec le ligand L^{NS_2} , modèle bio-inspiré de la nitrogénase à vanadium.

Par diffraction des rayons X nous avons pu résoudre la structure de ce nouveau complexe de vanadium(III), montrant que deux ions chlorure sont également coordonnés au vanadium, $[VCl_2L^{NS_2}]^+$. En solution, ces ions chlorure peuvent s'échanger avec des molécules de solvant. De plus, ce complexe se dégrade en présence de la moindre trace d'oxygène moléculaire, rendant son étude encore plus complexe.

Notre objectif était de tester la réactivité de ce complexe vis à vis de la réduction de l'hydrazine en ammoniac. En effet l'hydrazine, un des intermédiaires formés lors de la réduction du diazote, est souvent utilisée comme substrat test dans la mesure où elle peut être assez facilement réduite en ammoniac selon un mécanisme à deux électrons et deux protons. Dans ce but nous avons réduit chimiquement notre complexe en dérivés du vanadium(II) dans le THF et le DMF. Malgré de nombreuses tentatives, nous n'avons pas pu caractériser les espèces du vanadium(II) qui, mises en présence d'hydrazine, forment immédiatement un précipité. Aucun adduit vanadium-hydrazine n'a pu être isolé et caractérisé. Par contre, l'addition de protons entraîne la formation d'un complexe soluble de vanadium(IV), mais nous n'avons pas pu mettre en évidence la production concomitante d'ammoniac. L'analyse par chromatographie ionique s'est révélée être inefficace à cause de la présence du donneur de protons que nous avons utilisé. D'autres techniques d'analyse, comme la mise en évidence par spectroscopie visible d'un adduit ammoniac-indophénol ou la chromatographie en phase gazeuse, vont être rapidement testées. Bien que ces résultats de réactivité soient préliminaires, ils n'en demeurent pas moins extrêmement prometteurs et cette étude va être poursuivie dans le cadre d'une nouvelle thèse au laboratoire.

Introduction

Nitrogenases are bacterial enzymes capable of catalysing the reduction of atmospheric dinitrogen into bioavailable ammonia. They are responsible for cycling around 10^8 tonnes of N_2 per year from the atmosphere to the soil. Nitrogenases are two component enzymes, where in an ATP-dependent process, electrons are shuttled by the nitrogenase iron protein to the dinitrogenase reductase, which contains the active site.¹ The nitrogenase active site consists of a biologically unique iron-sulfur cluster which contains an interstitial carbon atom ($[MFe_7S_9C]$).^{2,3} The Fe-S cluster is then bound via three sulfur bridges to either a molybdenum (Mo)-, vanadium (V)-, or iron (Fe)- metal ion centre (Scheme 3.1). The three homologous nitrogenases are all similar in primary sequence and cluster type.⁴ Although these three different nitrogenase are all capable of catalysing the reduction of N_2 to NH_3 with the concomitant reduction of protons to molecular hydrogen, they differ in their catalytic rates and efficiencies, including the stoichiometry of NH_3 and H_2 produced per mol of N_2 reduced.

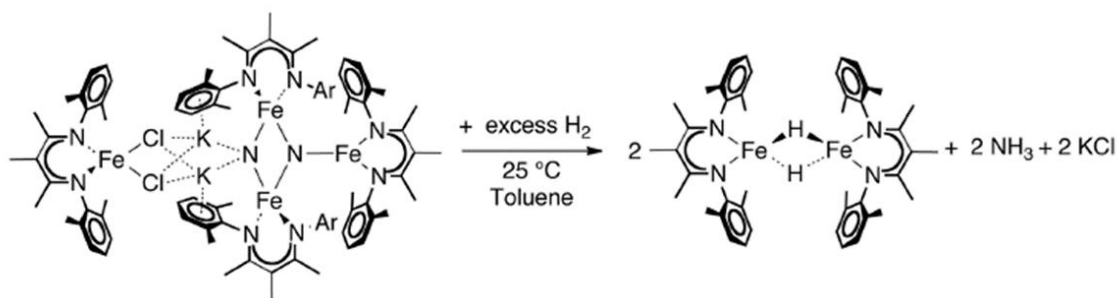


Scheme 3.1. X-ray structure of the FeMo-cofactor from *Azotobacter vinelandii* (X= C) and the balanced chemical equation for the catalytic reduction of N_2 into NH_3 .

The Mo-nitrogenase active site is the most common nitrogenase enzyme, the most efficient system, and the most studied. It is the only nitrogenase that has been crystallographically characterised. Its active-site structure is shown in Scheme 3.1. Despite the similarities between V-nitrogenase (V-Nase) and Mo-nitrogenase, studies of the V-Nase system have taken longer and have proven more complicated than the Mo-nitrogenase. However, the recent discovery of its CO-reducing capacity into alkenes and alkanes has put it in the spotlight.⁵

As stated above, nitrogenases are the connections between the atmospheric reservoir of inorganic nitrogen molecules and the biosphere, where nitrogen is an essential element

to all life. At present, dinitrogen reduction is reproduced in the commercial Haber–Bosch process (involving H_2 as the reducing agent), but this process occurs under extreme temperature and pressure conditions, utilising 1.4 % of global energy consumption.⁶ However, this reaction is vital for the production of synthetic fertilizers, which are needed to produce food for the world’s expanding population.⁷ Consequently, it is still a great challenge for chemists to reproduce this catalytic process under mild conditions, because of the intrinsic chemical inertia of N_2 (due to the high dissociation energy of the triple bond, $\Delta H^0_d = 945 \text{ kJ mol}^{-1}$, and to the high HOMO-LUMO gap, $\Delta E_{HL} = 23 \text{ eV}$). The competition between N_2 and proton reduction during the catalytic process is a further complication.⁸ Understanding how nature activates the strongest homodinuclear bond in chemistry, the triple bond of N_2 , is the key for the future design of molecular catalysts.

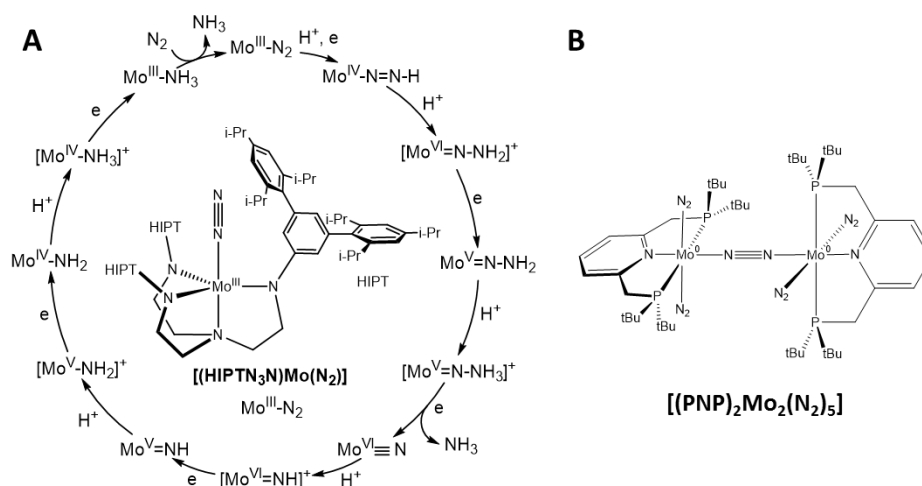


Scheme 3.2. Quantitative reduction of N_2 into NH_3 using the Fe-based complex of Holland and coworkers.⁹

The catalytic cycle, to date, is far from being understood. A consensus view has yet to emerge on whether the Fe-S cluster and/or the additional metal is the key player in substrate binding during nitrogenase catalysis.^{10,11} Many authors have favoured the iron hypothesis, based on the existence of the three different nitrogenases,¹² on energetic considerations,¹³ and on other assumptions and indirect evidence.^{14–16} Very recently, Holland and co-workers reported the first example of a molecular iron complex (Scheme 3.2) capable of reducing N_2 into NH_3 . This reaction proceeds at room temperature and atmospheric pressure, in the presence of a reducing agent and protons (or H_2).⁹ However, this system is not catalytic.

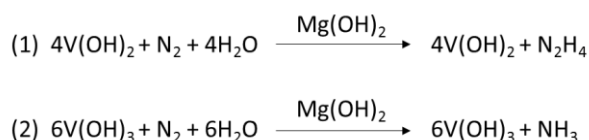
There is also a lot of support towards the ‘additional metal centre’ (Mo-, V-, or Fe-) being the site for substrate binding. Indeed, the three homologous nitrogenases differ in their reactivity. Furthermore, examples of N_2 binding at V-, and Mo- metal centres have been previously reported. Finally, the only two known molecular transition metal ion

complexes, capable of reducing N_2 catalytically at room temperature and atmospheric pressure are Mo-based systems: the Schrock complex $[(HIPTN_3N)Mo(N_2)]$ (Scheme 3.3A)¹⁷ and the Nishibayashi complex $[(PNP)_2Mo_2(N_2)_5]$ (Scheme 3.3B).¹⁸ However, the amount of generated NH_3 is limited to approximately 8 and 12 molar equivalents per Mo ion, for **A** and **B**, respectively.

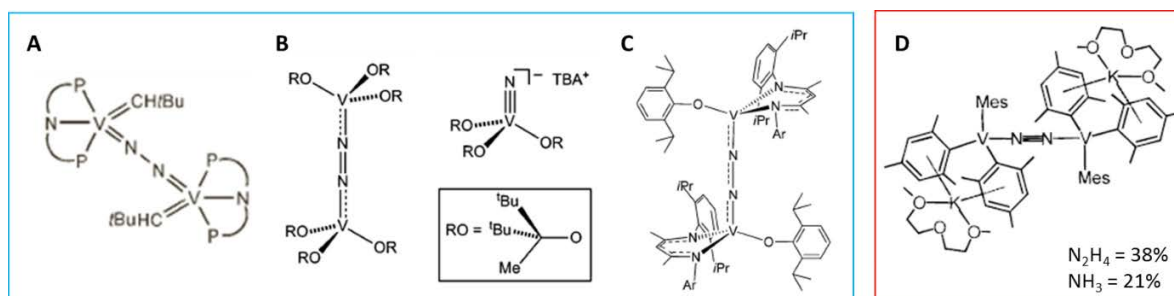


Scheme 3.3. The Mo-based mononuclear Schrock complex (**A**) and the dinuclear Nishibayashi complex (**B**) as catalysts for N_2 reduction. The proposed catalytic mechanism for $[(HIPTN_3N)Mo]$ is also shown.

Vanadium is an interesting metal choice for the activation of dinitrogen, as firstly, in 1970 Shilov *et al.* showed that a binuclear V^{II} - and Mg^{II} - hydroxide species was able to convert N_2 into NH_3 and N_2H_4 (Scheme 3.4).^{19,20}



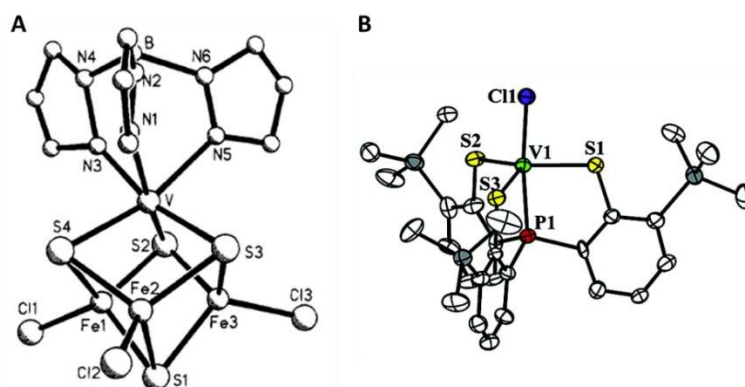
Scheme 3.4. The reaction of Shilov's binuclear V^{II} -, Mg^{II} - hydroxide nitrogenase model.



Scheme 3.5. Vanadium- N_2 adducts (**A**) $[(PNP)_2V_2(N_2)]$,³² (**B**) the two V- N_2 adducts, dinuclear $[(OR)_6V_2(N_2)]$ and mononuclear $[(OR)_3VN]$,³⁰ (**C**) $[(nacnac)_2(ODiP)_2V_2(N_2)]$,³¹ and (**D**) $[(Mes)_6V_2(N_2)_2][(K(digly))]$.²⁹

In addition, a number of vanadium compounds capable of fixing dinitrogen,²¹⁻³¹ have been already reported (see Scheme 3.5 for some examples). Although the catalytic cycle is still unknown, it has been shown from molecular model studies, that V^{II} is required to fix N₂. Among these V-based complexes, only one (Scheme 3.5D) has been shown to reduce N₂. It converts N₂ into NH₃ (21%) and N₂H₄ (38%) stoichiometrically not catalytically. The V-N₂ adducts all contain O-, N- or P- based donor ligands, whereas the nitrogenase active site is sulfur-rich.

Two thiolate V^{III} molecular models have been previously described and are shown in Scheme 3.6.^{33,34} Both are capable of catalytically reducing N₂H₄ into NH₃, in the presence of cobaltocene as the reducing agent and 2,6-lutidinium chloride as the proton donor. In both cases, they have shown that the substrate binding occurs in the V^{II} oxidation state.^{34,35} However, neither were able to activate N₂. Hydrazine is often used as a substrate, because only 2e⁻ are necessary to reduce it into NH₃, while 6e⁻ are required for the reduction of N₂ into NH₃. Furthermore, hydrazine is one of the intermediate species during the 6e⁻ reduction process from N₂ to NH₃.



Scheme 3.6. V-S ligated complexes (A) [Fe₃S₄VL]²⁺ and (B) [(PS₃)VCl]⁻ capable of catalytically reduce N₂H₄ into NH₃.

In terms of functional molecular models of nitrogenase, although there are some catalytic models, as reported above, their efficiency is still very limited in terms of TON. Therefore, the chemistry of nitrogen fixation and reduction under ambient conditions remains one of the most challenging research domains in chemistry. Indeed, dinitrogen is extremely inert, therefore the formation of metal-N₂ adducts is a key first step in nitrogen activation. In this context, we have synthesised a mononuclear V^{III}-thiolate complex with the purpose of activating N₂H₄.

In this chapter we present a summary of preliminary results we have obtained. A V^{III} starting complex has been synthesised and characterised crystallographically. Using this V^{III} complex we have attempted to chemically generate the reduced V^{II} derivative. In addition, the reactivity of the V^{II} derivative has been tested toward hydrazine.

Results and Discussion

3.1 Synthesis and Characterisation of the $[VCl_2L^{NS2}]^-$ complex

$K[VCl_2L^{NS2}]$ was prepared from a THF solution of K_2L^{NS2} and $VCl_3 \cdot 3THF$. Because it is air sensitive, all manipulations were carried out under an argon atmosphere. Single crystals of the PPN salt suitable for X-ray diffraction were obtained by addition of PPNCl (bis(triphenylphosphine)iminium chloride) to a CH_2Cl_2 solution of the K salt, followed by slow diffusion of Et_2O . X-ray collection and refinement data are given in the Appendix. The structure of the $[VCl_2L^{NS2}]^-$ anion is presented in Figure 3.1, while selected bond distances and angles are listed in Table 3.1.

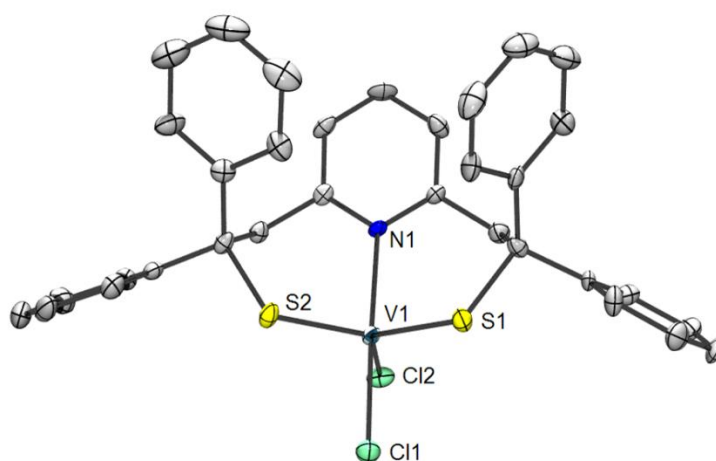


Figure 3.1 ORTEP diagram of the $[VCl_2L^{NS2}]^-$ anion. The thermal ellipsoids are drawn at 50% probability level. The cation PPN^+ ion, solvent molecules (CH_2Cl_2) and hydrogen atoms have been omitted for clarity.

The structure of $PPN[VCl_2L^{NS2}] \cdot 2CH_2Cl_2$ consists of a $[VCl_2(L^{NS2})]^-$ anion, one PPN^+ cation and two CH_2Cl_2 solvent molecules. The V^{III} centre is five-coordinate, with the two alkyl thiolate sulfur atoms of L^{NS2} and one chloride ion forming a trigonal plane, while the other chloride ion and the pyridine nitrogen atom of L^{NS2} lie mutually *trans* along the trigonal axis. This results in a mononuclear trigonal bipyramidal V^{III} complex with a structural index of $\tau = 1.02$ [$= (\beta - \alpha)/60$, β is the axial angle $N1-V-Cl1$ (176.02°) and α is the angle $S1-V-Cl1$ (114.56°)],³⁶ showing perfect trigonal bipyramidal geometry. The V-S

(2.269 and 2.293 Å) and V-Cl bond distances (2.381 and 2.31 Å) are consistent with those found in previously described trigonal bipyramidal V^{III} thiolate complexes (V^{III} -Salkyl 2.25 -2.38 Å, V^{III} -Cl 2.30 -2.38 Å).^{34,37-39}

All further experiments were carried out using the potassium salt of the complex ($K[VCl_2L^{NS_2}]$) as the synthesis is reproducible and the isolation of pure material easier than with PPN^+ . ESI-Mass spectrometry has confirmed that the vanadium complex anion is the same with both counter cations. We have also obtained single crystals of the $[VCl_2(L^{NS_2})]^-$ anion with Et_3NH^+ as the counter cation. This structure displays an identical coordination sphere about the V^{III} ion. Nevertheless, only the crystal structure with counter cation PPN^+ , which displays a better resolution than with Et_3NH^+ , is presented here.

Table 3.1. Selected bond lengths (Å) and angles (°) for the X-ray structure of $[VCl_2L^{NS_2}]PPN \cdot CH_2Cl_2$.

Bond lengths (Å)			
V-N1	2.204(4)	V-Cl1	2.3814(15)
V-S1	2.2685(16)	V-Cl2	2.3100(18)
V-S2	2.2928(17)		
Angles (°)			
N1-V-S1	93.37(12)	S2-V-Cl2	122.81(7)
N1-V-S2	93.84(12)	N1-V-Cl1	176.02(13)
S1-V-S2	114.56(7)	S1-V-Cl1	82.93(6)
N1-V-Cl2	88.69(13)	S2-V-Cl1	86.41(6)
S1-V-Cl2	122.31(7)	Cl2-V-Cl1	94.51(6)

The electronic absorption spectra are identical between the three different salts of the complex. This confirms that the environment of the V^{III} ion is similar in the three complexes. In the solid state, the $[VCl_2L^{NS_2}]^-$ anion is highly unstable and even with a small trace of O_2 , oxidation of the V^{III} ion occurs into a vanadyl species as seen by EPR. Furthermore, it is well known that V^{III} mononuclear complexes can undergo disproportionation into their corresponding V^{IV} and V^{II} species.⁴⁰ Indeed, a small amount of V^{IV} species is observed in the X-band EPR spectra of $K[VCl_2L^{NS_2}]$ in all solvents (DMF, THF, CH_2Cl_2 and MeCN).

$K[VCl_2L^{NS_2}]$ has been characterised by UV-Visible spectroscopy in four different solvents: CH_2Cl_2 , MeCN, DMF and THF (Figure 3.2). It can be seen that solvent has a major effect on the electronic properties of $K[VCl_2L^{NS_2}]$. The transition at 414 nm is consistent in all solvents, but its intensity is significantly larger in CH_2Cl_2 compared to

those observed in the spectra recorded in MeCN, DMF and THF. In addition, the spectra in DMF shows an additional transition in the visible region, at 488 nm. These findings are consistent with solvent coordination. Solvent effects have been previously reported in a vanadium aromatic thiolate complex (Scheme 3.6B, $[(PS_3)VCl]^-$) which contains a single ligated chloride.³⁷ Chu *et. al.* observed that the transition at 450 nm of this thiolate V^{III} complex in CH_2Cl_2 is significantly more intense than in MeCN. They have shown that this is due to exchange of the chloride anion with an MeCN solvent molecule. In addition, from the intensity of the 414 nm transition, it can be concluded that DMF and THF show a higher affinity toward solvent coordination than MeCN.

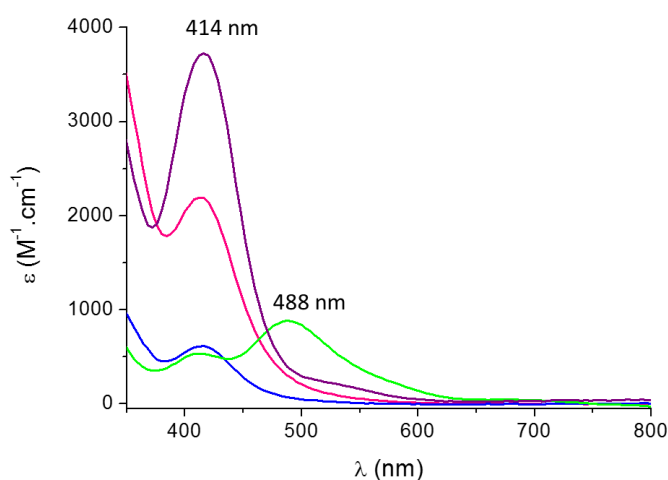


Figure 3.2. The electronic absorption of $K[VCl_2L^{NS_2}]$ in CH_2Cl_2 (violet), MeCN (pink), DMF (green) and THF (blue).

3.2 Reduction of $K[VCl_2L^{NS_2}]$

As stated in the introduction, the only vanadium complexes capable of activating dinitrogen are V^{II} complexes.^{19,29,31,41,42} For this purpose, we have attempted to chemically reduce $K[VCl_2L^{NS_2}]$ into its V^{II} counterpart, in different solvents such as DMF, THF, CH_2Cl_2 and MeCN, and using 5% Na/Hg amalgam as the reducing agent. In CH_2Cl_2 and MeCN, all attempts to reduce $K[VCl_2L^{NS_2}]$ failed. We attribute this to the fact that chloride anion(s) is/are still coordinated to the vanadium ion, thus preventing the chemical reduction. In fact, we have observed by UV-Visible spectroscopy that in CH_2Cl_2 both chloride anions remain coordinated, and that MeCN has a low affinity for vanadium coordination compared to both DMF and THF.

The chemical reduction has been followed by UV-Visible and EPR spectroscopy. As can be seen by UV-Visible spectroscopy (Figure 3.3A), $K[VCl_2L^{NS_2}]$ is completely reduced in DMF using 2 eq of 5% Na/Hg amalgam. Only two hours are required to complete the

reduction with the total disappearance of the three transitions at 414, 488 and 690 nm, and the concomitant appearance of a single transition at 470 nm for the reduced species. The EPR spectra (Figure 3.3B) show that the small amount of V^{IV} species present in the initial solutions has completely disappeared after the addition of 5% Na/Hg amalgam. If more of the reducing agent is added, degradation of the complex is observed.

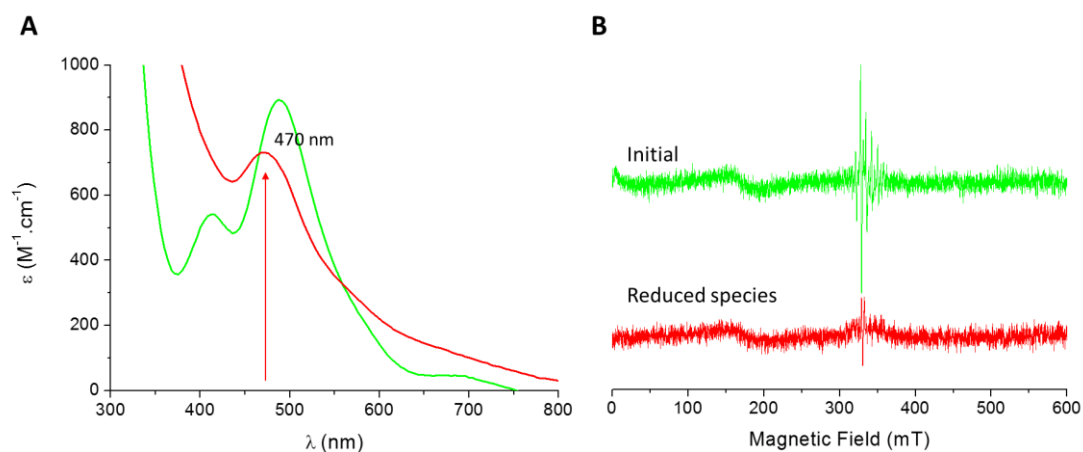


Figure 3.3. Electronic absorption (A) and EPR (B) spectra of a solution of $K[VCl_2L^{NS_2}]$, before (green) and after (red) the addition of 2 eq of 5 % Na/Hg amalgam in DMF.

In theory, V^{II} complexes (d^3 , $S = 3/2$) should be EPR active. However, even at low temperature (5 K), we were unable to observe a signal (Figure 3.3B). In fact, to the best of our knowledge, V^{II} EPR spectroscopy is very rare, with only two solid state EPR investigations, with one being a V^{II} species doped into a diamagnetic host lattice.^{31,43} Unfortunately in solution, it seems that the sensitivity of cw X-band EPR spectroscopy toward V^{II} is too low to observe a signal.

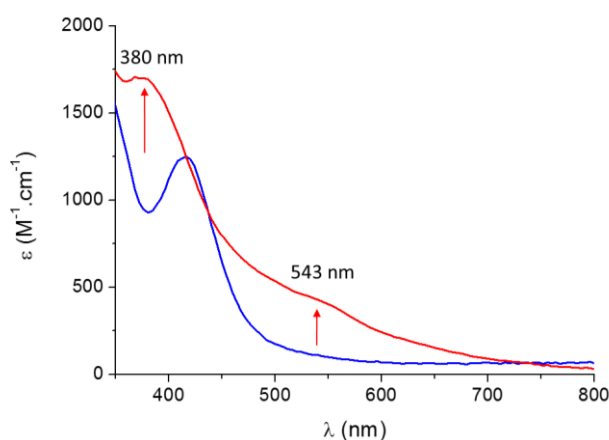


Figure 3.4. Electronic absorption spectra of a solution of $K[VCl_2L^{NS_2}]$, before (blue) and after (red) the addition of 2 eq of 5 % Na/Hg amalgam in THF.

In THF, the reduction reaction is harder to perform than in DMF; two or more days are required. Furthermore, sequential filtration and addition of about 1 eq of 5 % Na/Hg amalgam is required every two hours. However, THF is a more suitable solvent for further manipulations of the reduced species (isolation and characterisation of the products), especially when working in a glove-box.

By UV-Visible spectroscopy (Figure 3.4), the most notable difference in the spectra observed between the initial solution and after the chemical reduction is the complete disappearance of the transition at 414 nm characteristic of the V^{III} species, and the concomitant appearance of two transitions at 380 nm and 543 nm. As in DMF, the EPR spectrum of the reduced solution is silent. Although the reduced species display two different UV-Visible spectra in DMF and THF, we assign them both as two different V^{II} species. It is not surprising that two inequivalent V^{II} derivatives are generated, as the two starting V^{III} complexes have different coordination spheres, due to the solvent exchange equilibrium with the chloride anion.

3.3 Reaction of V^{II} species with Hydrazine

When the reduced species obtained from $K[VCl_2L^{NS2}]$ generated in THF reacts with 2 eq of N_2H_4 , a very fine brown precipitate is formed immediately, that we were unable to recover. This is consistent with the binding of N_2H_4 to the V^{II} species, resulting in a neutral insoluble V^{II} compound. In an attempt to isolate this product, we have carried out the reaction in DMF. Unfortunately the same fine powder, also insoluble in DMF, precipitates instantly.

In the presence of the weak acid, lutidinium BF_4 ($LutH^+$) as the proton source, we observed solubilisation of the hydrazine derivative in both solvents. This reaction has been followed by UV-Visible (Figure 3.5A) and EPR spectroscopy (Figure 3.5B). The same UV-Visible spectra are observed after the addition of 4 eq of $LutH^+$ (Figure 3.5A) with a single transition observed at 404 nm in both DMF and THF. We have verified that this transition cannot be assigned to the lutidine. The EPR spectra recorded in both THF and DMF show the appearance of a V^{IV} EPR signal, which is not characteristic of a vanadyl unit. When this EPR tube is opened to air, we observe the appearance of new signal which is consistent with the formation of a vanadyl complex, as shown by the hyperfine lines at 288, 298 and 308 mT. Therefore, we can unambiguously assign the signal observed after the addition of $LutH^+$ to a V^{IV} species. This is consistent with a $2H^+/2e^- N_2H_4$ reduction process with the concomitant oxidation of V^{II} to V^{IV} .

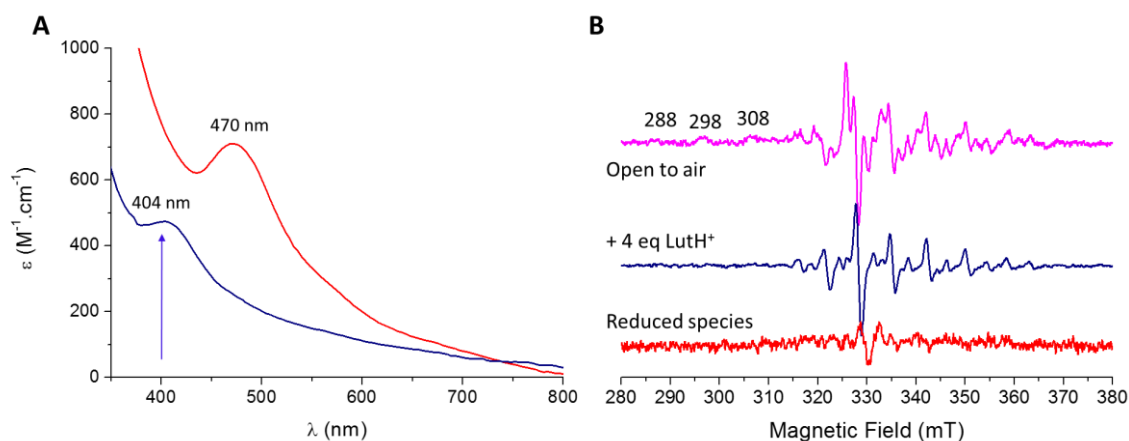


Figure 3.5. (A) UV-Visible spectra of the chemically reduced species of $\text{K}[\text{VCl}_2\text{L}^{\text{NS}_2}]$ (red) and after the addition of 2 eq of hydrazine and 4 eq of LutH^+ (blue) in DMF. (B) EPR spectra of the chemically reduced species of $\text{K}[\text{VCl}_2\text{L}^{\text{NS}_2}]$ (red), after the addition of 2 eq of hydrazine and 4 eq of LutH^+ (blue), and the sample open to air (pink) in DMF.

Conclusion

In conclusion, we have successfully synthesised and characterised a V^{III} complex containing a tridentate bis-thiolate ligand and two coordinated chloride anions. In solution the chloride anion(s) can be exchanged with solvent molecule(s) as a function of the nature of the solvent.

Chemical reduction of $\text{K}[\text{VCl}_2\text{L}^{\text{NS}_2}]$ using 5% Na/Hg amalgam has been carried out in order to obtain the more reactive V^{II} species. The reaction only proceeds in DMF and THF and gives two different V^{II} species. It is important to note that the chemical reduction, using 5% Na/Hg amalgam, is long and extremely difficult to control especially in THF. We have begun testing the reduction with different reducing agents, such as zinc dust and potassium graphite.

We have tested the reactivity of the resulting V^{II} species toward hydrazine. Upon reaction of this V^{II} species with hydrazine, precipitation is observed, consistent with the binding of N_2H_4 to the V^{II} ion. Unfortunately, we were not able to isolate and characterise this hydrazine-V adduct. More interestingly, this precipitate reacts in the presence of protons leading to the same soluble V^{IV} species in both DMF and THF.

The V^{III} complex $\text{K}[\text{VCl}_2\text{L}^{\text{NS}_2}]$ has exhibited some very interesting properties in terms of modelling V-nitrogenase. In fact, our preliminary results suggest that this V^{III} complex is a precursor to a complex capable of the activation of N_2H_4 . We have attempted to confirm the production of ammonia. The method that we have employed so far is ion chromatography. Unfortunately, by this technique, we cannot properly separate the

LutH⁺ and NH₄⁺. Consequently, another analytical method such as the use of indophenol should be used. In addition, we have also tested the reactivity of the **K[VCl₂L^{NS2}]** complex toward N₂. However, as of yet, we have been unable to obtain reproducible results.

There are also major draw-backs with this complex, including the instability of **K[VCl₂L^{NS2}]** both in solid state and solution, together with its V^{II} derivatives. In order to stabilise both the V^{III} and the V^{II} compounds, we wish to insert the V^{III} complex directly into the nitrogenase metalloprotein. This project will be initiated in collaboration with the groups of Borovik and Ribbe. Also, changing the tridentate ligand to the tetradentate ligand (L^{N2S2}, as seen in chapter II), may aid in the stabilisation of the V^{III} and V^{II} complexes. We have already made initial attempts to synthesise the V^{III} complex. Small crystals have already been obtained, and the crystallisation conditions are now being optimised in order to isolate suitable crystals for X-ray diffraction.

References

- (1) McGlynn, S. E.; Boyd, E. S.; Peters, J. W.; Orphan, V. J. *Front. Microbiol. Chem.* **2013**, *3*, 419.
- (2) Ramaswamy, S. *Science* **2011**, *334*, 914–915.
- (3) Lancaster, K. M.; Roemelt, M.; Ettenhuber, P.; Hu, Y.; Ribbe, M. W.; Neese, F.; Bergmann, U.; DeBeer, S. *Science* **2011**, *334*, 974–977.
- (4) Eady, R. R. *Coord. Chem. Rev.* **2003**, *237*, 23–30.
- (5) Hu, Y.; Lee, C. C.; Ribbe, M. W. *Dalton Trans.* **2012**, *41*, 1118–1127.
- (6) Schrock, R. R. *Proc. Natl. Acad. Sci.* **2006**, *103*, 17087–17087.
- (7) Smil, V. *Sci. Am.* **1997**, *277*, 76–81.
- (8) Ogo, S.; Kure, B.; Nakai, H.; Watanabe, Y.; Fukuzumi, S. *Appl. Organomet. Chem.* **2004**, *18*, 589–594.
- (9) Rodriguez, M. M.; Bill, E.; Brennessel, W. W.; Holland, P. L. *Science* **2011**, *334*, 780–783.
- (10) Howard, J. B.; Rees, D. C. *Proc. Natl. Acad. Sci.* **2006**, *103*, 17088–17093.
- (11) Hoffman, B. M.; Dean, D. R.; Seefeldt, L. C. *Accounts Chem. Res.* **2009**, *42*, 609–619.
- (12) Eady, R. R. *Chem. Rev.* **1996**, *96*, 3013–3030.
- (13) Neese, F. *Angew. Chem. Int. Ed.* **2006**, *45*, 196–199.
- (14) Sellmann, D.; Sutter, J. *Accounts Chem. Res.* **1997**, *30*, 460–469.
- (15) Dos Santos, P. C.; Igarashi, R. Y.; Lee, H.-I.; Hoffman, B. M.; Seefeldt, L. C.; Dean, D. R. *Accounts Chem. Res.* **2005**, *38*, 208–214.
- (16) Lukoyanov, D.; Dikanov, S. A.; Yang, Z.-Y.; Barney, B. M.; Samoilo, R. I.; Narasimhulu, K. V.; Dean, D. R.; Seefeldt, L. C.; Hoffman, B. M. *J. Am. Chem. Soc.* **2011**, *133*, 11655–11664.
- (17) Yandulov, D. V.; Schrock, R. R. *Science* **2003**, *301*, 76–78.
- (18) Arashiba, K.; Miyake, Y.; Nishibayashi, Y. *Nat. Chem.* **2011**, *3*, 120–125.
- (19) Shilov, A.; Denisov, N.; Efimov, O.; Shuvalov, N.; Shuvalova, N.; Shilova, A. *Publ. Online 18 June 1971* *Doi101038231460a0* **1971**, *231*, 460–461.
- (20) Bazhenova, T. A.; Shilov, A. E. *Coord. Chem. Rev.* **1995**, *144*, 69–145.
- (21) Song, J.-I.; Berno, P.; Gambarotta, S. *J. Am. Chem. Soc.* **1994**, *116*, 6927–6928.
- (22) Berno, P.; Hao, S.; Minhas, R.; Gambarotta, S. *J. Am. Chem. Soc.* **1994**, *116*, 7417–7418.
- (23) Buijink, J. K. F.; Meetsma, A.; Teuben, J. H. *Organometallics* **1993**, *12*, 2004–2005.
- (24) Ferguson, R.; Solari, E.; Floriani, C.; Chiesi-Villa, A.; Rizzoli, C. *Angew. Chem. Int. Ed. Engl.* **1993**, *32*, 396–397.
- (25) Rehder, D.; Woitha, C.; Priebisch, W.; Gailus, H. *J. Chem. Soc. Chem. Commun.* **1992**, 364–365.
- (26) Woitha, C.; Rehder, D. *Angew. Chem. Int. Ed. Engl.* **1990**, *29*, 1438–1440.
- (27) Leigh, G. J.; Prieto-Alcón, R.; Sanders, J. R. *J. Chem. Soc. Chem. Commun.* **1991**, 921–922.
- (28) Edema, J. J. H.; Meetsma, A.; Gambarotta, S. *J. Am. Chem. Soc.* **1989**, *111*, 6878–6880.
- (29) Ferguson, R.; Solari, E.; Floriani, C.; Osella, D.; Ravera, M.; Re, N.; Chiesi-Villa, A.; Rizzoli, C. *J. Am. Chem. Soc.* **1997**, *119*, 10104–10115.
- (30) Groysman, S.; Villagrán, D.; Freedman, D. E.; Nocera, D. G. *Chem. Commun.* **2011**, *47*, 10242.
- (31) Tran, B. L.; Pinter, B.; Nichols, A. J.; Konopka, F. T.; Thompson, R.; Chen, C.-H.; Krzystek, J.; Ozarowski, A.; Telser, J.; Baik, M.-H.; Meyer, K.; Mindiola, D. J. *J. Am. Chem. Soc.* **2012**, *134*, 13035–13045.
- (32) Kilgore, U. J.; Sengelaub, C. A.; Pink, M.; Fout, A. R.; Mindiola, D. J. *Angew. Chem. Int. Ed.* **2008**, *47*, 3769–3772.
- (33) Kovacs, J. A.; Holm, R. H. *Inorg. Chem.* **1987**, *26*, 702–711.
- (34) Chu, W.-C.; Wu, C.-C.; Hsu, H.-F. *Inorg. Chem.* **2006**, *45*, 3164–3166.
- (35) Malinak, S. M.; Demadis, K. D.; Coucouvanis, D. *J. Am. Chem. Soc.* **1995**, *117*, 3126–3133.
- (36) Addison, A. W.; Rao, T. N.; Reedijk, J.; Rijn, J. van; Verschoor, G. C. *J. Chem. Soc. Dalton Trans.* **1984**, 1349–1356.
- (37) Hsu, H.-F.; Chu, W.-C.; Hung, C.-H.; Liao, J.-H. *Inorg. Chem.* **2003**, *42*, 7369–7371.
- (38) Davies, S. C.; Hughes, D. L.; Janas, Z.; Jerzykiewicz, L.; Richards, R. L.; Roger Sanders, J.; Sobota, P. *Chem. Commun.* **1997**, 1261–1262.
- (39) Davies, S. C.; Hughes, D. L.; Janas, Z.; Jerzykiewicz, L. B.; Richards, R. L.; Sanders, J. R.; Silverston, J. E.; Sobota, P. *Inorg. Chem.* **2000**, *39*, 3485–3498.
- (40) Dobson, J. C.; Taube, H. *Inorg. Chem.* **1989**, *28*, 1310–1315.
- (41) Zones, S. I.; Palmer, M. R.; Palmer, J. G.; Doemeny, J. M.; Schrauzer, G. N. *J. Am. Chem. Soc.* **1978**, *100*, 2113–2121.
- (42) Zones, S. I.; Vickrey, T. M.; Palmer, J. G.; Schrauzer, G. N. *J. Am. Chem. Soc.* **1976**, *98*, 7289–7295.
- (43) Jacobsen, C. J. H.; Pedersen, E.; Villadsen, J.; Weihe, H. *Inorg. Chem.* **1993**, *32*, 1216–1221.

**Nickel Alkyl-Thiolate Molecular Models for
Metalloenzymes CODH and NiSOD**

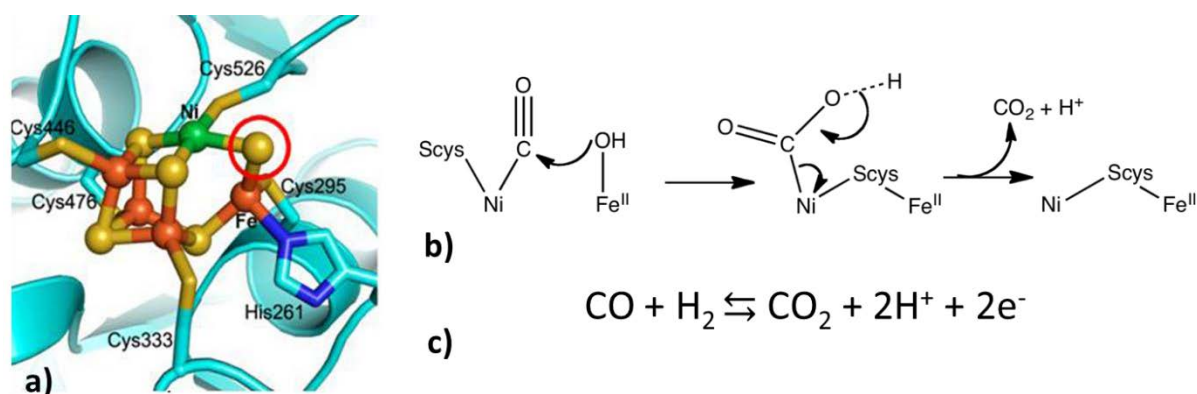
Résumé

Le chapitre IV est consacré à l'étude de complexes du nickel à ligands thiols aliphatiques, modèles bio-inspirés de la CO deshydrogénase (CODH) et de la superoxide dismutase à Ni (Ni-SOD). La CODH est une enzyme qui est capable d'activer le monoxyde de carbone en l'oxydant de manière réversible en dioxyde de carbone. Son site actif contient un atome de nickel dans un environnement riche en soufre, responsable de l'activation du CO. Avec comme objectif l'obtention d'adduits Ni-CO, nous avons synthétisé deux complexes du nickel(II) en utilisant le ligand L^{NS_2} afin de laisser un site vacant pour la coordination du CO. En effet, il avait été suggéré que le manque de réactivité des complexes précédents étudiés au laboratoire vis à vis du CO était dû à l'absence d'au moins un site vacant sur l'ion nickel. Deux complexes ont été obtenus : un dinucléaire de nickel(II) total inerte et un complexe mononucléaire de nickel(II). Les propriétés redox de ce dernier complexe ont été étudiées. Malheureusement, il ne nous a pas été possible malgré de nombreuses tentatives de générer d'adduits Ni-CO, ni avec le complexe de nickel(II), ni avec sa forme réduite nickel(I).

Dans une deuxième partie, nous avons étudié la réactivité d'un complexe mononucléaire du nickel(II), $[NiL^{N_2S_2}]$, précédemment décrit au laboratoire, vis à vis du tert-butylhydroperoxide (TBHP). Notre but était d'isoler un nouveau complexe peroxy pour modéliser les intermédiaires réactionnels du cycle catalytique de la NiSOD, qui réalise la réaction de disproportionnement du radical anion superoxide en H_2O_2 et O_2 . Le site actif de cette enzyme est formée d'un complexe mononucléaire du Ni possédant deux ligands cystéines. Très peu d'espèces actives de l'oxygène basées sur le nickel ont été décrites dans la littérature, dont seulement quatre complexes mononucléaires peroxy, aucun d'entre eux ne comportant de ligand thiol. De manière surprenante, en présence de TBHP nous avons pu générer un complexe mononucléaire tert-butylperoxy de nickel(III), remarquablement stable à température ambiante ($t_{1/2} = 3h$). Sa structure, totalement originale, a été prédite par une procédure d'optimisation par calculs DFT. Ce complexe a été caractérisé par spectroscopie d'absorption UV-visible, par RPE et par spectrométrie de masse. Ce complexe peroxy, qui présente un caractère électrophile faible, est capable d'oxyder la triphénylphosphine, mais pas les sulfures. Par ailleurs, le complexe initial $[NiL^{N_2S_2}]$ est régénéré lors de la réaction d'oxydation de la triphénylphosphine, ce qui suggère qu'il peut agir comme un vrai catalyseur.

Introduction

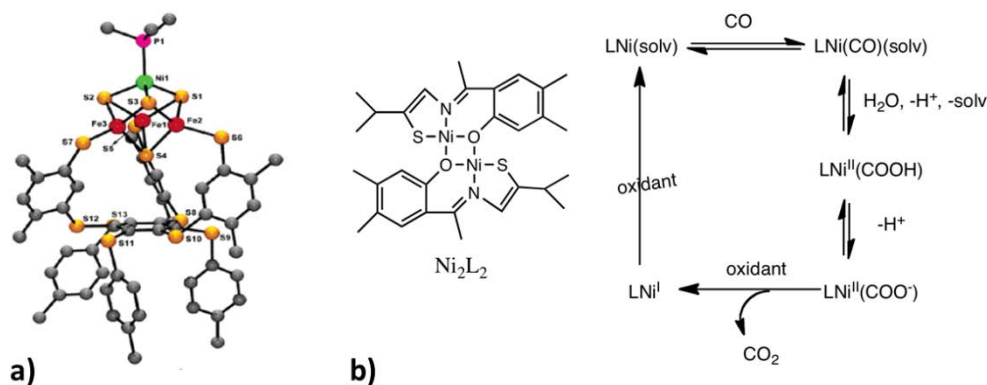
In recent years, mainly due to the discovery of metalloenzymes containing active sites with unprecedented structures and functions, bioinspired nickel coordination chemistry has grown into a large and broad research domain.¹ One of the most interesting facts about nickel in nature is that all of the well-established nickel sites are rather unique with respect to their structure and/or function. Only eight have been isolated to date, including four which are thiolate-rich, *via* cysteines bound to the nickel ion. The nickel-iron hydrogenase, which reversibly catalyses the reduction of protons into hydrogen, has been the subject of intense research, as an inspiration for cheap H₂-producing catalysts. Both acetyl coenzyme A synthase (ACS) and carbon monoxide dehydrogenase (CODH), which are capable of activating CO, are rich in thiolate groups with several cysteines bound to the nickel ion. Finally, nickel-superoxide dismutase (NiSOD), which is the most recent addition to the ubiquitous family of SODs, catalytically disproportionates the superoxide radical into hydrogen peroxide and molecular dioxygen. During my PhD, we have focused primarily on Ni-thiolate model complexes that mimic the active sites of the CODH, and NiSOD enzymes.



Scheme 4.1. **a)** The active site of metalloenzyme CODH (C cluster), **b)** part of the catalytic cycle mechanism and **c)** the catalytic reaction.

CODH is found in anaerobic bacteria, and along with ACS is responsible for the removal of more than one billion tonnes of CO per year from the atmosphere. In addition, CODH reduces CO₂ reversibly into CO (Scheme 4.1C). Although, the active site of CODH has been fully described, its catalytic cycle still remains unclear. The active site of CODH, the C-cluster (Scheme 4.1a), consists of a heteronuclear [Fe₃NiS₄] complex. The nickel metal centre coordinates four sulfur atoms resulting in a square planar geometry.²⁻⁴ A suggested reaction mechanism for CO activation is represented in Scheme 4.1b. To date the Ni oxidation state upon CO binding is still a matter of debate.

Although non-biologically-relevant phosphine donor groups were used in the C-cluster model reported by the group of Holm (Scheme 4.2a), this tetranuclear Fe_3NiS_4 complex provides the most accurate structural mimic for the CODH active site.⁵ Even with the large number of heteronuclear Ni/Fe complexes that have been synthesized to prepare structural and/or functional models of the NiFe hydrogenase active site, no conversion of CO to CO_2 has been reported with these systems. In fact, CO preferentially binds to Fe over Ni. This makes it difficult to form a Ni-CO adduct in such synthetic systems.

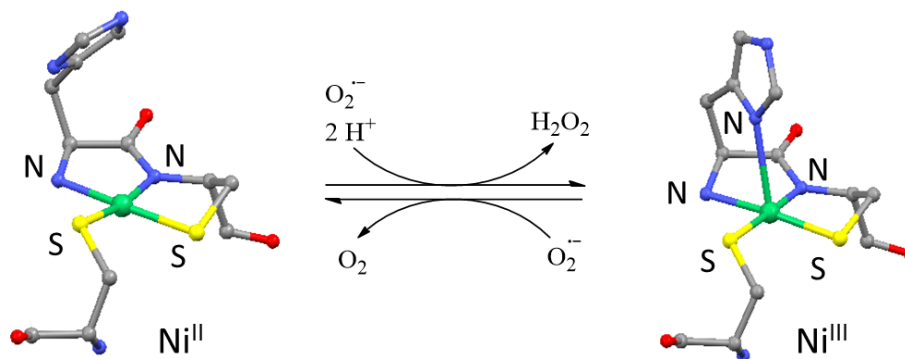


Scheme 4.2. Previously described structural (a) and functional (b) models of CODH.

Only one functional Ni-containing model has been described so far (Scheme 4.2b). In the nineties, Crabtree's group reported a dinuclear nickel complex with aryl thiolate ligands, that catalytically oxidizes CO in aqueous solution using methyl viologen as a sacrificial oxidant.⁶ However the proposed mechanism, which involves the intermediate formation of $\text{Ni}^{\text{I}}\text{-CO}$ and $\text{Ni}^{\text{II}}\text{-COOH}$ adducts, is based on kinetic studies alone, and no intermediate has been characterized.

Superoxide dismutases (SODs) are oxidoreductases that catalyse the disproportionation of the superoxide radical anion ($\text{O}_2^{\bullet-}$) into hydrogen peroxide and molecular dioxygen. Therefore SODs are important metalloproteins that protect living cells from oxidative damage. The superoxide radical anion has been linked to the aging process and to various disorders and diseases ranging in severity from inflammatory to neurodegenerative.⁷⁻⁹ There are three well characterized SODs, with active sites containing either mononuclear Mn or Fe, or a heterometallic Cu/Zn complex.¹⁰ Although the NiSOD shares the same function, the structure of the active site, especially the ligand environment around the nickel centre, is notably different, in contrast to the other SODs. The active site of NiSOD incorporates two cysteine thiolate S-donor atoms which can be subject to S-oxygenation processes in the presence of oxidants such as the superoxide

radical anion or H_2O_2 . Furthermore, the nickel ion is also bound to three different types of nitrogen-based ligands, a histidine and two less common types, namely an amide issuing from the peptide back bone and the terminal amine of the polypeptide. Finally, in contrast to the other SODs, no aqua/hydroxo ligand is present around the Ni centre.

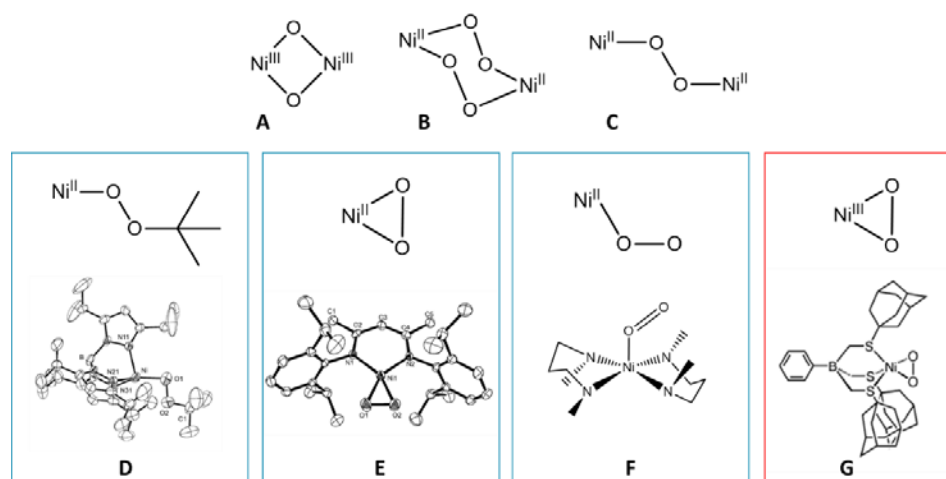


Scheme 4.3. Schematic representation of the NiSOD active site.

During the catalytic cycle of NiSOD, the Ni ion cycles between +II and +III oxidation states, accompanied by a notable structural rearrangement (Scheme 4.3). In the reduced state, the Ni^{II} centre is in a square planar $[\text{N}_2\text{S}_2]$ environment, containing the two S-thiolate ligands, the N-amidate, and N-terminal amino groups. Upon oxidation, the environment of the nickel ion is converted into a $[\text{N}_3\text{S}_2]$ square pyramid *via* coordination of the axial N-imidazole moiety of the histidine. This redox-state-dependant change in metal coordination number is crucial for SOD activity.¹¹

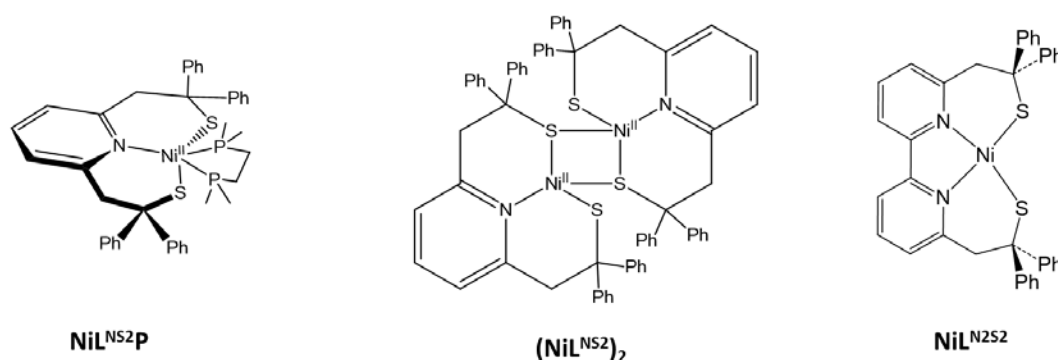
Another important aspect in the NiSOD mechanism is that the binding of the superoxide radical anion to the Ni ion is required at both oxidation states during the catalytic cycle. However, no peroxo intermediate has been evidenced or characterised to date.

As far as synthetic complexes are concerned, the majority of nickel active oxygen species are dinuclear nickel complexes. Both bis(μ -oxo)dinickel(III) (Scheme 4.4A),¹²⁻¹⁷ and bis(μ -1,2-superoxo)dinickel(II) (Scheme 4.4B) complexes,^{17,18} have been characterised by X-ray diffraction, while (μ -1,2-peroxo)dinickel(II) species (Scheme 4.4C)^{18,19} have only been spectroscopically observed. On the other hand, mononuclear peroxo nickel complexes are very rare. At present, two complexes have been characterised by X-ray crystallography (a (*tert*-butylperoxo)nickel(II) complex,²⁰ and a (η^2 -superoxo)nickel(II) complex,²¹ Scheme 4.4 D and E, respectively), while two superoxo complexes have only been observed spectroscopically (a (η^1 -superoxo)nickel(II) complex,²³ and a (η^2 -superoxo)nickel(III) complex²², Scheme 4.4 F and G, respectively).



Scheme 4.4. The previously reported dinuclear and mononuclear Ni^{II} and Ni^{III} active oxygen complexes.

Among the four mononuclear nickel active oxygen species previously described, only one (**G**) incorporates sulfur atoms, these being thioether S-donor atoms. More research needs to be carried out on mononuclear Ni^{II} and Ni^{III} active oxygen complexes which contain alkyl thiolate ligands, in order to further understand the mechanism of the NiSOD active site, especially with respect to peroxo intermediates.



Scheme 4.5. Nickel complexes discussed in this chapter.

In this chapter, we present our attempts to synthesise and characterise molecular models for both CODH and NiSOD metalloenzymes. In this context, we have synthesised three different Ni complexes (Scheme 4.5). The mononuclear **NiL^{NS2}P** and dinuclear **[Ni₂(L^{NS2})₂]** complexes have been investigated as molecular models for CODH. Their redox properties have been studied and their reactivity towards CO activation tested. In the second part of this chapter we have investigated the reactivity of **NiL^{NS2}S**, which has been previously described by our group,²⁴ towards different oxidants such as TBHP (*tert*-butyl peroxide). Our aim is to obtain nickel peroxo complexes with alkyl thiolate ligands for modelling intermediates implicated in the NiSOD catalytic cycle.

Results and Discussion

4.1 Synthesis and Characterisation of the $[\text{Ni}_2(\text{L}^{\text{NS}_2})_2]$ Complex

The L^{NS_2} ligand has previously been described in chapter II. $[\text{Ni}_2(\text{L}^{\text{NS}_2})_2] \cdot 2\text{THF}$ ($[\text{Ni}_2(\text{L}^{\text{NS}_2})_2]$) was obtained from the reaction with $\text{Na}_2\text{L}^{\text{NS}_2}$ with $\text{Ni}(\text{ClO}_4)_2 \cdot 6\text{H}_2\text{O}$ in THF. Single crystals of $[\text{Ni}_2(\text{L}^{\text{NS}_2})_2]$ suitable for X-ray diffraction were obtained from the reaction solution upon standing. Its molecular structure is presented in Figure 4.1. X-ray collection and refinement data are given in the Appendix, while selected bond distances and angles are listed in Table 4.1.

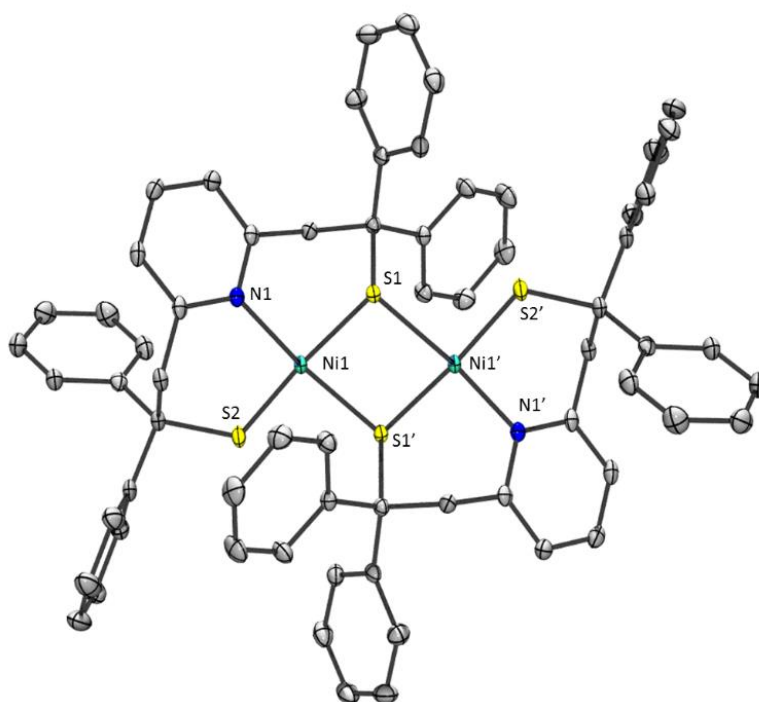


Figure 4.1. ORTEP diagram of $[\text{Ni}_2(\text{L}^{\text{NS}_2})_2] \cdot 2\text{THF}$. The thermal ellipsoids are drawn at the 30% probability level. All hydrogen atoms and THF solvent molecules are omitted for clarity.

There is a single plane of symmetry between the two Ni^{II} metal centres resulting in two identical Ni^{II} coordination environments. Both Ni^{II} ions are bound to three aliphatic thiolates S2 (or S2'), S1 and S1', the latter two forming a bridge between the two Ni^{II} ions. The pyridine unit of the L^{NS_2} ligand completes the square planar geometry of both Ni^{II} ions.

The bond distances between the metal ions and the bridging sulfur atoms Ni-S1 and Ni-S1' (2.2303 and 2.2085 Å) are within the expected range for Ni-S_{bridging} bond distances (2.19 – 2.26 Å).^{25,26} The Ni-S2 (2.1661 Å) distance is also comparable to Ni-thiolate bond distances reported in the literature (2.17 – 2.18 Å).^{24,27} The larger distance observed

with the bridging sulfur atoms than the Ni-thiolate bonds is normal, as the bridging sulfur atoms are less electron donating, acting more like the weaker thioether bond. The bond distance between the nickel and the pyridine nitrogen (Ni-N1, 1.9124 Å) has a typical bond distance for Ni-N_{pyridine} bonds (1.89 – 1.93 Å).²⁸ With respect to the packing environment of **[Ni₂(L^{NS₂)₂]}** the major intermolecular interactions are π–π interactions between pyridine rings (N1 and N1') as can be seen in Figure 4.2. These are offset by 1.501 Å with a centroid to centroid distance of 3.639 Å, which lies well below the maximum literature value for π–π interactions (3.8 Å).^{29,30}

Table 4.1 Selected bond lengths (Å) and angles (°) for the X-ray structure of **[Ni₂(L^{NS₂)₂]}**.

Bond Lengths (Å)			
Ni-N1	1.9124	Ni-S1	2.2303
Ni-S2	2.1661	Ni-S1'	2.2085
Angles (°)			
N1-Ni-S2	93.90	S2-Ni-S1	174.70
N1-Ni-S1	90.85	S2-Ni-S1'	91.18
N1-Ni-S1'	174.04	S1-Ni-S1'	83.96

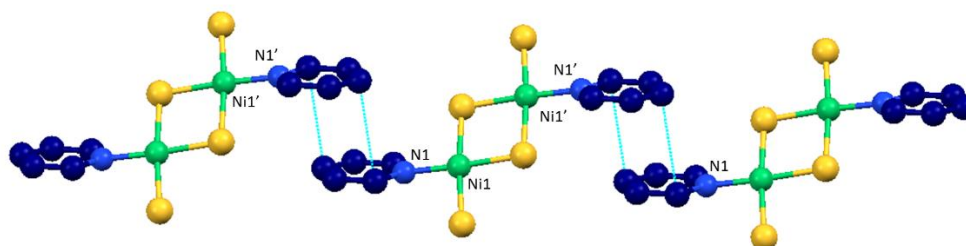
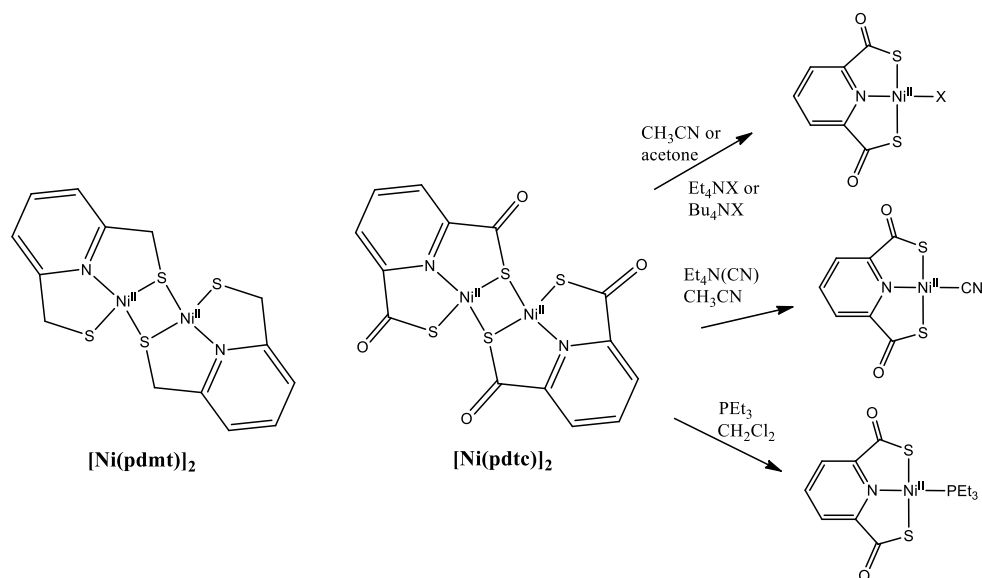


Figure 4.2. Intermolecular π – π interactions between pyridine rings of **[Ni₂(L^{NS₂)₂]}**.

It has previously been shown that this type of dinuclear Ni-(μ₂-S)-Ni complexes is useful as a precursor for the synthesis of mononuclear complexes. In particular, the group of Holm has shown the ability of the similar complexes **[Ni(pdmt)]₂**²⁷ and **[Ni(pdtc)]₂**²⁸ (Scheme 4.6) to carry out bridge cleavage reactions in the presence of potential ligand molecules. The complex **[Ni(pdtc)]₂** is considerably more reactive than **[Ni(pdmt)]₂** and is able to undergo facile bridge cleavage reactions to give an enormous variety of mononuclear complexes (see Scheme 4.6 for examples). In contrast, in the case of **[Ni(pdmt)]₂**, only strong nucleophilic ligands are able to cleave the sulfur bridge. This is obviously due to differences in the electronic properties of the sulfurs in both complexes. In **[Ni(pdtc)]₂**, a mesomeric effect occurs with the carbonyl group, rendering the sulfur atoms less nucleophilic than in **[Ni(pdmt)]₂**. Therefore, the μS bridge is

weaker in $[\text{Ni}(\text{pdtc})]_2$ and easier to cleave. Nevertheless, in the case of $[\text{Ni}_2(\text{L}^{\text{NS}2})_2]$, all of our attempts to carry out similar bond cleavage reactions using many different molecules (halogens, bipyridine, PPh_3 , etc), have failed. This is consistent with the work of Holm *et al.* The additional bulkiness of the two phenyl groups on the adjacent carbon atom in $\text{L}^{\text{NS}2}$ further lowers the reactivity of the thiolates compared to $[\text{Ni}(\text{pdmt})]_2$.



Scheme 4.6. The $[\text{Ni}(\text{pdmt})]_2$ and $[\text{Ni}(\text{pdtc})]_2$ complexes and the formation of various mononuclear complexes *via* bridge cleavage reactions.

4.2 Synthesis and Characterisation of the $[\text{NiL}^{\text{NS}2}\text{dmpe}]$ Complex

$[\text{NiL}^{\text{NS}2}\text{dmpe}]$ ($\text{NiL}^{\text{NS}2}\text{P}$, Scheme 4.5) was synthesised from the reaction of $\text{Na}_2\text{L}^{\text{NS}2}$ with $\text{Ni}(\text{ClO}_4)_2 \cdot 6\text{H}_2\text{O}$ and 1,2-Bis(dimethylphosphino)ethane. A powder of $\text{NiL}^{\text{NS}2}\text{P}$ was obtained on rapid precipitation by addition of Et_2O as soon as the reaction occurs. If this reaction is left for more than 30 minutes the dimer $[\text{Ni}_2(\text{L}^{\text{NS}2})_2]$ is obtained.

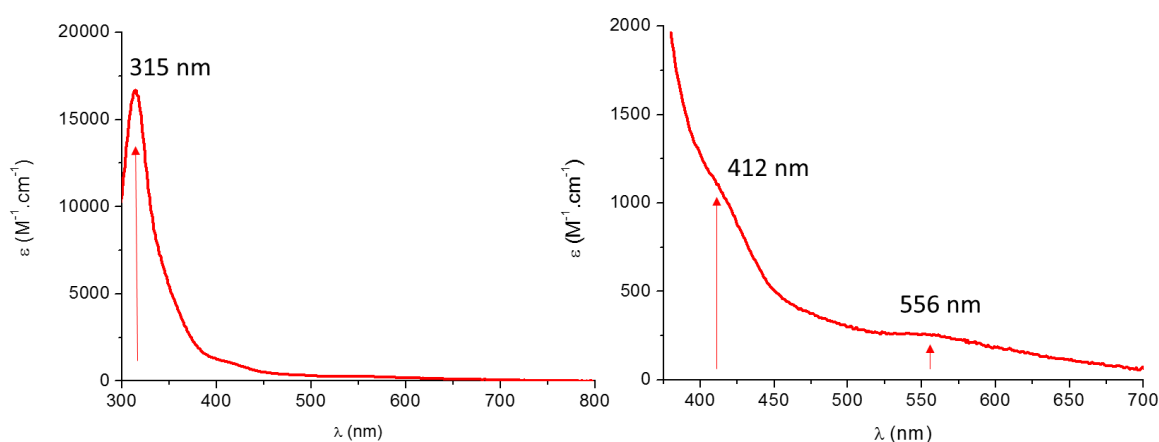


Figure 4.3. UV-Visible spectrum of $\text{NiL}^{\text{NS}2}\text{P}$ in CH_2Cl_2

We were unable to characterise **NiL^{NS2}P** by X-ray crystallography, because the thermodynamically stable product is the **[Ni₂(L^{NS2})₂]** complex. The electronic absorption spectrum of **NiL^{NS2}P** shows three transitions (Figure 4.3), that can be assigned to one LMCT at 315 nm ($\epsilon = 16640 \text{ M}^{-1}\cdot\text{cm}^{-1}$), and two d-d transitions at 405 nm ($\epsilon = 1076 \text{ M}^{-1}\cdot\text{cm}^{-1}$) and 555 nm ($\epsilon = 265 \text{ M}^{-1}\cdot\text{cm}^{-1}$).

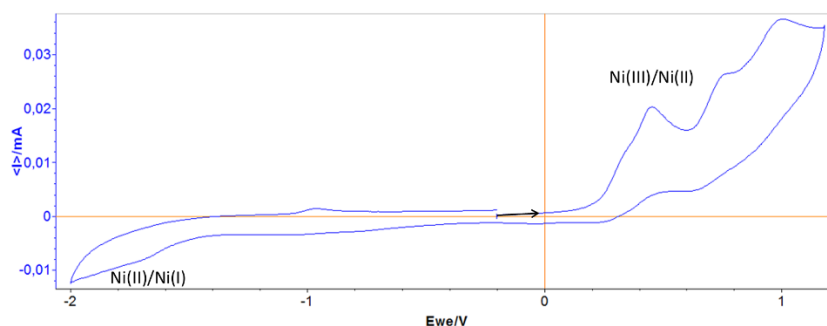


Figure 4.4. CV of **NiL^{NS2}P** (1.0 mM) in CH_2Cl_2 , 0.1 M Bu_4NClO_4 . Scan rate of $100 \text{ mV}\cdot\text{s}^{-1}$. Ref: Ag^+/Ag .

The electrochemical properties of **NiL^{NS2}P** were investigated in CH_2Cl_2 (Figure 4.4). The cyclic voltammogram (CV) displays two irreversible one-electron metal-based processes; a $\text{Ni}^{\text{III}}/\text{Ni}^{\text{II}}$ oxidation wave at $E_{1/2} = +0.3 \text{ V vs Ag}^+/\text{Ag}$, and a $\text{Ni}^{\text{II}}/\text{Ni}^{\text{I}}$ reduction wave at $E_{1/2} = -1.5 \text{ V}$ ($E_p = 180 \text{ mV}$). The irreversibility of these two redox systems reflects substantial structural changes during the oxidation and reduction processes.

Characterisation of the electro-generated oxidised and reduced species

To isolate the oxidised species, an exhaustive electrolysis was carried out at $+0.5 \text{ V}$. A notable change of colour was observed during the one electron oxidation, specifically the appearance of a transition at 365 nm , with the disappearance of the transitions associated with **NiL^{NS2}P**. To isolate the reduced species observed at -1.50 V , an exhaustive electrolysis at -1.60 V was run. In contrast to the facile generation of the oxidised species, the reduction at -1.60 V was significantly longer.

To determine whether the oxidation and reduction processes are centred on the nickel ion or on the ligand, the reactions were followed by EPR spectroscopy. An advantage of nickel is that the EPR signatures are specific towards its oxidation state, $\text{Ni}^{\text{II}}(\text{d}^8)$, $\text{Ni}^{\text{I}}(\text{d}^9)$ and $\text{Ni}^{\text{III}}(\text{d}^7)$. Ni^{II} complexes are always X-band EPR silent, independent of the spin state ($S = 1$, or $S = 0$). The EPR signature of Ni^{III} depends on its spin state, ($S=3/2$ or $S=1/2$). Finally Ni^{I} complexes always display the signature of an $S=1/2$ system.

The EPR spectrum of the oxidised species shows an $S=1/2$ axial signal, consistent with a low spin mononuclear Ni^{III} complex ($\text{NiL}^{\text{NS}2}\text{P}^{\text{ox}}$, Figure 4.5A) with $g_{\parallel} = 2.23$ and $g_{\perp} = 2.07$. In the g_{\perp} component, hyperfine coupling can be observed ($A_{\perp} = 4.5$ MHz). The triplet indicates a coupling between the single electron of Ni^{III} and the pyridine nitrogen of $\text{L}^{\text{NS}2}$ ($I=1$), suggesting a partial delocalisation of spin density over the ligand.

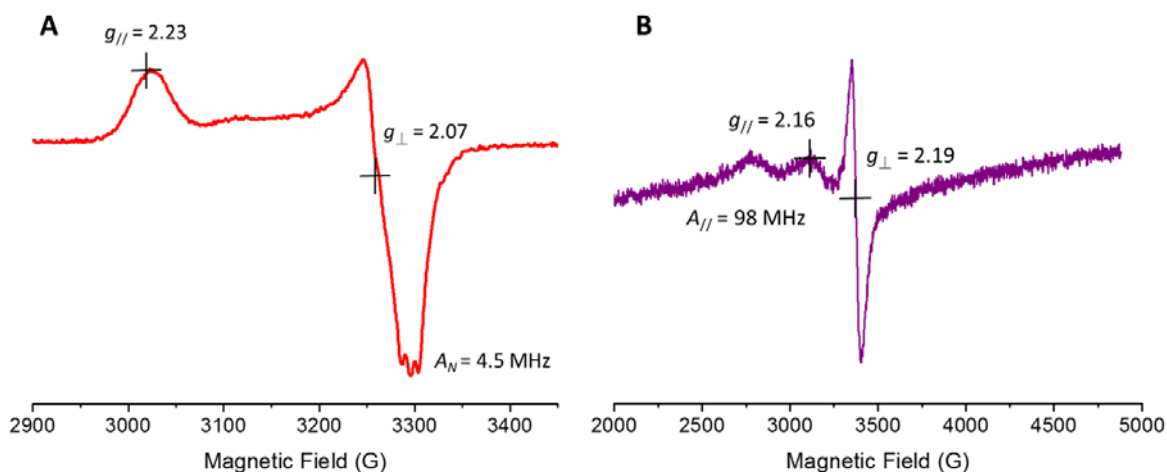


Figure 4.5. Experimental X-band EPR spectrum of **A)** $\text{NiL}^{\text{NS}2}\text{P}^{\text{ox}}$ and **B)** $\text{NiL}^{\text{NS}2}\text{P}^{\text{red}}$ in CH_2Cl_2 recorded at 100 K.

The EPR spectrum of the reduced species shows an $S=1/2$ axial signal consistent with a mononuclear Ni^{I} complex ($\text{NiL}^{\text{NS}2}\text{P}^{\text{red}}$, Figure 4.5B) with $g_{\parallel} = 2.16$ and $g_{\perp} = 1.99$. The axial component is split into three lines, as a result of the interaction of the unpaired electron with the nitrogen of the pyridine of $\text{L}^{\text{NS}2}$. The hyperfine value ($A_{\parallel} = 98$ MHz) is significantly larger than that seen in $\text{NiL}^{\text{NS}2}\text{P}^{\text{ox}}$, suggesting a larger delocalisation of the spin density over the ligand in the reduced species, to stabilise the Ni^{I} oxidation state. This is comparable with that previously reported for the one-electron reduced species of $\text{NiL}^{\text{N}2\text{S}2}$, $[\text{NiL}^{\text{N}2\text{S}2}]^-$ ($A_{\parallel} = 212$ MHz).³¹ In this case, it has been calculated by DFT that in the SOMO, 10 % of the electron density is located on each nitrogen atom of the bipyridine of the $\text{L}^{\text{N}2\text{S}2}$ ligand.

4.3 Activation of Carbon Monoxide

Our goal was to isolate a Ni-CO adduct with alkyl thiolate ligands. The previously synthesised $\text{NiL}^{\text{N}2\text{S}2}$ complex and its electrochemically one-electron reduced form $[\text{NiL}^{\text{N}2\text{S}2}]^-$ ³¹ were shown to exhibit no reactivity in the presence of CO. It was proposed that by decreasing the denticity of the coordinating ligand, a coordination site could be opened up, allowing CO coordination. The $\text{L}^{\text{NS}2}$ ligand was then the perfect candidate for this purpose.

Multiple attempts to obtain a Ni-CO adduct were carried out by bubbling CO through a solution of electro-generated $\text{NiL}^{\text{NS2P}^{\text{red}}}$ and also NiL^{NS2P} . In the case of NiL^{NS2P} no reaction was observed. With $\text{NiL}^{\text{NS2P}^{\text{red}}}$, a change in the UV-visible spectrum was observed; however, it appears that the resulting species was re-oxidized to a Ni^{II} complex during the reaction with CO. This is evidenced by the absence of an EPR signal from the final solution. Before considering new tests, it is necessary to develop a more reliable set-up to eliminate the presence of oxygen. More importantly, the L^{NS2} ligand presents two major draw-backs; (i) the facile generation of a thermodynamically stable dimer, and (ii) the difficulty in generating the Ni^{I} species.

4.4 Characterisation of the $[\text{NiL}^{\text{N2S2}}]$ Complex

As stated in the introduction, one of our goals was to isolate a Ni peroxo species with alkyl thiolate ligands. For this purpose, we have used the previously described NiL^{N2S2} complex (Scheme 4.6).^{31,32} NiL^{N2S2} has been characterised by X-ray diffraction (Figure 4.6), and it displays a distorted square planar geometry about the Ni^{II} centre.

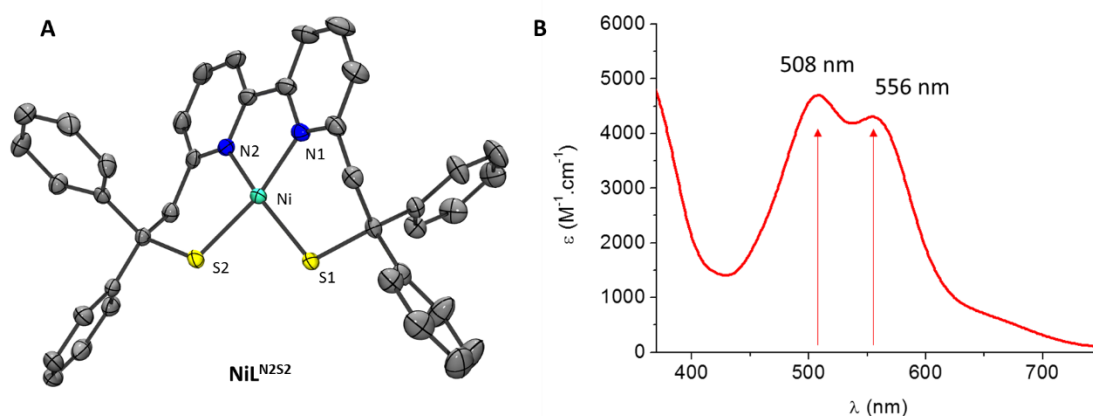


Figure 4.6. A) ORTEP diagram of complexes NiL^{N2S2} . The thermal ellipsoids are drawn at the 30% probability level. All hydrogen atoms, and H_2O molecules are omitted for clarity. Selected bond distances (\AA); Ni-N1 1.934, Ni-N2 1.935, Ni-S1 2.173, Ni-S2 2.176). **B)** UV-Visible spectrum of NiL^{N2S2} in CH_2Cl_2 .

The UV-Visible spectrum of NiL^{N2S2} (Figure 4.6B), displays two intense transitions at 508 nm ($\epsilon = 4800 \text{ M}^{-1}\cdot\text{cm}^{-1}$) and 556 nm ($\epsilon = 4500 \text{ M}^{-1}\cdot\text{cm}^{-1}$), characteristic of such complexes.^{27,33} Based on a TD-DFT investigation, they have been assigned to an LMCT and a d-d transition, respectively.²⁴

Reactivity of NiL^{N2S2} in the presence of TBHP

To isolate a Ni peroxo species, initially, H_2O_2 was chosen as the oxidant. However, after the addition of H_2O_2 at room temperature to a CH_2Cl_2 solution of NiL^{N2S2} , the degradation of the complex was observed and is attributed to the oxygenation of the

thiolates. In contrast, when using *tert*-butyl hydroperoxide (TBHP) as oxidant, the formation of an intermediate species was seen.

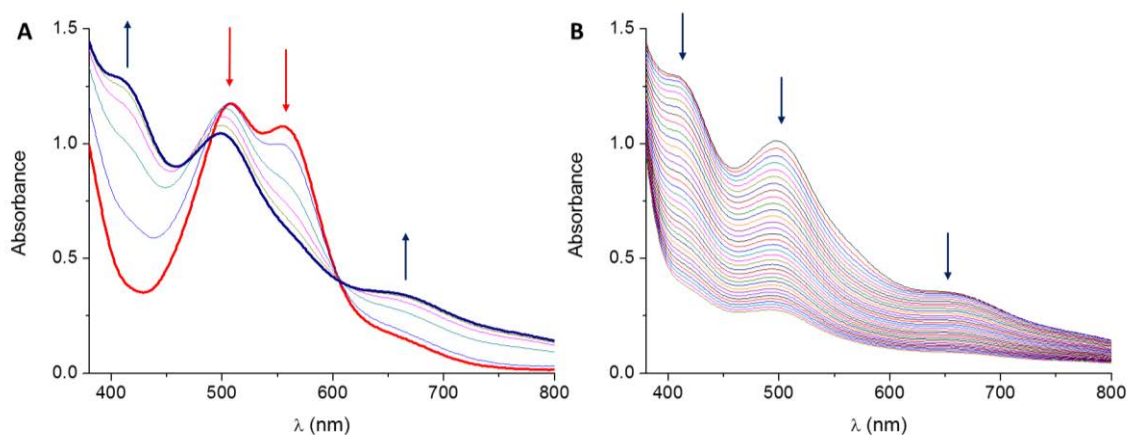


Figure 4.7. Evolution of the UV-Visible spectrum of NiL^{N2S2} (red) in the presence of two equivalents of TBHP until the formation of the maximum intermediate species (blue) (12 minutes) in CH_2Cl_2 (0.25 mM) (A) and its degradation (6 hours) (B). Spectra are taken every two minutes.

The best conditions to obtain the maximum amount of this intermediate at room temperature with a slow degradation process is with the addition of two equivalents of TBHP. Figure 4.7A presents the formation of the intermediate species. At time zero, two equivalents of TBHP were added to a solution of NiL^{N2S2} in CH_2Cl_2 . After 12 minutes, the maximum amount of the intermediate species is generated. The notable differences between the two absorbance spectra are; (i) the disappearance of the transition at 556 nm, (ii) the appearance of two new transitions at 410 nm and 656 nm and (iii) the shift of the 508 nm transition to 499 nm. Figure 4.7B shows the degradation of the intermediate species, starting after 12 minutes of reaction. The intermediate species is fully degraded only after six hours, resulting in a $t_{1/2} = 3$ h, implying an unexpectedly stable intermediate species.

The reaction has also been followed by EPR spectroscopy (Figure 4.8). The initial NiL^{N2S2} spectrum shows no features, as expected for a square planar Ni^{III} complex. After the addition of TBHP, an EPR signal appears, whose intensity increases during the initial 12 minutes and then decreases. The spectrum recorded just after the addition of TBHP and at 12 minutes corresponds to a mixture of two species. One is characterised by an isotropic signal at $g_{\text{iso}} = 2.17$ with a maximum intensity at 12 minutes. It has been assigned to the intermediate species. Consequently, it can be concluded that it is a mononuclear Ni^{III} complex. The second signal is rhombic with $g_1 = 2.41$, $g_2 = 1.98$, and $g_3 = 1.69$. This signal is present at a low concentration throughout the course of the

reaction and can be attributed to a mononuclear Ni^{III} by-product. We propose that this species is **NiL^{N2S2}Oo*t*Bu**, which can be formed in the by reaction with the *t*BuOH formed from the reduction of TBHP.

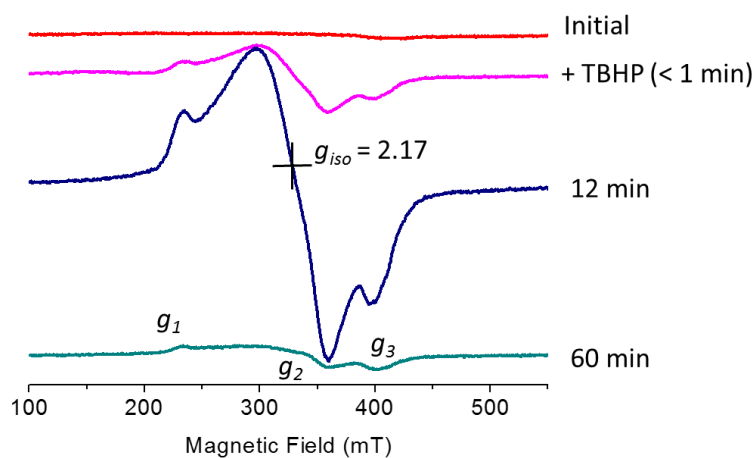


Figure 4.8. X-band EPR spectra at 100 K of the evolution of the reaction between **NiL^{N2S2}** and TBHP (1 min, 12 min, and 1 hour).

An ESI-Mass spectrum recorded on a solution of **NiL^{N2S2}** and TBHP displays a peak ($m/z = 725.0$) corresponding to a mononuclear Ni^{III} peroxy species (**NiL^{N2S2}Oo*t*Bu**), evidencing the first reported nickel peroxy species containing alkyl thiolate ligands.

*Structural properties of NiL^{N2S2}Oo*t*Bu*

We have attempted to crystallise the intermediate species **NiL^{N2S2}Oo*t*Bu** at low temperature. However, the crystals that have been obtained break as soon as we attempt to manipulate them. An optimised structure has been calculated by DFT (denoted **NiL^{N2S2}Oo*t*Bu***), shown in Figure 4.9.

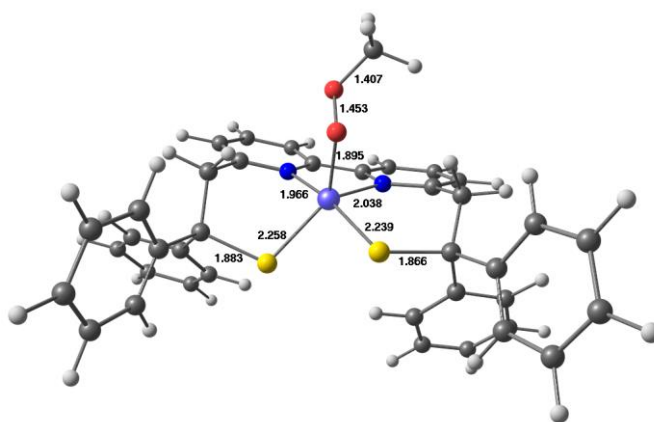
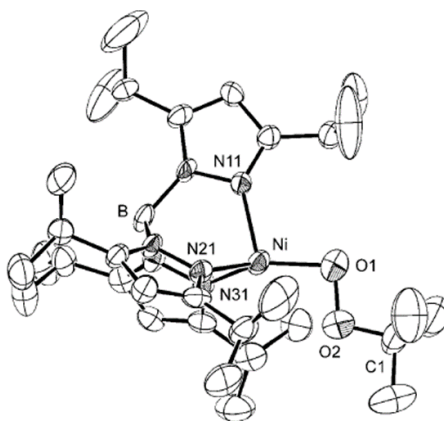


Figure 4.9. DFT optimised structure of **NiL^{N2S2}Oo*t*Bu***. Selected bond distances (Å) and angles (°): Ni-N1 1.966, Ni-N2 2.038, Ni-S1 2.258, Ni-S2 2.239, Ni-O1 1.895, Ni-O2 2.766, and Ni-O1-O2 110.7.

The optimised structure **NiL^{N2S2}OOtBu*** displays a square pyramidal geometry about the Ni^{III} ion, with the two aliphatic thiolate sulfur atoms and the two bipyridine nitrogen atoms from **L^{N2S2}** in the plane, and the oxygen atom from the TBHP unit in the apical position. All of the Ni-N and Ni-S bond distances are longer than those reported for the Ni^{II} complex **NiL^{N2S2}**,²⁴ consistent with a change in the geometry from square planar to square pyramidal.^{34–36} The O-O bond distance (1.453 Å) is within the typical range for peroxide bond lengths.^{20,37–39}

As stated in the introduction, there is only one characterised Ni^{II} complex containing an alkylperoxo unit shown in Scheme 4.7.²⁰ The Ni^{II} metal centre is coordinated to three nitrogen atoms and one oxygen atom from THBP, resulting in a trigonal pyramidal geometry.



Scheme 4.7. The Ni^{II}OOtBu complex previously described by Hikichi *et al.*²⁰

The coordination mode of the OOt-Bu ligand in **NiL^{N2S2}OOtBu*** is η^1 (end-on binding), while the previously reported complex Ni^{II}peroxo (Scheme 4.7) displays a coordination mode in between η^1 and η^2 side-on binding. This is evidenced by two structural properties. The large value of the observed Ni-O1-O2 angle in **NiL^{N2S2}OOtBu*** (110.7°) compared to that in the Ni^{II}peroxo complex (96.2°), as well as the larger distance between the Ni ion and the distal oxygen atom (O2) in **NiL^{N2S2}OOtBu*** (2.766 Å) with respect to the Ni^{II}peroxo complex (2.467 Å), are consistent with a pure end-on binding for **NiL^{N2S2}OOtBu***. The EPR parameters for **NiL^{N2S2}OOtBu*** have also been predicted by DFT calculations. A good agreement is found between the experimental and calculated g values (Calc. $g_{iso} = 2.14$ and Exp. $g_{iso} = 2.17$).

4.5 Reactivity of the Intermediate Species toward Oxidation

Previously reported nickel peroxo species have been tested towards the oxidation of several substrates such as triphenyl phosphine (PPh_3) and thioanisole, in order to evaluate their electrophilic character. The reactivity of $\text{NiL}^{\text{N}_2\text{S}_2}\text{OO}t\text{Bu}$ toward PPh_3 and thioanisole has thus been investigated. At $t = 12$ minutes, when the maximum amount of the $\text{NiL}^{\text{N}_2\text{S}_2}\text{OO}t\text{Bu}$ species had been generated, either one equivalent of PPh_3 or thioanisole was added. UV-Visible spectroscopy was used to follow the reaction. Figure 4.10A shows the evolution of the intensity of the transition of $\text{NiL}^{\text{N}_2\text{S}_2}\text{OO}t\text{Bu}$ at $\lambda = 410$ nm during its formation and degradation.

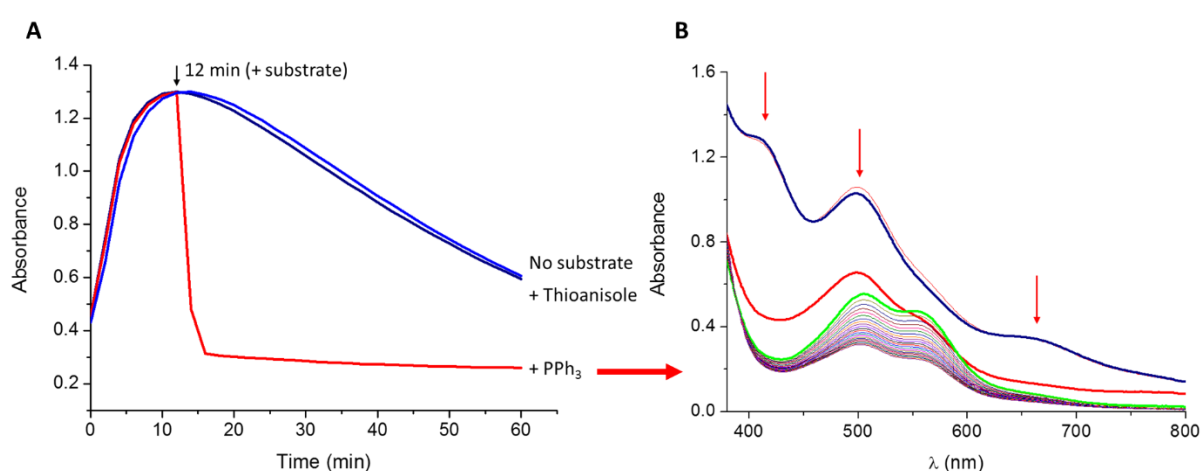
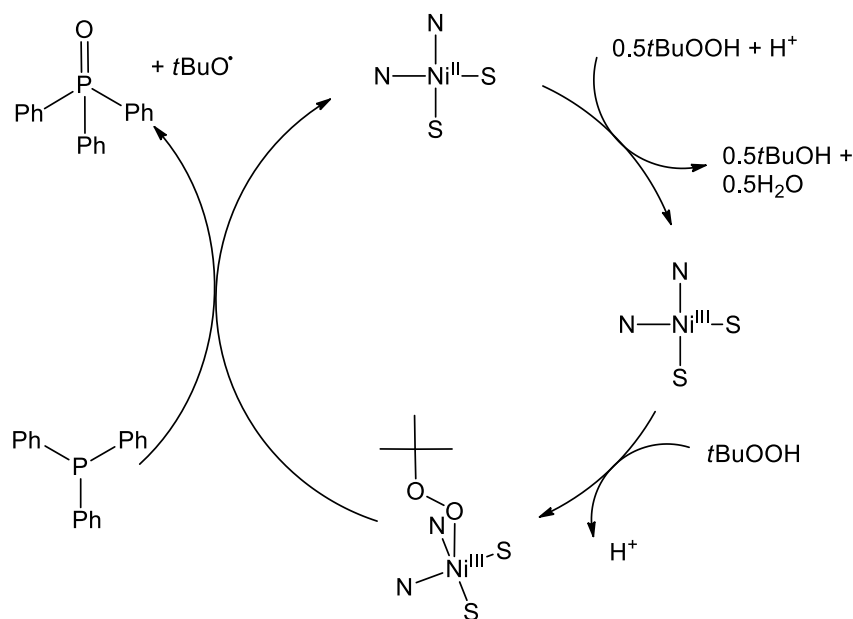


Figure 4.10. **A)** Evolution of the intensity of the $\lambda = 410$ nm transition of $\text{NiL}^{\text{N}_2\text{S}_2}\text{OO}t\text{Bu}$ after the addition of 2 eq of TBHP at $t=0$, in the absence of substrate (dark blue) and after the addition of thioanisole (blue) and PPh_3 (red) at $t = 12$ min. **B)** Evolution of the absorbance spectrum of $\text{NiL}^{\text{N}_2\text{S}_2}\text{OO}t\text{Bu}$ (dark blue) after the addition of PPh_3 (red) giving the regeneration of $\text{NiL}^{\text{N}_2\text{S}_2}$ (green) in CH_2Cl_2 (0.5 mM). Spectra were taken at two minute intervals.

Firstly, it can be seen that there is no difference between the kinetics of the degradation of $\text{NiL}^{\text{N}_2\text{S}_2}\text{OO}t\text{Bu}$ with or without the addition of thioanisole, showing that $\text{NiL}^{\text{N}_2\text{S}_2}\text{OO}t\text{Bu}$ is not capable of oxidising thioanisole. However, a significant change in the kinetics of the degradation of $\text{NiL}^{\text{N}_2\text{S}_2}\text{OO}t\text{Bu}$ is observed after the addition of PPh_3 . In less than four minutes the intermediate species completely disappears.

In Figure 4.10B, the evolution of the absorbance of a solution containing a maximum amount of $\text{NiL}^{\text{N}_2\text{S}_2}\text{OO}t\text{Bu}$ is shown after the addition of PPh_3 . The transitions observed at 410 nm and 656 nm in the spectrum of $\text{NiL}^{\text{N}_2\text{S}_2}\text{OO}t\text{Bu}$ immediately disappear, with a decrease in the intensity of the transition at 500 nm. More importantly partial regeneration of the initial complex, $\text{NiL}^{\text{N}_2\text{S}_2}$, is also observed after four minutes.

To confirm the formation of OPPh_3 , the reaction was followed by ^{31}P NMR. After the addition of PPh_3 to a solution of $\text{NiL}^{\text{N}_2\text{S}_2}\text{OotBu}$, there is a unique peak at 29.3 ppm, characteristic of OPPh_3 , while no trace of the PPh_3 (-5.4 ppm) is observed.



Scheme 4.8. Suggested catalytic mechanism of $\text{NiL}^{\text{N}_2\text{S}_2}$ with TBHP in the presence of PPh_3 .

A catalytic mechanism for the reaction of $\text{NiL}^{\text{N}_2\text{S}_2}$ with TBHP in the presence of PPh_3 has been devised and is shown in Scheme 4.8. The first step involves the oxidation of the Ni^{II} ion to a Ni^{III} centre by reduction of 0.5 eq of TBHP into tert-butyl alcohol and water. $\text{NiL}^{\text{N}_2\text{S}_2}\text{OotBu}$ is formed *via* reaction with TBHP, which then reacts with PPh_3 to give OPPh_3 and $t\text{BuO}^\bullet$ regenerating $\text{NiL}^{\text{N}_2\text{S}_2}$. Theoretically, 1.5 equivalents of TBHP should be sufficient to form $\text{NiL}^{\text{N}_2\text{S}_2}\text{OotBu}$. However, in these conditions the rate of the formation is slow and the maximum amount of the $\text{NiL}^{\text{N}_2\text{S}_2}\text{OotBu}$ generated is lower than with the addition of 2 equivalents of TBHP.

Conclusion

In the first section of this chapter, we presented two different Ni^{II} alkyl thiolate complexes, containing the ligand L^{NS_2} , with the goal of obtaining Ni-CO adducts. The tridentate ligand was used to open a coordination site on the Ni ion, as in our group we had previously found that the tetradentate ligand $\text{L}^{\text{N}_2\text{S}_2}$, showed no reactivity toward CO. However, there are significant drawbacks using this ligand, mainly the consistent formation of a thermodynamically stable μS -bridged Ni^{II} dimer. Furthermore, when we were able to obtain a mononuclear Ni^{II} complex with L^{NS_2} , as the redox potential of the $\text{Ni}^{\text{II}}/\text{Ni}^{\text{I}}$ couple was very low, it was difficult to electrochemically or chemically generate

the Ni^I species. Multiple attempts to activate CO were carried out with the Ni^{II} complexes and the electro-generated reduced Ni^I species. However, none of these were successful. Therefore, in order to further study the activation of CO, new ligand design has to be carried out.

In the second section, the reactivity of the previously described **NiL^{N2S2}** complex with *tert*-butyl hydroperoxide was investigated. Surprisingly, an extremely stable ($t_{1/2} = 3\text{h}$) intermediate Ni^{III} species has been observed at room temperature, as evidenced by both EPR and UV-Visible spectroscopy. ESI-Mass spectrometry confirmed the formation of **NiL^{N2S2}OotBu**, representing an unprecedented mononuclear Ni^{III} alkyl-thiolate peroxy species. Due to the observed stability of this complex, we aimed to characterise **NiL^{N2S2}OotBu** by X-ray diffraction. However, low temperature facilities are required for this as the crystals we have already obtained crack upon manipulation at room temperature. The solution of the crystal structure of **NiL^{N2S2}OotBu** would give the first fully characterised molecular compound which accurately models a potential NiSOD intermediate active oxygen species, with the unique coordination of thiolate ligands.

Furthermore, **NiL^{N2S2}OotBu** is active towards the oxidation of PPh₃. However, it only exhibits weak electrophilic oxidising properties as it is not able to oxidise thioanisole. A similar reactivity was found with the previously described Ni^{II} alkyl peroxy complex of Hikichi *et. al.* It is also interesting to note that the initial Ni^{II} species (**NiL^{N2S2}**) is regenerated during the reaction of **NiL^{N2S2}OotBu** with PPh₃, suggesting that it has the potential to act as a catalyst.

References

- (1) Sigel, A.; Sigel, H.; Sigel, R. K. O. *Nickel and Its Surprising Impact in Nature: Metal Ions in Life Sciences*; John Wiley & Sons, 2007.
- (2) Darnault, C.; Volbeda, A.; Kim, E. J.; Legrand, P.; Vernede, X.; Lindahl, P. A.; Fontecilla-Camps, J. C. *Nat. Struct. Biol.* **2003**, *10*, 271–279.
- (3) Dobbek, H.; Svetlitchnyi, V.; Gremer, L.; Huber, R.; Meyer, O. *Science* **2001**, *293*, 1281–1285.
- (4) Drennan, C. L.; Heo, J.; Sintchak, M. D.; Schreiter, E.; Ludden, P. W. *Proc. Natl. Acad. Sci.* **2001**, *98*, 11973–11978.
- (5) Panda, R.; Berlinguette, C. P.; Zhang, Y.; Holm, R. H. *J. Am. Chem. Soc.* **2005**, *127*, 11092–11101.
- (6) Lu, Z.; Crabtree, R. H. *J. Am. Chem. Soc.* **1995**, *117*, 3994–3998.
- (7) McCord, J. M. In *Methods in Enzymology*; Lester Packer, Ed.; Academic Press, 2002; Vol. Volume 349, pp. 331–341.
- (8) Beyer, W.; Imlay, J.; Fridovich, I. *Prog. Nucleic Acid Res. Mol. Biol.* **1991**, *40*, 221–253.
- (9) Landis, G. N.; Tower, J. *Mech. Ageing Dev.* **2005**, *126*, 365–379.
- (10) Bryngelson, P. A.; Maroney, M. J. In *Nickel and Its Surprising Impact in Nature*; Sigel, A.; Sigel, H.; Sigel, R. K. O., Eds.; John Wiley & Sons, Ltd, 2007; pp. 417–443.
- (11) Bryngelson, P. A.; Arobo, S. E.; Pinkham, J. L.; Cabelli, D. E.; Maroney, M. J. *J. Am. Chem. Soc.* **2004**, *126*, 460–461.
- (12) Hikichi, S.; Yoshizawa, M.; Sasakura, Y.; Akita, M.; Moro-oka, Y. *J. Am. Chem. Soc.* **1998**, *120*, 10567–10568.
- (13) Itoh, S.; Bandoh, H.; Nagatomo, S.; Kitagawa, T.; Fukuzumi, S. *J. Am. Chem. Soc.* **1999**, *121*, 8945–8946.
- (14) Shiren, K.; Ogo, S.; Fujinami, S.; Hayashi, H.; Suzuki, M.; Uehara, A.; Watanabe, Y.; Moro-oka, Y. *J. Am. Chem. Soc.* **2000**, *122*, 254–262.
- (15) Mandimutsira, B. S.; Yamarik, J. L.; Brunold, T. C.; Gu, W.; Cramer, S. P.; Riordan, C. G. *J. Am. Chem. Soc.* **2001**, *123*, 9194–9195.
- (16) Itoh, S.; Bandoh, H.; Nakagawa, M.; Nagatomo, S.; Kitagawa, T.; Karlin, K. D.; Fukuzumi, S. *J. Am. Chem. Soc.* **2001**, *123*, 11168–11178.
- (17) Schenker, R.; Mandimutsira, B. S.; Riordan, C. G.; Brunold, T. C. *J. Am. Chem. Soc.* **2002**, *124*, 13842–13855.
- (18) Kieber-Emmons, M. T.; Schenker, R.; Yap, G. P. A.; Brunold, T. C.; Riordan, C. G. *Angew. Chem. Int. Ed.* **2004**, *43*, 6716–6718.
- (19) Schenker, R.; Kieber-Emmons, M. T.; Riordan, C. G.; Brunold, T. C. *Inorg. Chem.* **2005**, *44*, 1752–1762.
- (20) Hikichi, S.; Okuda, H.; Ohzu, Y.; Akita, M. *Angew. Chem. Int. Ed.* **2009**, *48*, 188–191.
- (21) Yao, S.; Bill, E.; Milsman, C.; Wieghardt, K.; Driess, M. *Angew. Chem. Int. Ed.* **2008**, *47*, 7110–7113.
- (22) Fujita, K.; Schenker, R.; Gu, W.; Brunold, T. C.; Cramer, S. P.; Riordan, C. G. *Inorg. Chem.* **2004**, *43*, 3324–3326.
- (23) Kieber-Emmons, M. T.; Annaraj, J.; Seo, M. S.; Van Heuvelen, K. M.; Tosha, T.; Kitagawa, T.; Brunold, T. C.; Nam, W.; Riordan, C. G. *J. Am. Chem. Soc.* **2006**, *128*, 14230–14231.
- (24) Gennari, M.; Orio, M.; Pécaut, J.; Neese, F.; Collomb, M.-N.; Duboc, C. *Inorg. Chem.* **2010**, *49*, 6399–6401.
- (25) Panja, A.; Eichhorn, D. M. *Inorganica Chim. Acta* **2012**, *391*, 88–92.
- (26) Cerrada, E.; Falvello, L. R.; Hursthouse, M. B.; Laguna, M.; Luquín, A.; Pozo-Gonzalo, C. *Eur. J. Inorg. Chem.* **2002**, *2002*, 826–833.
- (27) Krueger, H. J.; Holm, R. H. *Inorg. Chem.* **1989**, *28*, 1148–1155.
- (28) Huang, D.; Deng, L.; Sun, J.; Holm, R. H. *Inorg. Chem.* **2009**, *48*, 6159–6166.
- (29) Hunter, C. A.; Sanders, J. K. M. *J. Am. Chem. Soc.* **1990**, *112*, 5525–5534.
- (30) Brennan, T. D.; Scheidt, W. R.; Shelnut, J. A. *J. Am. Chem. Soc.* **1988**, *110*, 3919–3924.
- (31) Gennari, M.; Orio, M.; Pécaut, J.; Bothe, E.; Neese, F.; Collomb, M.-N.; Duboc, C. *Inorg. Chem.* **2011**, *50*, 3707–3716.
- (32) Gennari, M.; Retegan, M.; DeBeer, S.; Pécaut, J.; Neese, F.; Collomb, M.-N.; Duboc, C. *Inorg. Chem.* **2011**, *50*, 10047–10055.
- (33) Maroney, M. J.; Choudhury, S. B.; Bryngelson, P. A.; Mirza, S. A.; Sherrod, M. J. *Inorg. Chem.* **1996**, *35*, 1073–1076.
- (34) Barondeau, D. P.; Kassmann, C. J.; Bruns, C. K.; Tainer, J. A.; Getzoff, E. D. *Biochemistry (Mosc.)* **2004**, *43*, 8038–8047.
- (35) Fiedler, A. T.; Bryngelson, P. A.; Maroney, M. J.; Brunold, T. C. *J. Am. Chem. Soc.* **2005**, *127*, 5449–5462.
- (36) Hanss, J.; Krüger, H.-J. *Angew. Chem. Int. Ed.* **1998**, *37*, 360–363.

-
- (37) DiPasquale, A. G.; Kaminsky, W.; Mayer, J. M. *J. Am. Chem. Soc.* **2002**, *124*, 14534–14535.
- (38) DiPasquale, A. G.; Hrovat, D. A.; Mayer, J. M. *Organometallics* **2006**, *25*, 915–924.
- (39) Chavez, F. A.; Mascharak, P. K. *Accounts Chem. Res.* **2000**, *33*, 539–545.

Characterisation of the Electronic Structure of Cobalt (II) and (III) Thiolate Complexes and an Investigation of their Reactivity

Gennari, M.; Gerey, B.; Hall, N.; Pécaut, J.; Vezin, H.; Collomb, M.-N.; Orio, M.; Duboc, C. *Dalton Trans.* **2012**, *41*, 12586.

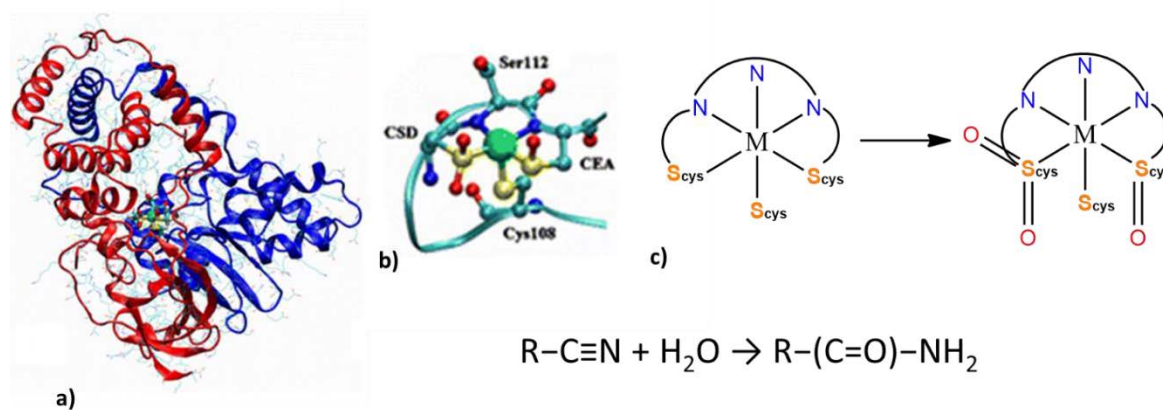
Résumé

L'objectif du travail présenté dans ce chapitre était de synthétiser des complexes du cobalt à partir du ligand $L^{N_2S_2}$ et, plus particulièrement, d'étudier leur réactivité vis à des réactions de S-oxygénation et S-alkylation. Dans la première partie, nous nous sommes intéressés à la synthèse et à la caractérisation d'un complexe mononucléaire de cobalt(II), $[CoL^{N_2S_2}]$, puis à sa réactivité vis à vis de l'iodure de méthyle. Au laboratoire, il avait été montré que des complexes du nickel et du zinc du ligand $L^{N_2S_2}$ réalisent des réactions de S-méthylation avec CH_3I . Avec le complexe du nickel(II) un seul ligand thiol était méthylé, alors qu'avec celui de zinc(II) les deux fonctions thiols étaient méthylées et se dé-coordonnaient. L'ion cobalt(II) étant souvent utilisé en biochimie comme substitut structural et fonctionnel du zinc(II), notre objectif était de voir si le complexe de cobalt présentait la même réactivité que son homologue contenant le zinc. La structure résolue par diffraction des rayons X du complexe $[CoL^{N_2S_2}]$ a permis de mettre en évidence le premier exemple d'un complexe du cobalt(II) à ligands thiols présentant une géométrie plan carrée. En présence de CH_3I , une seule fonction thiol est méthylée, provoquant la commutation de la configuration bas spin ($S = 1/2$) caractérisant $[CoL^{N_2S_2}]$ à une configuration haut spin ($S = 3/2$). Le complexe de cobalt(II) présente donc une réactivité comparable à celle du complexe du nickel, mais différente de celle du zinc. Ainsi, même si le cobalt(II) est un bon substitut structural de l'ion zinc(II), il est inapproprié comme substitut fonctionnel dans le cas particulier des réactions de S-alkylation.

Un autre objectif, présenté dans la deuxième partie de ce chapitre, était de synthétiser des complexes du cobalt(III) pouvant modéliser la réactivité de la nitrile hydratase. Le site actif, de cette enzyme est un complexe mononucléaire du cobalt(III). Pour qu'il soit actif ses deux ligands cystéines doivent être oxydés, l'un en acide sulfénique et l'autre en acide sulfinique. Dans ce contexte, nous avons oxydé $[CoL^{N_2S_2}]$ et obtenu un complexe dinucléaire de cobalt(II), provenant de la réduction de l'ion Co^{III} en Co^{II} avec l'oxydation simultanée d'un ligand thiol pour former un pont disulfure intermoléculaire. Nous avons ainsi obtenu le premier complexe dinucléaire de cobalt(II) à pont disulfure. En présence d'ions chlorure, le complexe mononucléaire $[CoL^{N_2S_2}Cl]$ a pu être isolé et caractérisé par diffraction des rayons X. En présence de peroxyde d'hydrogène, trois atomes d'oxygène sont incorporés dans le complexe, démontrant ainsi que les fonctions thiols du ligand $L^{N_2S_2}$ ont été oxygénés en acide sulfénique et en acide sulfinique, modélisant ainsi la réactivité de la nitrile hydratase.

Introduction

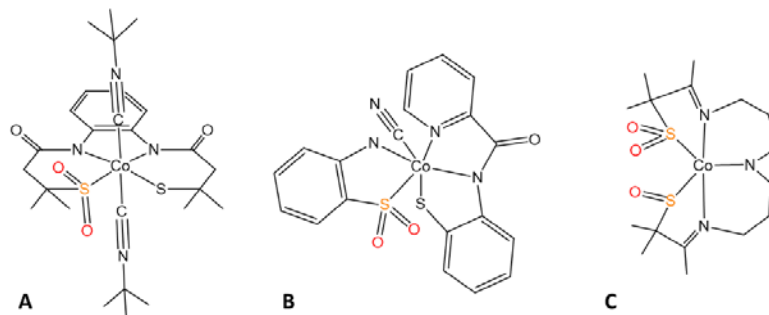
In nature, the metal cobalt is rare compared with all the known essential trace elements. Although cobalt is less frequently encountered in metalloenzymes than many of the other first-row transition metals, it nevertheless plays an important role in essential biological pathways. It has two more common oxidation states (Co^{II} and Co^{III}), but can exhibit oxidation states from +I to +IV.¹ The most studied cobalt containing metalloenzymes are the vitamin- B_{12} -dependant enzymes, in which the cobalt ion is located in a substituted corrin macrocycle.² On the other hand, there are very few proteins containing non-corrin cobalt centres that have been fully characterised, one of which is the cobalt nitrile hydratase (CoNHase). CoNHase catalyses the hydration of nitriles to amides (Scheme 5.1).³ This enzyme is of particular interest to our group, as the coordination sphere of the Co^{III} centre contains three bound cysteine units. As stated previously in the introductory chapter, bound thiolates display particular reactivities. In CoNHase, two of the bound cysteines undergo post-translational modification, one into cysteine-sulfinate and the other into cysteine-sulfenate (Scheme 5.1). Therefore the active state of CoNHase contains three different sulfur based ligands, a thiolate, a sulfinate and a sulfenate bound to the Co^{III} centre.⁴



Scheme 5.1. Crystallographic structure of **a)** *Pseudonocardia thermophile* JCM 3095 nitrile hydratase, **b)** the Co active site **c)** and a schematic drawing of the post-translational modification of the active Co^{III} site *via* S-oxygenation reactions.

The origin of this post-translational modification still remains unclear.⁵ However, it is certain that these three S-oxygenation processes are necessary to obtain the catalytically active enzyme,⁴ and specifically dissymmetrical oxidised thiolate groups are necessary. Furthermore in terms of molecular models, to date, in the literature there

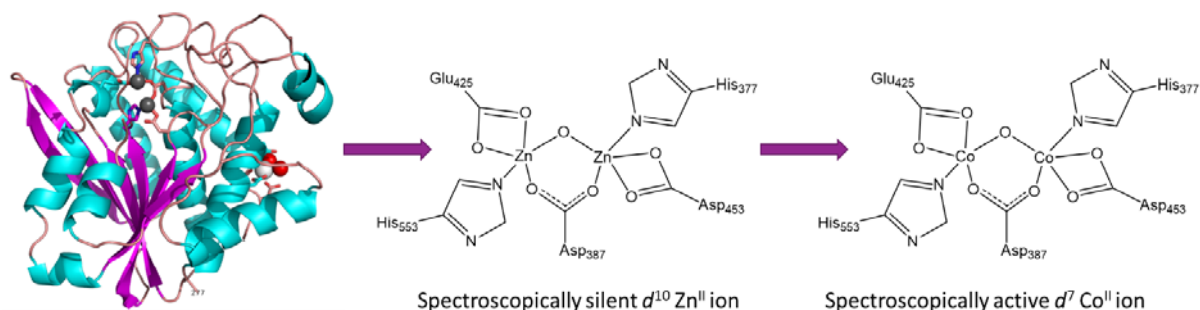
are only three model Co^{III} complexes capable of dissymmetrical S-oxygenation (Scheme 5.2).⁵⁻⁷ However, none of them are NHase active.



Scheme 5.2. The three previously described Co^{III} complexes capable of dissymmetrical S-oxygenation.

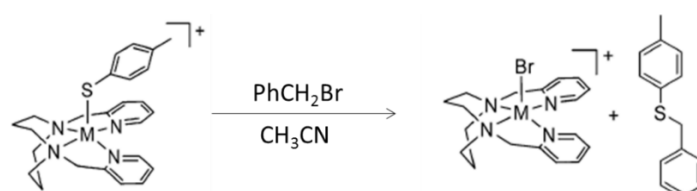
In the majority of cases, the cobalt ion present in metalloenzymes is in the oxidation state +III. However, Co^{II} is also very interesting as it has long been used as a spectroscopic probe for the active sites of zinc-containing enzymes.^{1,8-10} Zn^{II} being a diamagnetic d^{10} ion, no optical electronic absorption is observed and it is also EPR silent. To probe the direct environment of the metallic ion in the biological site, it is thus convenient to replace the Zn^{II} ion by the paramagnetic d^7 Co^{II} ion, which has been shown to represent the best structural and functional substitute for Zn^{II} in many cases.

Zinc enzymes are implicated in various biological activities. To date the most extensively studied Co^{II} -substituted enzyme is the di-zinc containing aminopeptidase (Scheme 5.3),¹¹⁻¹⁴ which catalyses the cleavage of amino acids from the amino terminus of protein substrates. The results of these studies have shown similar reactivity between the two metal centres and also, more importantly, has enabled direct evidence for the mechanism of the catalytic cycle.



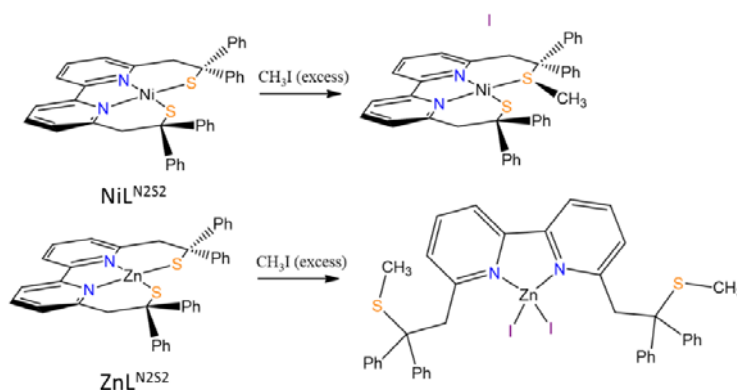
Scheme 5.3. Crystallographic structure of a Zn-containing aminopeptidase, the naturally occurring active site and the substituted Co^{II} active site.^{11,14}

Another class of Zn metalloenzymes is involved in thiolate methylation processes including methionine synthase,¹⁵ farnesyl transferase,¹⁶ and most prominently the Ada protein implicated in DNA repair.¹⁷ In an effort to further investigate such enzymes, the reactivity of synthetic thiolate-metal bound complexes towards S-alkylation has been investigated, mainly with Ni^{II} and Zn^{II} complexes.^{17–27} To the best of our knowledge, only one example employing a square pyramidal Co^{II} complex with a N4 ligand forming the square planar base and a monodentate aryl thiolate ligand in the axial position (Scheme 5.4) has been reported.²⁸ In the presence of benzyl bromide an S-alkylation occurs, leading to the formation of a thioether which de-coordinates from the Co^{II} ion with the concomitant binding of the bromide anion. Therefore, further study on the S-alkylated complexes cannot be achieved.



Scheme 5.4. Alkylation of Zn^{II} or Co^{II} – thiolate complexes with benzyl bromide.

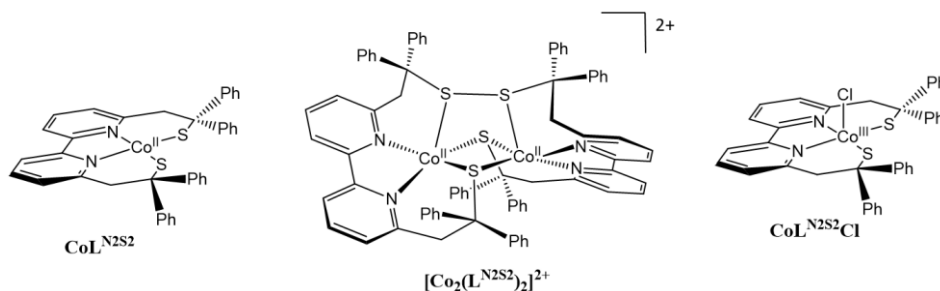
Our group has previously studied S-alkylation reactions with the complexes **NiL^{N2S2}** and **ZnL^{N2S2}** (Scheme 5.5).^{29,30} In the case of **NiL^{N2S2}**, upon the addition of an excess of CH₃I, only one of the two thiolates is methylated, whereas in the case of the **ZnL^{N2S2}** complex, both thiolates are methylated, resulting in the de-coordination of both sulfur atoms. In this case, the nickel centre does not exhibit the same reactivity as the zinc complex. It is therefore, of interest to study the reactivity of an iso-structural Co^{II} complex, [CoL^{N2S2}] toward S-alkylation (Scheme 5.6).



Scheme 5.5. Alkylation of previously described **L^{N2S2}** complexes, **NiL^{N2S2}** and **ZnL^{N2S2}**.

As seen here, there are very few studies of molecular models for CoNHase metalloenzymes. In this context, we have synthesised two different cobalt complexes (Scheme 5.6), a dinuclear Co^{II} and a mononuclear Co^{III} complex.

We have studied the redox properties, electronic structures and reactivity of these three new complexes. With respect to the reactivity of bound thiolates, we have investigated the reactivity of the mononuclear Co^{III} complex towards S-oxygenation and S-alkylation of the mononuclear Co^{II} complex.



Scheme 5.6. Cobalt complexes discussed in this chapter, $\text{CoL}^{\text{N}_2\text{S}_2}$, dinuclear $[\text{Co}_2(\text{L}^{\text{N}_2\text{S}_2})_2]^{2+}$, and $\text{CoL}^{\text{N}_2\text{S}_2}\text{Cl}$

Results and Discussion

5.1 Synthesis and Characterisation of the $[\text{CoL}^{\text{N}_2\text{S}_2}]$ Complex

The $\text{L}^{\text{N}_2\text{S}_2}$ ligand has previously been described in chapter II. To investigate whether Co^{II} is a suitable probe for Zn^{II} active sites, we have attempted to synthesise an isostructural Co^{II} complex to previously described $\text{ZnL}^{\text{N}_2\text{S}_2}$ (Scheme 5.5).³⁰

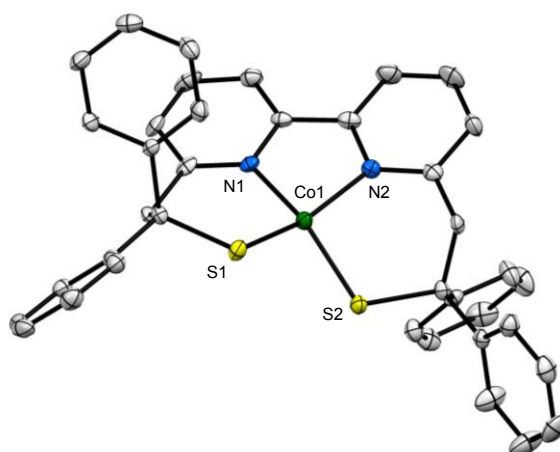
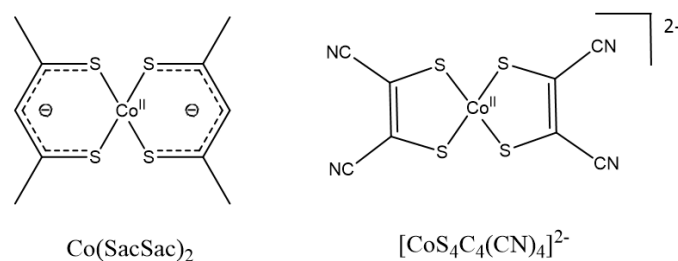


Figure 5.1 Molecular drawing of $\text{CoL}^{\text{N}_2\text{S}_2}$. The thermal ellipsoids are drawn at 50% probability level. All hydrogen atoms are omitted for clarity.

$\text{CoL}^{\text{N}_2\text{S}_2}$ was obtained by reaction of $\text{K}_2\text{L}^{\text{N}_2\text{S}_2}$ in THF with $\text{Co}(\text{BF}_4)_2 \cdot 6\text{H}_2\text{O}$, leading to a dark brown precipitate. Single crystals of $\text{CoL}^{\text{N}_2\text{S}_2}$ suitable for X-ray diffraction were

obtained by layering a solution of $\text{Co}(\text{BF}_4)_2$ in MeCN over an equimolar solution of $\text{K}_2\text{L}^{\text{N}_2\text{S}_2}$ in THF with a 1:1 THF:MeCN solution interposed between the two layers.

$\text{CoL}^{\text{N}_2\text{S}_2}$ is mononuclear as evidenced by X-ray analysis of single crystals (Figure 5.1). Selected bond distances and angles are listed in Table 5.1. The Co^{II} ion is bound to the two aliphatic thiolate sulfur atoms and to the two bipyridine nitrogen atoms from $\text{L}^{\text{N}_2\text{S}_2}$, resulting in a distorted square planar *cis*- N_2S_2 coordination environment. The Co^{II} coordination sphere is square planar rather than the more typical tetrahedral geometry, characterized by a dihedral angle of 34.36° between the (S1-Co-S2) and (N1-Co-N2) planes and τ_4 value of 0.33 (The four-coordinates τ_4 index is the sum of angles α and β , the two largest θ angles, subtracted from 360° , and divided by 141°).³¹



Scheme 5.7. The previously reported square planar Co^{II} complexes with aryl thiolates; $\text{Co}(\text{SacSac})_2$ ³² and $[\text{CoS}_4\text{C}_4(\text{CN})_4]^{2-}$.³³

To the best of our knowledge, $\text{CoL}^{\text{N}_2\text{S}_2}$ is the first four coordinate Co^{II} complex with alkyl thiolate ligands. Two others which adopt a square planar geometry have been described, but involve aryl thiolate ligands (Scheme 5.7).^{32,33} Also, all of the more common, tetrahedral thiolate Co^{II} complexes contain only aryl thiolate ligands.³⁴⁻³⁸ The square planar geometry observed in $\text{CoL}^{\text{N}_2\text{S}_2}$ is not only dictated by the rigidity of the ligand, since the analogous $\text{ZnL}^{\text{N}_2\text{S}_2}$ complex presents a larger twist angle (46.38°).³⁰

The Co-S bond distances of 2.1662(7) and 2.1703(7) Å are similar to those present in the two other square planar complexes (between 2.161 and 2.166 Å)^{32,33} but notably shorter than those in previously described neutral^{35,37-41} and anionic³⁶ tetrahedral Co^{II} complexes. The Co-N bond distances of 1.944(2) and 1.9446(18) Å are consistent with those reported in the literature. The distortions are evidenced by the fact that the Co, N and S atoms are displaced from the mean CoN_2S_2 plane from 0.02 to 0.45 Å due to the rigidity of the six-membered chelate rings in $\text{CoL}^{\text{N}_2\text{S}_2}$.

Table 5.1. Selected bond lengths (Å) and angles (°) from the X-ray structure of CoL^{N2S2} and the optimized structures $\text{CoL}^{\text{N2S2*}}$ and $\text{CoL}^{\text{N2S2Me*}}$.

	CoL^{N2S2} Exp.	$\text{CoL}^{\text{N2S2*}}$ Calc.
Bond distances (Å)		
Co-N1	1.944	1.927
Co-N2	1.945	1.927
Co-S1	2.1662	2.181
Co-S2	2.1703	2.181
Angles (°)		
N1-Co-N2	84.03	83.83
N1-Co-S1	98.14	98.76
N1-Co-S2	157.84	151.43
N2-Co-S1	155.31	151.43
N2-Co-S2	98.40	98.76
S1-Co-S2	88.80	92.36

It is well known that in a tetrahedral geometry, the d^7 Co^{II} ion shows a clear preference for the high-spin state configuration ($S = 3/2$), whereas in the square planar geometry, the low-spin configuration ($S = 1/2$) is favoured.⁹ Consequently, the Co^{II} ion in CoL^{N2S2} should exhibit a low-spin state configuration, as confirmed by EPR spectroscopy shown below.

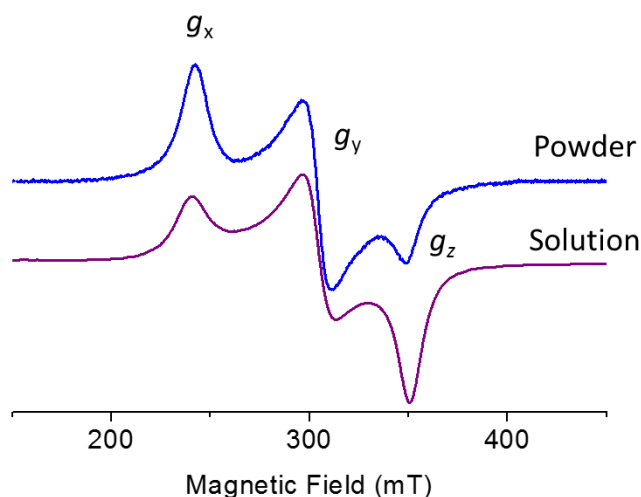


Figure 5.2 Experimental X-band EPR spectra (15 K) of CoL^{N2S2} recorded in powder and in a DMF solution.

The powder X-band EPR spectrum of CoL^{N2S2} displays an $S = 1/2$ rhombic signal consistent with a low spin configuration of the Co^{II} ion (Figure 5.2). A large g -anisotropy is observed with $g_x = 2.94$, $g_y = 2.32$ and $g_z = 2.01$ in agreement with a large contribution of a spin orbit coupling interaction. It should also be noted that the large broadening of

the EPR lines (about 50 mT) probably originates from unresolved Co hyperfine coupling interactions (^{59}Co , $I = 7/2$).

Low spin square planar Co^{II} complexes have been classified into two categories depending on the nature of their ground state.⁴² In type I, the unpaired electron is localized in a 3d-based molecular orbital with mainly a d_{z^2} character. The corresponding EPR spectra present an axial ($g_{\parallel} < g_{\perp}$) or rhombic ($g_x > g_y > g_z$ ($g_z > 1.97$)) signal. In contrast, type II complexes are characterized by a $(d_{yz})^1$ ground state and a rhombic EPR spectrum with $g_x > g_y \approx g_z$ ($g_z < 1.97$). From this classification, $\text{CoL}^{\text{N}2\text{S}2}$ can therefore be considered a type I low spin Co^{II} complex. It can be seen in Figure 5.2, that in a DMF solution, the distorted square planar geometry around the Co^{II} ion in $\text{CoL}^{\text{N}2\text{S}2}$ is retained as attested by the similarity of the solution and powder X-band EPR spectra (Figure 5.2).

Table 5.2 Principal experimental and theoretically calculated EPR parameters of $\text{CoL}^{\text{N}2\text{S}2}$.

	g-tensor				^{14}N hfc (MHz)			^{59}Co hfc (MHz)			
	g_1	g_2	g_3	g_{iso}	A_1	A_2	A_3	A_1	A_2	A_3	A_{iso}
<i>Exp</i>	2.94	2.32	2.01	2.42	-	-	2.2	-	-	-	3.8
<i>DFT</i>	2.28	2.21	2.04	2.18	-0.11	0.45	2.38	-88.6	-99.0	173.7	-4.6
<i>CASSCF</i> <i>/NEVPT2</i>	2.84	2.56	1.95	2.45	-	-	-	-	-	-	-

To gain insight into the distribution of the unpaired electron within the complex $\text{CoL}^{\text{N}2\text{S}2}$, pulsed EPR experiments were conducted using a 2D hyperfine-sublevel correlation experiment (2D-HYSCORE). This two-dimensional pulsed EPR technique allows the measurement of quadrupolar and hyperfine couplings (hfc) of the electronic spin with the surrounding nuclei so that it enables the proper assignment of various couplings with a large number of nuclei.

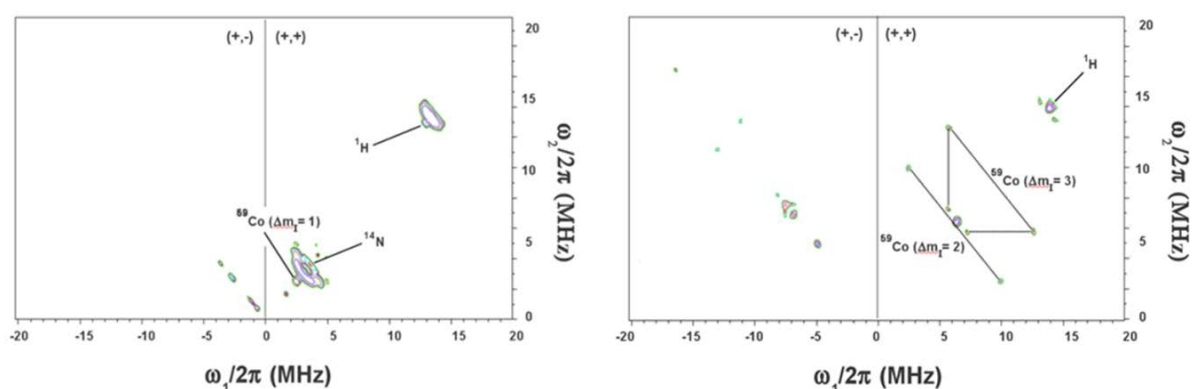


Figure 5.3. 2D-HYSCORE spectra of a DMF solution of $\text{CoL}^{\text{N}2\text{S}2}$ recorded at 4 K for the $g = 2.32$ (top) and $g = 2.94$ (bottom) values of the continuous-wave EPR spectrum. The τ value was set to 200 ns with 256 x 256 points along the t_1 and t_2 directions.

Pulsed EPR measurements were carried out at 4 K on a DMF solution of **CoL^{N2S2}** at the $g = 2.32$ and $g = 2.94$ values (Figure 5.3). Both spectra are characterized by a pair of cross-peaks centred at the ^1H Larmor nuclear frequency ($\nu_i = 15$ MHz). These symmetric cross-peaks appear in the (+,+) quadrant, indicating a weak hfc, estimated at 3.2 MHz, attributed to a population of distant protons that are likely attached to the bipyridine moiety. A second pair of cross-peaks centred at $\nu_i = 3$ MHz is detected in the (+,+) quadrant of the $g = 2.32$ spectrum and assigned to the ^{14}N Larmor nuclear frequency. This pair indicates a weak hfc, estimated at 2.2 MHz (Table 5.2) and attributed to the two equivalent amino nitrogen nuclei of the bipyridine unit. More interestingly, several pairs of cross-peaks are observed in the (+,+) quadrant of the $g = 2.94$ spectrum centred, respectively, at $\nu_i = 6$ MHz and $\nu_i = 9$ MHz along the diagonal and also in the $g = 2.32$ spectra at $\nu_i = 3$ MHz. Keeping in mind that ^{59}Co has an $I = 7/2$ nuclear spin, these features can be assigned to Δm_I transitions and the isotropic component (A_{iso}) of the ^{59}Co hfc is estimated at 3.6 MHz. The HYSORE experiments have thus revealed a non-negligible delocalization of the unpaired electron over the ligand.

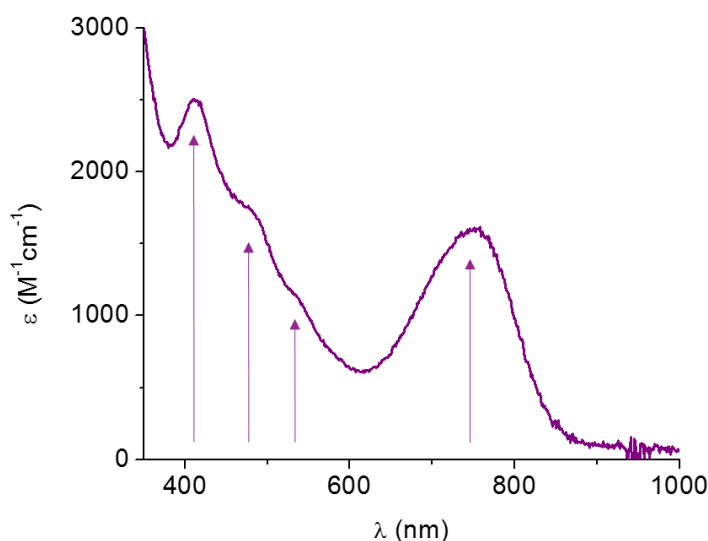


Figure 5.4. Electronic absorbance spectrum of **CoL^{N2S2}**.

The electronic absorbance spectrum recorded in DMF displays several features with comparable intensities at 420, 460, 500 and 760 nm (Figure 5.4). The absence of a transition in the near infrared region is consistent with a type I system, since such a transition is expected only in the case of a type II complex.⁴²

Electronic structure of $\text{CoL}^{\text{N}_2\text{S}_2}$ and interpretation of its spectroscopic properties.

To further investigate the electronic structure of the complex $\text{CoL}^{\text{N}_2\text{S}_2}$, quantum chemical calculations have been carried out. The resulting optimized geometry of $\text{CoL}^{\text{N}_2\text{S}_2}$ (denoted $\text{CoL}^{\text{N}_2\text{S}_2*}$) compares well with the crystallographic data, thus validating the computational approach for the optimisation process of such systems (Table 5.1).

With respect to its electronic structure, the singly occupied molecular orbital (SOMO) of $\text{CoL}^{\text{N}_2\text{S}_2}$ displayed in Figure 5.5 indicates partial delocalization of the unpaired electron over both the metal (85 %) and the ligand, in particular over the sulfur atoms (10.5 %). The unpaired electron is partially localized in a 3d-MO, which corresponds to a mixture of d_{z^2} and d_{xz} orbitals. The high sulfur contribution to the SOMO indicates a certain degree of covalency of the Co-S bond. However, this covalency is weak with respect to a $\text{Cu}^{\text{II}}\text{-S}$ or $\text{Ni}^{\text{II}}\text{-S}$ bond,^{10,29-32} but notably larger than for a $\text{Zn}^{\text{II}}\text{-S}$ bond, which has a predominant ionic character. Even if the unpaired electron is poorly delocalized on the nitrogen atoms (1 %), HYSCORE experiments have allowed the observation of the coupling between the nucleus of these atoms and the unpaired electron.

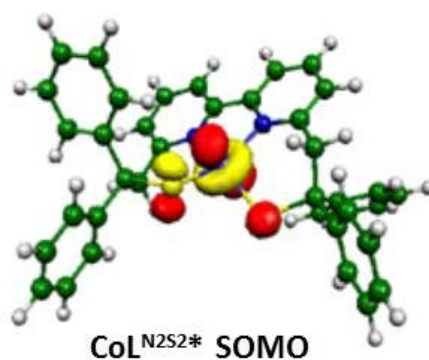


Figure 5.5. Localized SOMO for $\text{CoL}^{\text{N}_2\text{S}_2*}$. Carbon (green), sulfur (yellow) and nitrogen (blue).

Relating to the spectroscopic properties of $\text{CoL}^{\text{N}_2\text{S}_2}$, we first focus on the prediction of the EPR parameters. To the best of our knowledge, no such example of theoretical calculations has been reported so far on low spin mononuclear Co^{II} complexes. In this context, different methodologies have been used to calculate both the g -anisotropy and the ^{14}N hyperfine coupling in $\text{CoL}^{\text{N}_2\text{S}_2*}$ (Table 5.2). The hyperfine parameters predicted by DFT calculations are in relatively good agreement with the experimental data and further confirm the previous HYSCORE interpretation. However, DFT methods fail in

reproducing the large g -anisotropy of CoL^{N2S2} , especially the $\Delta(g_3-g_2)$ value that is underestimated by a factor of 4. Such deviation from the experimental data is quite common for the DFT approach.^{43,44} Consequently more sophisticated computational methods have been employed i.e. the complete active space self-consistent field (CASSCF) method together with the second-order N -electron valence perturbation theory (NEVPT2). A good agreement is found between the experimental and calculated g -tensors (Table 5.2) since both the averaged g -value (g_{iso} of 2.42 and 2.45, respectively) and the g -anisotropy are nicely reproduced by this approach ($\Delta(g_3-g_1)$ of 0.93 and 0.89, respectively).

Table 5.3. Comparison between experimental data and predicted TD-DFT transitions (energies and intensities) for the CoL^{N2S2} * complex.

	Calc.		λ (nm)	Exp. ϵ ($\text{M}^{-1}\text{cm}^{-1}$)	Assignment
	λ (nm)	f			
$\beta\text{HOMO-2} \rightarrow \beta\text{LUMO}$	742	0.038	750	1300	d-d transition
$\beta\text{HOMO-3} \rightarrow \beta\text{LUMO}$	543	0.073	530	1100	LMCT
$\beta\text{HOMO-6} \rightarrow \beta\text{LUMO}$	457	0.072	460	1900	LMCT
$\beta\text{HOMO-7} \rightarrow \beta\text{LUMO}$	438	0.071	420	2600	LMCT

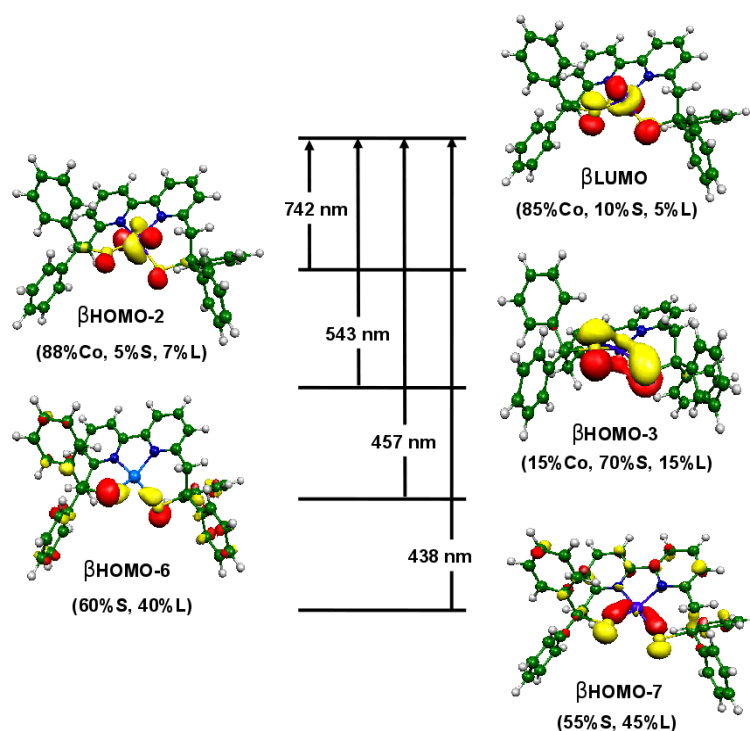


Figure 5.6. TD-DFT assignment of the calculated transitions for CoL^{N2S2} in DMF. The population of the relevant MOs (HOMO: highest occupied molecular orbital, LUMO: lowest unoccupied molecular orbital) is indicated in parentheses as well as the wavelength of the optical transitions. Legend: Co stands for the metal, S the sulfur atoms and L the rest of the ligand.

To gain insight into the optical properties of CoL^{N2S2} , TD-DFT calculations were undertaken on its optimized structure, $\text{CoL}^{\text{N2S2}*}$. By employing this computational method, we can provide the assignment of its salient features by calculating the main transition energies and their relative intensities (Figure 5.6). Our calculations adequately reproduce the energy of the key features of the experimental spectrum, namely, the four bands at 750, 530, 460 and 420 nm (*calc*: 742, 543, 457 and 438 nm) (Table 5.3). With respect to the intensity of the transitions, a fair agreement is found since the calculations predict higher f^{calc} for the 460 and 420 nm transitions than for that at 750 nm. Figure 5.6 shows that the three higher energy transitions arise mainly from ligand-to-metal charge transfer (LMCT) transitions since the acceptor orbital, namely the β -LUMO, is mainly metal-centred, and the donor orbitals are ligand-based MOs essentially distributed over the two sulfur atoms. The 750 nm transition is attributed to a d-d transition and involves the β -LUMO as the acceptor orbital, and the d_{xy} as the donor orbital. Such d-d transitions with relatively large molar extinction coefficients ($\epsilon = 1300 \text{ M}^{-1}\cdot\text{cm}^{-1}$) have already been observed in previously reported aryl thiolate Co^{II} complexes ($\epsilon = 1200 \text{ M}^{-1}\cdot\text{cm}^{-1}$ at 600 nm).⁴⁵

Redox Properties of CoL^{N2S2}

The electrochemical properties of CoL^{N2S2} were investigated in DMF (Figure 5.7). The cyclic voltammogram (CV) displays two one-electron metal based processes: a quasi-reversible $\text{Co}^{\text{III}}/\text{Co}^{\text{II}}$ oxidation wave at $E_{1/2} = -0.33 \text{ V vs Ag/Ag}^+$ ($\Delta E_p = 95 \text{ mV}$) and a quasi-reversible $\text{Co}^{\text{II}}/\text{Co}^{\text{I}}$ reduction wave at $E_{1/2} = -1.7 \text{ V}$ ($\Delta E_p = 85 \text{ mV}$). Similar redox properties have been observed for other Co^{II} complexes, which contain at least one thiolate ligand.^{28,46,47}

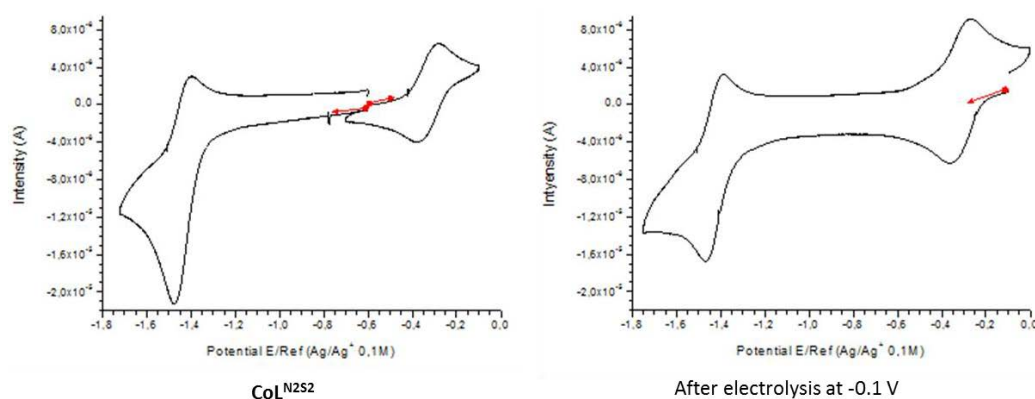


Figure 5.7 CV of CoL^{N2S2} (0.3 mM) in DMF, 0.1 M Bu_4NPF_6 and after electrolysis at -0.1 V. Scan rate of $100 \text{ mV}\cdot\text{s}^{-1}$.

To confirm that the oxidation process observed at -0.3 V is metal based, an exhaustive electrolysis at -0.1 V was carried out. The CV after electrolysis (Figure 5.7) is identical to that of $\text{CoL}^{\text{N}2\text{S}2}$ evidencing that the one-electron oxidised species is stable.

This reaction has also been followed by UV-Visible spectroscopy (Figure 5.8) and EPR spectroscopy. The one-electron oxidised solution of $\text{CoL}^{\text{N}2\text{S}2}$ is EPR silent, as expected for a mononuclear Co^{III} complex. As can be seen in figure 5.8, the most notable difference between the UV-Visible spectra of $\text{CoL}^{\text{N}2\text{S}2}$ and that of its oxidised form, is the complete disappearance of the broad transition at 750 nm, with the appearance of a broad transition centred at 660 nm.

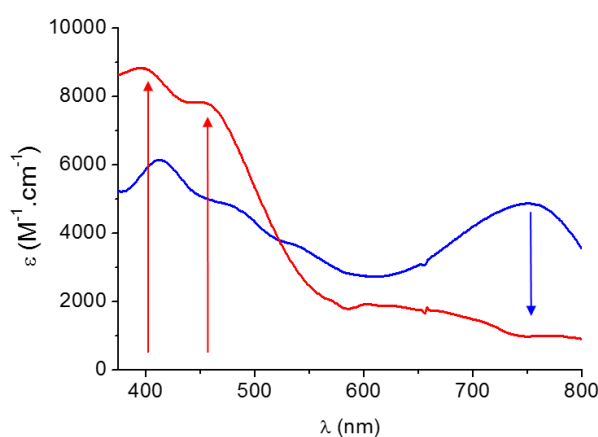


Figure 5.8. UV-Visible spectra of $\text{CoL}^{\text{N}2\text{S}2}$ (blue) and its electrochemically generated one-electron oxidised form (red) in anhydrous DMF (0.3 mM).

We were unable to crystallise this one electron oxidised form of $\text{CoL}^{\text{N}2\text{S}2}$ from the electrochemical solution. We were only able to isolate this mononuclear Co^{III} complex in the presence of chloride, while in the absence of a fifth coordinating ligand, a Co^{II} dimer is obtained.

5.2 Synthesis and Characterisation of the $[\text{Co}_2(\text{L}^{\text{N}2\text{S}2})_2](\text{PF}_6)_2$ Complex

As stated above, we have been unable to isolate the mononuclear Co^{III} complex, without the presence of a chloride. Instead, the crystallisation process gave a crystal of a dinuclear Co^{II} complex. The molecular structure of $[\text{Co}_2(\text{L}^{\text{N}2\text{S}2})_2](\text{PF}_6)_2 \cdot 2\text{MeCN}$ is shown in Figure 5.9, with important bond distances and angles presented in Table 5.4. X-ray collection and refinement data are given in the Appendix. The presence of two counter anions and a disulfide bond in the structure of the dinuclear Co complex imply a +II oxidation state for both Co^{II} ions. This is consistent with the reduction of the Co ion from

the +III oxidation state to the +II oxidation state concomitant with the oxidation of two of the thiolates into a disulfide bridge.

Table 5.4. Selected bond lengths (Å) and angles (°) for $\text{CoL}^{\text{N2S2Cl}}$ and $(\text{CoL}^{\text{N2S2}})_2(\text{PF}_6)_2 \cdot 2\text{CH}_3\text{CN}$.

	$\text{CoL}^{\text{N2S2Cl}}$	$\text{CoL}^{\text{N2S2Cl}}^*$	$[\text{Co}_2(\text{L}^{\text{N2S2}})_2]^{2+}$	
	Exp	Calc	Exp	
Co-N1	1.9915(14)	1.917	Co-N1	2.072(2)
Co-N2	2.0267(14)	1.962	Co-N2	2.111(2)
Co-S1	2.1957(5)	2.164	Co-S1	2.3795(7)
Co-S2	2.2056(5)	2.263	Co-S1'	2.3272(8)
Co-Cl1	2.3336(5)	2.271	Co-S2	2.5342(8)
			S2-S2'	2.0243(13)
N1-Co-N2	80.99(6)	83.2	N1-Co-N2	78.92(9)
N1-Co-S1	92.57(5)	95.4	N1-Co-S1	91.80(6)
N1-Co-S2	163.72(5)	176.7	N1-Co-S1'	133.34(7)
N2-Co-S1	142.15(4)	130.9	N1-Co-S2	137.88(6)
N2-Co-S2	97.73(4)	99.9	N2-Co-S1	145.91(6)
S1-Co-S2	78.427(19)	83.1	N2-Co-S1'	113.77(6)
N1-Co-Cl1	91.57(4)	85.5	N2-Co-S2	83.90(6)
N2-Co-Cl1	98.73(4)	92.3	S1-Co-S2	81.41(3)
S1-Co-Cl1	118.80(2)	136.7	S1'-Co-S2	88.78(3)
S2-Co-Cl1	104.64(2)	93.5		

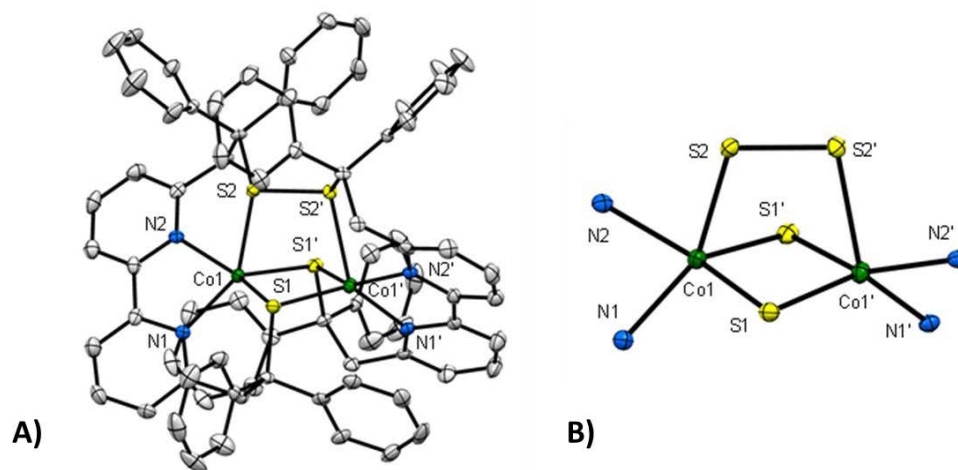


Figure 5.9. ORTEP diagram of (a) $[\text{Co}_2(\text{L}^{\text{N2S2}})_2](\text{PF}_6)_2 \cdot 2\text{MeCN}$ and (b) the binuclear core. Thermal ellipsoids are drawn at the 50% probability level. Hydrogen atoms, PF_6^- counterions and solvent MeCN molecules are omitted for clarity.

There is a plane of symmetry in $[\text{Co}_2(\text{L}^{\text{N2S2}})_2]^{2+}$ resulting in the two Co^{II} centres being equivalent. The geometry about each Co ion is a highly distorted square pyramid. The square planar base is formed by the two nitrogen atoms of the bipyridine (N1 & N2), one sulfur atom (S1) from the same ligand and an additional sulfur atom (S1') from the second ligand. The axial coordination site is occupied by the sulfur atom (S2) of the

disulfide bond. The axial Co-S2 bond distance (2.5342(8) Å) is significantly longer than the equatorial bonds Co-S1 and Co-S1' (2.3795(7) and 2.3272(8) Å). This is due to the fact that the axial sulfur forms the disulfide bond, and thus is less electron donating than the equatorially bound sulfur atoms. It should be noted that this is the first dinuclear Co complex which has a direct disulfide bond as a bridging ligand between the two Co^{II} ions. The equatorially bound bridging Co-S bond distances are consistent with those previously reported in the literature (2.20 – 2.32 Å).⁴⁸⁻⁵¹

We have tried to obtain a mononuclear Co^{III} complex, specifically to attempt to model CoNHase. Nevertheless, we were unable to stabilise the mononuclear complex in the absence of a strong donor ligand, such as a chloride anion.

5.3 Synthesis and Characterisation of [CoL^{N2S2}Cl]

CoL^{N2S2}Cl was obtained by reaction with K₂L^{N2S2} in THF with CoCl₂·6H₂O, leading to a black solution mixture. To this mixture 4-bromobenzenediazonium tetrafluoroborate was added to oxidise the Co^{II} into Co^{III}. Crystals suitable for X-ray diffraction were obtained by diffusion of diethyl ether into the THF solution. The molecular structure of **CoL^{N2S2}Cl** is shown in Figure 5.10. Selected bond distances and angles are listed in Table 5.4 and X-ray collection and refinement data are given in the Appendix. The Co^{III} ion is bound to two aliphatic thiolates and to the bidentate bipyridine unit from L^{N2S2}, coordinating in a distorted square planar *cis*-N₂S₂ fashion. In addition a chloride is axially-bound to the Co^{III}, giving a distorted square pyramidal geometry. This distortion is not only due to the constraints associated with the ligand as observed in **CoL^{N2S2}**, but also due to the apical binding of the chloride; this is evidenced by the Co^{III} being 0.458 Å above the plane of the donor atoms of the L^{N2S2} ligand.

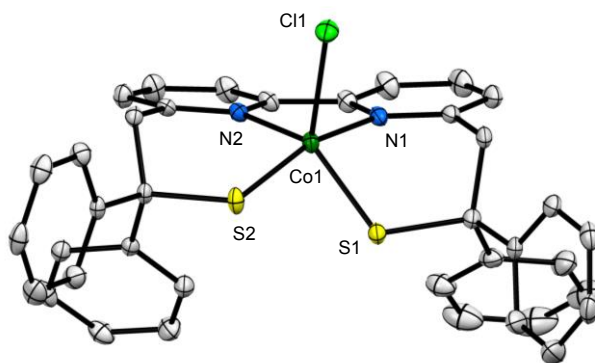


Figure 5.10. ORTEP diagram of [CoL^{N2S2}Cl]. Thermal ellipsoids are drawn at 30% probability level. Hydrogen atoms are omitted for clarity.

The Co-S bond distances of 2.1957(5) and 2.2056(5) Å are significantly longer than observed in **CoL^{N2S2}** (2.1662(7) and 2.1703(7) Å) consistent with a change in geometry from square planar to square pyramidal. The Co-S bond distances in **CoL^{N2S2}Cl** are also notably longer than those reported for a neutral square pyramidal Co^{III} complex (2.16 and 2.17 Å)⁵² and shorter than those in previously described neutral⁵³ and cationic^{54,55} octahedral Co^{III} complexes (between 2.22 and 2.23 Å). The Co-N distances (1.9915(14) and 2.0267(14) Å) are consistent with the mean Co^{III}-N_{aromatic} literature values (1.971 Å).

The redox properties of **CoL^{N2S2}Cl** have also been investigated in DMF. The CV of **CoL^{N2S2}Cl** shows a quasi-reversible reduction peak at $E_{1/2} = -0.45\text{V}$ ($\Delta E_p = 167\text{mV}$) which can be attributed to the redox couple Co^{III}/Co^{II}. This system is less reversible than the redox couple Co^{III}/Co^{II} in the case of **CoL^{N2S2}** (Figure 5.7). Due to the presence of the electronegative donor chloride ligand in the coordination sphere of the Co^{III}, a decrease of the redox potentials of the Co^{III}/Co^{II} couple is observed when comparing with **CoL^{N2S2}**. To confirm that the reduction process observed at -0.5 V is metal based, an exhaustive electrolysis at -0.8 V has been carried out. This reaction was also followed by UV-Visible spectroscopy, as shown in Figure 5.11. After electrolysis, **CoL^{N2S2}** is recovered as attested by its UV-Visible spectrum (Figure 5.11).

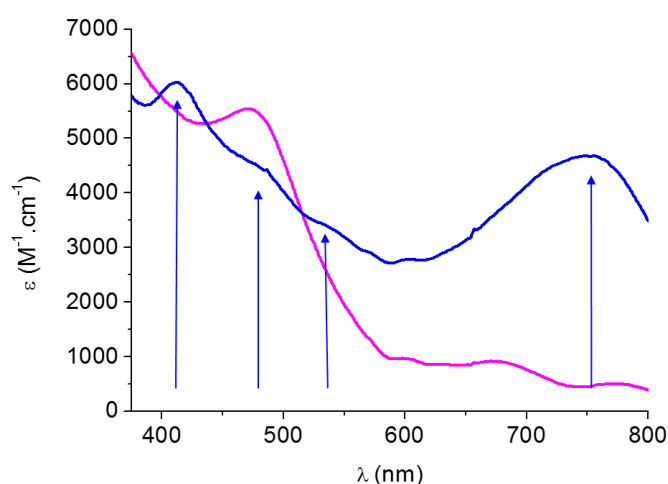


Figure 5.11. UV-Visible spectra of **CoL^{N2S2}Cl** (pink, initial spectrum) and after electrolysis at -0.8 V giving Co(II) species **CoL^{N2S2}** (blue) in DMF (0.2 mM)

*Reactivity of **CoL^{N2S2}Cl** towards S-Oxidation*

As previously mentioned, in order to generate the active state of CoNHase, dissymmetric S-oxygenation is necessary. Therefore, the propensity of **CoL^{N2S2}Cl** to perform S-oxygenation reactions has been explored with a H₂O₂: **CoL^{N2S2}Cl** ratio of 10:1 in DMF. After one minute of reaction, the solution was analysed by mass spectrometry.

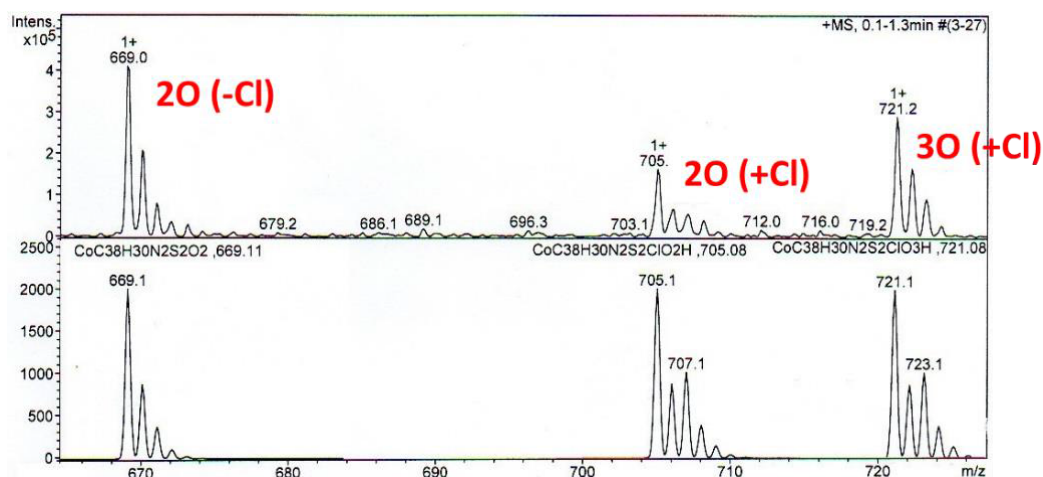


Figure 5.12. ESI-Mass spectra of experimental (above) and simulated (bottom) $\text{CoL}^{\text{N}_2\text{S}_2}\text{Cl}$ with 10 eq of H_2O_2 .

The ESI-Mass spectrum is shown in Figure 5.12. Peaks corresponding to three types of products have been observed, namely $[\text{CoL}^{\text{N}_2\text{S}_2}(\text{O})_2]^+$, $[\text{HCoL}^{\text{N}_2\text{S}_2}(\text{O})_2\text{Cl}]^+$ and $[\text{HCoL}^{\text{N}_2\text{S}_2}(\text{O})_3\text{Cl}]^+$ (peaks $m/z = 669, 705$ and 721 respectively). This suggests incorporation of three oxygen atoms, thereby providing evidence that a dissymmetrical S-oxygenation can occur in our model, with one thiolate becoming a sulfenate and the second a sulfinate. This accurately models the process that has been observed during the activating step of the CoNHase.

It should be stated here, that although the mass between the simulated and experimental spectrum are a good fit, the simulation pattern differs from that of the experimental. Therefore, more work is needed to confirm how many oxygen atoms and chloride anions are incorporated on the Co^{III} complex.

Electronic structure of $\text{CoL}^{\text{N}_2\text{S}_2}\text{Cl}$ and interpretation of its spectroscopic properties.

To further investigate the electronic structure of $\text{CoL}^{\text{N}_2\text{S}_2}\text{Cl}$, quantum chemical calculations have been carried out. The resulting optimised geometry of $\text{CoL}^{\text{N}_2\text{S}_2}\text{Cl}$ ($\text{CoL}^{\text{N}_2\text{S}_2}\text{Cl}^*$) shown in Figure 5.13, compares well with the crystallographic data, validating the computational approach (Table 5.4).

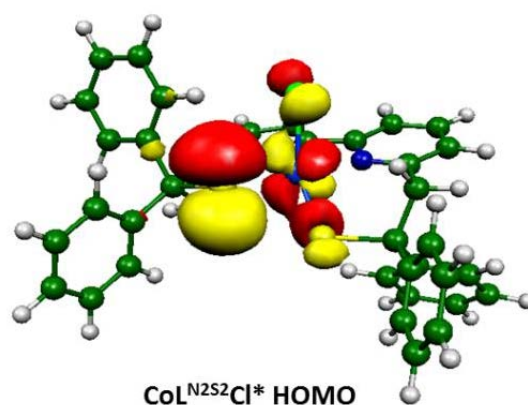


Figure 5.13. The HOMO for **CoL^{N2S2}Cl***. Carbon (green), sulfur (yellow) and nitrogen (blue).

Table 5.5. Experimental and calculated electronic absorption parameters for **CoL^{N2S2}Cl**

Transition (MO number)	λ_{expt} (nm)	ϵ ($\text{M}^{-1}\text{cm}^{-1}$)	λ_{calc} (nm)	f_{calc}	Assignment
$\beta\text{HOMO-2} \rightarrow \beta\text{LUMO}$	798	1560	839	0.015	d-d
$\beta\text{HOMO-5} \rightarrow \beta\text{LUMO}$	671	1240	658	0.021	LMCT
$\beta\text{HOMO-10} \rightarrow \beta\text{LUMO}$	474	5870	536	0.015	LMCT

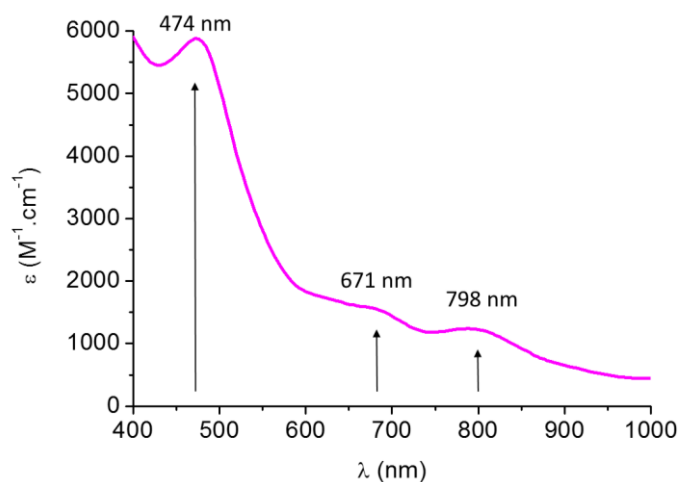


Figure 5.14. Electronic absorption spectrum into the NIR of **CoL^{N2S2}Cl** (1.0 mM) in DMF.

The nature of the HOMO indicates a partial delocalization of the electron density over the metal (19 %) and a majority on the sulfur atoms (71 %), with only a small amount localised on the chloride ligand (4 %). The high sulfur contribution to the HOMO indicates a large degree of covalency for the Co-S bond. To further understand the optical properties of **CoL^{N2S2}Cl**, TD-DFT calculations were undertaken on its optimized structure, **CoL^{N2S2}Cl***. The calculations showed three transitions at 839, 657 and 536 nm (Table 5.5). The presence of a predicted transition in the NIR region of the calculated spectrum, led us to revisit the experimental data.

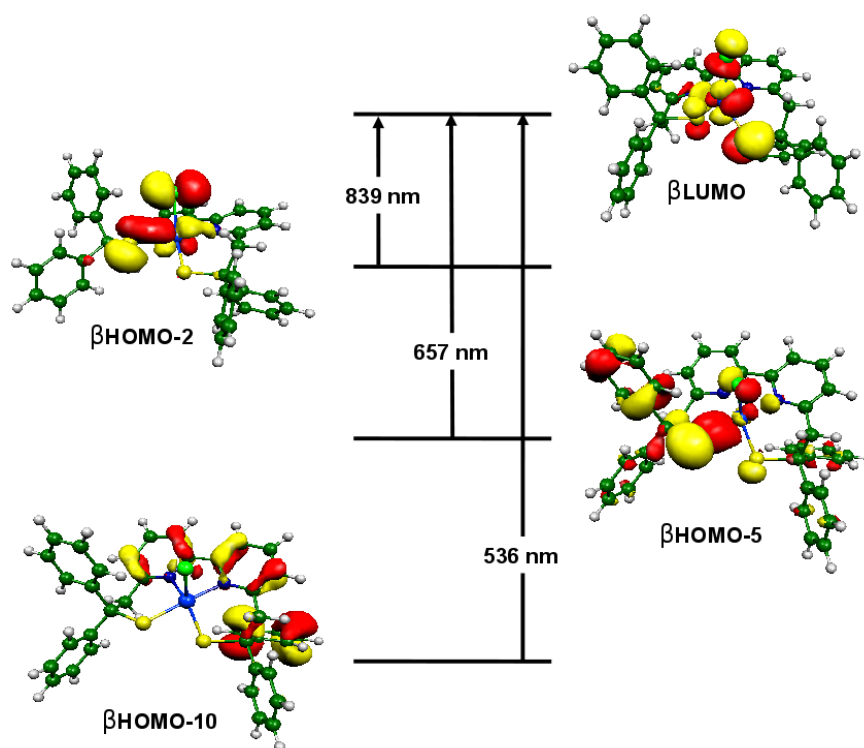


Figure 5.15. TD-DFT assignment of the calculated transitions for $\text{CoL}^{\text{N}_2\text{S}_2}\text{Cl}^*$ in DMF.

The electronic absorption spectrum recorded in the extended NIR region is shown in Figure 5.14, and shows a transition at 798 nm in agreement with the calculated value. Therefore the calculations are reasonably consistent with the experimental spectrum (798, 671, and 474 nm). Figure 5.15 shows that the two higher energy transitions arise mainly from ligand-to-metal charge transfer (LMCT) transitions since the acceptor orbital, namely the β -LUMO, is mainly metal-centred, and the donor orbitals are ligand-based MOs. The transition at 839 nm is attributed to a d-d transition.

5.4 Reactivity of $[\text{CoL}^{\text{N}_2\text{S}_2}]$ toward S-Alkylation

To see whether Co^{II} is a good probe to mimic the reactivity of Zn enzymes involved in S-alkylation reactions, the reactivity of $\text{CoL}^{\text{N}_2\text{S}_2}$ has been tested with methyl iodide as the alkylating agent. The reaction of $\text{CoL}^{\text{N}_2\text{S}_2}$ with an excess (20 eq) of CH_3I in DMF has been followed by UV-visible spectroscopy under anaerobic conditions (Figure 5.16). During the course of the reaction (1h), the most notable change is the complete disappearance of the transition at 760 nm.

The resulting solution was analysed by mass spectrometry (ESI-MS) showing that the S-methylation reaction is selective. In fact, only one peak corresponding to the mono-S-methylated cationic fragment $[\text{CoL}^{\text{N}_2\text{S}_2}\text{Me}]^+$ is observed even after 12 hours.

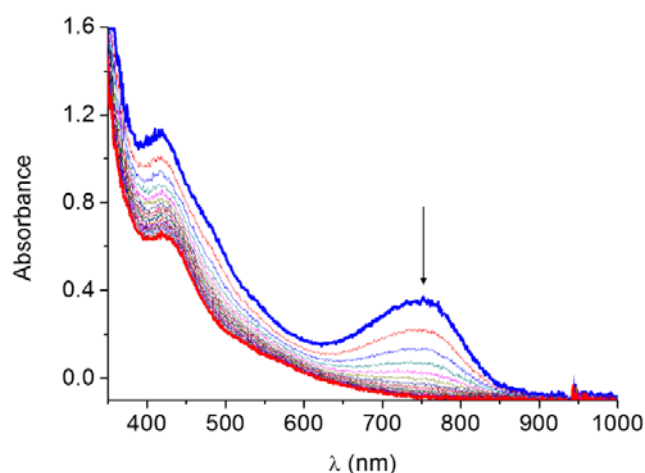


Figure 5.16. Absorption spectra of a DMF solution of CoL^{N2S2} (blue) and in the presence of 20 equivalents of CH_3I at room temperature to give $\text{CoL}^{\text{N2S2Me}}$ (red).

The reaction has also been followed by EPR spectroscopy (Figure 5.17). The typical $S = 1/2$ signal of CoL^{N2S2} disappears during the course of the reaction and a new signal centred at $g = 4.16$, characteristic of a high spin Co^{II} complex ($S = 3/2$) grows in.⁵⁶ This strongly suggests that a notable structural modification of the geometry occurs during the S-alkylation process, in agreement with DFT calculations (see below).

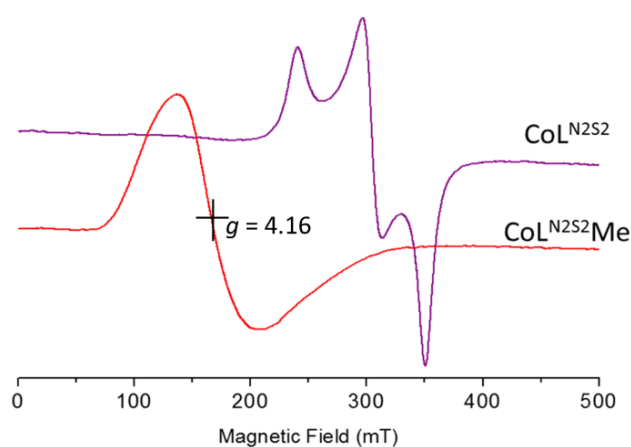


Figure 5.17. Experimental X-band EPR spectra (15 K) of CoL^{N2S2} in a DMF solution before (purple) and after (red) the addition of 20 equivalents of CH_3I .

Structural properties of $\text{CoL}^{\text{N2S2Me}}$

As the structure of the mono S-alkylated product could not be resolved by X-ray crystallography, its geometry has been optimized, starting from the isostructural Ni^{II} complex previously described (Scheme 5.5),²⁹ in which the Ni^{II} ion has been substituted by a Co^{II} ion (Figure 5.18).

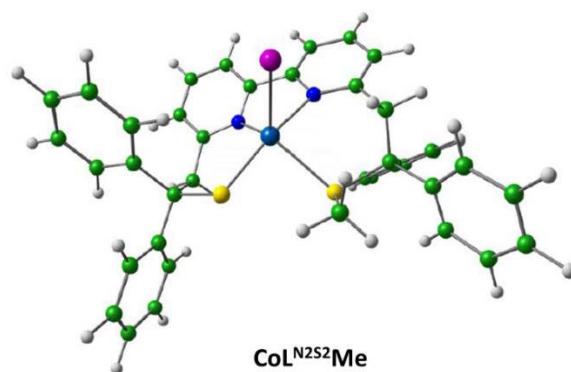
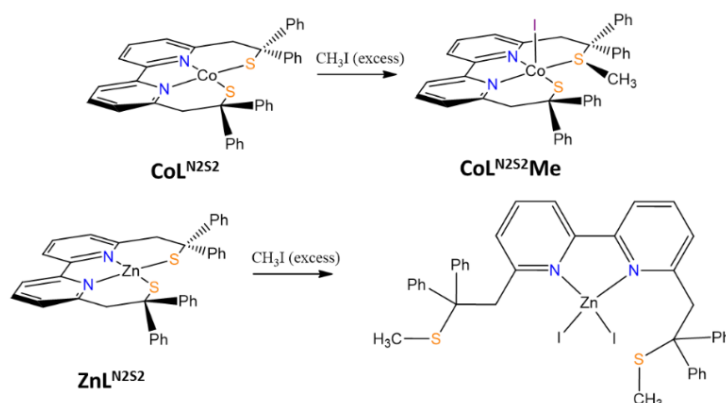


Figure 5.18. Computationally calculated structure of **CoL^{N2S2}Me***. Selected bond distances (Å): Co-I 2.750, Co-N1 2.170, Co-N2 2.116, Co-S1 2.538, Co-S2 2.295.

Because the Co^{II} ion can be low ($S = 1/2$) or high ($S = 3/2$) spin, both possibilities have been considered. A difference of 8.7 kcal/mol has been calculated in favour of the high spin configuration, in agreement with the EPR data. Therefore, in the rest of the description, only the quartet optimized structure (denoted **CoL^{N2S2}Me***) will be considered.



Scheme 5.8. Reactivity of **CoL^{N2S2}** and **ZnL^{N2S2}** with an excess of CH_3I to give S-methylated species **CoL^{N2S2}Me** and **ZnI₂L^{N2S2}Me** respectively.

The optimised structure **CoL^{N2S2}Me*** shows that the Co^{II} ion exhibits a five coordinate square pyramidal geometry. The two aliphatic thiolate sulfur atoms and the two bipyridine nitrogen atoms from **L^{N2S2}** constitute the plane, while the iodide ligand binds in the apical position. Therefore the change in spin state observed by EPR spectroscopy during the S-methylation reaction is consistent with a notable modification in the geometry from square planar into square pyramidal. It can also be noted that the generated thioether remains coordinated to the Co^{II} ion, in contrast to the Zn^{II} derivate (Scheme 5.8). This clearly shows that the metal-thioether bond is stronger in the Co^{II} complex compared to the Zn^{II}, this can potentially be attributed to the full 3d orbitals of

the Zn^{II} ion. This results in higher ionic character of the Zn^{II}-thiolate bond, and therefore upon creation of a thioether bond, decoordination.

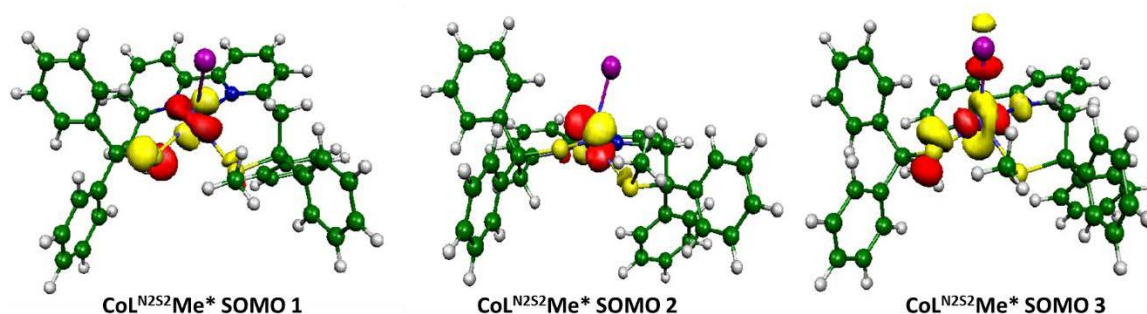


Figure 5.19. Localized SOMOs in the $\text{CoL}^{\text{N2S2Me}^*}$ complex.

The three unpaired electrons of $\text{CoL}^{\text{N2S2Me}^*}$ are partially localized in three MOs, which correspond to a mixture of the d_{xy} and d_{yz} orbitals for SOMO1, d_{yz} for SOMO2 and a mixture of the d_{z^2} and d_{xy} orbitals for SOMO3 (Figure 5.19). In both SOMO1 and SOMO3, the unpaired electron is delocalized over the metal (78.5 and 77.6 %, respectively) and the ligand, especially over the sulfur atom of the thiolate function (12.5 and 7.8 %, respectively). In the case of the SOMO2, the unpaired electron is mainly localized on the Co^{II} ion (92.2 %). There is no electronic density spread on the sulfur atom of the thioether function in any of these SOMOs.

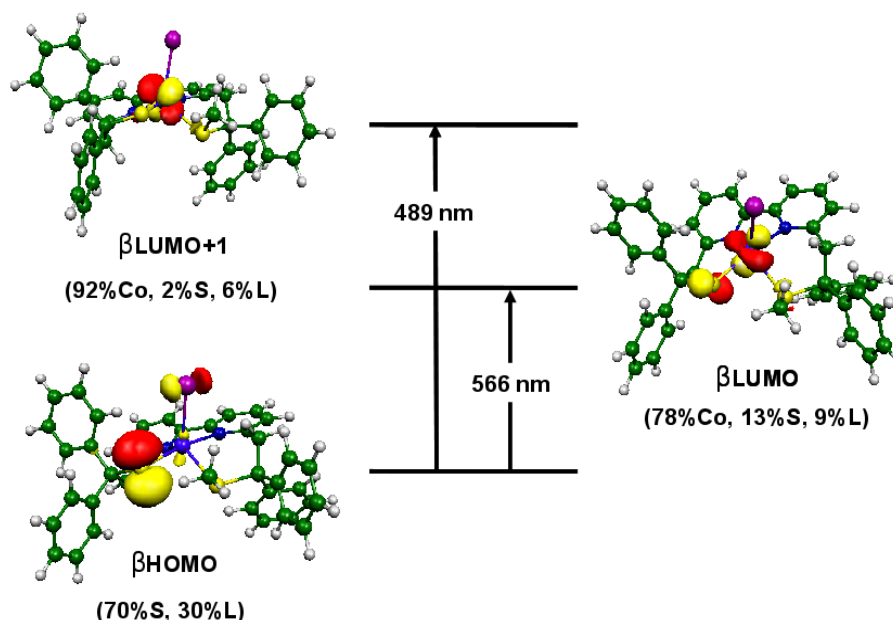


Figure 5.20. TD-DFT assignment of the calculated transition for $\text{CoL}^{\text{N2S2Me}^*}$ in DMF. The population of the relevant MO (HOMO: highest occupied molecular orbital, LUMO: lowest unoccupied molecular orbital) is indicated in parentheses as well as the wavelength of the optical transitions. Legend: Co stands for the metal, S the sulfur atoms and L the rest of the ligand.

TD-DFT calculations were also undertaken on **CoL^{N2S2}Me***. Our calculations reproduce the energies of the key features of the experimental spectrum, the 530 and 450 nm absorptions (*calc*: 566 and 489 nm), which can be attributed to LMCT and d-d transitions, respectively (Table 5.6). For the 450 nm, the acceptor orbital, namely the β -LUMO, is mainly metal-centred, while the donor orbital is principally a ligand-based MO essentially localized over the thiolate sulfur and iodide ions (Figure 5.20). The 530 nm transition is attributed to a d-d transition with the β -LUMO as the acceptor orbital, and the d_{yz} as the donor orbital.

Table 5.6. Comparison between experimental data and predicted TD-DFT transitions (energies and intensities) for the **CoL^{N2S2}Me** complex.

	Calc.		Exp.	
	λ (nm)	f	λ (nm)	ϵ (M ⁻¹ cm ⁻¹)
β HOMO \rightarrow β LUMO	566	0.005	530	350
β HOMO \rightarrow β LUMO+1	489	0.028	450	1050

Conclusion

Three different cobalt complexes have been described, a mononuclear Co^{III} complex and two novel Co^{II} complexes: a mononuclear alkyl dithiolate complex and a dinuclear Co^{II} complex in which the two cobalt ions are bridged by a disulfide bridge unit.

CoL^{N2S2} represents an unprecedented example of an alkyl thiolate Co^{II} complex exhibiting a quasi-square planar geometry. The mono S-methylation reaction of this complex, leading to **CoL^{N2S2}Me**, induces a switch of the spin state configuration of the Co^{II} ion, from low spin state ($S = 1/2$) to high spin state ($S = 3/2$). A detailed investigation of the spectroscopic properties of both complexes has been undertaken. In particular, HYSCORE experiments on **CoL^{N2S2}** gave access to the distribution of the spin density over the complex. The S-alkylation reactivity of **CoL^{N2S2}** is comparable to that of **NiL^{N2S2}** but differs substantially from that of **ZnL^{N2S2}**, for which the double S-methylated, complex, [ZnL^{Me2}I₂], has been obtained. Another important difference between the reactivity of the Co and Zn complexes is that the produced thioether remains coordinated to the Co^{II} ion, whereas it is de-coordinated from the metal centre in the case of the Zn complex. Consequently, even if the Co^{II} ion is a suitable structural substitute for Zn-containing metalloenzymes, it may be inappropriate as a functional substitute in particular cases such as, S-alkylation.

By using strong donor ligand, *i.e.* a chloride ion, we were able to obtain a mononuclear alkyl thiolate Co^{III} complex, **CoL^{N2S2}Cl**, displaying a distorted square pyramidal geometry. The S-oxygenation reaction of **CoL^{N2S2}Cl** results in the incorporation of three oxygen atoms, evidencing dissymmetrical S-oxygenation, accurately modelling the process that has been observed during the activating step of CoNHase. It is also important to note that in the absence of a strong donor ligand, we were unable to isolate the tetradentate mononuclear Co^{III} complex. Instead a dinuclear (Co^{II})₂ complex has been obtained; this has resulted from the reduction of the Co^{III} ions into Co^{II} ions with the simultaneous oxidation of two thiolate sulfur atoms originating from two ligands, forming a disulfide bridge. This has led to the first dinuclear Co^{II} complex which has a direct disulfide bridge as a bridging ligand between the two Co^{II} centres.

References

- (1) Kobayashi, M.; Shimizu, S. *Eur. J. Biochem.* **1999**, *261*, 1–9.
- (2) Kräutler, B. *Biochem. Soc. Trans.* **2005**, *33*, 806–810.
- (3) Kobayashi, M.; Shimizu, S. *Nat. Biotechnol.* **1998**, *16*, 733–736.
- (4) Peplowski, L.; Kubiak, K.; Nowak, W. *J. Mol. Model.* **2007**, *13*, 725–730.
- (5) Bourles, E.; Alves de Sousa, R.; Galardon, E.; Giorgi, M.; Artaud, I. *Angew. Chem. Int. Ed.* **2005**, *44*, 6162–6165.
- (6) Tyler, L. A.; Noveron, J. C.; Olmstead, M. M.; Mascharak, P. K. *Inorg. Chem.* **2003**, *42*, 5751–5761.
- (7) Kung, I.; Schweitzer, D.; Shearer, J.; Taylor, W. D.; Jackson, H. L.; Lovell, S.; Kovacs, J. A. *J. Am. Chem. Soc.* **2000**, *122*, 8299–8300.
- (8) Vallee, W. M. B. L. In *Methods in Enzymology*; James F. Riordan and Bert L. Vallee, Ed.; Academic Press, 1993; Vol. Volume 226, pp. 52–71.
- (9) Bennett, B. In *Metals in Biology*; Hanson, G.; Berliner, L., Eds.; Biological Magnetic Resonance; Springer New York, 2010; pp. 345–370.
- (10) Bennet, B. *Curr. Top. Biophys.* **2002**, *26*, 49–57.
- (11) Davis, M. I.; Bennett, M. J.; Thomas, L. M.; Bjorkman, P. J. *Proc. Natl. Acad. Sci.* **2005**, *102*, 5981–5986.
- (12) Bennett, B.; Antholine, W. E.; D'souza, V. M.; Chen, G.; Ustinyuk, L.; Holz, R. C. *J. Am. Chem. Soc.* **2002**, *124*, 13025–13034.
- (13) Muni, P.; Moulin, A.; Stamper, C. C.; Bennett, B.; Ringe, D.; Petsko, G. A.; Holz, R. C. *J. Inorg. Biochem.* **2007**, *101*, 1099–1107.
- (14) McGowan, S.; Oellig, C. A.; Birru, W. A.; Caradoc-Davies, T. T.; Stack, C. M.; Lowther, J.; Skinner-Adams, T.; Mucha, A.; Kafarski, P.; Grembecka, J.; Trenholme, K. R.; Buckle, A. M.; Gardiner, D. L.; Dalton, J. P.; Whisstock, J. C. *Proc. Natl. Acad. Sci.* **2010**, *107*, 2449–2454.
- (15) Peariso, K.; Zhou, Z. S.; Smith, A. E.; Matthews, R. G.; Penner-Hahn, J. E. *Biochemistry (Mosc.)* **2001**, *40*, 987–993.
- (16) Tobin, D. A.; Pickett, J. S.; Hartman, H. L.; Fierke, C. A.; Penner-Hahn, J. E. *J. Am. Chem. Soc.* **2003**, *125*, 9962–9969.
- (17) Myers, L. C.; Terranova, M. P.; Ferentz, A. E.; Wagner, G.; Verdine, G. L. *Science* **1993**, *261*, 1164–1167.
- (18) Wilker, J. J.; Lippard, S. J. *Inorg. Chem.* **1997**, *36*, 969–978.
- (19) Hammes, B. S.; Carrano, C. J. *Inorg. Chem.* **2001**, *40*, 919–927.
- (20) Grapperhaus, C. A.; Mullins, C. S.; Mashuta, M. S. *Inorganica Chim. Acta* **2005**, *358*, 623–632.
- (21) Morlok, M. M.; Janak, K. E.; Zhu, G.; Quarless, D. A.; Parkin, G. *J. Am. Chem. Soc.* **2005**, *127*, 14039–14050.
- (22) Ji, M.; Benkmil, B.; Vahrenkamp, H. *Inorg. Chem.* **2005**, *44*, 3518–3523.
- (23) Rombach, M.; Seebacher, J.; Ji, M.; Zhang, G.; He, G.; Ibrahim, M. M.; Benkmil, B.; Vahrenkamp, H. *Inorg. Chem.* **2006**, *45*, 4571–4575.
- (24) Farmer, P. J.; Reibenspies, J. H.; Lindahl, P. A.; Darensbourg, M. Y. *J. Am. Chem. Soc.* **1993**, *115*, 4665–4674.
- (25) Musie, G.; Reibenspies, J. H.; Darensbourg, M. Y. *Inorg. Chem.* **1998**, *37*, 302–310.
- (26) Bellefeuille, J. A.; Grapperhaus, C. A.; Derecskei-Kovacs, A.; Reibenspies, J. H.; Darensbourg, M. Y. *Inorganica Chim. Acta* **2000**, *300–302*, 73–81.
- (27) Green, K. N.; Brothers, S. M.; Jenkins, R. M.; Carson, C. E.; Grapperhaus, C. A.; Darensbourg, M. Y. *Inorg. Chem.* **2007**, *46*, 7536–7544.
- (28) Fox, D. C.; Fiedler, A. T.; Halfen, H. L.; Brunold, T. C.; Halfen, J. A. *J. Am. Chem. Soc.* **2004**, *126*, 7627–7638.
- (29) Gennari, M.; Orio, M.; Pécaut, J.; Bothe, E.; Neese, F.; Collomb, M.-N.; Duboc, C. *Inorg. Chem.* **2011**, *50*, 3707–3716.
- (30) Gennari, M.; Retegan, M.; DeBeer, S.; Pécaut, J.; Neese, F.; Collomb, M.-N.; Duboc, C. *Inorg. Chem.* **2011**, *50*, 10047–10055.
- (31) Yang, L.; Powell, D. R.; Houser, R. P. *Dalton Trans.* **2007**, 955–964.
- (32) Gregson, A. K.; Martin, R. L.; Mitra, S. *Chem. Phys. Lett.* **1970**, *5*, 310–311.
- (33) Maki, A. H.; Edelstein, N.; Davison, A.; Holm, R. H. *J. Am. Chem. Soc.* **1964**, *86*, 4580–4587.
- (34) Otto, J.; Jolk, I.; Viland, T.; Wonnemann, R.; Krebs, B. *Inorganica Chim. Acta* **1999**, *285*, 262–268.
- (35) Lee, H. K.; Lam, C. H.; Li, S.-L.; Zhang, Z.-Y.; Mak, T. C. W. *Inorg. Chem.* **2001**, *40*, 4691–4695.
- (36) Swenson, D.; Baenziger, N. C.; Coucouvanis, D. *J. Am. Chem. Soc.* **1978**, *100*, 1932–1934.
- (37) Thompson, J. S.; Marks, T. J.; Ibers, J. A. *J. Am. Chem. Soc.* **1979**, *101*, 4180–4192.
- (38) Téllez, F.; Flores-Parra, A.; Barba-Behrens, N.; Contreras, R. *Polyhedron* **2004**, *23*, 2481–2489.

- (39) Wei, G.; Hong, M.; Huang, Z.; Liu, H. *J. Chem. Soc. Dalton Trans.* **1991**, 3145–3148.
- (40) Mastropaolo, D.; Thich, J. A.; Potenza, J. A.; Schugar, H. J. *J. Am. Chem. Soc.* **1977**, *99*, 424–429.
- (41) Chang, S. C.; Karambelkar, V. V.; Sommer, R. D.; Rheingold, A. L.; Goldberg, D. P. *Inorg. Chem.* **2002**, *41*, 239–248.
- (42) Nishida, Y.; Kida, S. *Coord. Chem. Rev.* **1979**, *27*, 275–298.
- (43) McNaughton, R. L.; Roemelt, M.; Chin, J. M.; Schrock, R. R.; Neese, F.; Hoffman, B. M. *J. Am. Chem. Soc.* **2010**, *132*, 8645–8656.
- (44) Maganas, D.; Sottini, S.; Kyritsis, P.; Groenen, E. J. J.; Neese, F. *Inorg. Chem.* **2011**, *50*, 8741–8754.
- (45) Gorelsky, S. I.; Basumallick, L.; Vura-Weis, J.; Sarangi, R.; Hodgson, K. O.; Hedman, B.; Fujisawa, K.; Solomon, E. I. *Inorg. Chem.* **2005**, *44*, 4947–4960.
- (46) Brines, L. M.; Shearer, J.; Fender, J. K.; Schweitzer, D.; Shoner, S. C.; Barnhart, D.; Kaminsky, W.; Lovell, S.; Kovacs, J. A. *Inorg. Chem.* **2007**, *46*, 9267–9277.
- (47) Brines, L. M.; Villar-Acevedo, G.; Kitagawa, T.; Swartz, R. D.; Lugo-Mas, P.; Kaminsky, W.; Benedict, J. B.; Kovacs, J. A. *Inorganica Chim. Acta* **2008**, *361*, 1070–1078.
- (48) Rabinowitz, H. N.; Karlin, K. D.; Lippard, S. J. *J. Am. Chem. Soc.* **1977**, *99*, 1420–1426.
- (49) Chakraborty, P.; Chandra, S. K.; Chakravorty, A. *Inorg. Chem.* **1994**, *33*, 4959–4965.
- (50) Smucker, B. W.; VanStipdonk, M. J.; Eichhorn, D. M. *J. Inorg. Biochem.* **2007**, *101*, 1537–1542.
- (51) Xu, X.; Jiao, G.; Sun, H.; Li, X. *Z. Für Anorg. Allg. Chem.* **2011**, *637*, 430–435.
- (52) Ghilardi, C. A.; Laschi, F.; Midollini, S.; Orlandini, A.; Scapacci, G.; Zanello, P. *J. Chem. Soc. Dalton Trans.* **1995**, 531–540.
- (53) Hakimi, M.; Takjoo, R.; Erfaniyan, V.; Schuh, E.; Mohr, F. *Transit. Met. Chem.* **2010**, *35*, 959–965.
- (54) Takjoo, R.; Centore, R.; Hakimi, M.; Ali Beyramabadi, S.; Morsali, A. *Inorganica Chim. Acta* **2011**, *371*, 36–41.
- (55) Viñuelas-Zahfños, E.; Luna-Giles, F.; Torres-García, P.; Fernández-Calderón, M. C. *Eur. J. Med. Chem.* **2011**, *46*, 150–159.
- (56) Jones, R.; Summerville, D.; Basolo, F. *Chem. Rev.* **1979**, *79*, 139–179.

Jahn-Teller Effect in a Mononuclear Copper(II) Complex Containing a Hexadentate Ligand

Hall, N. A., Orio, M., Wills, C., Molton, F., Duboc, C., Blackman, A.G. *Inorg. Chem.* Submitted October 2013.

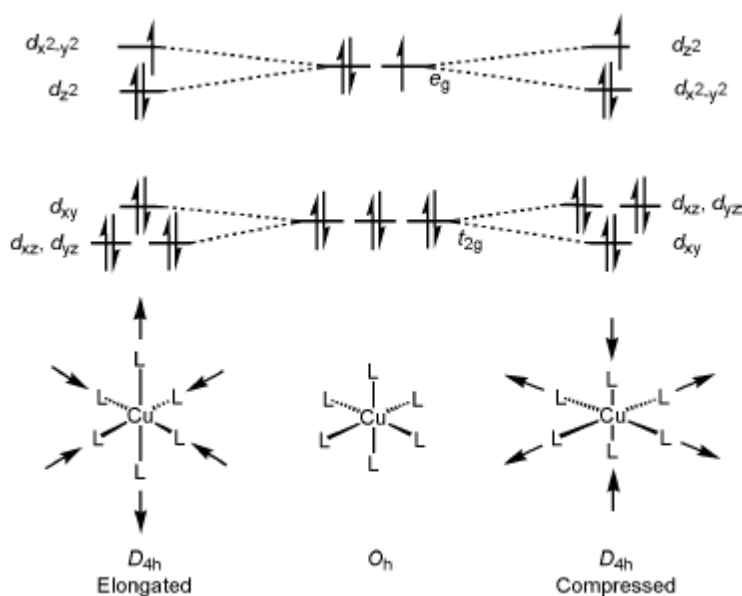
Résumé

Ce dernier chapitre est consacré à un projet de recherche initié lors de mon Master réalisé en Nouvelle-Zélande, à l'Université d'Otago à Dunedin, sous la supervision du Professeur Alan Blackman. Au cours de mon stage de Master, j'ai synthétisé un ligand possédant 6 sites de coordination azotés (bmet) pour l'obtention de complexes octaédriques de différents ions de métaux de transition. Plus particulièrement, un de nos objectifs était d'étudier l'effet d'un tel ligand sur les propriétés structurales et électroniques de complexes octaédriques susceptibles de présenter des distorsions dues à l'effet Jahn-Teller. Les complexes octaédriques de cuivre(II) sont les systèmes les plus étudiés dans ce cadre, car ils sont stables et présentent des signatures RPE très informatives.

Au cours de mon Master, j'ai synthétisé le complexe $[\text{Cu}(\text{bmet})]^{2+}$ avec différents contre-anions et leur structure a été résolue par diffraction des rayons X. Puis, au cours de ma thèse, je me suis plus particulièrement intéressé aux propriétés électroniques de ces complexes en combinant des études de spectroscopie RPE et des calculs théoriques. La structure du cation $[\text{Cu}(\text{bmet})]^{2+}$ est similaire quelque soit la nature du contre-anion, bien que son arrangement tridimensionnel soit différent. Une analyse de la structure enregistrée à 100 K est en accord avec un octaèdre présentant une compression. Ce type de distorsion est extrêmement rare dans les complexes de cuivre(II). A ce jour, seuls deux systèmes présentant une « vraie » compression ont été décrits dans la littérature. Dans le cas de quatre autres complexes décrits dans la littérature, il s'agit d'une compression « dynamique ». Ce type d'effet peut être mis en évidence par le fait que les longueurs de liaison métal-ligand varient en fonction de la température à laquelle la structure a été enregistrée. Une autre technique pour identifier la nature de la distorsion est la spectroscopie de RPE. La poudre $[\text{Cu}(\text{bmet})]^{2+}$ présente un spectre RPE à 298 K caractéristique d'un état fondamental $\{d_z^2\}^1$ en accord avec un système compressé. Néanmoins, le spectre change notablement quand l'enregistrement est réalisé à une température plus basse, indiquant un changement de configuration électronique de $\{d_z^2\}^1$ à $\{d_{x^2-y^2}\}^1$, en accord avec une élongation de l'octaèdre. La structure optimisée de $[\text{Cu}(\text{bmet})]^{2+}$, calculée par DFT, correspond à un octaèdre présentant une élongation. Cette structure calculée est donc en accord avec la configuration électronique de $[\text{Cu}(\text{bmet})]^{2+}$ déterminée à basse température. La comparaison entre les deux structures, expérimentales et calculées, montre que les changements structuraux observés lors du passage de la structure allongée au pseudo compressé peuvent être associés à une suppression de l'élongation Jahn-Teller plutôt qu'à une réelle compression. Ainsi cette étude a permis de caractériser le premier complexe synthétisé avec un ligand N6 présentant une rare compression Jahn-Teller dynamique.

Introduction

In 1937, Jahn and Teller used symmetry arguments to demonstrate that a non-linear system in a degenerate energy state cannot be stable. Therefore, it will spontaneously distort itself in some way so that its energy state will split to remove its degeneracy.¹ This is particularly common in transition metal centres, where the splitting of the d-energy levels in a ligand field can often lead to degenerate electron configurations.^{2,3} For example, in octahedral symmetry d^1 , d^2 , d^4 (both spin states), d^5 (low spin), d^6 (high spin), d^7 (both spin states) and d^9 all have orbital degenerate electron configurations that should be Jahn-Teller active.^{2,4} Ions with degenerate occupancy of the e_g subshell nearly always exhibit strong Jahn-Teller distortions, like six coordinate d^9 copper(II) ions.

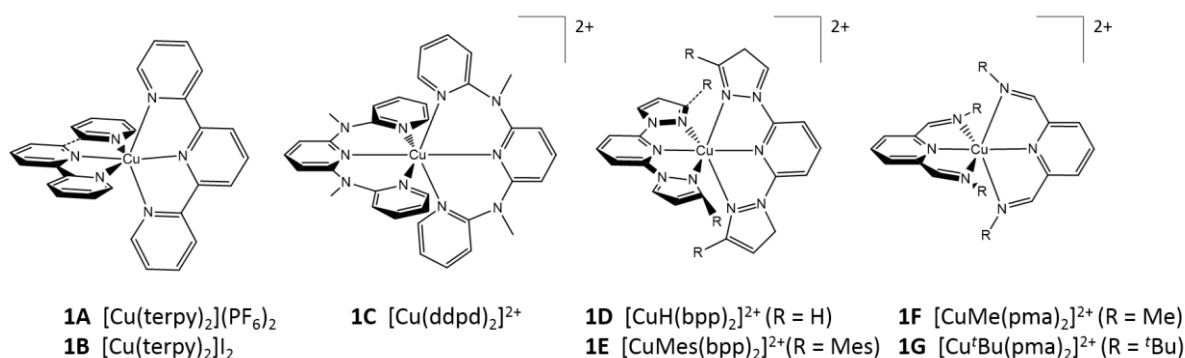


Scheme 6.1 Diagram showing the two possible Jahn-Teller splittings of the d -energy levels in an octahedral $[\text{CuL}_6]^{2+}$ complex, and the structural distortions that result from them.

Six-coordinate copper(II) compounds are the most common, and the most studied, molecular Jahn-Teller systems.⁵ This is because copper(II) compounds are user-friendly. They are commonly air- and moisture-stable, and have informative and easy to obtain electronic absorption and EPR spectroscopic signatures. The stereochemical flexibility of copper(II) compounds also means that they adopt a wider range of coordination geometries.⁶ Many of the attributes listed are consequences of the d^9 electron configuration. In octahedral copper(II) compounds, the Jahn-Teller theorem predicts that the degeneracy of the 2E_g ground state will be split, reflecting a concomitant elongation or compression of the Cu-ligand bonds parallel to one of the three molecular

axes (Scheme 6.1).⁷ While both distortions are possible, Jahn-Teller elongations are by far preferred due to the $4s-3d_z^2$ orbital mixing, which lowers the energy of $3d_z^2$ compared to $3d_{x^2-y^2}$.⁸ This additional stabilisation is greater in a Jahn-Teller elongated copper(II) ion, than in a Jahn-Teller compressed one.

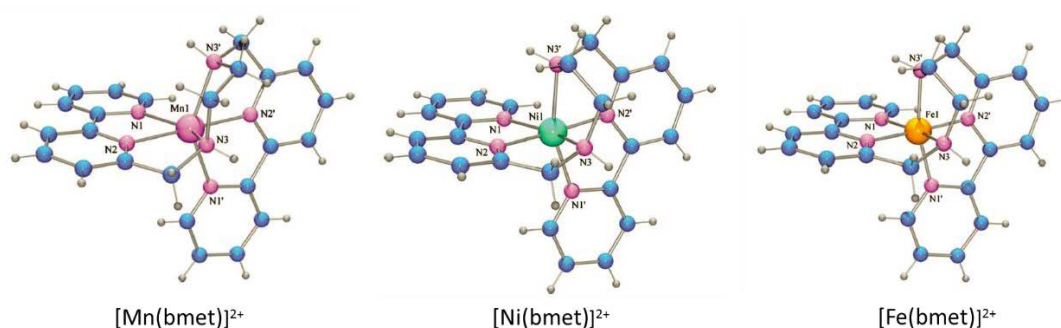
In principle, the detection of Jahn-Teller distortion in an octahedron is straightforward by looking at the metal-ligand distances. In the case of copper(II) centres, in general, the long and short Cu-ligand bond lengths differ by > 20%. EPR spectroscopy is also an appropriate tool to determine the nature of the Jahn-Teller distortion, because the distortion (elongation or compression) dictates the electronic ground state, with the unpaired electron occupying the $d_{x^2-y^2}$ or d_z^2 orbital, respectively (hereafter denoted $\{d_{x^2-y^2}\}^1$ and $\{d_z^2\}^1$ electronic configurations). These yield very different powder EPR spectra, whose lineshapes are diagnostic with respect to which d -orbital in the molecule is singly occupied. For a $\{d_{x^2-y^2}\}^1$ complex, a $g_1 > g_2 \geq g_3 > 2.00$ pattern is expected while a $\{d_z^2\}^1$ complex yields $g_1 \geq g_2 > g_3 \approx 2.00$.⁹⁻¹¹



Scheme 6.2. Structures of previously described Cu^{II} complexes that display dynamic (**1A-1D**, **1F**) or real (**1E-1G**) Jahn-Teller compressions.

To date in the literature, there are very few ‘true’ Jahn-Teller compressed copper(II) compounds. The majority of these are inorganic salts, KAlCuF₆ being the first to unambiguously demonstrate a tetragonal compressed molecular structure.^{12,13} To the best of our knowledge there are only two true Jahn-Teller compressed multidentate octahedral Cu^{II} complexes (Scheme 6.2, **1E-1G**), both being described by the group of Halcrow.^{14,15} Both complexes contain meridional tridentate ligands, that were synthesised as a part of a series of Cu^{II} complexes of varying bulkiness of the distal group on the ligand. They found that the addition of large steric groups is required to generate unambiguous Jahn-Teller compressed Cu^{II} centers.

Until recently it was thought that $[\text{Cu}(\text{terpy})_2]^{2+}$ and related complexes also displayed an axially compressed octahedral geometry. However, through variable temperature X-ray crystallography and EPR investigations, it has been shown that these compounds exhibit a 'dynamic' Jahn-Teller distortion (Scheme 6.2, **1A-1D**, **1F**).^{8,16-19} This reflects disorder of a Jahn-Teller axis over four of the Cu-ligand bonds, leading to EPR spectra with characteristic $\{d_{z^2}\}^1$ electronic configurations. As the temperature decreases, the Jahn-Teller becomes more localized in one of the two disordered orientations and gives rise to the typical spectrum of a $\{d_{x^2-y^2}\}^1$ Cu^{II} center. The $[\text{Cu}(\text{bpp})]^{2+14}$ and $[\text{Cu}(\text{pma})]^{2+15}$ complexes, which contain sterically non-bulky ligands, (Scheme 6.2, **1D-1F**) display this dynamic behavior.



Scheme 6.4. Previously described M^{II} complexes with the **bmet** ligand

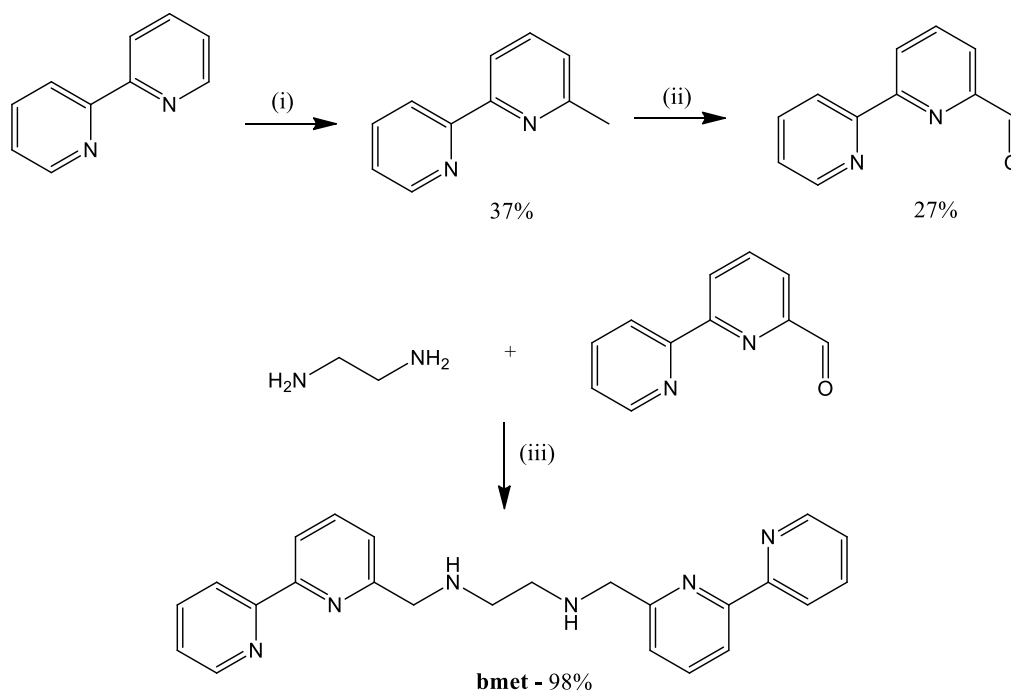
In this chapter, I will focus on work that was initiated during my MSc and pursued during my PhD. During my MSc, I synthesised novel N6 ligands in order to synthesise various mononuclear octahedral transition metal ion complexes, including Mn^{II} , Ni^{II} , and Fe^{II} complexes (Scheme 6.4).^{20,21} I will focus here on the characterisation of Cu^{II} complexes that have been carried out during my Ph.D. In particular, an in-depth multi-frequency EPR spectroscopy investigation has been performed at different temperatures together with DFT calculations, to rationalize the experimental results.

Results and Discussion

6.1 Ligand Synthesis

2,2'-bipyridine-6-carbaldehyde was prepared by acylation of 6-methyl-2,2'-bipyridine with SeO_2 . 6-methyl-2,2'-bipyridine was obtained from the reaction of 2,2'-bipyridine with MeLi. The **bmet** ligand was prepared by the method of Baird and co-workers (Scheme 6.5)²⁰ from the reductive amination of 2,2'-bipyridine-6-carboxaldehyde with

ethane-1,2-diamine, using NaBH_4 , and was isolated as the free base in excellent yield. It was characterised by elemental analysis, ESI-MS, and ^1H NMR spectroscopy.



Scheme 6.5. Synthesis of **bmet** (overall yield of 10%) (i) MeLi in Et_2O , Heat 90°C under Vacuum; (ii) SeO_2 , H_2O , refluxing for 30 h in Dioxane; (iii) Reflux for 30 min in MeOH, NaBH_4 .

Three metal complexes have been obtained, two copper(II) complexes with different counter anions $[\text{Cu}(\text{bmet})](\text{ClO}_4)_2$ and $[\text{Cu}(\text{bmet})](\text{Br})_2$ and a Zn derivative $[\text{Zn}(\text{bmet})](\text{ClO}_4)_2$, which is isomorphous to the $[\text{Cu}(\text{bmet})](\text{ClO}_4)_2$ complex. These complexes were prepared by reaction of the appropriate metal salt with the bmet ligand in a 1:1 mole ratio in MeCN under aerobic conditions. They were isolated as crystalline solids either on standing overnight or by slow evaporation of the solvent.

6.2 X-Ray Structure Investigations

$[\text{Cu}(\text{bmet})](\text{ClO}_4)_2 \cdot \text{H}_2\text{O}$

The structure of $[\text{Cu}(\text{bmet})](\text{ClO}_4)_2 \cdot \text{H}_2\text{O}$ in the solid state was established by X-ray diffraction using a single blue crystal obtained from the reaction solution upon standing. X-ray collection and refinement data are given in the Appendix, a summary of important bond lengths and angles is given in Table 6.1 and an ORTEP diagram of the Cu^{II} cation is given in Figure 6.1.

The $[\text{Cu}(\text{bmet})]^{2+}$ cation displays a distorted octahedral geometry with the ligand exhibiting an *mffm* configuration. The Cu^{II} ion is bound to all six nitrogen atoms of the bmet ligand, with bond distances ranging from 1.972(5) to 2.253(6) Å. The two Cu-

$N_{\text{aliphatic}}$ bond distances (Cu–N3, Cu–N4; 2.178(5), 2.253(6) Å) are longer than the four Cu – N_{aromatic} bond distances (Cu–N1, Cu–N2, Cu–N5 and Cu–N6; 2.130(5), 1.972(5), 2.015(4) and 2.235(4) Å). The Cu– $N_{\text{aliphatic}}$ bond distances are also considerably longer than the median $\text{Cu}^{\text{II}}\text{--}N_{\text{aliphatic}}$ literature value (2.022 Å), while the Cu– N_{aromatic} bond distances are consistent with the median $\text{Cu}^{\text{II}}\text{--}N_{\text{aromatic}}$ literature value (2.013 Å). In the crystal structure, the Cu–N distances along the N2–Cu–N5 axis are notably shorter than the other Cu–N distances, consistent with a compressed octahedral geometry.

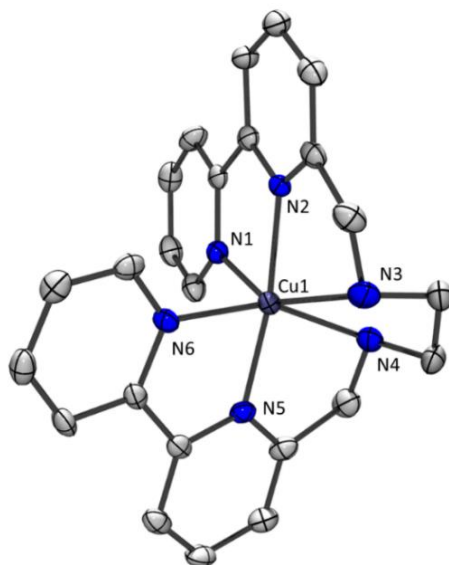
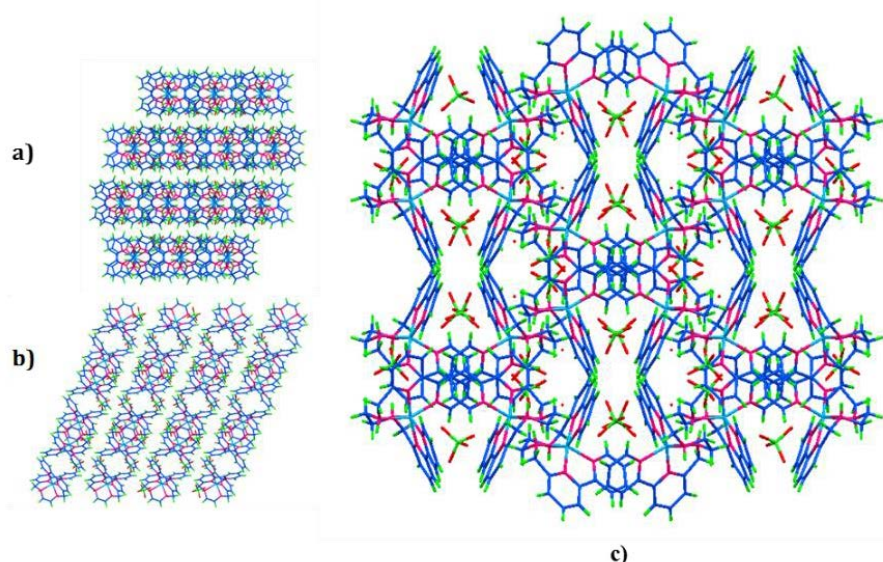


Figure 6.1 ORTEP diagram of the cation of $[\text{Cu}(\text{bmet})](\text{ClO}_4)_2 \cdot \text{H}_2\text{O}$. Perchlorate anions, the water molecule and hydrogen atoms have been omitted for clarity.

The three dimensional structure is composed of one dimensional chains down the **a**- and **b**- axes (Figure 6.2). The projection down the **c**-axis shows an encapsulation of the perchlorate anions. A medium strength hydrogen bond between the perchlorate oxygen atom (O7) and the amine hydrogen atom on N4 of the cation (O7 \cdots N4, 3.038 Å) is present. The perchlorate O8 oxygen atom also forms a medium strength H-bond to the amine hydrogen atom on N3 (O8 \cdots N3, 3.076 Å). A water molecule bridges two perchlorate anions, with O6 \cdots O9 = 2.933 Å and O9 \cdots O4 = 2.948 Å. All hydrogen-bonds seen in $[\text{Cu}(\text{bmet})](\text{ClO}_4)_2 \cdot \text{H}_2\text{O}$ are within the range of medium strength hydrogen-bond interactions (2.5 – 3.2 Å). The hydrogen-bond interactions and short contacts can be seen in Figure 6.3.

Table 6.1 Selected bond lengths and angles for [Cu(bmet)](ClO₄)₂·H₂O, [Cu(bmet)](Br)₂·2MeCN and [Zn(bmet)](ClO₄)₂·H₂O

	[Cu(bmet)](ClO ₄) ₂ ·H ₂ O	[Cu(bmet)](Br) ₂ ·2MeCN	[Zn(bmet)](ClO ₄) ₂ ·H ₂ O
Bond Lengths (Å)			
M – N1	2.130(5)	2.171(7)	2.201(3)
M – N2	1.972(5)	1.979(6)	2.082(3)
M – N3	2.178(5)	2.210(7)	2.206(3)
M – N4(N1')	2.253(6)	2.171(7)	2.186(3)
M – N5(N2')	2.015(4)	1.979(6)	2.086(3)
M – N6(N3')	2.235(4)	2.210 (7)	2.209(3)
Bond Angles (°)			
N1-M-N2	78.55(18)	77.9(2)	75.64(10)
N1-M-N3	154.77(18)	152.3(2)	150.40(11)
N1-M-N4(N1')	97.30(18)	101.6(3)	97.34(10)
N1-M-N5(N2')	96.48(17)	98.7(2)	96.63(10)
N1-M-N6(N3')	101.80(17)	94.8(2)	100.86(10)
N2-M-N3	78.78(19)	77.6(2)	76.99(10)
N2-M-N4(N1')	110.91(18)	98.7(2)	111.50(10)
N2-M-N5(N2')	171.28(18)	174.7(4)	169.25(10)
N2-M-N6(N3')	97.48(17)	106.6(2)	98.81(10)
N3-M-N4(N1')	80.6(2)	94.8(2)	82.38(11)
N3-M-N5(N2')	107.34(18)	106.6(2)	111.89(10)
N3-M-N6(N3')	92.00(18)	80.1(3)	94.23(10)
N4(N1')-M-N5(N2')	76.65(18)	152.3(2)	76.54(10)
N4(N1')-M-N6(N3')	148.41(17)	77.9(2)	147.69(10)
N5(N2')-M-N6(N3')	76.38(18)	77.6(2)	75.04(10)

**Figure 6.2** Packing diagrams of [Cu(bmet)](ClO₄)₂·H₂O viewed down the a-, b-, and c-axes.

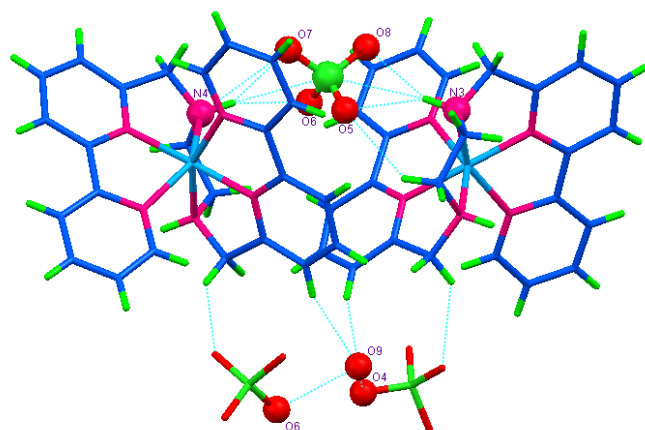


Figure 6.3 Hydrogen bonds in $[\text{Cu}(\text{bmet})](\text{ClO}_4)_2 \cdot \text{H}_2\text{O}$.

$[\text{Cu}(\text{bmet})](\text{Br})_2 \cdot 2\text{MeCN}$

Deep green crystals of $[\text{Cu}(\text{bmet})](\text{Br})_2 \cdot 2\text{MeCN}$ suitable for X-ray analysis were obtained by slow evaporation of an acetonitrile solution of the complex. An ORTEP diagram of the cation, X-ray collection and refinement data are given in the Appendix, while a summary of important bond lengths and angles is given in Table 6.1.

The structure consists of a $[\text{Cu}(\text{bmet})]^{2+}$ cation, two Br^- anions and two MeCN solvent molecules. The coordination environment around the Cu^{II} centre is essentially identical to that of $[\text{Cu}(\text{bmet})](\text{ClO}_4)_2 \cdot \text{H}_2\text{O}$, with bond distances ranging from 1.979(6) to 2.210(7) Å. The $\text{Cu}-\text{N}_{\text{aliphatic}}$ bond distances ($\text{Cu}-\text{N3}$, $\text{N3}'$; 2.210(7) Å) are longer than the $\text{Cu}-\text{N}_{\text{aromatic}}$ bond distances ($\text{Cu}-\text{N1}$, $\text{N1}'$ and $\text{Cu}-\text{N2}$, $\text{N2}'$; 2.171(7) and 1.979(6) Å, respectively).

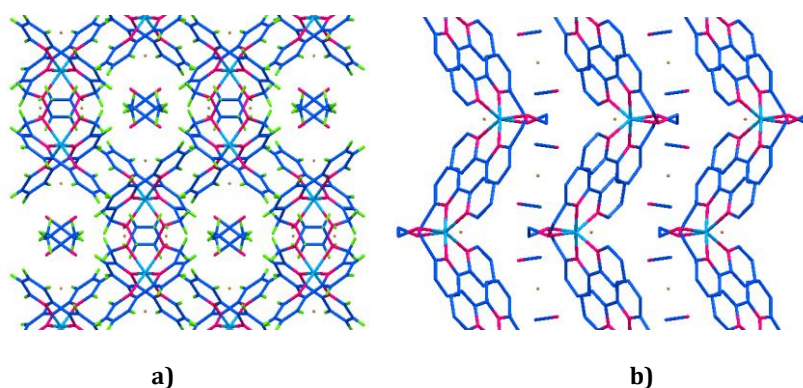


Figure 6.4 Packing diagrams of $[\text{Cu}(\text{bmet})](\text{Br})_2 \cdot 2\text{MeCN}$ viewed down **a)** the *b* axis and **b)** the *c* axis. Hydrogen atoms in **b)** have been removed for clarity.

On the other hand, the packing environment of $[\text{Cu}(\text{bmet})](\text{Br})_2 \cdot 2\text{MeCN}$ (Figure 6.4) is notably different than that of $[\text{Cu}(\text{bmet})](\text{ClO}_4)_2 \cdot \text{H}_2\text{O}$. The three-dimensional structure is

composed of one-dimensional ribbons (Figure 6.4b). These ribbons create channels occupied by the MeCN molecules and Br⁻ ions. Figure 6.5 shows that Br⁻ anions are also involved in weak hydrogen-bonds with the amine hydrogen atoms. The bromide anion is centered between two N3 atoms on adjacent cations. The N(H)⋯Br distance is 3.352(9) Å, consistent with literature values for weak hydrogen-bonds (>3.2 Å) and shorter than other reported N(H)⋯Br hydrogen bonds which range from 3.5 to 3.8 Å.²²

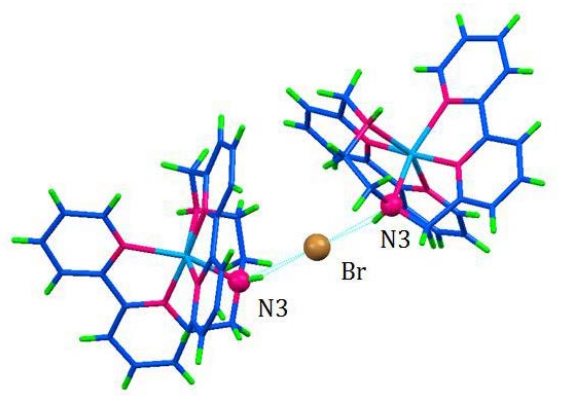


Figure 6.5 N(H)⋯Br hydrogen bonds projected along the c axis of the unit cell.

[Zn(bmet)](ClO₄)₂·H₂O

The structure of [Zn(bmet)](ClO₄)₂·H₂O has also been established by X-ray diffraction. A single colourless block crystal was obtained from the slow evaporation of a MeCN solution of the complex.

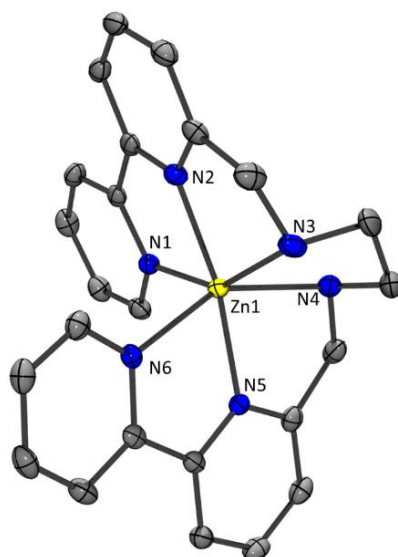


Figure 6.6 ORTEP diagram of the cation of [Zn(bmet)](ClO₄)₂·H₂O. Perchlorate anions, the water molecule and hydrogen atoms have been omitted for clarity.

X-ray collection and refinement data are given in the Appendix along with diagrams of the packing environment. A summary of important bond lengths and angles is presented in Table 6.1 and an ORTEP diagram of the cation is given in Figure 6.6. The crystal structure of $[\text{Zn}(\text{bmet})](\text{ClO}_4)_2 \cdot \text{H}_2\text{O}$ is isomorphous to the crystal structure of $[\text{Cu}(\text{bmet})](\text{ClO}_4)_2 \cdot \text{H}_2\text{O}$, implying a similar coordination sphere and the same packing environment.

The $[\text{Zn}(\text{bmet})]^{2+}$ cation displays a distorted octahedral geometry, with the ligand exhibiting an *mffm* configuration. The Zn^{II} ion coordinates to all six nitrogen atoms of the bmet ligand, with bond distances ranging from 2.082(3) to 2.209(3) Å. The aliphatic bond distances (Zn–N3; N4, 2.206(3), 2.186(3) Å, respectively) and the two terminal bond distances Zn–N1; N6 (2.201(3), 2.209(3) Å, respectively) are significantly greater than the median literature value for Zn–N_{aliphatic} bond distances (2.143 Å) and Zn–N_{aromatic} bond distances (2.119 Å) respectively, while the axial Zn–N2; N5 (2.082(3), 2.086(3) Å, respectively) bond distances are relatively similar to the literature value. As also found in the Cu^{II} cations, a compressed octahedral geometry obtains, with the two Zn–N bonds along the N2–Zn1–N5 axis being apparently shorter than the other four. As Zn^{II} is a d^{10} ion, the origin of the compression can only be explained by the constraints imposed by the six-coordinate bmet ligand.

TLS (Translation/Libration/Screw) Analysis

Closer inspection of the copper structures reveals a possible masked disorder of an elongated Jahn-Teller axis in both cases. TLS analysis of both structures using PLATON²³ gave evidence for significant librational effects along Cu1–N3, Cu1–N4 and Cu1–N6 in the perchlorate salt, and Cu1–N3 and Cu1–N3' in the bromide salt at 90 K. These observations are consistent with a disorder of the Jahn-Teller axis that is not immediately apparent from the ORTEP diagrams of the cations. The X-ray structure of the $[\text{Zn}(\text{bmet})]^{2+}$ cation displays no such librational effects.

DFT-optimized structure

In order to obtain further information on the role of the bmet ligand in obtaining a compressed octahedral geometry around the Cu^{II} metal centre, DFT calculations have been performed. Our objective was to determine whether or not an Jahn-Teller elongated distortion could be afforded in a Cu^{II} complex of the bmet ligand. The DFT optimized structure of the Cu^{II} bmet complex was initiated from both X-ray crystal structures.

The two resulting structures were identical and are denoted **Cu(bmet)***. The optimized geometry of **Cu(bmet)*** is displayed in Figure 6.7 (Structure **A**), together with the X-ray crystal structure of the $[\text{Cu}(\text{bmet})]^{2+}$ cation in $[\text{Cu}(\text{bmet})](\text{ClO}_4)_2 \cdot \text{H}_2\text{O}$ (Structure **B**). Interestingly, we observed that in the resulting octahedral structure **A** there are two long Cu-N distances along the N4-Cu-N6 axis (4.525 Å) and four short Cu-N distances along the N1-Cu-N3 and N2-Cu-N5 axes (4.225 Å and 4.015 Å, respectively), resulting in an apparent elongated structure. This suggests that a Jahn-Teller elongation can indeed occur around the Cu^{II} ion on coordination to the bmet ligand.

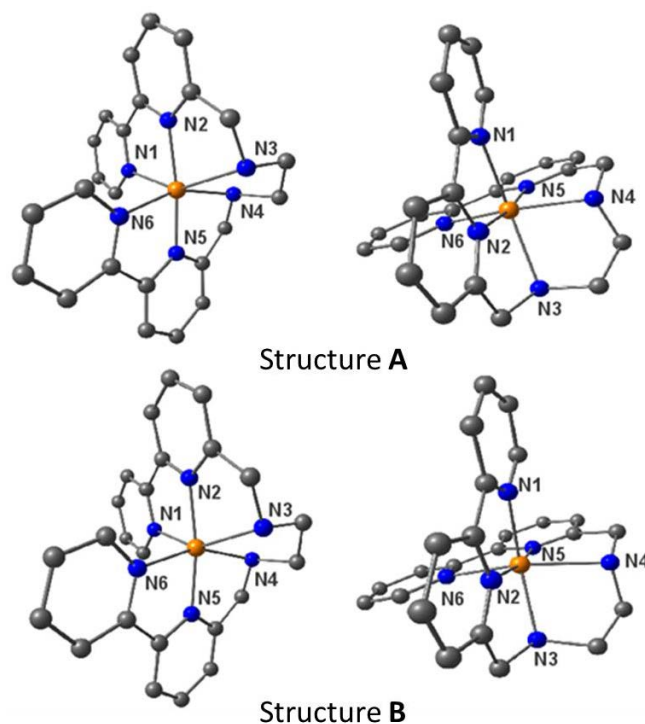


Figure 6.7. Depiction of the molecular structure of $[\text{Cu}(\text{bmet})]^{2+}$ obtained from the DFT-optimization procedure (structure **A**) and from the X-ray data (structure **B**). View along the N2-Cu-N5 (*z*) axis (left) and view along the N4-Cu-N6 (*y*) axis (right).

The calculated **Cu(bmet)*** structure displays six different Cu-N bond distances (Table 2), as also found in the X-ray structure of $[\text{Cu}(\text{bmet})](\text{ClO}_4)_2 \cdot \text{H}_2\text{O}$. Agreement between the observed and calculated Cu-N bond distances is good, with a maximum difference around 0.05 Å. The isomerisation between the two structures has mainly involved changes in the distances of the Cu-N bonds along the N1-Cu-N3 axis (from 4.308 Å to 4.225 Å for the DFT optimized structure). This compression is accompanied by an elongation of the Cu-N bonds along the N4-Cu-N6 axis (from 4.488 Å to 4.525 Å for the DFT optimized structure). No remarkable variations are observed along the N2-Cu-N5 “compressed” tetragonal axis observed in the X-ray structure (exp: 3.987 Å vs calc: 4.015 Å).

Table 6.2. Principal Cu-N bond distances and N-Cu-N axis lengths (Å) in [Cu(bmet)](ClO₄)₂·H₂O and Cu(bmet)*.

	[Cu(bmet)](ClO ₄) ₂ ·H ₂ O (structure B)	Cu(bmet)* (structure A)
Cu-N1	2.130(5)	2.096
Cu-N2	1.972(5)	1.962
Cu-N3	2.178(5)	2.129
Cu-N4	2.253(6)	2.237
Cu-N5	2.015(4)	2.053
Cu-N6	2.235(4)	2.288
N4-Cu- N6 ^a	4.488	4.525^b
N1-Cu- N3 ^a	4.308	4.225
N2-Cu- N5 ^a	3.987^b	4.015

^asum of the two bond lengths ^bthe tetragonal distorted axis

The combined X-ray and computational structures do not provide an unequivocal explanation of the way in which the Jahn Teller effect influences the electronic structure of the copper(II) complexes. To further investigate this, an EPR investigation has been carried out.

6.3 EPR Investigations

Solid State EPR

As stated in the introduction, EPR spectroscopy is a good technique to further investigate the electronic properties of octahedral Cu^{II} ion. In a Jahn-Teller system, the nature of the tetragonal distortion is related to the electronic ground state. Therefore, a $\{d_{x^2-y^2}\}^1$ electronic configuration is associated with structure **A** (DFT-optimised), while a $\{d_{z^2}\}^1$ electronic configuration is associated with structure **B** (X-ray structure, Figure 6.7). These yield very different powder EPR spectra; for a $\{d_{x^2-y^2}\}^1$ ground state complex, a $g_1 > g_2 \geq g_3 > 2.00$ pattern is expected, while a $\{d_{z^2}\}^1$ ground state complex yields a $g_1 \geq g_2 > g_3 \approx 2.00$ pattern.⁹⁻¹¹

Both [Cu(bmet)](ClO₄)₂·H₂O and [Cu(bmet)]Br₂·2MeCN exhibit the same powder EPR spectra, implying no influence from the counter anion. This is consistent with the fact that both structures exhibit a similar coordination sphere around the Cu^{II} ion. Therefore, the rest of the EPR investigation was carried out using only [Cu(bmet)](ClO₄)₂·H₂O. The X-band EPR powder spectra of [Cu(bmet)](ClO₄)₂·H₂O were recorded between 5 K and 298 K. They all display similar isotropic signals, whose intensity increases as the temperature decreases, following a Curie law behaviour expected for an S = ½ system (Figure 6.8).

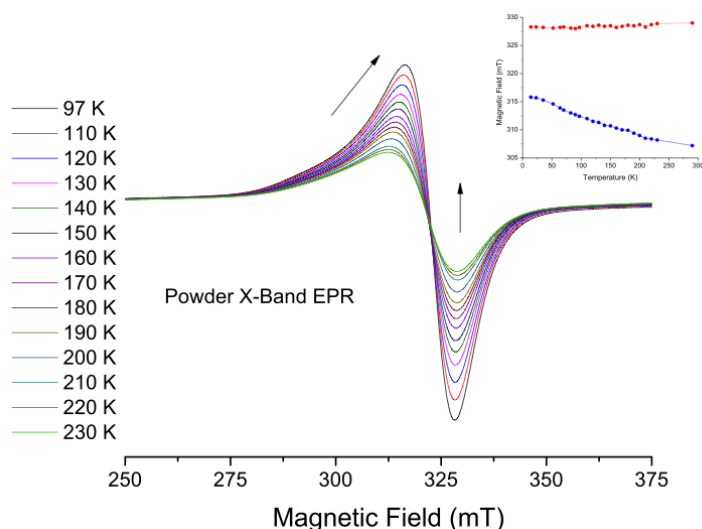


Figure 6.8. Powder X-Band EPR spectra of $[\text{Cu}(\text{bmet})](\text{ClO}_4)_2 \cdot \text{H}_2\text{O}$ recorded between 97 K and 230 K. Inset: field position of the top and bottom of the transition between 5 K and 298 K.

On careful examination of the spectra, we observed that the temperature does not affect the field position of the minimum of the EPR transition. However, this is not the case for its maximum, which is slightly shifted to higher fields when the temperature decreases (inset of Figure 6.8). This suggests that a dynamic process maybe occurring in this copper system. However, due to the lack of resolution of the EPR spectra, no conclusion can be made. Consequently, we have carried out experiments at a higher frequency (Q-band).

Powder Q-band EPR spectra have been recorded at different temperatures (between 15 K and 200 K, and at 298 K). Unfortunately, a complete range of temperatures between room temperature and 15 K has not been performed because the Q-band set up is only functional with helium or at ambient temperature.

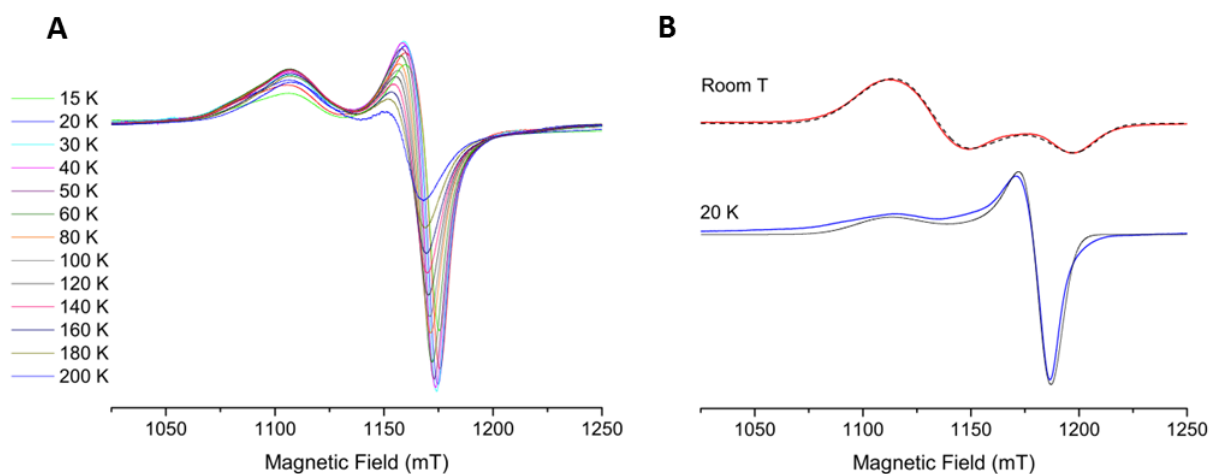


Figure 6.9. Experimental powder Q-band EPR spectra of $[\text{Cu}(\text{bmet})](\text{ClO}_4)_2 \cdot \text{H}_2\text{O}$ **A)** between 15 K and 200 K and **B)** at room temperature (red) and 20 K (blue).

As expected, at this frequency, the g -anisotropy can be resolved. Two features are obvious in the experimental spectra (Figure 6.9), and the three precise g -values of the \mathbf{g} -tensor can be obtained by simulation (Table 6.3). At temperatures below 200 K, the EPR spectrum of $[\text{Cu}(\text{bmet})](\text{ClO}_4)_2 \cdot \text{H}_2\text{O}$ displays a quasi axial signal, consistent with a $\{d_{x^2-y^2}\}^1$ electronic configuration for the Cu^{II} centre (Figure 6.9A). The notable broadening of the low field transition could originate from unresolved hyperfine coupling to the Cu^{II} ion. At 298 K, the Q-band EPR spectrum is significantly different to that at low-temperature (Figure 6.9B). A quasi axial signal is still observed, but it is now consistent with a $\{d_{z^2}\}^1$ electronic configuration (Table 6.3). From Figure 6.9B, it clearly appears that the EPR spectrum is temperature dependent and that a transition occurs between the two electronic configurations. In addition, Figure 6.9A shows that this transition from a static system at low temperature to a dynamic system at ambient temperature is continuous. Consequently, it can be concluded that no weak cooperative effects occur during the process, as in other previously described complexes (Scheme 6.1 and 6.6, **1A-1D**, **1F**).

In order to obtain higher resolution of the g -tensor at X-band frequency, $[\text{Cu}(\text{bmet})]^{2+}$ was doped into the diamagnetic isomorphous zinc(II) complex giving the magnetically diluted $[\text{Zn}_{100-x}\text{Cu}_x(\text{bmet})](\text{ClO}_4)_2$ (with $x = 5\%$, from elemental analysis) (**Zn(Cu)(bmet)**). The magnetic dilution should diminish intermolecular dipole dipole interactions resulting in spectra with higher resolution, in which even the hyperfine couplings should be observed. As expected, the resulting powder X-band EPR spectra of **Zn(Cu)(bmet)** displays well resolved axial signals with resolved hyperfine coupling in the g_1 component (Figure 6.10). However, the shape of the spectra recorded at all temperatures from room temperature down to 15 K is similar, consistent with a pseudo-Jahn-Teller elongated copper(II) centre (structure **A**), in agreement with a $\{d_{x^2-y^2}\}^1$ electronic configuration.

The EPR parameters (Table 6.3) of **Zn(Cu)(bmet)** are slightly different than those obtained from the powder Q-band spectra of $[\text{Cu}(\text{bmet})]^{2+}$ recorded at low temperature. It appears that the doping of $[\text{Cu}(\text{bmet})]^{2+}$ in the isomorphous $[\text{Zn}(\text{bmet})](\text{ClO}_4)_2$ host lattice, has a notable effect on its electronic structure as the signature of structure **B** is no longer observed even at room temperature. This result differs from what has been previously reported with the $[\text{Cu}(\text{terpy})_2]^{2+}$ and $[\text{Cu}(\text{ddpd})_2]^{2+}$ complexes, for which the electronic structure was not affected when doped in a diamagnetic isomorphous iron(II)

or zinc(II) host lattice.^{19,24} However, in the case of the $[\text{Cu}(\text{bpp})_2]^{2+}$ complex, while it exhibits a $\{d_{x^2-y^2}\}^1$ ground state as a pure compound, a change to $\{d_z^2\}^1$ is observed when doped into a host lattice.²⁴

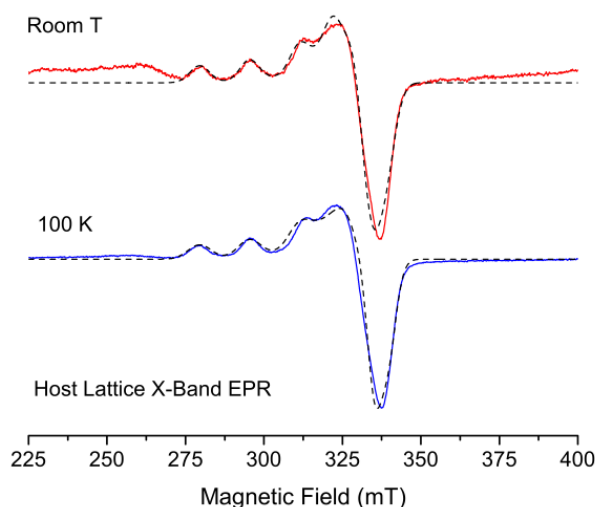


Figure 6.10. Experimental (straight line) and simulated (dashed line) powder X-band EPR spectra recorded on $[\text{Zn}(\text{Cu})(\text{bmet})]^{2+}$ at room temperature (red) and 100 K (blue).

Solution EPR

Another possible way of obtaining well-resolved EPR spectra is to record them in solution. An MeCN solution of $[\text{Cu}(\text{bmet})](\text{ClO}_4)_2 \cdot \text{H}_2\text{O}$ exhibits a steady change of the X-band EPR spectra as a function of temperature. A shift in g -values occurs, consistent with a dynamic system that evolves from a preferentially $\{d_{x^2-y^2}\}^1$ electronic ground state at low temperature to a $\{d_z^2\}^1$ electronic configuration as the temperature is increased (Figure 6.11 and Table 6.3).

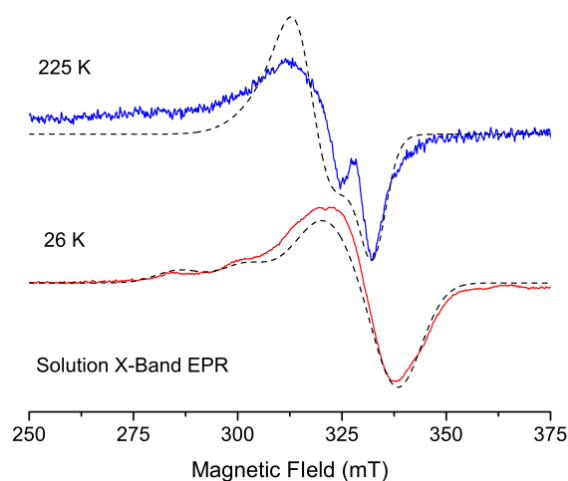


Figure 6.11. Experimental (straight line) and simulated (dashed line) X-band EPR spectra recorded on an MeCN solution of $[\text{Cu}(\text{bmet})]^{2+}$ at 26 K (red) and 225 K (blue).

The low-quality resolution of the spectra, which is a result of the very low solution concentrations required to observe the hyperfine coupling interactions, precludes a precise quantitative analysis. These low concentrations, coupled with the lower sensitivity of the EPR spectrometer at the Q-band frequency, meant that no Q-band EPR signal could be observed.

DFT Calculations

The single occupied molecular orbitals (SOMOs) of structures **A** and **B** have been calculated and are displayed in Figure 6.12. They are consistent with the EPR data: the SOMO calculated for the DFT-optimized structure (structure **A**) features a $3d_{x^2-y^2}$ metal character (68% of copper contribution) while the SOMO corresponding to the X-ray structure (structure **B**) features a $3d_{z^2}$ metal character (69 % of copper character).

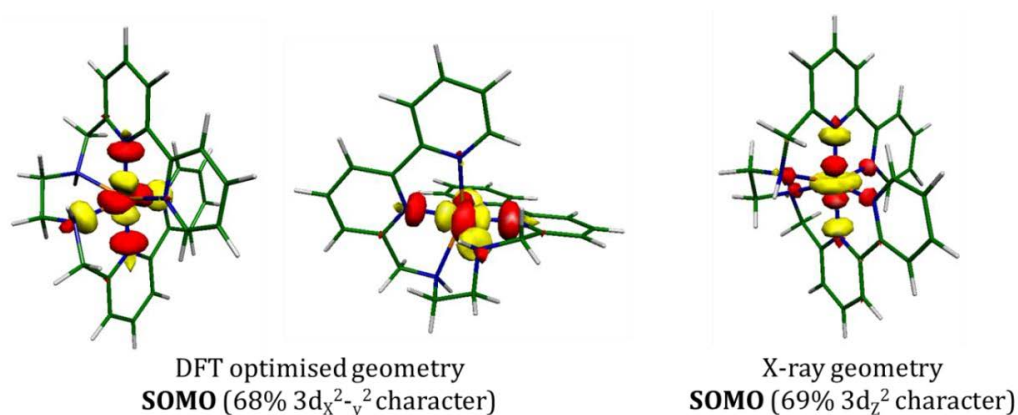
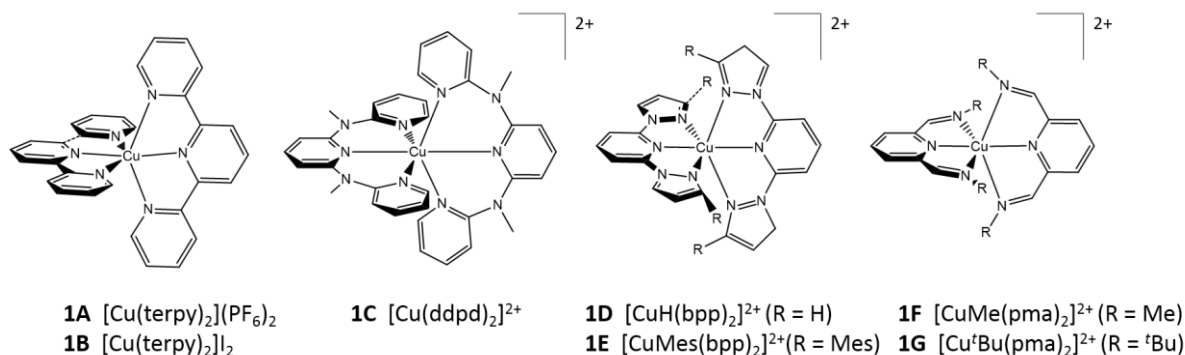


Figure 6.12. DFT calculated SOMOs of structures **A** and **B**.

The EPR parameters have also been predicted by DFT calculations on both the optimized **Cu(bmet)*** and experimental $[\text{Cu}(\text{bmet})](\text{ClO}_4)_2 \cdot \text{H}_2\text{O}$ structures (Table 6.3). The calculated values are in good agreement with the experimental data. Indeed, the calculated values obtained from structure **A** nicely reproduce the experimental g - and A_1 -values determined from both the powder and solution spectra of $[\text{Cu}(\text{bmet})](\text{ClO}_4)_2 \cdot \text{H}_2\text{O}$ at low temperature as well as those of **Zn(Cu)(bmet)**. Conversely, the parameters calculated from structure **B** reproduce the EPR data obtained from the powder and solution spectra of $[\text{Cu}(\text{bmet})](\text{ClO}_4)_2 \cdot \text{H}_2\text{O}$ recorded at room temperature. These calculations confirm the electronic structure and the nature of the Jahn-Teller distortion in both structures **A** and **B**.



Scheme 6.6. Structures of previously described Cu^{II} complexes that display dynamic (**1A-1D**, **1F**) or real (**1E-1G**) Jahn-Teller compressions.

Table 6.3. EPR parameters obtained in this work together with those determined for relevant previously reported Cu^{II} complexes (Scheme 1).

	Ground State	Phase	<i>T</i> /K	<i>g</i> ₁	<i>g</i> ₂	<i>g</i> ₃	<i>A</i> ₁	<i>A</i> ₂	<i>A</i> ₃	Ref.
Exp. [Cu(bmet)] ²⁺	{ <i>d</i> _z ² } ¹	Powder	298	2.030	2.145	2.196				this work
	{ <i>d</i> _{x²-y²}} ¹		30	2.054	2.058	2.193				
	{ <i>d</i> _z ² } ¹	MeCN	225	2.035	2.135	2.170				this work
	{ <i>d</i> _{x²-y²}} ¹		26	2.034	2.081	2.195	480			
Calc. [Cu(bmet)] ²⁺	{ <i>d</i> _z ² } ¹			2.015	2.123	2.176	-562			this work
	{ <i>d</i> _{x²-y²}} ¹			2.039	2.084	2.180	-450			
[Zn(Cu)(bmet)] ²⁺	{ <i>d</i> _{x²-y²}} ¹	Powder	298	2.020	2.086	2.227	485			this work
	{ <i>d</i> _{x²-y²}} ¹		100	2.020	2.086	2.227	485			
[Cu(terpy)](PF ₆) ₂ 1A	{ <i>d</i> _z ² } ¹	Powder	298	2.191	2.191	2.023				8
			77	2.230	2.160	2.020				
	{ <i>d</i> _{x²-y²}} ¹		4	2.256	2.123	2.020				
[Cu(ddpd)] ²⁺ 1C	{ <i>d</i> _z ² } ¹	Powder	293	2.150	2.150	2.066	82	82		19
	{ <i>d</i> _{x²-y²}} ¹		103	2.228	2.054	2.054	145			
[CuH(bpp)] ²⁺ 1D	{ <i>d</i> _z ² } ¹	Powder	290	2.195	2.195	2.045				14
			120	2.228	2.160	2.040				
	{ <i>d</i> _{x²-y²}} ¹		5	2.32	2.093	2.042	200	-	-	
[CuMes(bpp)] ²⁺ 1E	{ <i>d</i> _z ² } ¹	Powder	290	2.237	2.157	2.017	104	-	94	14
			115	2.248	2.145	2.015	110	-	94	
			115	2.200	2.200	2.007	77	77	97	
[Cu ^t Bu(pma)] ²⁺ 1G	{ <i>d</i> _z ² } ¹	Powder	292	2.231	2.202	2.005	-	-	155	15
			110	2.231	2.202	2.000	-	-	155	
			10	2.219	2.219	1.998	-	-	161	
			110	2.220	2.215	2.001	-	-	165	

Table 6.4. Relevant structural data for [Cu(bmet)]Br₂·2MeCN, [Cu(bmet)](ClO₄)₂·H₂O, [Zn(bmet)](ClO₄)₂·H₂O, the DFT-optimized **Cu(bmet)*** structure, and related compounds displayed in Scheme 1.

Compounds	<i>T</i> , K	<i>a</i> _{equatorial} Å ^{<i>a</i>}		<i>a</i> _{axial} Å ^{<i>a,b</i>}	Δ_{e-a} , Å ^{<i>c</i>}	Ref.
[Cu(bmet)]Br ₂ ·2MeCN	89	2.191	2.191	1.979	0.21	this work
[Cu(bmet)](ClO ₄) ₂ ·H ₂ O	89	2.207	2.192	1.994	0.21	this work
Cu(bmet)*		2.113	2.008	2.263	-0.20	this work
[Zn(bmet)](ClO ₄) ₂ ·H ₂ O	89	2.204	2.197	2.084	0.11	this work
[Cu(terpy)](PF ₆) ₂ 1A	298	2.179	2.179	1.977	0.20	8
	4	1.980	2.100	2.260	-0.20	
[Cu(terpy)]I ₂ 1B	4	2.083	2.083	1.912	0.17	8
[Cu(ddpd)] ₂ ²⁺ 1C	263	2.191	2.149	2.021	0.15	19
	100	2.026	2.025	2.332	-0.31	
[CuH(bpp)] ₂ ²⁺ 1D	300	2.208	2.158	1.991	0.19	14
	31	1.998	2.066	2.286	-0.25	
[CuMes(bpp)] ₂ ²⁺ 1E	180	2.139	2.242	1.960	0.23	14
[Cu ^t Bu(pma)] ₂ ²⁺ 1G	150	2.385	2.300	1.945	0.40	15

^{*a*} *a* is the average axis distances, ^{*b*} the axial axis corresponds to the axis, which displays the tetragonal Jahn Teller distortion observed in the X-ray structures ^{*c*} $\Delta_{e-a} = (\sum a_{\text{equatorial}}/2) - a_{\text{axial}}$

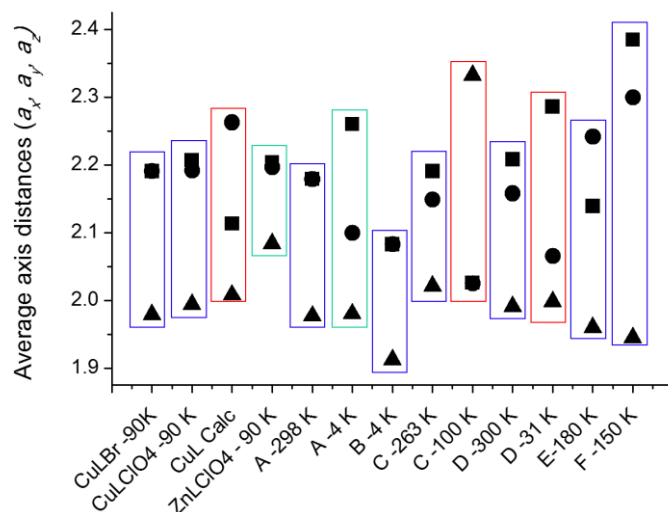


Figure 6.13. Graph of the more relevant Cu^{II} complexes with the average axis length (*a_x* = square, *a_y* = circle, *a_z* = triangle) illustrating the Jahn-Teller distortion (compression = blue, neutral = green, elongation = red).

6.4 Comparison with Literature

Table 6.4 and Figure 6.13 gives relevant structural data for compressed octahedral Cu^{II} complexes, which have been previously described in the literature (Scheme 6.2 and 6.6). [Cu(bmet)]²⁺ represents the first complex containing a relatively rigid hexadentate ligand, which can only adopt one configuration around the copper centre, that displays a dynamic Jahn-Teller distortion. The *mffm* configuration is similar to that given by two

meridional tridentate ligands. The constraints associated with the ligand contribute to particularly short M–N bonds involving the mutually *trans* pyridine rings along the tetragonal axis (*z*-axis). Such short M–N bonds have been observed previously in Co^{III},²⁰ Mn^{II}, Fe^{II} and Ni^{II} complexes containing the bmet ligand,²¹ and are also present in the *d*¹⁰ [Zn(bmet)]²⁺ complex.

The extent of the tetragonal distortion can be seen by the Δ_{e-a} parameter (Table 6.4). Using this, a value of zero corresponds to no distortion, a negative result shows an axially elongated system, and the more positive the result, the more axially compressed the complex. The positive tetragonal distortion ($\Delta_{e-a} = 0.11 \text{ \AA}$) found in [Zn(bmet)]²⁺ is consistent with a compressed octahedron, but it must originate solely from the steric constraints imposed by the ligand itself because no electronic factors will be important in this *d*¹⁰ system. Therefore, in both [Cu(bmet)]²⁺ complexes, the larger Δ_{e-a} values (0.21 \AA for the Cu vs 0.11 \AA for the Zn) are indicative of the additional Jahn-Teller electronic effect.

There are very few Jahn-Teller compressed Cu^{II} compounds. More common are those which exhibit dynamic Jahn-Teller distortions (scheme 6.6 **1A-1D**),^{8,14,19} meaning that at room temperature a Jahn-Teller compression is observed, while an elongation is present as the temperature decreases. Rarer are those, which exhibit a real Jahn-Teller compression (scheme 6.6 **1E-1G**),^{14,15} meaning that their structural properties are independent of temperature. In complexes **1A**,⁸ **1C**¹⁹ and **1D**,¹⁴ the tetragonal compression is located along the *z*-axis at high temperature, while at low temperature the tetragonal elongation arises along either the same axis (complex **1C**), or along the *x*-axis (complexes **1A** and **1D**). In the case of [Cu(bmet)](ClO₄)₂·H₂O, a change in the tetragonal axis is also observed, from the *z*-axis in the X-ray structure (structure **B** with a compressed tetragonal axis) to the *y*-axis in the DFT-optimized structure (structure **A** with an elongated tetragonal axis).

It can also be noticed when comparing the structural data of [Cu(bmet)](ClO₄)₂·H₂O and [Cu(bmet)]Br₂·2MeCN with those of literature, that the tetragonal distortion ($\Delta_{e-a} = 0.21 \text{ \AA}$ for both the Br⁻ and ClO₄⁻ derivatives) is relatively pronounced for a dynamic system (highest value for the terpy complex with $\Delta_{e-a} = 0.20 \text{ \AA}$).⁸ This can be explained by the constraints imposed by the hexadentate bmet ligand and, more importantly, by its structure leading to two axes, in which the nature of the ligands is different, *i.e.* a pyridine (N1 and N6) *trans* to an amine (N4 and N3, respectively). On the other hand, in

the other mononuclear Cu^{II} complexes displaying a compressed tetragonal Jahn-Teller distortion, the symmetric tridentate ligands that have been used, result in octahedra in which the donor atom is identical along each of the three axes.

The best tool to unambiguously determine the nature of a Jahn-Teller distortion in an octahedral mononuclear Cu^{II} complex is EPR spectroscopy because it is directly related to the electronic ground state of the metal ion. From Table 6.3, the nature of the Jahn-Teller compression can be fully elucidated. As suggested from the structural data of complexes **1A**,⁸ **1C**,¹⁹ and **1D**,¹⁴ these complexes display a dynamic Jahn-Teller distortion. At room temperature a $\{d_z^2\}^1$ ground state is observed, while a $\{d_{x^2-y^2}\}^1$ ground state occurs at low temperature. Similar behaviour is seen for [Cu(bmet)](ClO₄)₂·H₂O. On the other hand, a real Jahn-Teller compression is seen in the case of complexes **1E**¹⁴ and **1G**.¹⁵ Indeed their EPR spectra at all recorded temperatures are characteristic of a $\{d_z^2\}^1$ ground state.

This study has also shown that the electronic structure of [Cu(bmet)]²⁺ is different in different phases of matter. As an amorphous powder, the electronic configuration changes with temperature from $\{d_z^2\}^1$ to $\{d_{x^2-y^2}\}^1$ corresponding to a dynamic compressed structure. This interpretation is supported by the crystal structure recorded at 100 K displaying a compressed octahedral geometry while the DFT optimized structure, which corresponds to a low temperature structure, is consistent with an elongated structure. In solution, a similar behaviour is observed but the resolution of the EPR spectra precluded an in-depth analysis of the data. More interestingly, when [Cu(bmet)](ClO₄)₂·H₂O was doped into the isomorphous diamagnetic Zn^{II} complex, the dynamic process is completely removed. As stated above, structure **B** (Jahn-Teller compression) has only been observed in a few compounds with tridentate ligands in a D_{2d} symmetry, in *trans*-[Cu(X)_{4/2}(Y)₂] complexes^{25,26} or [Cu(OH/D₂)₆]²⁺.^{27,28} It has been shown that several factors can lead to this unusual structure: steric hindrance, ligand conformational strain or the basicity of the ligand donor atoms.^{15,29} However in the case of [Cu(bmet)]²⁺, the environment of the copper(II) center in the Zn host appears to prevent the dynamic process occurring. This certainly originates from the constraints associated with the particular structure of this N₆ ligand.

As stated in the introduction, there are very few Jahn-Teller compressed Cu^{II} compounds. More common are those which exhibit 'dynamic' Jahn-Teller distortions,

meaning that at room temperature a Jahn-Teller compression is observed, while an elongation is present as the temperature decreases. Rarer are those which exhibit a 'true' Jahn-Teller compression, meaning that their structural properties are independent from the temperature.

Conclusion

In this work, we report on two mononuclear octahedral Cu^{II} complexes that have been synthesized with an N6 hexadentate ligand. The unique difference in these two compounds is the nature of the counter anion. However even if the packing environment determined from X-ray diffraction is different, their structural and electronic properties are similar.

This study has shown that the electronic structure of [Cu(bmet)]²⁺ is different in different phases of matter. As an amorphous powder, the compound exhibits an EPR spectrum with *g*-values that are consistent with a {*d_z²*}¹ ground state at 298 K. However, this spectrum changes consistently and significantly upon cooling, indicating that the electronic configuration changes with temperature from {*d_z²*}¹ to {*d_x²-y²*}¹ corresponding to a dynamic compressed structure. This interpretation is supported by the crystal structure recorded at 100 K displaying a compressed octahedral geometry while the DFT optimized structure, which corresponds to a low temperature structure, is consistent with an elongated structure.

In solution, a similar behavior is observed but the resolution of the EPR spectra avoided an in-depth analysis of the data. More interestingly, when the Cu^{II} complex is placed into a diamagnetic host forming by the isomorphous Zn^{II} complex, the dynamic process is completely removed. This was unexpected because different effects have been observed on the other Cu^{II} complexes whose electronic properties exhibit similar temperature dependence. This certainly originates from the constraints associated with the particular structure of this N6 ligand.

In conclusion this is the first investigation of Jahn-Teller distortions present in Cu^{II} complexes containing a hexadentate N6 ligand. With the use of X-ray diffraction, DFT calculations and multi-frequency EPR spectroscopy, we have been able to show that the [Cu(bmet)]²⁺ complexes display a 'dynamic' Jahn-Teller distortion. Furthermore, by insertion into a diamagnetic host lattice, we are able to block the 'dynamic' process and lock the [Cu(bmet)]²⁺ complex in a Jahn-Teller elongated distortion.

References

- (1) Jahn, H. A.; Teller, E. *Proc. R. Soc. Lond. Ser. - Math. Phys. Sci.* **1937**, *161*, 220–235.
- (2) Bersuker, I. B. In *Electronic Structure and Properties of Transition Metal Compounds*; John Wiley & Sons, Inc., 2010; pp. 238–323.
- (3) Bersuker, I. B. *Chem. Rev.* **2001**, *101*, 1067–1114.
- (4) Murphy, B.; Hathaway, B. *Coord. Chem. Rev.* **2003**, *243*, 237–262.
- (5) Halcrow, M. A. *Chem. Soc. Rev.* **2013**, *42*, 1784–1795.
- (6) Echeverría, J.; Cremades, E.; Amoroso, A. J.; Alvarez, S. *Chem. Commun.* **2009**, 4242.
- (7) Halcrow, M. A. *Dalton Trans.* **2003**, 4375–4384.
- (8) Folgado, J. V.; Henke, W.; Allmann, R.; Stratemeier, H.; Beltran-Porter, D.; Rojo, T.; Reinen, D. *Inorg. Chem.* **1990**, *29*, 2035–2042.
- (9) Goodman, B. A.; Raynor, J. B. In *Advances in Inorganic Chemistry and Radiochemistry*; Emelus, H. J.; Sharpe, A. G., Eds.; Academic Press, 1970; Vol. Volume 13, pp. 135–362.
- (10) Hathaway, B. J.; Billing, D. E. *Coord. Chem. Rev.* **1970**, *5*, 143–207.
- (11) Hathaway, B. J. *Struct. Bond. Berl.* **1984**, *57*, 55.
- (12) Atanasov, M.; Hitchman, M. A.; Hoppe, R.; Murray, K. S.; Moubaraki, B.; Reinen, D.; Stratemeier, H. *Inorg. Chem.* **1993**, *32*, 3397–3401.
- (13) Masters, V. M.; Riley, M. J.; Hitchman, M. A. *J. Synchrotron Radiat.* **1999**, *6*, 242–243.
- (14) Solanki, N. K.; McInnes, E. J. L.; Mabbs, F. E.; Radojevic, S.; McPartlin, M.; Feeder, N.; Davies, J. E.; Halcrow, M. A. *Angew. Chem. Int. Ed.* **1998**, *37*, 2221–2223.
- (15) Holland, J. M.; Liu, X.; Zhao, J. P.; Mabbs, F. E.; Kilner, C. A.; Thornton-Pett, M.; Halcrow, M. A. *J. Chem. Soc. Dalton Trans.* **2000**, 3316–3324.
- (16) Allmann, R.; Henke, W.; Reinen, D. *Inorg. Chem.* **1978**, *17*, 378–382.
- (17) Henke, W.; Reinen, D. *Z. Für Anorg. Allg. Chem.* **1977**, *436*, 187–200.
- (18) Narr, E.; Zimmermann, H.; Godt, A.; Goldfarb, D.; Jeschke, G. *Phys. Chem. Chem. Phys.* **2003**, *5*, 3959–3967.
- (19) Mack, K.; Wünsche von Leupoldt, A.; Förster, C.; Ezhevskaya, M.; Hinderberger, D.; Klinkhammer, K. W.; Heinze, K. *Inorg. Chem.* **2012**, *51*, 7851–7858.
- (20) Baird, L. J.; Black, C. A.; Blackman, A. G. *Polyhedron* **2007**, *26*, 378–384.
- (21) Hall, N. A.; Duboc, C.; Collomb, M.-N.; Deronzier, A.; Blackman, A. G. *Dalton Trans.* **2011**, *40*, 12075.
- (22) Gowda, B. T.; Foro, S.; Terao, H.; Fuess, H. *Acta Crystallogr. Sect. E Struct. Reports Online* **2009**, *65*, o1445–o1445.
- (23) Speck, A. L. *Acta. Cryst.* **2009**, 148–155.
- (24) Docherty, R.; Tuna, F.; Kilner, C. A.; McInnes, E. J. L.; Halcrow, M. A. *Chem. Commun.* **2012**, *48*, 4055–4057.
- (25) Simmons, C. J.; Stratemeier, H.; Hitchman, M. A.; Reinen, D.; Masters, V. M.; Riley, M. J. *Inorg. Chem.* **2011**, *50*, 4900–4916.
- (26) Hanic, F.; Čakajdová, J. A. *Acta Crystallogr.* **1958**, *11*, 610–612.
- (27) Hitchman, M. A.; Yablokov, Y. V.; Petrashen, V. E.; Augustyniak-Jabokov, M. A.; Stratemeier, H.; Riley, M. J.; Aukaszewicz, K.; Tomaszewski, P.; Pietraszko, A. *Inorg. Chem.* **2002**, *41*, 229–238.
- (28) Hitchman, M. A.; Maaskant, W.; van der Plas, J.; Simmons, C. J.; Stratemeier, H. *J. Am. Chem. Soc.* **1999**, *121*, 1488–1501.
- (29) Kilner, C. A.; Halcrow, M. A. *Acta Crystallogr B* **2010**, *66*, 206–212.

CHAPTER VII

Conclusion

Résumé

Ce travail de thèse a concerné la synthèse et la caractérisation de complexes bio-inspirés à liaisons métal-thiol aliphatiques, avec comme objectif principal la modélisation de métalloprotéines comportant ce type de coordination. Plus particulièrement, notre but était de mieux comprendre le rôle que peuvent jouer les ligands thiols aliphatiques au sein des sites actifs de ces métalloprotéines. Dans ce contexte, des complexes de différents ions de métaux de transition à ligands thiols ont été synthétisés, à savoir des complexes de vanadium(III), (IV) et (V), ainsi que de nickel et de cobalt (II) et (III), avec soit le ligand tétradenté $L^{N_2S_2}$, soit le ligand tridenté L^{NS_2} . Ces deux ligands possèdent un ligand azoté mono- ou bidentate (pyridine ou bipyridine) et deux ligands thiols encombrés. Nous avons étudié les propriétés structurales et électroniques de ces complexes, ainsi que leurs réactivités.

Trois nouveaux complexes du vanadium ont été synthétisés et caractérisés. Ainsi, le premier complexe dioxo de vanadium(V) contenant au moins un ligand thiol aliphatique ($VO_2L^{NS_2}$) a été obtenu et sa structure a été résolue par diffraction des rayons X. Un complexe oxo de vanadium(IV) a aussi été synthétisé ($VOL^{N_2S_2}$). La réactivité de ces deux complexes a été testée vis-à-vis de la sulfoxydation du thioanisole en utilisant le peroxyde d'hydrogène comme oxydant. Ils se sont révélés être de bons catalyseurs, efficaces et sélectifs pour la formation du sulfoxyde, aucune trace de sulfone n'étant produite. Ces complexes sont les premiers catalyseurs de sulfoxydation comportant des ligands thiols aliphatiques. Leur efficacité est comparable à celle de catalyseurs contenant uniquement des ligands oxygénés et/ou azotés. Notre étude a montré que $VO_2L^{NS_2}$ est plus efficace (rendements et vitesse de réaction), mais moins stable que $VOL^{N_2S_2}$. Une étude spectroscopique combinée à des calculs théoriques a montré que cette différence de réactivité pouvait être corrélée à la symétrie de l'unité peroxy dans les deux intermédiaires actifs cis-oxo peroxy du vanadium(V). Dans $VO(O_2)L^{NS_2}$ l'unité peroxy présente une plus basse symétrie que dans $VO(O_2)L^{N_2S_2}$, ce qui est en accord avec sa plus grande réactivité et sa moins bonne stabilité en catalyse.

Le troisième complexe du vanadium décrit est un complexe de vanadium(III) contenant le ligand L^{NS_2} et deux ions chlorure. Il a été synthétisé comme modèle moléculaire de la nitrogénase à vanadium. La réactivité du complexe réduit vanadium(II) a été testée vis-à-vis de l'hydrazine. Les résultats préliminaires suggèrent que l'adduit vanadium-hydrazine qui est formé peut réagir avec des protons pour générer un complexe de vanadium(IV). L'oxydation de l'adduit vanadium(II)-hydrazine en vanadium(IV) suggère que l'hydrazine a été réduite en ammoniac par un processus impliquant deux électrons et deux protons.

Avec comme objectif, isoler et caractériser des espèces actives de l'oxygène de complexes du nickel, en relation avec la NiSOD, nous avons étudié la réactivité avec le TBHP d'un complexe du nickel(II) précédemment décrit au laboratoire, $NiL^{N_2S_2}$. De manière surprenante, un intermédiaire

remarquablement stable a été observé à température ambiante. Les données obtenues par spectroscopie RPE et spectrométrie de masse ont montré qu'il s'agissait d'un complexe original mononucléaire de nickel(III) tert-butylperoxo. La capacité de ce complexe peroxo à oxyder des substrats externes a été testée. Nous avons observé qu'il présente un caractère électrophile faible, puisqu'il est capable d'oxyder la triphénylphosphine, mais pas les sulfures. Par ailleurs, le complexe initial $\text{NiL}^{\text{N}_2\text{S}_2}$ est régénéré lors de la réaction d'oxydation de la triphénylphosphine par le complexe peroxo, suggérant qu'il peut potentiellement agir comme un vrai catalyseur.

Nous avons également synthétisé et caractérisé le premier complexe du cobalt(II), $\text{CoL}^{\text{N}_2\text{S}_2}$, possédant une géométrie plan carrée avec des ligands thiols aliphatiques. Pour évaluer si l'ion cobalt(II) est un bon substitut du zinc(II) dans les enzymes à zinc, nous avons étudié la réactivité de ce complexe en S-alkylation. En présence d'un excès d'iodure de méthyle, la formation d'un complexe mono-S-méthylé a été observée, le ligand thioether restant coordonné au cobalt(II). Dans le cas du complexe de zinc(II), dans les mêmes conditions de réaction, les deux ligands thiols sont méthylés et les deux ligands thioether se dé-coordonnent du zinc(II). Ainsi, même si le cobalt(II) est un bon substitut structural de l'ion zinc(II), il est inapproprié comme substitut fonctionnel dans le cas particulier des réactions de S-alkylation. Par ailleurs, lors de l'oxydation chimique de $\text{CoL}^{\text{N}_2\text{S}_2}$, nous n'avons pas pu isoler de complexe mononucléaire de cobalt(III). En revanche un complexe dinucléaire de cobalt(II) a été obtenu, résultant de la réduction du cobalt(III) en cobalt(II) avec l'oxydation concomitante de deux ligands thiols en pont disulfure de manière intermoléculaire. Il s'agit là du premier complexe dinucléaire de cobalt avec un ligand disulfure pontant les deux ions cobalt(II)

Dans toutes ces études, il est particulièrement intéressant de noter que la réactivité des ligands thiols aliphatiques varie en fonction de la nature du métal auquel il est lié. Dans les complexes du vanadium et du nickel, nous avons pu montrer que des espèces peroxo pouvaient être générées sans oxydation intramoléculaire des ligands thiols. Ainsi, contrairement à ce qu'il pouvait être anticipé, ces complexes représentent une nouvelle classe de catalyseurs potentiels pour les réactions d'oxydation. Dans le cas de la réactivité des fonctions thiols pour la S-alkylation, notre étude a apporté de nouvelles informations permettant de mieux comprendre pourquoi la Nature a choisi le zinc pour réaliser ce type de réactions.

De manière générale, nous avons pu ainsi mieux comprendre certaines propriétés particulières des complexes possédant des ligands thiols aliphatiques, ainsi que leur réactivité. Cette étude a aussi permis d'approfondir notre compréhension du choix d'ions métalliques et de ligands particuliers fait par la Nature pour réaliser des réactions spécifiques.

Conclusion

This thesis presents the synthesis and characterisation of bio-inspired molecular complexes containing metal alkyl thiolate bonds with the goal of modelling metalloproteins. In particular, we have attempted to improve our knowledge on the role that the bound alkyl thiolate plays in metalloproteins. In this context, different M^{n+} -thiolate complexes have been synthesized (V^{III} , V^{IV} , V^V , Ni^{II} , Ni^{III} , Co^{II} and Co^{III}), with either a tetradentate $L^{N_2S_2}$ or a tridentate L^{NS_2} ligand. Both ligands consist of aromatic nitrogen (bipyridine or pyridine) donor atom(s) and also two bulky S-thiolate donor atoms. We have investigated the structural features, electronic properties and also the reactivity of the resulting compounds.

Three new mononuclear vanadium complexes have been synthesised and characterised. This includes the isolation of the first dioxo alkyl thiolate V^V complex with the tridentate ligand L^{NS_2} ($VO_2L^{NS_2}$), for which the structure has been resolved by X-ray diffraction. A neutral oxo alkyl thiolate V^{IV} complex with the tetradentate ligand $L^{N_2S_2}$ (VOL^{NS_2}) has also been synthesised. The reactivity of both of these complexes has been tested toward sulfoxidation of thioanisole, using H_2O_2 as the oxidising agent. Both catalysts have proven to be efficient and selective, with 100% selectivity toward the production of sulfoxide. These are the first catalytic sulfoxidation results reported for oxo vanadium complexes containing alkyl thiolates. Their efficiency is comparable to that observed with oxo vanadium catalysts containing O- and/or N- donor atoms reported in the literature. Significant differences between the two catalysts have been found. The $VO_2L^{NS_2}$ catalyst exhibits higher efficiency, but is less stable compared to the VOL^{NS_2} catalyst. Combined experimental and computational investigations have allowed us to propose that this is in part related to a difference in the symmetry observed in the peroxo unit of the two *cis*-oxo peroxo V^V active intermediates. The peroxo unit in $[VO(O_2)L^{NS_2}]^-$ being less symmetric than that in the $[VO(O_2)L^{N_2S_2}]^-$ complex, meaning $[VO(O_2)L^{NS_2}]^-$ is more reactive but less stable, consistent with the experimental findings.

The third vanadium complex described is a V^{III} complex containing the L^{NS_2} ligand and two coordinated chloride anions ($K[VCl_2L^{NS_2}]$). It has been synthesised as a molecular model for V-nitrogenase. The reactivity of the chemically reduced V^{II} species has been tested toward hydrazine. Preliminary results show that a V-hydrazine adduct is formed which further recats with protons to lead to a V^{IV} complex. This oxidation of the V^{II} species to a V^{IV} species suggests a concomitant $2H^+/2e^-$ reduction of N_2H_4 to NH_3 .

In an attempt to model Ni-based active oxygen species in relation to NiSOD, the reactivity of the previously described **NiL^{N2S2}** complex with oxidant TBHP was investigated. Surprisingly, an extremely stable intermediate species has been observed at room temperature. EPR spectroscopy and ESI-Mass spectrometry confirmed the formation of **NiL^{N2S2}OotBu**, representing an unprecedented mononuclear Ni^{III} alkylthiolate peroxo species. Furthermore, we have tested the reactivity of this peroxo complex towards oxidation. We found that it only exhibits weak electrophilic oxidising properties as it is not able to oxidise thioanisole, but is capable of the oxidation of PPh₃. It is also interesting to note that the initial Ni^{II} species (**NiL^{N2S2}**) is regenerated during the reaction of **NiL^{N2S2}OotBu** with PPh₃, suggesting that it has the potential to act as a catalyst.

We have synthesised and characterised an unprecedented example of an alkyl thiolate Co^{II} complex exhibiting a quasi-square planar geometry (**CoL^{N2S2}**). In order to test whether the Co^{II} ion is a good substitute for Zn^{II} in Zn-containing metalloenzymes, the reactivity of **CoL^{N2S2}** toward S-methylation has been tested. In the presence of an excess of CH₃I, we observed the formation of a mono S-methylated Co^{II} complex (**CoL^{N2S2}Me**), the generated thioether remaining coordinated to the metal. In the case of the Zn^{II} derivate, **ZnL^{N2S2}**, a double S-methylation occurs followed by the decoordination of the thioether ligands. Consequently, even if the Co^{II} ion is a suitable structural substitute for Zn-containing metalloenzymes, it may be inappropriate as a functional substitute in particular cases such as S-alkylation. Furthermore upon oxidation of **CoL^{N2S2}**, we were unable to isolate a mononuclear Co^{III} complex. Instead, a dinuclear (Co^{II})₂ complex has been obtained, which results from the reduction of the Co^{III} ion into a Co^{II} with the concomitant intermolecular oxidation of two thiolates into a disulfide bridge. This has led to the first reported dinuclear Co^{II} complex, which contains a disulfide bridge between the two Co^{II} centres.

What is interesting to note from all these studies, is that the reactivity of the alkyl thiolate depends greatly on the metal ion of choice. In both the vanadium and nickel study we have been able to produce metal-peroxo species, without intramolecular S-oxygenation. These represent some of the first studies using alkyl thiolate complexes as catalysts for oxidation. It has been widely supposed that under oxidising conditions the alkyl thiolate would undergo oxygenation, this work proving otherwise, therefore, opens an entire field for oxygenation catalysts. Furthermore, the work carried out on S-

alkylation, we have been able to gain insight into why in biology S-alkylation reactions are carried out by zinc containing metalloenzymes. A similar reactivity between the nickel and cobalt derivatives has been found, which is completely different to that of the zinc derivative.

In general, we have been able to obtain a further understanding of the particular properties and reactivity of metal bound alkyl thiolates, which in all cases provides new key elements to enhance our comprehension on why nature chooses specific metal ions and particular donor ligands to carry out specific tasks.

EXPERIMENTAL SECTION

General Methods

All reagents and solvents were used as received. THF and Et₂O were distilled over Na/benzophenone prior to use.

Elemental analyses

Elemental analyses were carried out with a Perkin-Elmer 240, C, H, N analyzer (SCA, CNRS).

X-ray Diffraction

Single-crystal diffraction data for **VO₂L^{NS2}** were obtained using a Bruker AXS Enraf-Nonius Kappa CCD diffractometer (MoK α radiation, graphite monochromator, λ 0.71073 Å). The molecular structure was solved by direct methods and refined with the TEXSAN software package.¹

Single-crystal diffraction data for all other structurally characterised compounds were taken using an Oxford-Diffraction XCallibur S Kappa geometry diffractometer (MoK α radiation, graphite monochromator, λ 0.71073 Å). The ABSPACK Oxford-diffraction program² was used for absorption correction with transmission factors in the range 0.770-0.877. The molecular structures were solved by direct methods and refined on F² by full matrix least-squares techniques using the SHELXTL package.³ All non-hydrogen atoms were refined anisotropically and hydrogen atoms were placed in ideal positions and refined with a riding model.

Nuclear Magnetic Resonance

¹H NMR measurements were carried out using a Bruker AM 400 spectrometer. ⁵¹V NMR spectra were recorded on a Bruker AM 500 spectrometer.

Mass spectroscopy

The electrospray ionisation mass spectrometry (ESI-MS) analyses were performed on a Bruker Esquire 3000 Plus ion trap spectrometer equipped with an electrospray ion source (ESI). The sample was analysed in either negative or positive ionization mode by direct perfusion in the ESI-MS interface (ESI capillary voltage = 2kV, sampling cone voltage = 40 V).

UV-visible absorption spectroscopy

UV-visible experiments were performed on a Perkin-Elmer Lambda 650 using quartz cells. The cells dimension (*i.e.* optical path length) was been chosen to obtain an absorption in the linear region of a Beer-Lambert plot.

EPR spectroscopy

X- and Q-band EPR spectra were recorded with a Bruker EMX, equipped with the ER-4192 ST Bruker cavity and ER-4131 VT for the X-band at 100 K experiments and the ER-5106 QTW Bruker cavity and an Oxford Instruments ESR-900 continuous-flow helium cryostat for the Q-band at 4.5 K experiments.

Computational Chemistry

All theoretical calculations were performed with the ORCA program package.⁴ Full geometry optimizations were carried out for all complexes using the GGA functional BP86⁵⁻⁷ in combination with the TZV/P⁸ basis set for all atoms and by taking advantage of the resolution of the identity (RI) approximation in the Split-RI-J variant⁹ with the appropriate Coulomb fitting sets.¹⁰ To properly model the interaction via H bonding in **1**, the TZV/P++ basis set (the same basis set augmented with diffuse functions on all atoms) was employed for the relevant O and H atoms. Increased integration grids (Grid4 in the ORCA convention) and tight SCF convergence criteria were used. Solvent effects were accounted for according to the experimental conditions. For this purpose, we used the CH₃OH ($\epsilon = 32.63$) solvent within the framework of the conductor like screening (COSMO) dielectric continuum approach.¹¹ Electronic structures as well as Molecular Orbitals were obtained using the hybrid functional B3LYP^{7,12} and the TZV/P basis set. *g*-tensors and hyperfine coupling constants were obtained from single-point calculations employing the hybrid functional B3LYP. The triply polarized core property basis set CP(PPP)¹³ was applied for the metal while the EPR-II basis set was used for all remaining atoms. Special care was also taken to ensure accurate results by increasing the size of the integration grid to 7 (ORCA convention) for the metal center.

The chemical shift tensors were obtained from additional single-point calculations using the EPR/NMR module and the IGLO procedure as implemented in the ORCA program package. The B3LYP functional and an IGLO-II^{14,15} basis set were employed for the calculation of NMR parameters. The calculated shielding tensors were transformed to relative chemical shifts δ by subtracting the calculated chemical shift of VOCl₃.

Electrochemistry

The electrochemical measurements were run under an argon atmosphere at room temperature. When CH₃CN or DMF were used as solvent, the electrochemical measurements were performed in a dry-glove box. Cyclic voltammetry experiments were performed using an EG&G model 173 potentiostat/galvanostat equipped with a PAR model universal programmer and a PAR model 179 digital coulometer. A standard three-electrode electrochemical cell was used. Potentials were referred to an Ag/0.01 M AgNO₃ reference electrode in CH₃CN + 0.1 M [Bu₄N]ClO₄. Potentials referred to the Ag/AgNO₃ system can be converted to the ferrocene/ferricinium couple by subtracting 87 mV, to the saturated calomel electrode (SCE) by adding 298 mV or to the normal hydrogen electrode (NHE) by adding 548 mV. The working electrode was a carbon vitreous disk, 3 mm in diameter for cyclic voltammetry, polished with 2 μ m diamond paste (Mecaprex Presi). The auxiliary electrode was a Pt wire in CH₃CN + 0.1 M [Bu₄N].

Gas chromatography

Standard conditions were as follows: 1 mM solution of catalyst **1** (1.37 mg, 2 μ mol) or **2** (1.29 mg, 2 μ mol) in either CH₃CN or CH₂Cl₂: CH₃CN (1:1) respectively, containing thioanisole (23.5 μ L, 200 μ mol) under an argon atmosphere at room temperature (final volume, 2 mL). The reaction was started by adding H₂O₂ (17.1 μ L) with the ratio catalyst:sulfide:oxidant, 1:100:100. The internal standard (benzophenone, 5.0 mM) was then added and the organic products were quantified by GC. Unambiguous identification

of the products was made by comparison with pure compounds prepared independently. All reactions were followed using a Perkin Elmer Autosystem XL gas chromatograph equipped with a Perkin Elmer Elite-5 capillary column (30m x 0.32mm x 0.25 μ m) and an FID detector. All blank reactions have been performed in the absence of catalyst under all experimental conditions used in this work. No sulfoxide or sulfone are produced.

Ligand Preparation

THF and diethyl ether were dried and distilled before use. The syntheses of all the compounds, except **a3** and **a4**, were performed under an inert atmosphere (Ar) using Schlenk or glove-box techniques.

Diphenylmethanethiol (a1)

Diphenylmethylchloride (13.0 g, 64.14 mmol) and thiourea (4.5 g, 58.69 mmol) were refluxed in ethanol (30 mL) for 2 h, after which the solution was cooled to room temperature. Upon the addition of NaOH (4 g, 3 M aq.) a precipitate formed and refluxing was continued for a further 2 h. The reaction mixture was then cooled to ambient temperature and the oil was separated. H₂SO₄ (1 mL in 10 mL of water) was added to the aqueous phase, which was then extracted with Et₂O. Et₂O phases were combined with the oil phase and dried over Na₂SO₄, filtered and reduced to an oil. The oil was then dissolved in Et₂O (~15 mL) and put in fridge to crystallise over 24h. The resulting mixture was filtered to remove impurities, and the filtrate was reduced to give the product as an oil (10.0 g, 79 %). ¹H NMR (400 MHz, CDCl₃): δ 7.74 (1H, t, *J* = 8 Hz, H-bipy), 7.41 (2H, d, *J* = 8 Hz, H-bipy), 4.57 (4H, s, CH₂).

2-[(Diphenylmethyl)thiol]tetrahydro-2H-pyran (a2)

HCl (1 mL, 37%) was added dropwise to a stirring solution of **2** (10.0 g, 50 mM) and 2,3-dihydropyran, giving a colour change from light yellow to dark brown. After 3 h of stirring Et₂O (200 mL) was added and the mixture was then washed with Na₂CO₃ (sat. aq. 2 \times 100 mL). The organic phase was extracted and washed with NaCl (sat. aq. 2 \times 50 mL). Organic phases were then combined and dried over Na₂SO₄, filtered and reduced to give an orange oil. The orange oil was then dissolved in a minimum amount of pentane and left to crystallise in the fridge. ¹H NMR (400 MHz, CDCl₃): δ 7.51 (1H, d, Ph), 7.41 – 7.20 (8H, m, Ph), 5.36 (1H, s, Ph₂CH), 4.63 (1H, m, H-THP), 3.53 – 3.46 (1H, m, H-THP), 1.92 (2H, m, H-THP), 1.529 (6H, m, H-THP).

Preparation of H₂L^{N2S2}

6,6'-dibromo-2,2'-bipyridine (b1)

This preparation was modified from a reported procedure by Uchida, Y. *et al.*¹⁶ A solution of *n*-BuLi (2.5 M in hexane, 42.3 mL, 105.75 mmol) was added to a mixture of 2,6-dibromopyridine (25 g, 105.53 mmol) in diethyl ether (400 mL) at -60 °C. After 2 h at -40 °C, SOCl₂ (2.5 mL, 34.27 mmol) was slowly added (at -40 °C). After 2 h the reaction mixture was warmed to room temperature and water (100 mL) and chloroform (250 mL) were added. The organic layer was separated and the aqueous suspension was

extracted with chloroform (3 × 200 mL). All the organic phases were combined and dried over Na₂SO₄. Following filtration and removal of the solvent in vacuo, the residual solid was filtered washed with methanol and diethyl ether and dried, yielding the crude product. This was purified by column chromatography (silica gel, CHCl₃:pentane 4:3), giving a colourless microcrystalline powder (**b1**, 4g, 12.74 mmol, 24 %). ¹H NMR (400 MHz, CDCl₃): δ 8.37 (2H, d, J = 7.4 Hz, CH *para*-Br), 7.66 (2H, t, J = 7.7 Hz, CH *para*-N), 7.50 (2H, d, J = 7.9 Hz, CH).

2,2'-bipyridine-6,6'-dicarbaldehyde (**b2**)

b1 (4 g, 12.74 mmol) was dissolved in THF (150 mL) and slowly added to a solution of *n*-BuLi (2.5 M in hexane, 10.5 mL, 26.74 mmol) in THF (80 mL) at -78 °C. After 45 min at -78 °C, DMF (3.5 mL, 45.20 mmol) was added dropwise to the mixture. After 1 h at -78 °C the dark violet mixture was warmed to -30 °C and quenched with 4 M HCl (45 mL). It was basified with Na₂CO₃ (aq, sat) and concentrated under vacuum to remove the organic solvent. The aqueous suspension was extracted with CHCl₃ (5 × 100 mL). The organic layers were mixed and dried with Na₂SO₄. Following filtration and removal of the solvent under vacuum, the residual solid was washed with methanol (45 mL) and diethyl ether and dried in vacuo, yielding **b2** as a pale yellow powder (2.0 g, 9.42 mmol, 74 %). ¹H NMR (400 MHz, CDCl₃): δ 10.19 (2H, s, CHO), 8.83 (dd, *J*_{ortho} = 7.2 Hz, *J*_{meta} = 2.0 Hz, 2H, CH *para*-CHO), 8.05 (m, 4H, CH).

2,2'-bipyridine-6,6'-diyl dimethanol (**b3**)

This was prepared as reported by Newkome *et. al.*¹⁷ **b2** (0.36 g, 1.68 mmol) and NaBH₄ (0.16 g, 4.20 mmol) in methanol (30 mL) was stirred at ambient temperature for 2 h. HCl (0.12 mM, 40 mL) was added to the solution and stirring was continued. After 10 min the mixture was basified with Na₂CO₃ (aq, sat) and concentrated under vacuum to remove the organic solvent. The aqueous suspension was extracted with CHCl₃ (5 × 100 mL). The organic layers were combined and dried with Na₂SO₄. Following filtration and removal of the solvent under vacuum, the residual solid was washed with methanol (45 mL) and diethyl ether and dried in vacuo, yielding **b3** as a pale cream powder (0.25 g, 1.13 mmol, 68 %). ¹H NMR (400 MHz, CDCl₃): δ 8.36 (d, J = 4.3 Hz, 2H, CH *para*-CH₂OH), 7.84 (d, J = 7.8 Hz, 2H, CH *para*-N), 7.27 (d, 2H, CH), 4.84 (d, J = 4.3 Hz, 4H, CH₂), 3.97 (t, J = 4.3 Hz, 2H, OH).

6,6'-bis(bromomethyl)-2,2'-bipyridine (**b4**)

PBr₃ (2 mL, 21.28 mmol) was added to a solution of **b3** (1.9 g, 8.79 mmol) in CHCl₃. The mixture was refluxed for 3 h. After cooling to room temperature, it was basified with NaHCO₃ (aq, sat, 100 mL). The organic layer was separated and the aqueous suspension was washed with CHCl₃ (5 × 100 mL). The organic phases were combined and dried over Na₂SO₄. The pale white solid was washed with methanol (3 × 15 mL) and redissolved in THF. The insoluble fraction was filtered off and the solvent was removed in vacuo, yielding a pale white powder (1.88 g, 5.50 mmol, 63 %). ¹H NMR (400 MHz, CDCl₃): δ, 8.38 (d, J = 8.1 Hz, 2H, CH *meta*-N), 7.82 (d, J = 7.8 Hz, 2H, CH *para*-N), 7.47 (d, J = 7.8 Hz, 2H, CH *meta*-N), 4.62 (s, 4H, CH₂).

The syntheses of $((\text{THP})_2\text{L}^{\text{N2S2}})$ and $(\text{H}_2\text{L}^{\text{N2S2}})$ have been previously described by our group.¹⁸

2,6-Bis[2,2-diphenyl-2-[(tetrahydro-2H-pyran-2-yl)thio]ethyl]-2,2'-bipyridine $((\text{THP})_2\text{L}^{\text{N2S2}})$
A solution of **a2** (1.6 g, 6.04 mmol) in distilled diethyl ether (80 mL) was cooled to -80 °C, and *n*-BuLi (2.4 mL, 2.5 % in hexanes) was added. The solution was then allowed to warm to ambient temperature over 2 h. This solution was then cooled again to -80 °C and a solution of **b4** (1.0 g, 3.02 mmol) and HMPA (2 mL) in distilled THF (30 mL) was added. This solution was then allowed to warm to ambient temperature over 2 h, after which the reaction solution was quenched with water (200 mL) and the organic phase was separated. The aqueous phase was then extracted with EtOAc (3 × 100 mL). The organic fractions were then combined and dried over Na₂SO₄, filtered and reduced to an orange oil. The resulting oil was then dissolved in a minimal amount of acetone and left in the fridge overnight. The insoluble fraction was filtered and washed with acetone (3 × 20 mL) and Et₂O (3 × 20 mL) yielding a white solid (1.6 g, 2.14 mmol, 71 %). ¹H NMR (400 MHz, CDCl₃): δ 8.38 (d, *J* = 8.1 Hz, 2H, CH *meta*-N), 7.82 (d, *J* = 7.8 Hz, 2H, CH *para*-N), 7.47 (d, *J* = 7.8 Hz, 2H, CH *meta*-N), , 4.62 (s, 4H, CH₂).

2,6-Bis(2,2-diphenyl-1-2-mercaptoethyl)-2,2'-bipyridine $(\text{H}_2\text{L}^{\text{N2S2}})$

AgNO₃ (128.4 mg, 0.8 mmol) and pyridine (68.6 mg, 0.9 mmol) in 3 mL of MeOH was added to a mixture of **4** (248.3 mg, 0.4 mmol) in MeOH (3 mL) and EtOAc (3 mL). This reaction mixture was stirred for 2 h after which time the reactants had dissolved to give a yellow solution. This solution was reduced to dryness to give a yellow solid, which was washed with Et₂O (3 × 10 mL). The dry yellow product was then dissolved in the minimum amount of CH₂Cl₂ and degassed for five minutes. H₂S gas was then bubbled through the solution resulting in copious amounts of thick black precipitate. The mixture was then filtered through Celite and washed with CH₂Cl₂. The filtrate was washed with NaHCO₃ (aq. sat.) and extracted. The organic phase was dried over NaSO₄, filtered and reduced under vacuum to give a yellow oil. To this was added Et₂O and the volume was reduced to give a white fluffy solid. ¹H NMR (400 MHz, CDCl₃): δ 7.50 (1H, d, *J*=7.45, H-pyridine), 7.40-7.27 (20H, m H-phenyl), 7.05 (2H, t, *J*=7.45, H-pyridine), 3.76 (4H, s, H- CH₂) ppm.

Preparation of $\text{H}_2\text{L}^{\text{NS2}}$

2,6-bis-(bromomethyl)pyridine (c1**)**

2,6-bis-(methanol)-pyridine was dissolved in CHCl₃ (50 mL). To this solution was added excess PBr₃ (technical grade, 2 mL). The mixture was then refluxed for 2 h, after which time the solution was cooled to room temperature. NaHCO₃ (sat. aq.) was added to the reaction mixture until pH 7/8 was reached. The organic phase was separated, and the aqueous phase was extracted with CHCl₃. Organic fractions were combined and dried over Na₂SO₄, filtered and rotavaped to dryness to give a white solid (1.25 g, 61%). ¹H NMR (400 MHz, CDCl₃): δ 7.736 (1H, t, *J* = 8 Hz, H-bipy) δ 7.405 (2H, d, *J* = 8 Hz, H-bipy) δ 4.568 (4H, s, CH₂) ppm.

2,6-Bis[2,2-diphenyl-2-[(tetrahydro-2H-pyran-2-yl)thio]ethyl]pyridine $((\text{THP})_2\text{L}^{\text{NS2}})$

$(\text{THP})_2\text{L}^{\text{NS2}}$ was prepared from **c1** (1.25 g, 4.72 mmol), by the method used for $(\text{THP})_2\text{L}^{\text{N2S2}}$ and was obtained as a white solid (2.20 g, 70%). ¹H NMR (400 MHz, CDCl₃):

δ 7.46 (1H, d, H-pyridine), 7.06 (20H, m H-phenyl), 6.75 (2H, t, H-pyridine), 4.23 (2H, t, H-THP), 3.95 – 3.65 (4H, m, H-THP), 3.16 (4H, m, H-THP), 1.69-1.32 (8H, m, H-THP) ppm.

2,6-Bis(2,2-diphenyl-1-2-mercaptoethyl)pyridine (**H₂L^{NS2}**)

H₂L^{NS2} was prepared from (**THP**)₂**L^{NS2}** (0.495 g, 0.74 mmol), by the method used for **H₂L^{N2S2}** and was obtained as a white solid (0.23 g, 79%). ¹H NMR (400 MHz, CDCl₃): δ 7.51 (1H, d, H-pyridine), 7.33 (20H, m H-phenyl), 6.81 (2H, t, H-pyridine), 3.84 (4H, s, H-CH₂) ppm.

Preparation of **bmet**

6-methyl-2,2'-bipyridine (**d1**)

CAUTION: MeLi is potentially pyrophoric when exposed to air.

This was synthesised on a 0.6 mol scale according to the method of Schmalzl and Summers.¹⁹

2,2'-bipyridine (10.02 g, 0.643 mol) was added to dry Et₂O (125 mL) under N₂ and the resulting solution was added with stirring over a period of about 15 min to a 1.60 M solution of MeLi in Et₂O (100 mL, 1.60 M) to give a deep red solution. Stirring was then continued for a further 3 hours. The deep red solution was poured slowly onto an ice-water mixture to give a yellow solution which was then extracted with Et₂O until the ether layer was colourless. Et₂O extracts were dried over Na₂SO₄, filtered, and reduced to dryness on a rotary evaporator to yield an orange oil. This was then heated for 2 h at 90 °C under vacuum. The crude product was purified by chromatography on a silica gel column (200-400 mesh, 0.040-0.063 mm) packed and eluted with hexane/ethyl acetate (6:1) solvent mix. The second band, was reduced (rotavap), yielding a pale yellow oil (4.04 g, 37%). ESI-MS: Calcd for C₁₁H₁₀N₂Na 193.0725; Found 193.0736. ¹H NMR (300 MHz, CDCl₃): δ 8.66 (1 H, d, H-bipy), 8.39 (1 H, d, H-bipy), 8.16 (1H, d, H-bipy) 7.78 (1 H, m, H-bipy) 7.68 (1H, t, H-bipy) 7.26 (1H, m, H-bipy) 7.14(1H, d, H-bipy) 2.62 (3 H, s, CH₃-bipy) ppm.

2,2'-bipyridine-6-carboxaldehyde (**d2**)

This was synthesised according to the method of Heirtzler *et al.*²⁰

A mixture of **d1** (4.0 g, 2.4 × 10⁻³ mol) and selenium dioxide (4.2 g, 4.0 × 10⁻³ mol) was refluxed in a solution of water (0.69 mL, 4.0 × 10⁻³ mol) and dioxane (113 mL) under N₂ gas for 3 h. The solution was cooled and water (69 μ L, 4.0 × 10⁻³ mol) and selenium dioxide (4.209 g, 4.0 × 10⁻³ mol) were added, with a slight change in colour to orange being observed. Refluxing was continued for a further 26 h. The hot reaction mixture was filtered to remove metallic selenium, and the insoluble material was washed (3 × 20 mL) with warm dioxane and warm ethyl acetate, causing the filtrate to turn a milky cream colour. The filtrate was reduced (rotavap) to give an orange oil. The crude product was purified by chromatography on a silica gel column (200-400 mesh, 0.040 – 0.063 mm) packed and eluted with ethyl acetate/dichloromethane (15:85). The product was reduced in volume (rotavap) to give a pale pink solid (1.2 g, 27%). *Anal.* Calcd for C₁₁H₈N₂O: C, 71.73; H, 4.35; N, 15.21. Found: C, 71.78; H, 4.52; N, 14.93. ¹H NMR (300

MHz, CDCl₃): δ 10.21 (1 H, s, bipy-C(=O)-H), 8.76 (1 H, d, H-bipy), 8.70 (1 H, d, H-bipy), 8.60 (1 H, d, H-bipy), 8.03 (2 H, m, H-bipy), 7.91 (1 H, m, H-bipy), 7.52 (1 H, m, H-bipy) ppm.

N,N'-bis(2,2'-bipyridin-6-ylmethyl)ethane-1,2-diamine·1.5MeOH·0.5H₂O (**bmet**)

The synthesis of **bmet** was based on the method used by Baird *et al.*²¹

A solution of ethane-1,2-diamine (74.3 μ L, 1.1×10^{-3} mol), and **2** (410 mg, 2.2×10^{-3} mol) in MeOH (16.4 mL) was heated at reflux for 30 min with stirring. NaBH₄ (99.2 mg, 2.6×10^{-3} mol) was then added slowly to the cooled solution and the mixture was stirred for a further 3 h. The solution was then reduced to dryness by rotary evaporation yielding a white solid, which was dissolved in water (10 mL) and extracted with CHCl₃ (3 \times 5 mL). The organic fractions were combined, dried over MgSO₄ and reduced to dryness (432 mg, 98%). *Anal.* Calcd. for C₂₄H₂₄N₆·1.5CH₃OH·0.5H₂O: C, 67.53; H, 6.89; N, 18.53. Found: C, 67.37; H, 6.89; N, 18.33. ¹H NMR (300 MHz, CDCl₃): δ 8.65 (2 H, d, H-bipy), 8.43 (2 H, d, H-bipy), 8.29 (2 H, d, H-bipy), 7.76 (4 H, m, H-bipy), 7.28 (4 H, m, H-bipy), 4.00 (4 H, s, bipy-CH₂), 2.90 (4 H, s, bipy-CH₂-NH-CH₂) ppm.

Preparation of Complexes

All complexes were synthesised in the glove-box.

Oxovanadium Complexes – Chapter II

*Et*₃NH[VO₂L^{NS2}]

A solution of H₂L^{NS2} (146.2 mg, 0.3 mmol) in THF (2 mL) was gently heated to 30°C. A suspension of ammonium metavanadate (33.4 mg, 0.3 mmol) in methanol (3 mL) was added dropwise with stirring. Et₃N (73.1 mg, 0.7 mmol) was then added and the reaction mixture was stirred and heated at 40°C for a further 2 h. A colour change from colourless to yellow was observed. The reaction mixture was then cooled to room temperature and stirred overnight to give a yellow precipitate. The precipitate was filtered and washed with a small amount of methanol and ether (2 \times 5 mL) to give the product as a yellow solid (VO₂L^{NS2}, 156.3 mg, 0.23 mmol, 76%). The yellow precipitate was then dissolved in a smallest amount of MeOH with heating and allowed to sit for 72h giving yellow/orange crystals suitable for X-ray crystallography. (VO₂L^{NS2}, 156.3 mg, 0.23 mmol, 76%). ESI-MS ($5 \cdot 10^{-5}$ M, CH₃CN, *m/z*, I%): 583.9, 100 [VO₂L^{NS2}]⁻. *Anal.* Calcd. for C₃₉H₄₃N₂S₂O₂V. (686.22): C, 68.20; H, 6.31; N, 4.08; Found: C, 68.04; H, 6.49; N, 4.05. Absorption spectrum in CH₃CN (λ_{\max} , nm (ϵ , M⁻¹ cm⁻¹)): 386 (2192).

[VOL^{N2S2}]⁻·2H₂O

Solid KH (30% in mineral oil, 46 mg, 0.40 mmol) was added to a solution of H₂L^{N2S2} (99 mg, 0.17 mmol) in THF (2 mL). After 20 min, the excess KH was filtered off and solid VOSO₄·4H₂O (30 mg, 0.2 mmol) was added to the yellow solution. The reaction was stirred for a further 12 h, to give a light green precipitate. The precipitate was filtered and washed with methanol (2 \times 10 mL) and ether (2 \times 10 mL) to give the product as a very light green solid (VOL^{N2S2}, 53 mg, 0.081 mmol, 48%). ESI-MS ($5 \cdot 10^{-5}$ M, CH₂Cl₂, *m/z*, I%): 646.2, 100 [VOL^{N2S2}H]⁺. *Anal.* Calcd. for C₃₈H₃₀N₂S₂O₂V·2H₂O (681.78): C, 66.95; H,

5.03; N, 4.11; Found: C, 67.78; H, 4.88; N, 4.09. Absorption spectrum in CH₂Cl₂ (λ_{\max} , nm (ϵ , M⁻¹ cm⁻¹): 292 (17000).

Vanadium(III) complexes – Chapter III

Crystals of [VCl₂L^{NS2}]PPN·2CH₂Cl₂

Solid NaH (60% in mineral oil, 15 mg, 0.36 mmol) was added to a solution of H₂L^{NS2} (87 mg, 0.17 mmol) in CH₂Cl₂ (1 mL). This solution was added to a stirred solution of VCl₃·3THF (64 mg, 0.17 mmol) in CH₂Cl₂ (1 mL). PPNCl (194 mg, 0.36 mmol) dissolved in CH₂Cl₂ (0.5 mL) was then added to the reaction solution giving a dark yellow solution. The volume of the solution was reduced to half under vacuum, and slow diffusion of Et₂O afforded deep orange crystals suitable for X-ray crystallography (83 mg, 42%). ESI-MS (5·10⁻⁵ M, CH₂Cl₂, *m/z*, I%): 622.1, 100 [VCl₂L^{NS2}]⁻.

[VCl₂L^{NS2}]K

KH (30% in mineral oil, 15 mg, 0.36 mmol) was added to a solution of H₂L^{NS2} (52 mg, 0.10 mmol) in THF (1 mL). This solution was added to a stirred solution of VCl₃·3THF (37 mg, 0.10 mmol) in THF (1 mL) giving a dark yellow solution. The solution was reduced to half under vacuo, and to give an orange powder. The resulting residue was washed with Et₂O (34 mg, 54%). Absorption spectrum (λ_{\max} , nm (ϵ , M⁻¹ cm⁻¹); CH₂Cl₂, 414 (3731); MeCN, 414 (2200); THF, 414 (616); DMF, 414 (522), 488 (889).

Nickel complexes – Chapter IV

[NiL^{NS2}dmpe]

Solid NaH (60% in mineral oil, 5 mg, 0.12 mmol) was added to a solution of H₂L^{NS2} (25 mg, 0.05 mmol) in THF (1 mL). After 5 minutes of stirring the reaction mixture was filtered to remove any excess NaH. This solution was added to a stirred solution of Ni(ClO₄)₂·6H₂O (16.5 mg, 0.05 mmol) in MeCN (1 mL) and 1,2-bis(dimethylphosphino)ethane (7.4 μ L, 0.05 mmol), instantly resulting in a dark red mixture. The reaction mixture was placed in the fridge for 30 minutes and the resulting brown precipitate was filtered. This was then washed with cold MeCN and Et₂O (16 mg, 50%). ESI-MS and C, H, N analysis to be submitted. Absorption spectrum in CH₂Cl₂ (λ_{\max} , nm (ϵ , M⁻¹ cm⁻¹): 315 (16705), 412 (1023), 556 (550).

[Ni₂(L^{NS2})₂]·2THF

Solid NaH (60% in mineral oil, 5 mg, 0.12 mmol) was added to a solution of H₂L^{NS2} (53 mg, 0.1 mmol) in THF (1 mL). After 5 minutes of stirring the reaction mixture was filtered to remove any excess NaH. This solution was added to a stirred solution of Ni(ClO₄)₂·6H₂O (35 mg, 0.1 mmol) in MeCN (1 mL) and stirred for 1 h. X-ray suitable crystals were obtained by slow cooling of the solution giving green crystals (26 mg, 23%). ESI-MS (5·10⁻⁵ M, CH₂Cl₂, *m/z*, I%): 1121.0, 100 [Ni₂(L^{NS2})₂H]⁺. C, H, N analysis to be submitted.

[NiL^{N2S2}]¹⁸

Solid NaH (60% in mineral oil, 8 mg, 0.18 mmol) was added to a solution of H₂L^{N2S2} (52 mg, 0.09 mmol) in THF (1 mL). The reaction mixture was stirred for 5 minutes and

filtered. This solution was added to a stirred solution of $\text{NiCl}_2 \cdot 6\text{H}_2\text{O}$ (22.0 g, 0.09 mmol) in THF (1 mL), to instantly give a dark purple precipitate. The solid was filtered and dissolved in CHCl_3 (10 mL). Any excess NaCl (white precipitate) was then filtered and the filtrate was reduced in vacuo. The residue was then washed with MeOH and dried under vacuum, giving the product as a purple solid ($\text{NiL}^{\text{N}_2\text{S}_2}$, 20 mg, 35%). $^1\text{H NMR}$ (400 MHz, ppm): δ 4.12 (s, 4H, CH_2), 6.82 (d, $J=7.2\text{ Hz}$, 2H, CH bipy *o*- CH_2), 7.12 (t, $J=7.2\text{ Hz}$, 4H, CH Ph), 7.21 (t, $J=7.2\text{ Hz}$, 8H CH Ph), 7.59 (m, 12H, CH, Ph + CH bipy). ESI-MS ($1.5 \cdot 10^{-6}\text{ M}$, $\text{CH}_2\text{Cl}_2:\text{H}_2\text{O}:\text{MeOH}$, m/z , I%): 637.2, 100 $[(\text{NiL})\text{H}]^+$; 1275.2, 9 $[(\text{NiL})_2\text{H}]^+$. Absorption spectrum in CH_2Cl_2 (λ_{max} , nm (ϵ , $\text{M}^{-1}\text{ cm}^{-1}$): 508 (4700), 556 (4298).

Cobalt complexes – Chapter V

$[\text{CoL}^{\text{N}_2\text{S}_2}]^{2+}$

Solid KH (30% in mineral oil, 28 mg, 0.209 mmol) was added to a solution of H_2L (55 mg, 0.095 mmol) in THF (15 ml). After 20 min, the excess KH was filtered off and solid $\text{Co}(\text{BF}_4)_2 \cdot 6\text{H}_2\text{O}$ (33 mg, 0.097 mmol) was added to the yellow solution to give a deep black mixture. After 1.5 h of stirring, the dark precipitate was filtered from the black solution, washed with THF (5 ml) and methanol (3 x 10 ml), dried and collected as a dark brown powder ($\text{CoL}^{\text{N}_2\text{S}_2}$, 52 mg, 0.081 mmol, 85%). IR (cm^{-1}): 3070w, 3036w, 3028w, 2955w, 1954w, 1883w, 1810w, 1603s, 1576w, 1566w, 1489m, 1441s, 1391m, 1262m, 1105s, 1071vs, 1035vs, 784m, 745m, 696s, 601w, 592w. ESI-MS ($5 \cdot 10^{-5}\text{ M}$, DMF: CH_3CN , m/z , I%): 637.1, 100 $[\text{CoL}]^+ + [\text{CoLH}]^+$. Anal. Calcd. for $\text{C}_{38}\text{H}_{30}\text{N}_2\text{S}_2\text{Co}$ (637.69): C, 71.57; H, 4.74; N, 4.39; Found: C, 71.73; H, 4.82; N, 4.19. Absorption spectrum in DMF (λ_{max} , nm (ϵ , $\text{M}^{-1}\text{ cm}^{-1}$): 750 (~1300), 530 (sh), 460 (sh), 420 (~2600). X-ray quality black single crystals of $\text{CoL}^{\text{N}_2\text{S}_2}$ were obtained by layering a solution of $\text{Co}(\text{BF}_4)_2$ in acetonitrile over an equimolar solution of K_2L in THF (see above). A 1:1 THF:acetonitrile solution was interposed between the two layers.

$[\text{CoL}^{\text{N}_2\text{S}_2}\text{Me}]$

Methylation of complex $\text{CoL}^{\text{N}_2\text{S}_2}$ was carried out in DMF (1.5 mM) in presence of 20 eq of iodomethane. The reaction was followed by UV-Vis spectrophotometry over a one hour time-frame and the final product was further analysed by ESI-MS and X-band EPR spectroscopy. Absorption spectrum in DMF (λ_{max} , nm (ϵ , $\text{M}^{-1}\text{ cm}^{-1}$): 530 (sh), 450 (1050). ESI-MS ($5 \cdot 10^{-5}\text{ M}$, DMF: CH_3CN , m/z , I%): 652.1, 100 $[\text{CoLCH}_3]^+$.

$[\text{CoL}^{\text{N}_2\text{S}_2}\text{Cl}]$

Solid KH (30% in mineral oil, 28 mg, 0.209 mmol) was added to a solution of H_2L (55 mg, 0.095 mmol) in THF (15 ml). After 20 min, the excess KH was filtered off and solid $\text{CoCl}_2 \cdot 6\text{H}_2\text{O}$ (33 mg, 0.097 mmol) was added to the yellow solution to give a deep black mixture. After 1.5 h of stirring, solid 4-bromobenzenediazonium tetrafluoroborate (28 mg, 0.103 mmol) was added in small portions to the dark mixture. The resulting black solution was stirred for 1.5 h and diethyl ether was diffused into it. After few days, X-ray suitable black single crystals of $\text{CoL}^{\text{N}_2\text{S}_2}\text{Cl}$ were obtained, filtered, washed with diethyl ether and dried ($\text{CoL}^{\text{N}_2\text{S}_2}\text{Cl}$, 44 mg, 0.069 mmol, 73%). IR (cm^{-1}): 3052m, 3027w, 1958w, 1890w, 1809w, 1602s, 1570m, 1488s, 1469m, 1443s, 1266w, 1184w, 1157w, 1126m, 1084m, 1060m, 1034m, 793m, 754m, 747m, 697vs. ESI-MS ($5 \cdot 10^{-5}\text{ M}$, CH_3CN , m/z , I%):

637.1, 100 [CoL]⁺, 820.0, 30 [CoL·CoCl₂(H₂O)]⁺. Anal. Calcd. for C₃₈H₃₀N₂S₂CoCl (673.14): C, 67.80; H, 4.49; N, 4.16 Found: C, 67.44; H, 4.71; N, 4.32. Absorption spectrum in DMF (λ_{\max} , nm (ϵ , M⁻¹ cm⁻¹): 775 (~100), 675 (~200), 632 (sh), 600 (sh), 475 (~1100), 294 (~7200), 264 (~6500).

Crystals of [Co^{II}(L^{N2S2})](PF₆)₂·2MeCN

Solid AgPF₆ (3.8 mg, 0.015 mmol) was added to a suspension of **CoL^{N2S2}Cl** (10 mg, 0.015 mmol) in CH₃CN (3 ml). After stirring for 5 min, the resulting white precipitate (AgCl) was filtered off. The obtained dark filtrate was analyzed by ESI-MS (5·10⁻⁵ M, CH₃CN, *m/z*, I%): 637.1, 100 [CoL]⁺; 1291.3, 100 [Co₂(LSSL)(OH)]⁺. X-ray quality black crystals of **[Co₂(L^{N2S2})₂](PF₆)₂·2CH₃CN** were obtained by slow diffusion of diethyl ether into this dark solution at -18 °C.

Copper & Zinc bmet complexes –Chapter VI

[Cu(bmet)](ClO₄)₂·0.5H₂O

The deep blue solution that formed on mixing solutions of bmet (54.0 mg, 1.3 × 10⁻⁴ mol) and Cu(ClO₄)₂·6H₂O (49.8 mg, 1.3 × 10⁻⁴ mol) gave the product as small deep blue crystals on standing at ambient temperature overnight. (65.3 mg, 75%) *Anal.* Calcd for [Cu(C₂₄H₂₄N₆)](ClO₄)₂·0.5H₂O: C, 43.16; H, 3.77; N, 12.59; Cl, 10.62. Found: C, 43.19; H, 3.62; N, 12.40; Cl, 10.84. ESI-MS: Calcd for C₂₄H₂₄ClCuN₆O₄⁺, 558.0838; found 558.0839 [M⁺].

[Cu(bmet)](Br)₂·2MeCN

Addition of solutions of bmet (47.2 mg, 1.2 × 10⁻⁴ mol) and CuBr₂ (26.6 mg, 1.2 × 10⁻⁴ mol) resulted in a green precipitate. Acetonitrile (1 mL) was added to the mixture and heating resulted in dissolution. A light green precipitate formed upon cooling and standing overnight. The precipitate was filtered and air dried, and the filtrate was then left to evaporate, giving dark green crystals. IR spectroscopy showed the precipitate and crystals to be identical. *Anal.* ESI-MS: Calcd for C₂₄H₂₃N₆Cu⁺, 458.1275; found 458.1237 [M⁺]. Acceptable microanalytical data for this complex could not be obtained.

[Zn(bmet)](ClO₄)₂·0.5H₂O

A light yellow solution formed on mixing solutions of bmet (50.3 mg 1.3 × 10⁻⁴ mol) and Zn(ClO₄)₂·6H₂O (46.5 mg, 1.3 × 10⁻⁴ mol). The solution was left to evaporate over a period of two weeks, giving colourless block crystals. (61.9 mg, 71%) *Anal.* Calcd. for [Zn(C₂₄H₂₄N₆)](ClO₄)₂·0.5H₂O: C, 43.05; H, 3.76; N, 12.55; Cl, 10.59. Found: C, 42.97; H, 3.76; N, 12.57; Cl, 10.66. ESI-MS: Calcd for C₂₄H₂₄ClN₆O₄Zn⁺, 559.0834; Found 559.0825 [M⁺].

References

- (1) *TEXSAN*; Single Crystal Structure Analysis Software; Molecular Structure Corp: The Woodlands, TX, 1995.
- (2) *ABSPACK*; CrysAlis PRO RED; Abingdon, Oxfordshire, England, 2010.
- (3) Sheldrick, G. M. *SHELXTL-Plus, Structure Determination Software Programs*; Madison, Wisconsin, USA, 1998.
- (4) Neese, F. *Wiley Interdiscip. Rev. Comput. Mol. Sci.* **2012**, *2*, 73–78.
- (5) Perdew, J. P. *Phys. Rev. B* **1986**, *33*, 8822–8824.
- (6) Perdew, J. P. *Phys. Rev. B* **1986**, *34*, 7406–7406.
- (7) Becke, A. *Phys. Rev.* **1988**, *38*, 3098–3100.
- (8) Schäfer, A.; Huber, C.; Ahlrichs, R. *J. Chem. Phys.* **1994**, *100*, 5829–5835.
- (9) Neese, F. *J. Comput. Chem.* **2003**, *24*, 1740–1747.
- (10) Weigend, F. *Phys. Chem. Chem. Phys.* **2006**, *8*, 1057–1065.
- (11) Klamt, A.; Schuurmann, G. *J. Chem. Soc.-Perkin Trans. 2* **1993**, 799–805.
- (12) Lee, C.; Yang, W.; Parr, R. G. *Phys. Rev. B* **1988**, *37*, 785–789.
- (13) Neese, F. *Inorganica Chim. Acta* **2002**, *337*, 181–192.
- (14) Kutzelnigg, W.; Fleischer, U.; Schindler, M. In *Deuterium and Shift Calculation; NMR Basic Principles and Progress*; Springer Berlin Heidelberg, 1991; pp. 165–262.
- (15) Huzinaga, S. *J. Chem. Phys.* **1965**, *42*, 1293–1302.
- (16) Uchida, Y.; Echikawa, N.; Oae, S. *Heteroat. Chem.* **1994**, *5*, 409–413.
- (17) Newkome, G. R.; Onishi, M.; Puckett, W. E.; Deutsch, W. A. *J. Am. Chem. Soc.* **1980**, *102*, 4551–4552.
- (18) Gennari, M.; Orio, M.; Pécaut, J.; Neese, F.; Collomb, M.-N.; Duboc, C. *Inorg. Chem.* **2010**, *49*, 6399–6401.
- (19) Schmalzl, K.; Summers, L. *Aust. J. Chem.* **1977**, *30*, 657–662.
- (20) Heirtzler, F. R.; Neuburger, M.; Zehnder, M.; Constable, E. C. *Liebigs Ann.* **1997**, *1997*, 297–301.
- (21) Baird, L. J.; Black, C. A.; Blackman, A. G. *Polyhedron* **2007**, *26*, 378–384.
- (22) Gennari, M.; Gerey, B.; Hall, N.; Pécaut, J.; Vezin, H.; Collomb, M.-N.; Orio, M.; Duboc, C. *Dalton Trans.* **2012**, *41*, 12586.

APPENDIX

X-Ray Diffraction Data

Crystal data and structure refinement for Et₃NH[VO₂L^{NS2}].MeOH

Empirical formula	C ₄₀ H ₄₇ N ₂ O ₃ S ₂ V
Formula weight	718.86
Crystal size, mm	0.4 x 0.28 x 0.08
Crystal system	Triclinic
Space group	<i>P</i> -1
<i>a</i> , Å	10.791(2)
<i>b</i> , Å	13.505(3)
<i>c</i> , Å	14.913(2)
α deg.	101.140(10)
β , deg.	105.14(2)
γ , deg.	108.55(2)
<i>V</i> , Å ³	1896.1(6)
<i>Z</i>	2
<i>T</i> , K	200(2)
ρ (calc), mg/m ³	1.259
μ , mm ⁻¹	0.410
θ range, deg.	1.48 to 26.00
No. of rflcn/obsv	35023 / 7475
GooF	1.087
<i>R</i> 1	0.0488
<i>wR</i> 2	0.1098

Crystal data and structure refinement for PPN[VCl₂L^{NS2}] \cdot 2CH₂Cl

Empirical formula	C ₇₁ H ₆₁ Cl ₆ N ₂ P ₂ S ₂ V
Formula weight	1331.92
Crystal size, mm	0.21 x 0.12 x 0.08
Crystal system	Triclinic
Space group	<i>P</i> -1
<i>a</i> , Å	11.2437(8)
<i>b</i> , Å	16.7554(9)
<i>c</i> , Å	17.8325(14)
α , deg.	88.901(5)
β , deg.	81.777(6)
γ , deg.	75.936(6)
<i>V</i> , Å ³	3224.9(4)
<i>Z</i>	2
<i>T</i> , K	150(2)
ρ (calc), mg/m ³	1.372
μ , mm ⁻¹	0.561
θ range, deg.	3.38 to 26.37
No. of rflcn/obsv	26326 / 13145
GooF	1.066
<i>R</i> 1	0.0830
<i>wR</i> 2	0.2043

Crystal data and structure refinement for $[\text{Ni}_2(\text{L}^{\text{NS}_2})_2] \cdot 2\text{THF}$

Empirical formula	$\text{C}_{82}\text{H}_{86}\text{N}_2\text{Ni}_2\text{O}_4\text{S}_4$
Formula weight	1409.19
Crystal size, mm	0.73 x 0.10 x 0.08
Crystal system	Triclinic
Space group	$P-1$
a , Å	10.0714(4)
b , Å	13.6763(6)
c , Å	14.2968(6)
α deg.	114.140(4)
β , deg.	90.309(3)
γ , deg.	106.268(4)
V , Å ³	1708.82(13)
Z	1
T , K	150(2)
ρ (calc), mg/m ³	1.369
μ , mm ⁻¹	0.728
θ range, deg.	3.43 to 30.51
No. of rflcn/obsv	20805 / 10349
GooF	1.014
$R1$	0.0499
$wR2$	0.0983

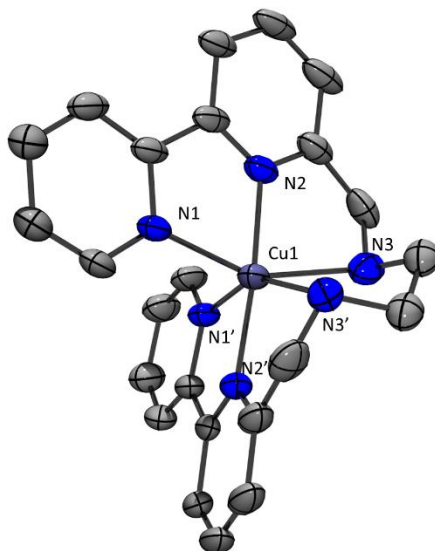
Crystal data and structure refinement for Co complexes presented in Chapter V

[CoL^{N2S2}] has been previously reported in

Gennari, M.; Gerey, B.; Hall, N.; Pécaut, J.; Vezin, H.; Collomb, M.-N.; Orio, M.; Duboc, C. *Dalton Trans.* **2012**, 41, 12586.

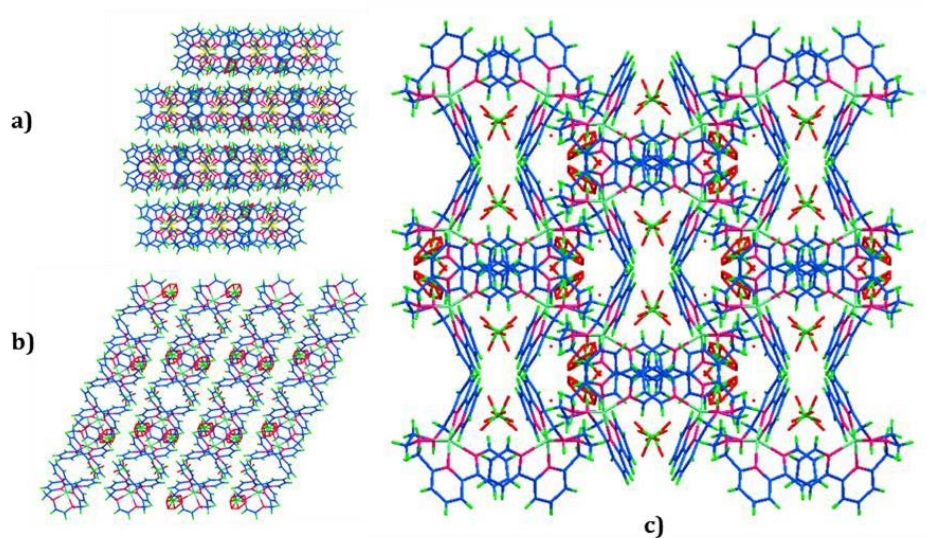
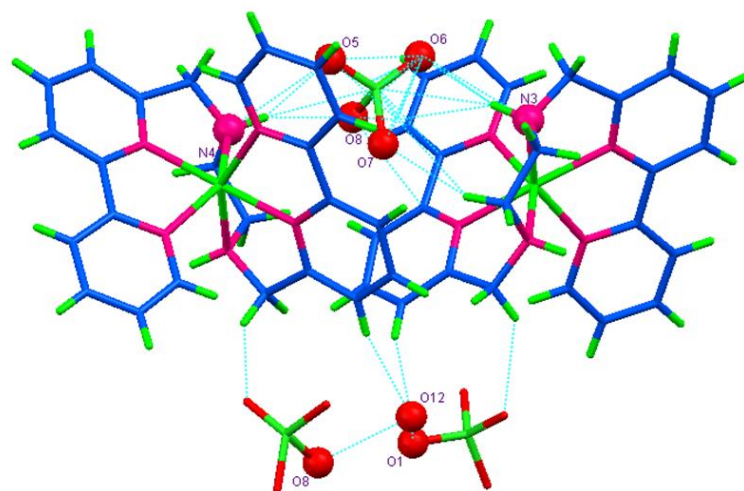
	[CoL ^{N2S2} Cl]	[Co ₂ (L ^{N2S2}) ₂](PF) ₆ ·2MeCN
Empirical formula	C ₃₈ H ₃₀ CoN ₂ S ₂ Cl	C ₈₀ H ₆₆ Co ₂ N ₆ S ₄ P ₂ F ₁₂
Formula weight	673.14	1647.43
Crystal size, mm	0.54x0.37x0.03	0.21x0.07x0.05
Crystal system	Monoclinic	Monoclinic
Space group	<i>P</i> 21/ <i>c</i>	<i>C</i> 2/ <i>c</i>
<i>a</i> , Å	14.6197(4)	19.9870(6)
<i>b</i> , Å	14.8634(3)	17.2448(5)
<i>c</i> , Å	15.9837(5)	22.0690(8)
α deg.	90.00	90.00.00
β, deg.	115.315(4)	112.265(4)
γ, deg.	90.00	90.00.00
<i>V</i> , Å ³	3139.70(18)	7039.4(4)
<i>Z</i>	4	4
<i>T</i> , K	150(2)	150(2)
ρ (calc), mg/m ³	1.424	1.554
μ, mm ⁻¹	0.796	0.720
θ range, deg.	3.45 to 28.28	3.29 to 26.37
No. of rflcn/obsv	33351 / 7783	30271 / 7189
GooF	0.785	0.764
<i>R</i> 1	0.0328	0.0390
<i>wR</i> 2	0.0524	0.0566

Crystal data and structure refinement for Cu complexes presented in Chapter VI



ORTEP diagram of the cation of $[\text{Cu}(\text{bmet})]\text{Br}_2 \cdot 2\text{MeCN}$. Bromide anions, solvent molecules and hydrogen atoms have been omitted for clarity.

	$[\text{Cu}(\text{bmet})]\text{Br}_2 \cdot 2\text{MeCN}$	$[\text{Cu}(\text{bmet})](\text{ClO}_4)_2 \cdot \text{H}_2\text{O}$	$[\text{Zn}(\text{bmet})](\text{ClO}_4)_2 \cdot \text{H}_2\text{O}$
Empirical formula	$\text{C}_{14}\text{H}_{15}\text{BrCu}_{0.50}\text{N}_4$	$\text{C}_{48}\text{H}_{48}\text{Cl}_4\text{Cu}_2\text{N}_{12}\text{O}_{18}$	$\text{C}_{48}\text{H}_{48}\text{Cl}_4\text{N}_{12}\text{O}_{18}\text{Zn}_2$
Formula weight	350.98	1349.86	1353.52
Crystal size, mm^3	0.53 x 0.39 x 0.39	0.5 x 0.41 x 0.41	0.44 x 0.41 x 0.35
Crystal system	Orthorhombic	Monoclinic	Monoclinic
Space group	<i>Pnna</i>	<i>C2/c</i>	<i>C2/c</i>
<i>a</i> , Å	16.185(5)	22.3900(15)	22.674(5)
<i>b</i> , Å	14.081(4)	14.3020(11)	14.380(3)
<i>c</i> , Å	12.616(4)	18.2440(14)	18.106(4)
α , deg.	90.00	90.00	90.00.00
β , deg.	90.00	112.878(4)	113.286(9)°
γ , deg.	90.00	90.00	90.00.00
<i>V</i> , Å ³	2875.2(16)	5382.6(7)	5423(2)
<i>Z</i>	8	4	4
<i>T</i> , K	89(2)	89(2)	89(2)
ρ (calc), mg/m^3	1.622	1.666	1.658
μ , mm^{-1}	3.572	1.076	1.168
θ range, deg.	2.17 to 24.47	1.73 to 25.50	2.45 to 25.50
No. of rflcn/obsv	45994 / 2368	49650 / 4998	34582 / 5047
GooF	1.076	1.183	1.280
<i>R</i> 1	0.0700	0.0678	0.0415
<i>wR</i> 2	0.1292	0.1815	0.1092

Packing Environment of $[\text{Zn}(\text{bmet})](\text{ClO}_4)_2 \cdot \text{H}_2\text{O}$ Packing diagram of $[\text{Zn}(\text{bmet})](\text{ClO}_4)_2 \cdot \text{H}_2\text{O}$ viewed down the *a*-, *b*- and *c*- axes.Hydrogen bonds in $[\text{Zn}(\text{bmet})](\text{ClO}_4)_2 \cdot \text{H}_2\text{O}$.

Abbreviations

Ligands –This work	
L ^{N2S2}	2,6-bis(2,2-diphenyl-1,2-mercaptoethyl)-2,2'-bipyridine
L ^{NS2}	2,6-bis(2,2-diphenyl-1,2-mercaptoethyl)pyridine
bmet	<i>N,N'</i> -bis(2,2'-bipyridin-6-ylmethyl)ethane-1,2-diamine

Ligands - Literature	
pdmt	Pyridine-2,6-dimethanethiolate
pdtc	Pyridine-2,6-dithiocarboxylate
bpp	2,6-bis(<i>N</i> -pyrazolyl)pyridine
bpp R = <i>Mes</i>	2,6-bis(3{5}-mesitylpyrazolyl)pyridine
pma R = <i>t</i> -But	2,6-bis(<i>tert</i> -butyliminomethyl)pyridine
pma R = Me	2,6-bis(methyliminomethyl)pyridine
terpy	2,2':6'2"-terpyridine
ddpe	<i>N,N'</i> -dimethyl- <i>N,N'</i> -dipyridin-2-yl-pyridin-2,6-diamine

Abstract

This thesis presents the synthesis and characterisation of bio-inspired molecular complexes containing metal alkyl thiolate bonds with the goal of modelling metalloenzymes. In particular, we have attempted to improve our knowledge on the role that the bound alkyl thiolate plays in metalloenzymes, including, structural features, electronic properties and also reactivity of the associated active sites. The bound alkyl thiolate undergoes two main reactions in metalloenzymes; S-alkylation and S-oxygenation. From the isolation and characterisation of the corresponding active sites, it can be seen that the reactivity of the bound alkyl thiolate depends greatly on the metallic ion. In this context, different M^{n+} -thiolate complexes have been synthesized (V^{III} , V^{IV} , V^V , Ni^{II} , Ni^{III} , Co^{II} and Co^{III}), with either a tetradentate $L^{N_2S_2}$ or a tridentate L^{NS_2} ligand. Both ligands consist of aromatic nitrogen (bipyridine or pyridine) donor atom(s) and also two bulky S-thiolate donor atoms.

We have shown that the Co^{II} ion is a suitable structural substitute for Zn-containing metalloenzymes, however, it is inappropriate as a functional substitute in the particular case of S-alkylation. Furthermore, we have been able to structurally model the activation step of cobalt nitrile hydratase, with the incorporation of three oxygen atoms on a Co^{III} bis alkyl thiolate complex evidencing dissymmetrical S-oxygenation. In contrast, using vanadium and nickel, metal-peroxo species have been generated, without intramolecular S-oxygenation. This research has led to some of the first examples of active oxygen nickel and vanadium complexes using alkyl thiolate ligands.

We have also attempted to model very difficult reactions carried out by sulfur rich metalloenzymes, especially the activation and reduction of dinitrogen realised by nitrogenases. To model this enzyme, a V^{III} alkyl thiolate complex has been synthesised and its reactivity investigated. Preliminary results suggest that the reduced V^{II} species has the ability to activate and reduce hydrazine into ammonia, which is proposed to be the final stage of dinitrogen reduction.

Résumé

Cette thèse présente la synthèse et la caractérisation de complexes moléculaires bio-inspirés à liaison métal-thiol avec l'objectif de modéliser le site actif de certaines métalloenzymes. En particulier, notre but était d'améliorer notre compréhension sur le rôle que joue cette liaison métal-thiol dans les métalloenzymes, notamment au niveau de ses propriétés structurales et électroniques ainsi que sur la réactivité des sites actifs associés. Le thiol lié à un métal peut être sujet à deux types de réaction dans métalloenzymes : les réaction de S- alkylation ou de S-oxygénation. Il a été montré que la réactivité de ces ligands thiols dépend fortement de la nature de l'ion métallique. Dans ce contexte, différents complexes thiolate M^{n+} ont été synthétisés (V^{III} , V^{IV} , V^V , Ni^{II} , Ni^{III} , Co^{II} et Co^{III}), soit avec un ligand $L^{N_2S_2}$ tétradentate ou L^{NS_2} tridentate. Ces deux ligands sont constitués d'un ou deux azote(s) aromatique(s) (bipyridine ou pyridine) et de deux thiols aliphatiques encombrants.

Nous avons montré que le Co^{II} ion représente un substitut structural satisfaisant pour les métalloenzymes contenant du zinc. Cependant, il n'est pas approprié comme substitut fonctionnel dans le cas particulier de la réaction de S- alkylation. En outre, nous avons pu modéliser l'étape d'activation de nitrile hydratase à cobalt, avec l'incorporation de trois atomes d'oxygène sur un complexe bis-thiolate de Co^{III} présentant la même dissymétrie que dans l'enzyme lors de la réaction de S- oxygénation. En revanche, avec le vanadium et le nickel, des espèces métal-peroxo ont pu être générées sans réaction intramoléculaire de S- oxygénation. Nos travaux ont ainsi conduit à l'obtention des premiers exemples de complexes peroxos du nickel et du vanadium possédant des liaisons métal-thiol.

Nous avons également tenté de modéliser des réactions réalisées par des métalloenzymes dont le site actif est riche en soufre, dont l'activation et la réduction du diazote en ammoniac, réaction réalisée par les nitrogénases. Pour modéliser ces enzymes, un complexe thiolate du V^{III} a été synthétisé et sa réactivité étudiée. Nos résultats préliminaires suggèrent que l'espèce réduite de V^{II} correspondante est capable d'activer et de réduire l'hydrazine en ammoniac, réaction correspondant à la dernière étape de la réduction du diazote.